– NACA 0021 –
Dynamic Airfoil Measurements at Low Reynolds Number through High Angles of Attack

vorgelegt von

M. Sc.
David Holst
ORCID: 0000-0002-9829-3416

an der Fakultät V - Verkehrs- und Maschinensysteme
der Technischen Universität Berlin
zur Erlangung des akademischen Grades

Doktor der Ingenieurwissenschaften
— Dr.-Ing. —

genehmigte Dissertation

Promotionsausschuss:

Vorsitzender:	Prof. Dr.-Ing. Paul Uwe Thamsen
Gutachter:	Prof. Dr.-Ing. Christian Oliver Paschereit
Gutachter:	Dr. René Woszidlo

Tag der wissenschaftlichen Aussprache:
14.11.2022

Berlin 2022

— **To my family** —

They have the power to transform a rough day
into one that is filled with joy.

Abstract

The demand in renewable energy is boosted by the shift of our society towards sustainability and the goal to decarbonize the power sector. Wind industry becomes more important these days and begins to enter urban environment. Smaller vertical axis wind turbines (VAWTs) are advantageous in this flow field of unsteady wind conditions and high turbulence. Literature often only covers incidence ranges up to stall angle. However, VAWTs experience angles far beyond stall, especially during start-up. The thesis describes the aerodynamic performance of a NACA 0021 airfoil section at Reynolds numbers relevant to small wind turbines. Typical wind tunnel blockage effects are reduced using an open test section. Surface pressure measurements and numerical simulations are performed to statically and dynamically gather lift, drag, and pitching moment data of the NACA 0021. The work consists of four publications.

Firstly, static experiments are carried out to investigate the lift, drag, and moment performance of the NACA 0021 airfoil at three Reynolds numbers ($Re = 100\,\mathrm{k}, 140\,\mathrm{k}, 200\,\mathrm{k}$) through 180 degree of incidence. The hysteresis investigations reveal a second hysteresis loop in the deep post stall region, which is strongly characterized by large standard deviations of the pressure signals. These variations are several orders of magnitude larger than those in the classical stall region.

The second study concentrates on dynamic sinusoidal pitching movements and compares them to the static lift curves of the first publication. The dynamic experiments vary in reduced frequency k and focus on three ranges of incidence: near stall, post stall, and deep stall. Various bi-stable flow states are discovered and discussed. Bi-stable data sets are separated by a manual binning procedure, allowing for an individual discussion of the various occurring flow phenomena. Further insights are provided by a detailed analysis of the airfoil's surface pressure distribution. The measurements reveal large lift fluctuations in both the post and deep stall regime. The amplitudes exceed the order of maximum lift in the static lift curves and are not captured by averaged measurements.

The third investigation assesses the systematic influences the setup has on the experiments. Numerical studies are used to gain additional insights of the flow field, whilst also simulating the experimental setup as well as a fully undisturbed flow situation. The comparison leads to correction factors that are used to eliminate the systematic influences in the experimental data. Simulations focus on recreating the static lift polars as well as chosen dynamic sinusoidal lift cycles, that were previously tested during the experiments. Numeric data is evaluated in order to discuss the numerical limits in dynamic cycle calculation.

The fourth paper is another combined investigation of experimental and numerical data. The focus lies on drag and moment coefficients that have not been included in the previous publications, and a detailed literature comparison is used to validate the experimental results. The simulation setups of the open field and wind tunnel are used to reproduce the experiments, achieving good agreement for static polars, barring some limitations concerning the moment coefficients. The correction factors introduced in the third work are extended to cover also the drag data, and a discussion on the differences in static stall angle and the extent of the hysteresis cycle is presented.

Finally, the thesis is completed by introducing an automated binning method. The application of such a method was proposed in the second publication to evade the manual selection of bins, but was not included. The `k-means++` clustering method is applied using the available experimental data. A detailed analysis of two selected test cases is able to provide further insights into the bi-stable behavior revealed in the second paper, as well as into the regime of the second hysteresis loop found in the first paper.

Kurzfassung

Die Transformation unserer Gesellschaft hin zu mehr Nachhaltigkeit und kohlenstoffneutraler Energieversorgung verstärkt die Nachfrage nach erneuerbaren Energien. Die Windkraftindustrie gewinnt aktuell weiter an Bedeutung und ist auch immer öfter im urbanen Umfeld anzutreffen. In den dort vorherrschenden Umgebungsbedingungen mit erhöhter Turbulenz und stark schwankenden Winden haben vertikalachsige Windkraftanlagen Vorteile. Die aerodynamischen Daten der hierfür relevanten Profile werden jedoch von der Literatur vorrangig nur in den Winkelbereichen bis kurz nach dem Strömungsabriss betrachtet. Die Flügel von vertikalachsigen Windkraftanlagen durchlaufen jedoch Anströmwinkel weit jenseits und dies insbesondere während des Anlaufvorgangs. Die vorliegende Arbeit beschreibt die aerodynamischen Eigenschaften eines NACA 0021 Profils bei Reynoldszahlen, die typisch für Kleinwindkraftanlagen sind. Oberflächendruckmessungen und numerische Simulationen ermöglichen neue Einsichten in das statische und dynamische Verhalten des NACA 0021 Profils. Die bei Windkanalversuchen typischerweise auftretenden Verblockungseffekte werden reduziert, da die Experimente in einer offenen Teststrecke durchgeführt werden. Das Kernstück dieser Arbeit wird durch vier Publikationen gebildet.

Die erste untersucht Auftriebs-, Widerstands- und Momentenverläufe bei drei verschiedenen Reynoldszahlen ($Re = 100\,\mathrm{k}, 140\,\mathrm{k}, 200\,\mathrm{k}$) über einen 180 Grad Anstellwinkelbereich. Zusätzliche Hystereseuntersuchungen zeigen einen zweiten Hysteresebereich weit jenseits des klassischen Strömungsabrisses. Dieser wird durch stark erhöhte Standardabweichungen charakterisiert, welche mehrere Größenordnungen über denen des klassischen Hysteresebereiches liegen.

Die zweite Studie konzentriert sich auf das dynamische Verhalten und untersucht dynamische sinusförmige Änderungen des Anstellwinkels und deren Auswirkungen auf den Auftrieb. Die gemessenen dynamischen Polaren werden mit den statischen Messungen der ersten Messkampagne verglichen. Die Versuche fokussieren sich auf drei Winkelbereiche: bis an den Strömungsabriss; im und jenseits des Strömungsabrisses. In jedem dieser Bereiche werden Versuche mit unterschiedlichen reduzierten Frequenzen k durchgeführt. Die Experimente zeigten mehrere bistabile Strömungsphanomäne, die im Rahmen der Arbeit weiter analysiert werden. Hierbei werden die Auftriebspolaren manuell gruppiert, um die Zustände einzeln zu diskutieren. Detaillierte Oberflächendruckverläufe bieten hierbei weitere Einsicht. Die dynamischen Experimente zeigen zusätzlich starke Auftriebsschwankungen jenseits des klassischen Strömungsabriss. Die Amplituden der Schwankungen haben eine Größenordnung, die dem Maximalauftrieb entspricht, und diese werden durch gemittelte Messungen nicht erfasst.

Der dritte Artikel konzentriert sich unter anderem auf den Einfluss des Versuchsaufbaus. Numerische Simulationen ermöglichen hierbei den Vergleich zwischen einer ungestörten 2D-Strömung und der simulierten offenen Teststrecke. Die Untersuchungen ermöglichen die Bereinigung der Messdaten durch das Einführen von Korrekturfaktoren. Die statischen und ausgewählte dynamische Experimente wurden zusätzlich numerisch simuliert. Die erhaltenen Daten bilden die Grundlage für eine Bewertung inwieweit die gewählte Simulation die dynamischen Effekte nachbilden kann.

Die vierte Publikation kombiniert erneut experimentelle und numerische Untersuchungen. Hierbei liegt der Fokus jedoch auf den Widerstands- und Momentenbeiwerten, die im vorhergehenden Artikel nicht betrachtet wurden. Ein weiterer Vergleich mit Literaturdaten bestätigt die experimentellen Messwerte. Die Wiederverwendung der simulierten Teststrecke und der ungestörten 2D-Strömung erzielt gute Übereinstimmungen bei den Widerstandswerten, beinhaltete jedoch Abweichungen bei den Momenten. Die in der drit-

ten Veröffentlichung eingeführten Korrekturfaktoren werden für die Widerstandsbeiwerte angepasst und entsprechend erweitert. Die Unterschiede zwischen Simulation und Experiment, insbesondere die Abweichungen bei der Hysterese und dem Strömungsabriss, werden detailliert analysiert.

Im Anschluss an die Publikationen wird eine automatisierte Gruppierung von Messdaten eingeführt. Die Verwendung einer solchen Methode wurde schon in der zweiten Veröffentlichung angeregt, um die manuelle Zuordnung zu ersetzen. Es wird hierzu die Clusterbildung mit Hilfe des `k-means++` Algorithmus getestet. Aus den bestehenden Messdaten der Veröffentlichungen werden zwei Testfälle ausgewählt: Zum einen das dynamische Experiment aus der zweiten Veröffentlichung, dass die Grundlage für die Untersuchungen der bistabilen Polaren bildete und zum anderen ein Fall, der den zweiten Hysteresebereich abdeckt, der im ersten Artikel analysiert wurde.

Contents

List of figures II

List of tables III

Nomenclature III

1 Introduction and motivation 1

2 Fundamental background information 4
2.1 Experimental basics 4
2.2 Hardware 5
2.3 Software 8

3 Publications 11
3.1 Exp. Analysis of a NACA 0021 Airfoil Section Through 180° AoA at low Re for Use in Wind Turbine Analysis 12
3.2 Experimental Analysis of a NACA 0021 Airfoil Under Dynamic AoA Variation and Low Re 24
3.3 Static and Dynamic Analysis of a NACA 0021 Airfoil Section at Low Re Based on Experiments and CFD 34
3.4 Static and Dynamic Analysis of a NACA 0021 Airfoil Section at Low Re - Drag and Moment Coefficients 44

4 Clustering for dynamic analysis 58
4.1 Clustering – The basic concept 58
4.2 Test case: Separate intermediate flow cases 62
4.3 Test case: Clustering highly fluctuating data 67

5 Concluding discussion 71
5.1 Challenges and possible improvements 71
5.2 Review of selected inflow conditions 74
5.3 Discussion of the results 75
5.4 Concluding remarks and future work 78

References 80

Associated publications 85

List of figures

1 Flow basics up to deep stall 5
2 Hermann Föttinger Institute's laminar wind tunnel. 6
3 Setup for dynamic and static measurements 6
4 Estimated amplitude and phase shift based on sensor mounting and tubing 7
5 Estimated system response 7
6 Setup communication structures 9
7 Motor velocity profiles 10
8 Concept of data clustering. 58
9 40 repetitions of sinusoidal airfoil movement between 0 deg to 20 deg at $Re = 140\,\text{k}$ and $k = 0.05$ 59
10 40 repetitions of sinusoidal airfoil movement between 0 deg to 20 deg at $Re = 140\,\text{k}$ and $k = 0.05$ separated into two clusters 60
11 Two cluster centroids of sinusoidal airfoil movement between 0 deg to 20 deg at $Re = 140\,\text{k}$ and $k = 0.05$ 60
12 Cluster 1 of 2: Pressure coefficient distribution of sinusoidal airfoil movement between 0 deg to 20 deg at $Re = 140\,\text{k}$ and $k = 0.05$. 61
13 Cluster 2 of 2: Pressure coefficient distribution of sinusoidal airfoil movement between 0 deg to 20 deg at $Re = 140\,\text{k}$ and $k = 0.05$. 61
14 40 repetitions of sinusoidal airfoil movement between 0 deg to 20 deg at $Re = 140\,\text{k}$ and $k = 0.05$ separated into seven clusters 63
15 Seven cluster centroids of sinusoidal airfoil movement between 0 deg to 20 deg at $Re = 140\,\text{k}$ and $k = 0.05$ 63
16 Cluster centroid 1 of 7: Pressure coefficient distribution of sinusoidal airfoil movement between 0 deg to 20 deg at $Re = 140\,\text{k}$ and $k = 0.05$. 64
17 Cluster centroid 2 of 7: Pressure coefficient distribution of sinusoidal airfoil movement between 0 deg to 20 deg at $Re = 140\,\text{k}$ and $k = 0.05$. 64
18 Cluster centroid 5 of 7: Pressure coefficient distribution of sinusoidal airfoil movement between 0 deg to 20 deg at $Re = 140\,\text{k}$ and $k = 0.05$. 65
19 Cluster centroid 6 of 7: Pressure coefficient distribution of sinusoidal airfoil movement between 0 deg to 20 deg at $Re = 140\,\text{k}$ and $k = 0.05$. 65
20 Cluster centroid 3 of 7: Pressure coefficient distribution of sinusoidal airfoil movement between 0 deg to 20 deg at $Re = 140\,\text{k}$ and $k = 0.05$. 66
21 Cluster centroid 7 of 7: Pressure coefficient distribution of sinusoidal airfoil movement between 0 deg to 20 deg at $Re = 140\,\text{k}$ and $k = 0.05$. 66
22 Cluster centroid 4 of 7: Pressure coefficient distribution of sinusoidal airfoil movement between 0 deg to 20 deg at $Re = 140\,\text{k}$ and $k = 0.05$. 67
23 Polars between 0 deg to 180 deg at $Re = 180\,\text{k}$ 68
24 Three cluster centroids of sinusoidal airfoil movement between 0 deg to 180 deg (90 deg to 180 deg shown) at $Re = 180\,\text{k}$ and $k = 0.0025$ 68
25 Cluster centroid 1 of 3: Pressure coefficient distribution of sinusoidal airfoil movement between 0 deg to 180 deg (focus on 90 deg to 180 deg) at $Re = 180\,\text{k}$ and $k = 0.0025$. 69
26 Cluster centroid 2 of 3: Pressure coefficient distribution of sinusoidal airfoil movement between 0 deg to 180 deg (focus on 90 deg to 180 deg) at $Re = 180\,\text{k}$ and $k = 0.0025$. 69
27 Cluster centroid 3 of 3: Pressure coefficient distribution of sinusoidal airfoil movement between 0 deg to 180 deg (focus on 90 deg to 180 deg) at $Re = 180\,\text{k}$ and $k = 0.0025$. 70

List of tables

1 Re_c and according inflow velocity u_∞ in correlation to real wind speeds u_{wind} at predefined TSRs of a wind turbine 74

Nomenclature

α	[deg]	Incidence or angle of attack (AoA)
$\ddot{\alpha}_{acc}$	[$^{\text{deg}}/_{\text{s}^2}$]	(Angular) acceleration
$\ddot{\alpha}_{dec}$	[$^{\text{deg}}/_{\text{s}^2}$]	(Angular) deceleration
$\dot{\alpha}_d$	[$^{\text{deg}}/_{\text{s}}$]	(Angular) drive velocity
$\dot{\alpha}_e$	[$^{\text{deg}}/_{\text{s}}$]	(Angular) end velocity
ν	[$^{\text{N m}}/_{\text{kg}}$]	Kinematic viscosity
ρ	[$^{\text{kg}}/_{\text{m}^3}$]	Density
c	[m]	Chord length
c_l	[-]	Lift coefficient
c_m	[-]	Moment coefficient
c_n	[-]	Normal force coefficient
c_p	[-]	Pressure coefficient
c_t	[-]	Tangential force coefficient
$c_{d,p}$	[-]	Pressure drag coefficient
c_d	[-]	Drag coefficient
N_α		Number of AoA steps in one movement cycle
N_c		Number of cycles in dynamic motor movement
p_{stat}	[Pa]	Static pressure of inflow
p_{surf}	[Pa]	Surface pressure
q	[Pa]	Dynamic pressure of inflow
s	[-]	Surface coordinate
s		Feature space for clustering
T	[s]	Signal period
u_∞	[$^{\text{m}}/_{\text{s}}$]	Inflow velocity
u_{tip}	[$^{\text{m}}/_{\text{s}}$]	Tip speed
u_{wind}	[$^{\text{m}}/_{\text{s}}$]	Wind speed

$X = x/c$	[-]	Normalized tangential profile coordinate
$Y = y/c$	[-]	Normalized normal profile coordinate
AoA		Angle of attack
CAN		Controller area network
FPGA		Field programmable gate array
LE		Leading edge
TE		Trailing edge
TSR		Tip speed ratio
VAWT		Vertical axis wind turbines

1 Introduction and motivation

2020 was a record year for wind energy for several countries in the world. China built more than 50 GW new capacity and additionally the United States, Norway, Sweden, and Belgium achieved all-time records [1]. Germany reached a net increase in wind power capacity of 1.4 GW in 2020 and a total installed wind power capacity of 62.2 GW which is more than 23 % of the national electricity demand [1]. The devastating events of 2022 highlighted the fragility of fossil fuel supply, leading to a further shift in energy production focus towards renewable energies, e.g., the German federal government aims to cover 80 % of their energy consumption by renewable sources by 2030 [2]. The industry mainly focuses on large wind turbines able to generate multi-megawatts, causing project costs for such systems to decrease over time. Meanwhile, the costs for distributed wind energy production did not decline, causing the IEA to initiate Task 41 [3] 'Enabling Wind Power to Contribute to a Distributed Energy Future' in the year of 2019, in order to address the topics related to distributed wind [1, 3]. Nearly 50 % of all commercial building's energy demand in 2019 was electricity. This figure is supposed to increase up to approx. 60 % in 2050 [4]. Wind turbines may serve to meet the energy demand of the building sector in general. Furthermore, the European Commission expects the share of electricity in the residential sector to grow to 50-70 % by 2050 [4]. The IEA Task 41 team identified a research need for 'international design and testing standards for small and mid-sized wind turbines' [3]. The smaller turbines are particularly significant for residential settings, either in the form of direct usage, or any overproduction may be fed into the grid [5]. They can also be easily combined with storage or photovoltaic systems. Acceptance and financial feasibility of a small wind turbine in distributed energy systems directly depends on the reliability of the turbine and the total costs of energy, which is one of the driving factors in economic decisions [6]. Financial decisions, i.e., the calculation of the pay-back period, are based on the power curve of a wind turbine, which is notably more difficult for smaller wind turbines than it is for larger ones. Often small wind turbines have inaccurate or even absent power curves [7]. A study of Simic et al. in 2013[8] showed that at certain wind speeds, the power curve data of 15 out of 43 turbines under investigation exceeded the maximal physically possible values of power per square meter – the Betz limit.

In terms of wind turbine application, a residential setting proves challenging due to the higher inflow turbulence and a greater number of obstacles in the surrounding area that may mitigate the turbine's performance. A study of Acosta et al. [9] depicted the importance of an accurate assessment of the wind energy resources in an urban area highlighting that average wind speeds are not sufficient. Their analysis revealed, that a worst case combination may result in a poor overall wind turbine efficiency of nearly 20 %, thus resulting in economically unsatisfying pay-back periods. The work of Acosta et al. shows that a minimum mean wind speed of up to 5.5 $^{m}/_{s}$ may be necessary in order to achieve at least a pay-back period of 15 years. Any higher wind speed would be questionable in urban environment [9], which is why in their study Grieser et al. assume average wind speeds in the range of 3-5.5 $^{m}/_{s}$ for urban settings in Germany [10]. Urban inflow conditions, i.e., high turbulence, gusts and fluctuating wind directions, are demanding and therefore not every type of turbine is suitable. The study of Eriksson et al. [11] assessed the topic and compared horizontal to vertical axis wind turbines and their according advantages. For residential settings vertical axis wind turbines (VAWT) show to be advantageous. The focus of these turbines lay on low cost, robust and simple construction resulting in as little maintenance as possible. A VAWT is indifferent to wind direction changes and performs better under adverse wind conditions [11]. The construction can be simplified by applying an a H-rotor concept instead of the classical Darrieus turbine. Straight blades and an

incomplex mechanical structure with a low number of moving parts reduce the risk of failure and lead to a maintenance friendly system [11].

Wind turbines in urban environment have to operate at low wind speeds [9, 10]. Thus, the start-up of the turbine is crucial to the overall performance, as the turbines require a low cut-in wind speed to operate sufficiently. Several studies investigated the start-up processes of wind turbines [12–15], indicating that an improved start-up performance may increase the energy yield by up to 40 % [14, 15]. An important aspect to this performance for VAWTs is the topic of self starting, which can be problematic for two-bladed designs [15]. Fortunately, three-bladed designs are able to overcome these issues, and the turbines are able start-up at much lower than datum speed [12]. The turbine optimization should concentrate on the maximum annual energy yield as its main objective. As design parameters, such as optimal rotational speed, solidity and airfoil dimensions, all depend on the inflow conditions [16], a turbine mismatching the local conditions will lead to a bad investment that may find it difficult to pay off [10]. A design should not just focus on a single point of operation but ensure a satisfying energy extraction over a wide range of conditions [16] and should be matched the given inflow conditions. Several different airfoil families, e.g. NACA-, AH-, and S-series, have been used for VAWT designs over the years. The review of Zhao et al. provides a good overview of airfoils used for turbines in literature [17]. The review assesses performance improvements of lift based turbines and states, that proper airfoil data matching the flow conditions of a VAWT are of interest. This is confirmed by further authors, i.e., Worasinchai et al. [15] and Bianchini et al. [16, 18, 19], highlighting that the prediction of the start up process and the energy yield directly depends on reliable airfoil data.

The present dissertation has the goal of providing airfoil data, covering relevant flow conditions of vertical axis turbines, as well as closing literature gaps. The latter often lacks airfoil polars at high angles of attack (AoA) beyond stall especially at low Reynolds numbers. The local chord based Reynolds number Re_c is especially low during start-up and at low tip speed ratios (TSR) , thus the information is crucial to energy yield predictions [15, 16]. Additionally, VAWTs are highly dynamic systems causing the blades to work under dynamic conditions. An example of this is die AoA, which, for a VAWT, changes periodically for every revolution. Intervals of $\pm$ 180 deg are of interest during start-up, whilst at low tip speed ratios (TSRs) dynamic changes in the range of $\pm$ 40 deg to $\pm$ 20 deg are of relevance [17]. Experimental and numerical analysis presented in this thesis focus on one airfoil type – the NACA 0021. This symmetric profile is part of the 4-digit NACA series and has a thickness of 21 %. Such thick airfoils are of interest for H-shaped VAWTs as they allow for stiff constructions with fewer struts. The latter having a beneficial effect on the energy yield [16]. The thickness is also advantageous if the airfoil chord is reduced, thus increasing the aspect ratio. The following aspects summarize the steps to be taken to achieve the goals of the thesis previously defined:

1. Provide aerodynamic polar data at low Reynolds number
    - Full range of AoA
    - Hysteresis analysis
2. Investigation of airfoil performance under dynamic periodical AoA variation
    - At stall range and beyond
    - Oscillation at different rates and amplitudes
3. Assessment of systematical influences and correction methods
    - Literature validation
    - Analysis by numerical investigations

This manuscript summarizes the results of experiments and analyses conducted in order to achieve these goals. Starting of in chapter 2, a brief introduction into the aerodynamic basics is presented, followed by details of the experimental setting. This part contains the information necessary to understand the basic idea of the experiments as well as comprehend the challenges of the experimental setup. The basics are rounded of by additional information on the setup in section 2.2 and the control software in section 2.3 which cannot be found in detail within the publications in chapter 3:

3.1 David Holst, Benjamin Church, Georgios Pechlivanoglou, Ergin Tüzüner, Joseph Saverin, Christian Navid Nayeri, and Christian Oliver Paschereit. Experimental analysis of a NACA 0021 airfoil section through 180-degree angle of attack at low Reynolds numbers for use in wind turbine analysis. *J Eng Gas Turb Power*, 141: 041012–1–10, November 2018, GTP-18-1576, DOI: 10.1115/1.4041651.

3.2 David Holst, Benjamin Church, Felix Wegner, Georgios Pechlivanoglou, Christian Navid Nayeri, and Christian Oliver Paschereit. Experimental analysis of a NACA 0021 airfoil under dynamic angle of attack variation and low Reynolds numbers. *J Eng Gas Turb Power*, 141:031020–1–10, October 2018, GTP-18-1434, DOI: 10.1115/1.4041146.

3.3 David Holst, Francesco Balduzzi, Alessandro Bianchini, Benjamin Church, Felix Wegner, Georgios Pechlivanoglou, Lorenzo Ferrari, Giovanni Ferrara, Christian Navid Nayeri, and Christian Oliver Paschereit. Static and dynamic analysis of a NACA 0021 airfoil section at low Reynolds numbers based on experiments and computational fluid dynamics. *J Eng Gas Turb Power*, 141:051015–1–10, January 2018, GTP-18-1435, DOI: 10.1115/1.4041150.

3.4 David Holst, Francesco Balduzzi, Alessandro Bianchini, Christian Navid Nayeri, Christian Oliver Paschereit, and Giovanni Ferrara. Static and Dynamic Analysis of a NACA 0021 Airfoil Section at Low Reynolds Numbers: Drag and Moment Coefficients. In *Proceedings of the ASME Turbo Expo 2019, June 17-21, Phoenix AZ, USA*, volume 9: Oil and Gas Applications; Supercritical CO2 Power Cycles; Wind Energy of *Turbo Expo: Power for Land, Sea, and Air*, 06 2019, V009T48A002, DOI: 10.1115/GT2019-90500.

The publications are ordered along the lines of the goals previously defined. The first paper 3.1 concentrates on polar data across a range of 0-180 deg which represents the full range for a symmetric airfoil. Hysteresis effects as well as local fluctuations are analyzed. The second paper 3.2 focuses on the airfoil's lift under dynamic AoA variations at different rates. The third paper 3.3 compares the experimental results with numerical simulations to gain further insights into the influence of the measurement setup on the experiment, as well as to validate the results. The last paper 3.4 completes the experimental overview by focusing on drag and moment data, which were not included in the previous papers. For every paper a literature validation is included.

The publications are extended by another analysis method discussed in chapter 4 which was proposed in a publication but not included. A discussion of all publications in the overall context is provided in the final chapter 5 analyzing shortcomings and summarizing the main findings of the experiments. Furthermore, incentives for future work conclude the thesis.

2 Fundamental background information

The following sections sketch only key parts in addition to the information already included in the publications 3.1 to 3.4. Nonetheless, a few experimental basics will be introduced first before hardware and software details are discussed.

2.1 Experimental basics

The experiments are conducted in air and provide information on the performance of the NACA 0021 airfoil section at low Reynolds numbers, which, in the present studies, uses the airfoil chord c as characteristic length and is defined by equation (2-1) [20]. Re is based on the inflow velocity u_∞, eq. (2-2). The air density ρ and kinematic viscosity ν represent the ambient conditions of the experiments.

$$Re = \frac{u_\infty \cdot c}{\nu} \tag{2-1}$$

$$u_\infty = \sqrt{\frac{2 \cdot \Delta p}{\rho}} \tag{2-2}$$

Lift and drag forces as well as the moment are used to analyze the performance of the airfoil section. These parameters are typically measured by gauges gaining only integral information over the entire section. Additional information, e.g., which part of the airfoil generates the lift, is missed and requires supplementary sensors. The measurements must work over full 360 deg range of incidence and therefore surface pressure measurements were used to gain further insights. The surface pressure p_{surf} of an airfoil can be used to calculate the relevant parameters, e.g., lift, drag and moment. This calculation is based on the normalized surface pressure coefficient c_p based on equation (2-3) [21]. The difference between the surface pressure p_{surf} and the inflow's static pressure p_{stat} is divided by the inflow's dynamic pressure q.

$$c_p = \frac{p_{\text{surf}} - p_{\text{stat}}}{q} = \frac{p_{\text{surf}} - p_{\text{stat}}}{\rho \, u_\infty^2} \tag{2-3}$$

The pressure coefficient is integrated over the normalized profile coordinate X to get the normal force coefficient, eq. (2-4), and subsequently over Y to calculate the tangential force coefficient, eq. (2-5). The integration over the airfoils surface s results in the moment coefficient, eq. (2-6). The coefficients for lift c_l, eq. (2-7), and drag c_d, eq. (2-8), depend from the AoA α [22].

$$c_n = \int_0^1 \Delta c_p(X) \mathrm{d}X \tag{2-4}$$

$$c_t = \int_0^1 \Delta c_p(Y) \mathrm{d}Y \tag{2-5}$$

$$c_m = \oint c_p(s) \mathrm{d}s \tag{2-6}$$

$$c_l = c_n \cdot \cos\alpha - c_t \cdot \sin\alpha \tag{2-7}$$

$$c_d \approx c_{d,p} = c_n \cdot \sin\alpha + c_t \cdot \cos\alpha \tag{2-8}$$

The drag calculated by eq. (2-8) is not the total but the pressure drag and excludes friction

drag which can't be measured by surface pressure measurements. This is negligible in the scope of the experiments because the focus lies on full range investigations and friction drag is just dominant at very small incidences with attached flow [22].

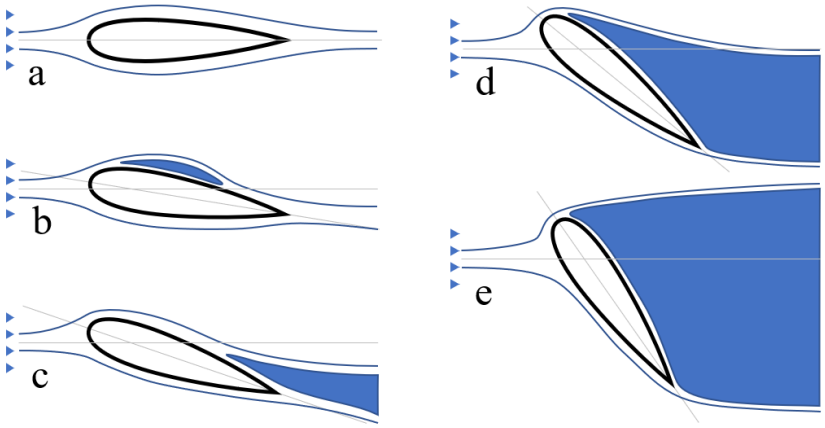

Figure 1: Flow basics up to deep stall — a. Attached flow; b. Laminar separation bubble; c. Trailing edge (TE) separation; d. Leading edge (LE) separation with separation point on suction side; e. Leading edge (LE) separation with separation point on pressure side

The typical flow phenomena expected during the experiments are sketched in figure 1. The attached flow in figure 1a without any separation bubble is not expected for thick airfoils at low Reynolds numbers because they tend to show a separation bubble (see fig. 1b), additionally combined with trailing edge stall (see fig. 1c) for increasing incidences [22]. Nevertheless, fully stalled flows (see fig. 1d & e) are expected. Switching between attached and stalled flow, and additional effects, i.e., dynamic stall, will occur when the AoA is changing dynamically and therefore time resolved measurements are crucial. Hardware and software solutions have to be found to ensure the necessary measurement quality and repeatability.

2.2 Hardware

The Hermann-Föttinger-Institute's laminar wind tunnel was designed for wall boundary layer measurements [23–26] and is sketched in figure 2. The closed loop tunnel has a closed circular measurement section with a maximum velocity of 35 $^{m}/_{s}$. The original test section is unfortunately not feasible to build a dynamic airfoil test setup. Therefore, the red marked original section in figure 2 is replaced by the setup shown in figure 3. The test section is replaced by a open dynamic setup with interchangeable airfoils between two splitter plates. The open section reduces blockage effects at high incidences and is directly attached to the nozzle, which has a contraction ratio of 18:1. This ensures a fixed distance to the nozzle and ensures the profile to be in the potential core of the open jet. The collector improves the energy efficiency as the wind tunnel is still a closed loop system. The setup provides room within the hollow shafts to mount time resolved pressure sensors, which are used to acquire the airfoil's surface pressure.

Repeatability and measurement accuracy are requirements for the dynamic measurements. The system in general is described in the publications in chapter 3 which includes setup as well as calibration procedures to improve accuracy. However, an in-situ calibration of the pressure sensors was not possible, thus an experimental analysis of the system's amplitude and phase shift was not conducted. Bergh and Tijdeman [27] suggest a model which simulates a pressure measuring system by assuming multiple series of connected

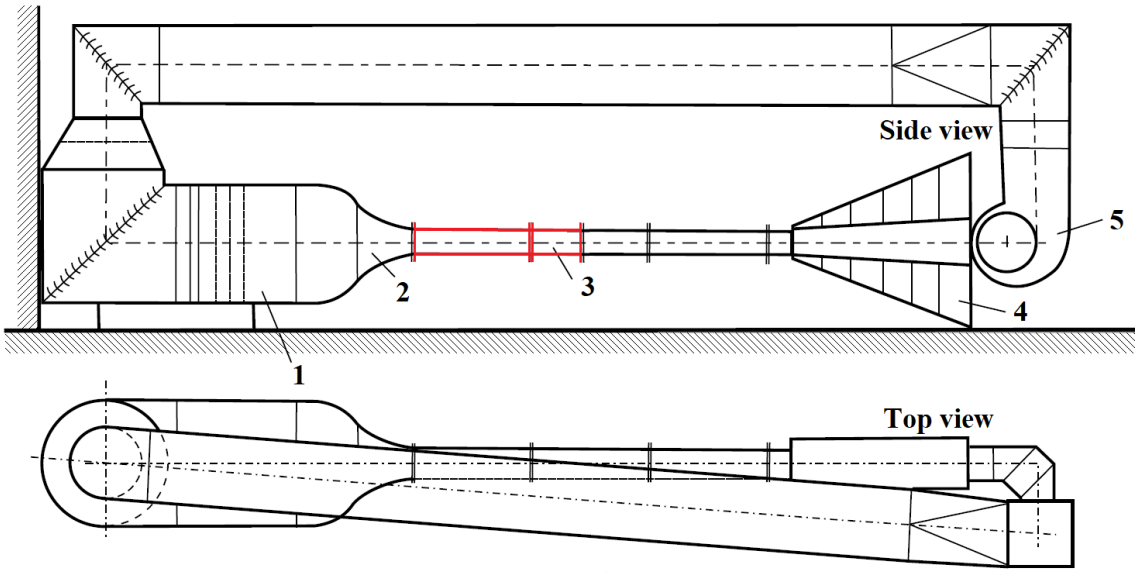

Figure 2: Hermann Föttinger Institute's laminar wind tunnel. 1 – Settling chamber; 2 – nozzle; 3 – former measurement section (replaced by setup in fig. 3); 4 – acoustic damper; 5 – radial fan

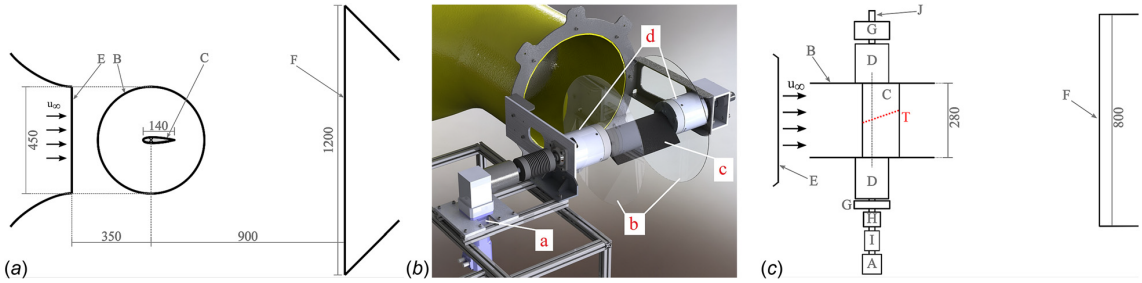

Figure 3: Setup for dynamic and static measurements including A – motor; B – splitter plates; C – NACA 0021 airfoil with pressure taps; D – hollow shaft with room to connect time resolved pressure sensors; E – nozzle; F – collector; G – bearings; H – flexible coupling; I – 1:10 angular gearbox; J – shaft; T – staggered surface pressure taps: (a) side view, (b) wind tunnel setup, and (c) top view (reprinted from publication 3.2 on page 24ff)

tubes and volumes and includes among others the following assumptions:

- Diameter of tubing << tubing length
- Laminar flow through tubing system
- Sinusoidal pressure disturbances are small

These simplifications are feasible for the setup. The measuring system is closed with no flow through the tubes and the mean differential pressure is expected to be below 1000 Pa. The pressure disturbances are small compared to the mean and should be in the order of $\mathcal{O}(10\,\text{Pa})$ or less. The tubing diameter is 0.5-1 mm and the tubing length is about 100-150 mm. Thus, the model is applicable to estimate the transfer function of the setup. Figure 4 visualizes the estimated amplitude and phase shift based on the model suggested. The reader is referred directly to the work of Bergh and Tijdeman [27] if interested in the detailed equations behind the model. Figure 4 reveals a minimal influence on the amplitude up to 100 Hz with a light amplification in the range of 60-80 Hz. Approximately above

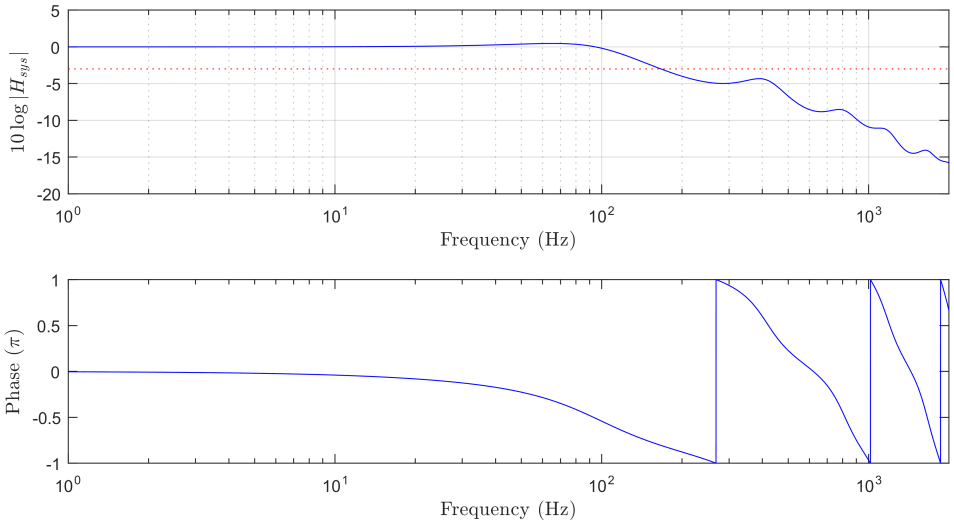

Figure 4: Estimated amplitude and phase shift based on sensor mounting and tubing based on Bergh and Tijdeman model [27]

140 Hz the amplitude is damped by more than -3 dB. The phase lag becomes significant in the range above 60 Hz.

Furthermore, the results visualized in figure 4 can be used to estimate a system response of the measurement system for a given excitation. The estimated system response provides insights into the system immanent signal distortion. This is assessed by two different types of excitations, a single sinus period and a rectangular signal. The sinus represents a continuous change in measurement signal and the according system response allows a qualitative evaluation up to which frequency deviations in shape are still acceptable. The rectangular input simulates an abrupt change in signal, e.g., a flow separation detaching and attaching. The analysis of the response provides information about the minimal signal duration necessary to be detectable in the post processing. Figure 5 summarizes both types of excitation and the resulting response, figure 5a shows a single sinus period, while figure 5b uses a rectangular input signal. The shape of the system response becomes less sinusoidal with increasing frequency, i.e., in the range of 100-200 Hz the gradual deterioration of signal quality becomes obvious in the second half of the pulse. The visualized rectangular signal periods T match the periods of the according sinus wave. Two aspects are revealed by figure 5b. First, the system needs approximately 1 ms to react on a step change and second additional 3 ms to reach the proper amplitude which occurs gradually.

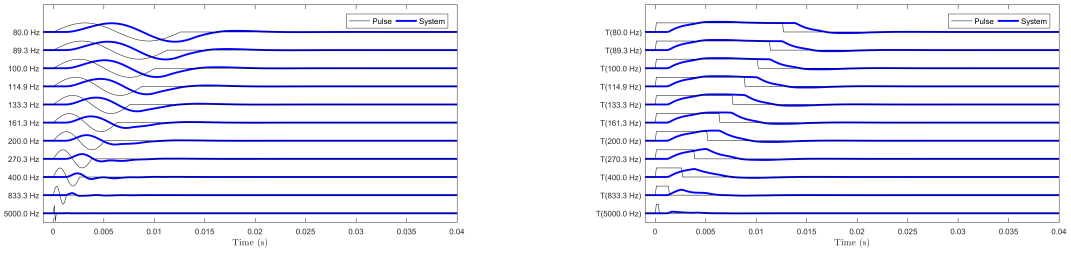

(a) sinus pulse excitation

(b) rectangle pulse excitation

Figure 5: Estimated system response

These deviations are expected because the system dampens high frequencies, which are crucial to represent a sharp step change. Comparable delays are visible during the step down at the end of the pulse, where the resulting system response decreases gradually. Consequentially, the pressure measuring system can acquire signals with a minimal duration of 5 ms in an acceptable quality. Shorter pulses can be detected but information regarding duration and amplitude degrades with decreasing signal length. The detectable frequencies are reduced with increasing tubing length of the systems and necessary connectors. In the present work, the sensors are mounted next to the airfoil within the rotating system to ensure the best possible signal transfer, which is described and visualized in more detail in publication 3.2.

The accuracy of pressure measurements is important to the calculation of the force coefficients previously defined in eq. (2-4) to (2-8), however, the angle of attack is a second parameter which has to be controlled precisely. On the one hand the AoA is necessary for the polar measurements and on the other hand the information can be used to trigger external hardware, e.g., cameras, at a defined AoA. The setup uses a servo motor with position feedback and deterministic motor control. The determinism is crucial to ensure a well defined positioning with reliable repeatability. The measurement and control hardware consists of the measurement PC, a real-time based controller (cRIO-9045 by NI [28]) and additional data acquisition units (cDAQ-9188 by NI [29]). The cRIO as well as the cDAQs are equipped with 16 bit analogue digital converter modules type NI-9215 [30] or NI-9220 [31], which are, i.e., connected to the pressure sensors. The cRIO is the central intelligence of the setup running a realtime operating system, RT Linux, ensuring the control software is not interrupted by other software, e.g., updates or antivirus programs. The most deterministic communication is handled by a chip on the cRIO which communicates with the motor, triggers each sample of the data acquisition, as well as provides trigger pulses based on the AoA of the airfoil. The entire communication and data acquisition are software controlled by a program written using LabVIEW™. Several key points will be discussed in the following section.

2.3 Software

A fully general data acquisition and control software is desirable but each experimental setup has its constrains regarding timing, acquisition rate and external hardware to be controlled. Each part of the setup serves predefined tasks which match their capabilities. Figure 6a visualizes the tasks of each component as well as the according order of timing precision. The PC running windows handles the user interface and the related tasks, i.e., settings, load and save data. Nonetheless, the Windows PC is not suitable to be a reliable controller for the measurement and triggering setup. The timing accuracy of complex programs running on Windows is in the order of 10 ms. A program running on Windows has a lower priority than system internal tasks, which may lead to slow-downs caused by software updates or virus scans. A faster timing is possible but cannot be guarantied. A delayed software control could lead to a wrong motor position or wrong acquisition timing. A real-time based measurement system, e.g., the cRIO-9045, runs a special operating system which ensures a undisturbed program timing. The program has highest priority which is beneficial and critical at the same time. If the control program is too CPU-consuming, even system relevant tasks, i.e., network communication of the device, may be delayed or aborted. Therefore, the software has to be optimized and the mean CPU load should not exceed 80 % to keep a backup for peak loads. An optimized program on a cRIO is capable to operate with a timing accuracy in the order of 1 ms which is unfortunately not fast enough to trigger the data acquisition if you need higher

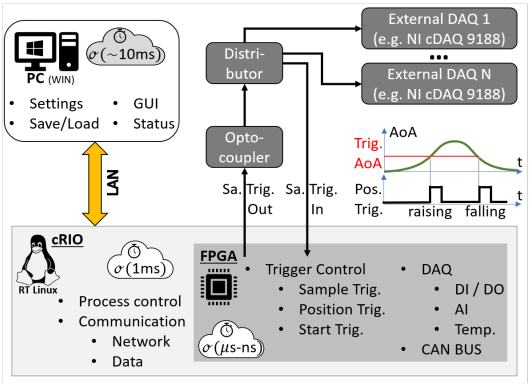

(a) Host - RT - FPGA software structure and trigger handling

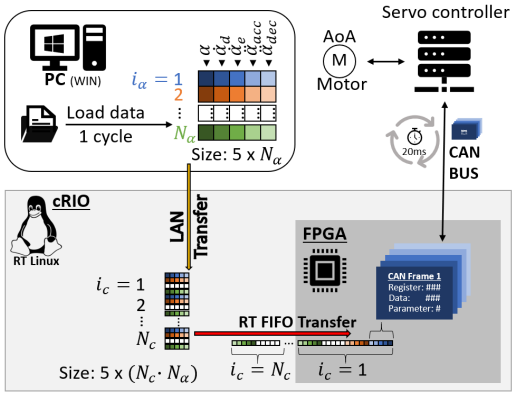

(b) Communication process of AoA positions from file to motor

Figure 6: Setup communication structures

rates than 1 kHz. The cRIO systems include a programmable chip which is capable to ensure a timing accuracy in the order of micro to nano seconds. The chip contains a Field Programmable Gate Array, FPGA, which offers adaptable electric circuit logic based on a software definition. LabVIEW in combination with the cRIO system offers the possibility to build programs for all the levels: PC, cRIO and FPGA. The program written for the FPGA chip is compiled afterward and loaded onto the chip to build the required circuit logic. The speed of the chip is comparable to "'pure"' electric solutions. This chip is finally responsible for all high precision timings within the dynamic setup.

Multiple processes need this timing precision, first of all, data acquisition. The setup provides a sample trigger for each data point and every acquisition is synchronized by this sample trigger. Figure 6a visualizes the sample trigger structure. The cRIO provides the sample trigger output signal which is connected to a distributor splitting the signal into multiple signal paths. An opto-coupler in-between the digital output and the distributor ensures a proper separation of ground levels which is important because the distributed signals are also used by the cRIO to trigger its data acquisition. The FPGA offers the possibility to build parallel processes, one to build and send the sample trigger and another to wait for an incoming trigger signal to acquire one data point. Another independent process provides a trigger signal based on the angle of attack. The FPGA software allows to synchronize external hardware based on the incidence. The user selects if the software sends a trigger signal passing the AoA of interest with increasing or decreasing incidences or in both cases. The incidence based trigger can be used to synchronously start external processes, i.e., cameras, at a defined airfoil position.

The dynamic variation of incidences within the present setup is a key part of the software and is not limited to a predefined movement. The FPGA software sends a new motor position every 20 ms using a Controller Area Network (CAN bus) [32]. The CAN is internationally standardized by ISO 11898 which was restructured into multiple parts ISO 11898-1 to 6 [33–38]. The CAN bus supports timed communication [36] which ensures a timed communication between software and motor controller and thus, a deterministic motor control. The CAN communication is based on data frames that contain among other parameters an identifier or register as well as the frame's data content. Every node within the network receives all messages but filters to receive only relevant messages. Every information needed for a new motor position has to be available at the controller within 20 ms.

Figure 6b visualizes the communication process of AoA positions commands from PC to the motor. A position command consists in the present setup of five components:

1. Target position α
2. Drive velocity $\dot{\alpha}_d$
3. End velocity $\dot{\alpha}_e$
4. Acceleration $\ddot{\alpha}_{acc}$
5. Deceleration $\ddot{\alpha}_{dec}$

Using the information provided the motor performs a simple movement sketched in figure 7a [39]. The motor accelerates at t_0 with $\ddot{\alpha}_{acc}$ until reaching the drive velocity $\dot{\alpha}_d = v_1$. Finally the motor decelerates with $\ddot{\alpha}_{dec}$ until the position α is reached at t_1 and the motor stops if the end velocity $\dot{\alpha}_e = 0$. The second position command is processed afterward and the motor starts turning from standstill. A continuous movement is possible if the next position command is provided during the previous movement. Figure 7b shows a next acceleration from v_1 to v_2 at t_1. The motor controller is capable to receive a new position command every 20 ms. Consequentially, the LabVIEW software uses this minimum timing to ensure high precision during the measurements if the airfoil is moving dynamically. All components of each position command are predefined in an according position file. Any series of angles can be loaded into the software as long as α, $\dot{\alpha}_d$, $\dot{\alpha}_e$, $\ddot{\alpha}_{acc}$ and $\ddot{\alpha}_{dec}$ are calculated on a 20 ms time-step basis. The calculation process can be simplified if $\dot{\alpha}_d = \dot{\alpha}_e$ and $\ddot{\alpha}_{acc} = \ddot{\alpha}_{dec}$. Finally, only the last command has to contain $\dot{\alpha}_e = 0$ to stop the motor movement. The file-based concept ensures best repeatability because the file can be reloaded at any time to reproduce the motor movement. The software offers the possibility to repeat the movement for several cycles. The position file contains just one cycle with N_α steps. The resulting 2D-array is transferred via LAN to the cRIO system and figure 6b additionally visualizes cRIO's cycle handling. The array is extended and contains finally N_c copies of the 2D-array loaded from file. The resulting data set has to be transferred to the FPGA chip. However, 2D-arrays consume a lot of resources on the FPGA chip, thus the 2D-array is reshaped into a 1D-array and sent via real time FIFO. The FPGA does not need the full information to communicate with the motor controller but only the components of the next position command. The components are written into multiple CAN frames which write the according data into predefined registers [39]. The motor controller is capable to read the information of the next step while processing the previous. Therefore, the precise timing of the FPGA ensures that every information is already available if the controller can read the next data. This concept ensures very high temporal repeatability in communication. Consequentially, the setup is able to run a nearly arbitrary AoA series as long as it matches physically the 20 ms motor timing.

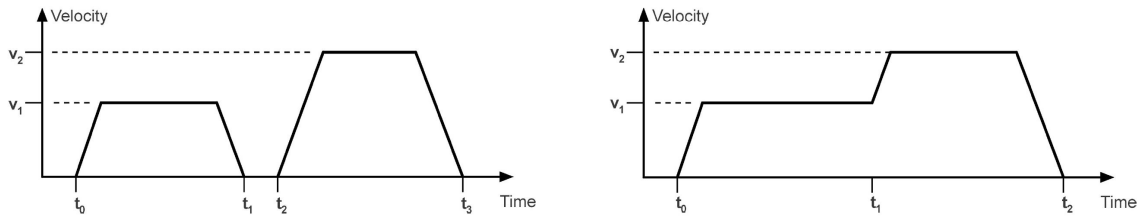

(a) Simple position commands **(b)** Continuous movements

Figure 7: Motor velocity profiles [39]

The different velocity profiles shown in figure 7 are both relevant for the experiments discussed chapter 3. On the one hand, single positioning – figure 7a – is relevant for static polar measurements, discussed in the first paper 3.1. The motor moves first, stops and the measurement starts after a predefined delay. Finally, the motor sets the next AoA and the process starts over. The continuous movement – figure 7b – is necessary for investigating sinusoidal AoA changes in papers 3.2-3.4.

3 Publications

The following chapter focuses on the experimental results and contains the following publications:

3.1 David Holst, Benjamin Church, Georgios Pechlivanoglou, Ergin Tüzüner, Joseph Saverin, Christian Navid Nayeri, and Christian Oliver Paschereit. Experimental analysis of a NACA 0021 airfoil section through 180-degree angle of attack at low Reynolds numbers for use in wind turbine analysis. *J Eng Gas Turb Power*, 141: 041012–1–10, November 2018, GTP-18-1576, DOI: 10.1115/1.4041651.

3.2 David Holst, Benjamin Church, Felix Wegner, Georgios Pechlivanoglou, Christian Navid Nayeri, and Christian Oliver Paschereit. Experimental analysis of a NACA 0021 airfoil under dynamic angle of attack variation and low Reynolds numbers. *J Eng Gas Turb Power*, 141:031020–1–10, October 2018, GTP-18-1434, DOI: 10.1115/1.4041146.

3.3 David Holst, Francesco Balduzzi, Alessandro Bianchini, Benjamin Church, Felix Wegner, Georgios Pechlivanoglou, Lorenzo Ferrari, Giovanni Ferrara, Christian Navid Nayeri, and Christian Oliver Paschereit. Static and dynamic analysis of a NACA 0021 airfoil section at low Reynolds numbers based on experiments and computational fluid dynamics. *J Eng Gas Turb Power*, 141:051015–1–10, January 2018, GTP-18-1435, DOI: 10.1115/1.4041150.

3.4 David Holst, Francesco Balduzzi, Alessandro Bianchini, Christian Navid Nayeri, Christian Oliver Paschereit, and Giovanni Ferrara. Static and Dynamic Analysis of a NACA 0021 Airfoil Section at Low Reynolds Numbers: Drag and Moment Coefficients. In *Proceedings of the ASME Turbo Expo 2019, June 17-21, Phoenix AZ, USA*, volume 9: Oil and Gas Applications; Supercritical CO2 Power Cycles; Wind Energy of *Turbo Expo: Power for Land, Sea, and Air*, 06 2019, V009T48A002, DOI: 10.1115/GT2019-90500.

All publications are reprinted in the final authenticated version. ASME granted the right of republication within this thesis. The papers are ordered to follow the experimental story line. Paper 3.1 investigates static polar data which builds the baseline for all other experiments whereas paper 3.2 concentrates on dynamic changes of incidences. Papers 3.3 and 3.4 explore numerical and experimental data to examine the influence of the setup as well as to validate the experimental setting.

D. Holst[1]
Chair of Fluid Dynamics,
Hermann-Föttinger-Institut,
Technische Universität Berlin,
Müller-Breslau-Str. 8,
Berlin 10623, Germany

B. Church
Chair of Fluid Dynamics,
Hermann-Föttinger-Institut,
Technische Universität Berlin,
Müller-Breslau-Str. 8,
Berlin 10623, Germany

G. Pechlivanoglou
Chair of Fluid Dynamics,
Hermann-Föttinger-Institut,
Technische Universität Berlin,
Müller-Breslau-Str. 8,
Berlin 10623, Germany

E. Tüzüner
Chair of Fluid Dynamics,
Hermann-Föttinger-Institut,
Technische Universität Berlin,
Müller-Breslau-Str. 8,
Berlin 10623, Germany

J. Saverin
Chair of Fluid Dynamics,
Hermann-Föttinger-Institut,
Technische Universität Berlin,
Müller-Breslau-Str. 8,
Berlin 10623, Germany

C. N. Nayeri
Chair of Fluid Dynamics,
Hermann-Föttinger-Institut,
Technische Universität Berlin,
Müller-Breslau-Str. 8,
Berlin 10623, Germany

C. O. Paschereit
Chair of Fluid Dynamics,
Hermann-Föttinger-Institut,
Technische Universität Berlin,
Müller-Breslau-Str. 8,
Berlin 10623, Germany
e-mail: David.Holst@TU-Berlin.de

Experimental Analysis of a NACA 0021 Airfoil Section Through 180-Deg Angle of Attack at Low Reynolds Numbers for Use in Wind Turbine Analysis

Wind turbine industry has a special need for accurate post stall airfoil data. While literature often covers incidence ranges [−10 deg, +25 deg], smaller machines experience a range of up to 90 deg for horizontal axis and up to 360 deg for vertical axis wind turbines (VAWTs). The post stall data of airfoils is crucial to improve the prediction of the start-up behavior as well as the performance at low tip speed ratios. The present paper analyzes and discusses the performance of the symmetrical NACA 0021 airfoil at three Reynolds numbers (Re = 100 k, 140 k, and 180 k) through 180 deg incidence. The typical problem of blockage within a wind tunnel was avoided using an open test section. The experiments were conducted in terms of surface pressure distribution over the airfoil for a tripped and a baseline configuration. The pressure was used to gain lift, pressure drag, moment data. Further investigations with positive and negative pitching revealed a second hysteresis loop in the deep post stall region resulting in a difference of 0.2 in moment coefficient and 0.5 in lift. [DOI: 10.1115/1.4041651]

Introduction

The wind industry needs airfoil data for higher angles of attack in contrast to typical aeronautical applications. Most of the literature data available for airfoils is limited to smaller angles of incidence. Selig et al. [1–3] offer one of the most extensive data source for low Reynolds airfoil data. Nevertheless their data are limited to a range of $\alpha \in [-10\,\text{deg}, +25\,\text{deg}]$. This is sufficient for most of the aeronautical but not for wind turbine applications. The angle of attack is not limited to small angles during stand still and startup of a wind turbine. Especially, vertical axis wind turbines (VAWTs) need data sets over the full incidence range of 180 deg [4,5] because they can experience the full range. There is a lack of data in post stall region for nearly every airfoil. One of the most referenced and cited full range data sets arises from measurements performed at the Sandia National Laboratories, which were mostly contributed by Sheldahl and Klimas [6]. Although Sheldahl and Klimas provide airfoil data for low Reynolds numbers, their data below Re = 350 k are based on the airfoil section characteristic synthesizer computer code PROFILE. Additionally, the NACA 0018, NACA 0021, and NACA 0025 data are completely computed and not measured within the Sandia report. Nevertheless, these thicker airfoils are used in VAWT simulations and experiments, e.g., the NACA 0021 was used for an H-type turbine investigated at the Politecnico di Milano [7] or NACA 0018 for the study by Bianchini et al. [8]. The estimation of VAWT performance is extremely dependent on the quality of polar data available. Investigations by Worasinchai et al. [9,10]

[1]Corresponding author.

Manuscript received August 20, 2018; final manuscript received September 8, 2018; published online November 19, 2018. Editor: Jerzy T. Sawicki.

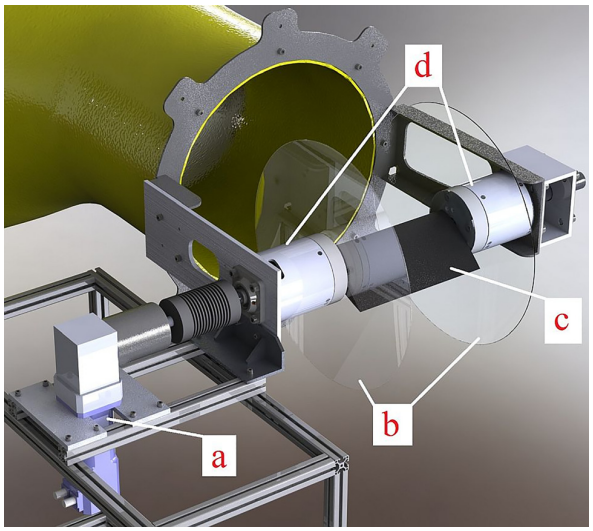

Fig. 1 Measurement setup for 180 deg polars: (*a*) motor including 1:10 gearbox, (*b*) splitter plates, (*c*) NACA 0021 airfoil with pressure taps, and (*d*) room for time-resolved pressure sensors

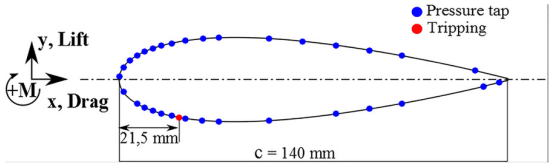

Fig. 2 Tripping and pressure tap location

and Du et al. [11,12] showed that polars are very sensitive to the wind tunnel configuration. Rainbird et al. [13,14] investigated the influence of a blockage tolerant wind tunnel in comparison to a closed configuration and showed substantial differences within the deep stall region. A second stall appeared after the first stall in configurations with less blockage or open jet configurations [5]. With this in mind, the present paper shows experiments that provide further insight into the NACA 0021 performance at the full range of incidences up to 180 deg. The effects of the open-loop configuration of the present setup in comparison to real free stream can be found in the study of Holst et al. [15].

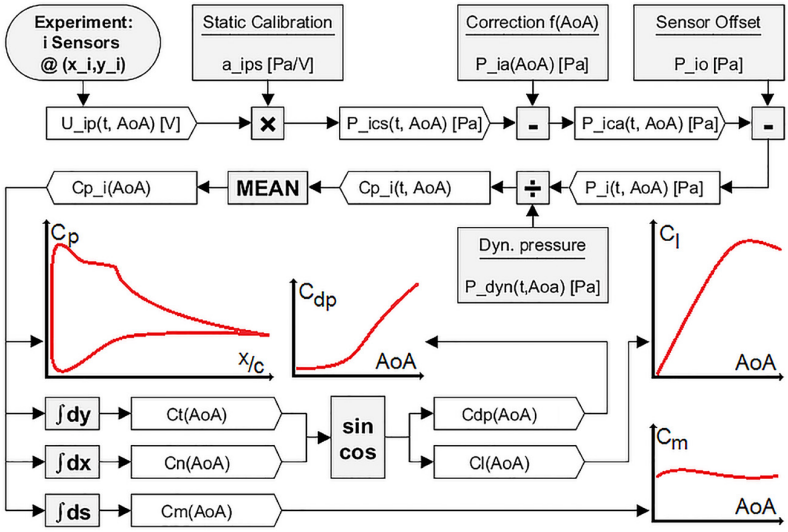

Fig. 3 Signal processing and data reduction of a single polar measurement

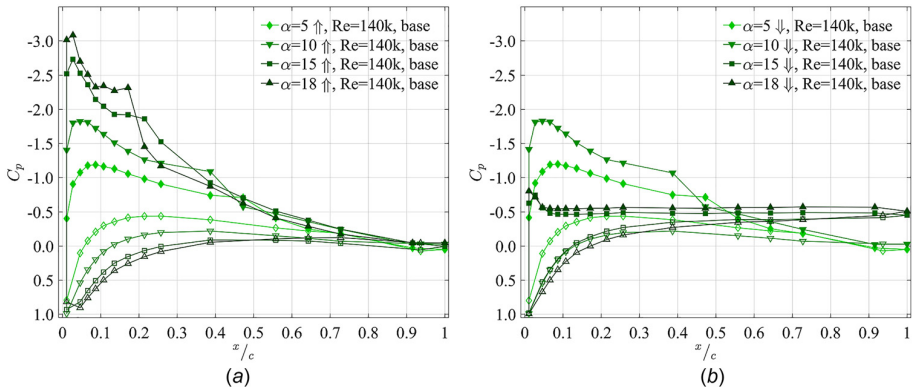

Fig. 4 NACA 0021: c_p distribution: (*a*) pitch up and (*b*) pitch down

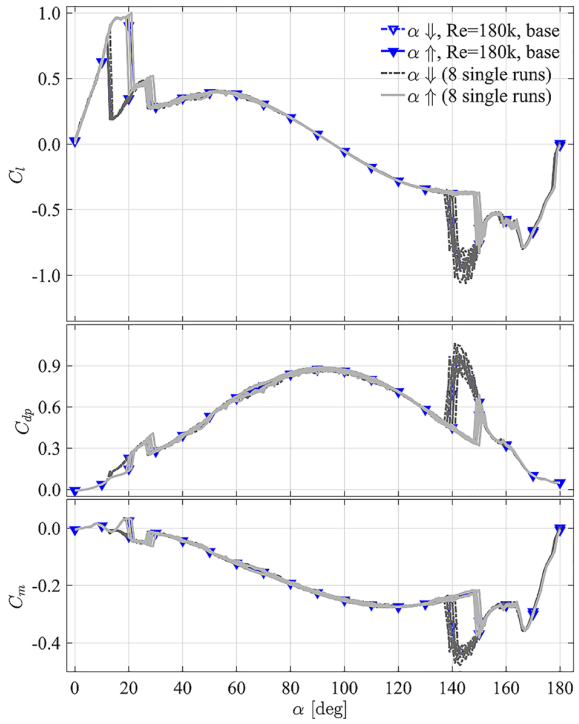

Fig. 5 NACA 0021: Repeatability study at Re = 180 k. Single runs α⇑ lighter gray; α⇓ darker gray; mean in blue with triangles.

Experimental Configuration

The wind tunnel experiments give further insight into the performance of NACA 0021 under low Reynolds conditions. The physical setup is described in this section and the detailed description of the experiments process can be found in the *procedure* section.

Setup. The experiments presented were conducted in the Hermann-Föttinger-Institute's laminar wind tunnel, which is a closed-loop tunnel with a circular cross section ($d = 0.45$ m). The formerly fully closed wind tunnel was modified and the new setup has an open test section, visualized in Fig. 1. The nozzle has no aerodynamic lip but measurements were done to validate the flow quality. The turbulence level did not exceed 1.0% within the potential core. The design of the airfoil mounting allows full $\alpha = \pm 360$ deg angle variations including surface pressure measurements up to the maximum speed of 20 m/s. A collector with a contraction ratio of 6 is placed 90 cm downstream of the trailing edge. The collector is not fully optimized but covers the wake area with a cross section of 80 cm spanwise and 120 cm in height. The angle of attack is controlled by a servo motor that ensures precise movements with errors less than 0.05 deg. The 32 time-resolved pressure sensors are mounted next to the airfoil to reduce the tubing length. The 1000 Pa probes have an accuracy of 0.1% full scale. The analogue output of the transducers was amplified before analog-digital conversion. The sensors were calibrated in situ against the same reference pressures in the range of ±1000 Pa to get the sensor specific gain a_{ips} at $\alpha = 0$ deg. The signal is additionally dependent on the orientation of the transducer because of gravity effects, and therefore of the angle of attack. No-flow measurements were conducted for each configuration and the resulting angle-dependent correction P_{ia} was always subtracted from the according measurement data. Additionally, the specific sensor offset P_{io} was subtracted, which was acquired at the beginning of each measurement. The inflow velocity is calculated using the pressure difference of a Prandtl probe p_{dyn} recorded by a pressure transducer with a maximum range of 1000 Pa and an an accuracy of 0.1% FS. Flow temperature, relative humidity, and absolute pressure were monitored. All signals were digitized using 16 bit analog input modules. The measurements were conducted at three different Reynolds numbers: Re = 100 k, 140 k, and 180 k. Each of the experiments was performed multiple times to ensure repeatability and get further insight into the statistical deviations at high angles of attack.

The NACA 0021 airfoil used within the present study is mounted between two splitter plates to ensure a 2D flow around the profile section and has a chord of $c = 14$ cm, a span of $b = 28$ cm, and thus an aspect ratio of AR = 2. The NACA 0021 is

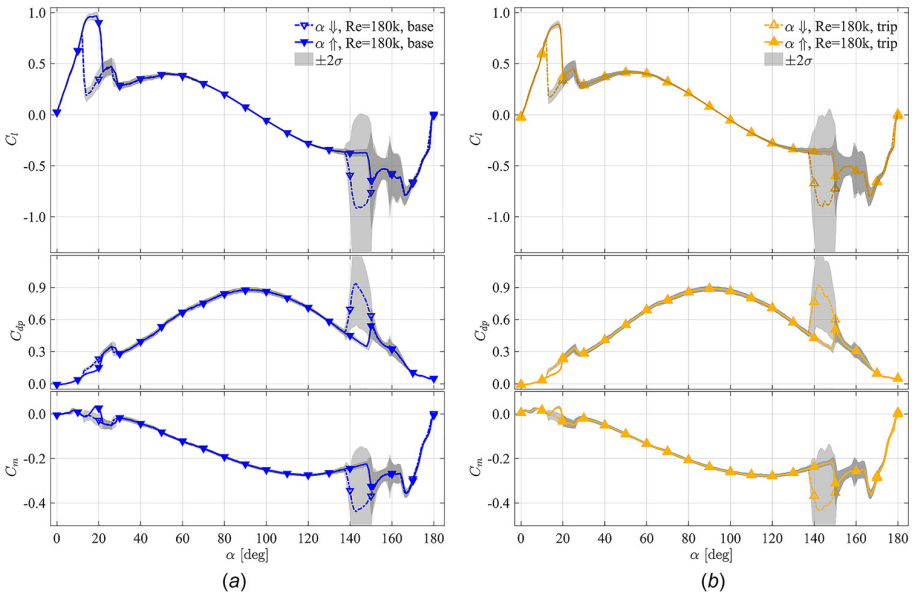

Fig. 6 NACA 0021: Statistical analysis at Re = 180 k. The gray area marks the ±2σ level. Statistics based on 5000 data points per angle: (*a*) baseline and (*b*) tripped.

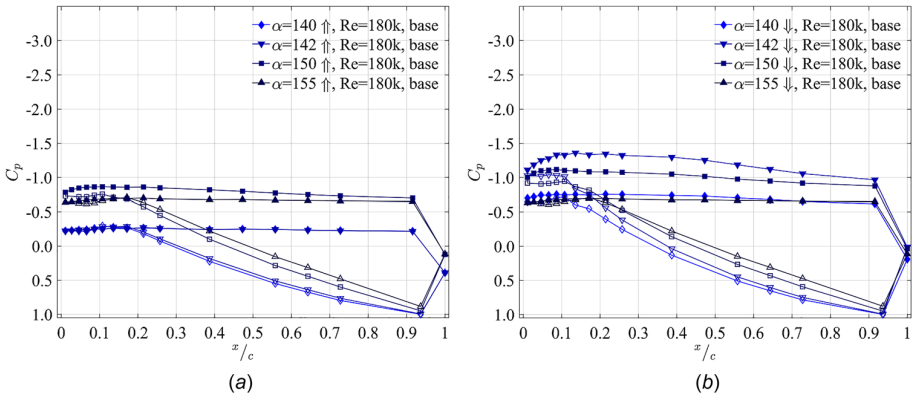

Fig. 7 NACA 0021: c_p distribution at Re = 180 k for angles within the second hysteresis loop for both pitching directions: (*a*) pitch up and (*b*) pitch down

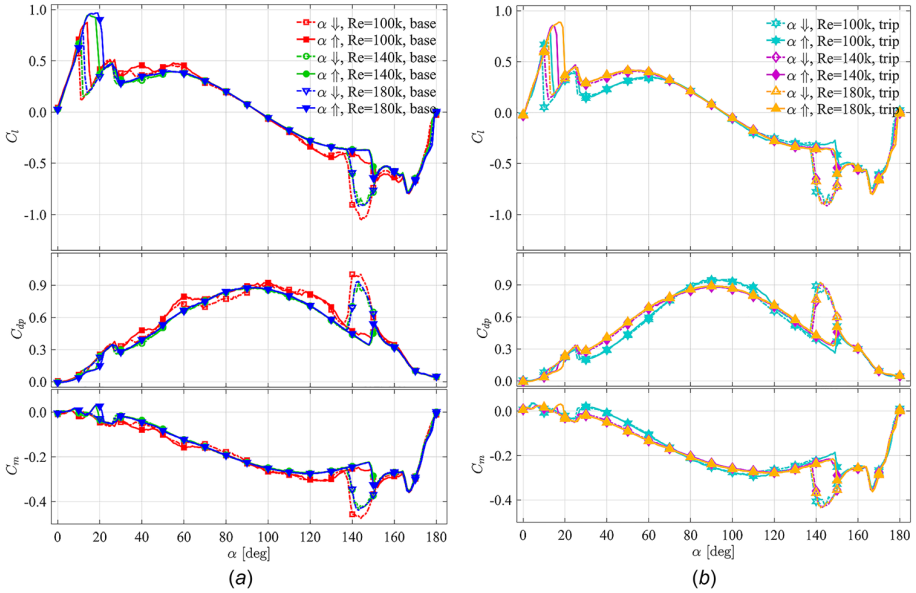

Fig. 8 NACA 0021: Reynolds study for baseline and tripped configuration: (*a*) baseline and (*b*) tripped

equipped with surface pressure taps, which provide further insight into the pressure coefficient distribution over a wide range of incident angles. The corresponding sketch is shown in Fig. 2. The profile is assembled of two separate 3D printed parts. The surface was refined using a 280 grit sanding paper and is therefore smooth but not polished. This is nearer to wind turbine reality than the polished airfoils used for aircraft airfoil studies. Based on the design, there is a small discontinuity within the surface of the pressure side that trips the flow. The tripping effect on the pressure side is minimal regarding positive angles of attack. The NACA 0021 is a symmetric airfoil and therefore measurements in the range of $\alpha \in 0$ deg, 180 deg are enough to characterize a full rotation of the airfoil. The negative angles are used to investigate the performance using a tripping. A measurement of 360 deg results in a 180 deg polar for the smooth and tripped case.

Procedure. The measurement starts with a pitch down motion at $\alpha = 360$ deg to -360 deg and continues with a pitch up motion back to $\alpha = 360$ deg. Each angle sweep consists therefore of four full revolutions (2 pitch down, 2 pitch up) and has 1441 measurement points. The two revolutions are necessary to check for the influence of movement history. This means if there is a difference when there is a pitch down or up movement before. The sweeps are repeated up to five times to analyze the repeatability. The resulting polars are divided into sections according to the smooth and tripped condition. Finally, each 180 deg polar is based on up to ten measurements (2 revolutions and 5 repetitions).

The present results are based on surface pressure measurements taken at 5000 Hz for 1 s in 1 deg steps. Figure 3 visualizes the entire data processing. The corrected pressure data are normalize by the dynamic pressure p_{dyn} and the resulting pressure coefficient c_{pi} is used to calculate lift c_l, pressure drag c_{dp}, and moment coefficients c_m. The current setup does not include a wake rake; therefore, there is no possibility to obtain the total drag coefficients c_d for all angles. Nonetheless, wake measurements were conducted for selected angles to identify the total drag. The coefficients are not corrected for solid and wake blockage because of the open jet configuration. The correction for the effect of streamline curvature used by Du et al. [11] was not applied because they concluded

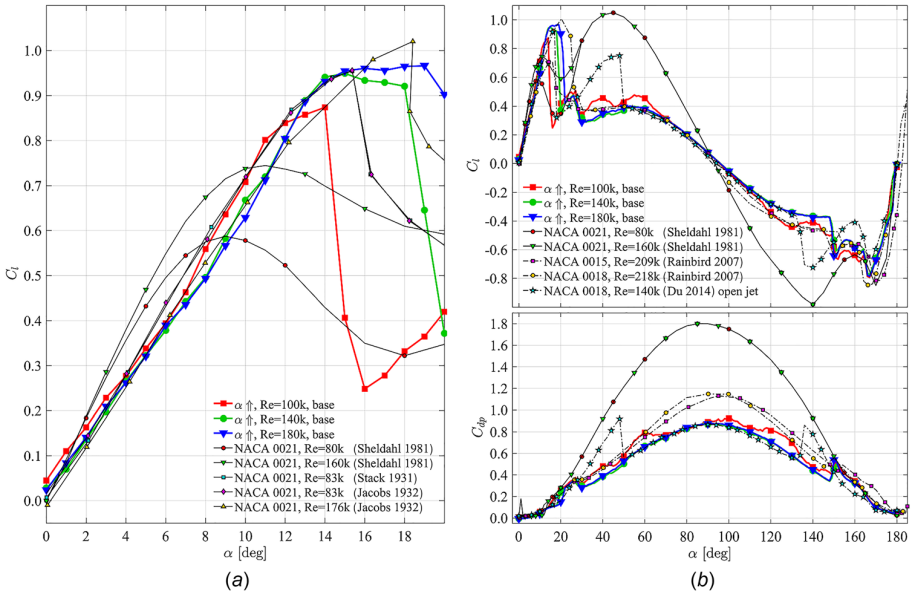

Fig. 9 Validation against literature data. Literature drag data are the total drag c_d while experimental data is pressure drag c_{dp}: (*a*) lift polars up to stall angle and (*b*) full lift polars.

their investigations that the existing corrections for open jet experiments reach the limits at high angles of attack. Therefore, we decided to present uncorrected data within this paper. Nevertheless, readers interested in the effect of different corrections are referred to another work of Holst et al. [16].

Experimental Results

The results in the present paper are based on the surface pressure measurements. Figure 4 shows that the resolution and location of the pressure taps are good enough to capture the characteristics of the airfoil. The graph in Fig. 4(*a*) visualizes the development of a separation bubble. This bubble is shifted toward the leading edge with increasing angle and the flow is attached until 18 deg. The c_p distribution changes during the pitch down sweep and shows the hysteresis effect. The flow is separated for 18 deg and 15 deg while the distribution for 10 deg is nearly unchanged compared with the pitch-up configuration.

The c_p distribution is used to calculate lift, drag, and moment coefficients. The measurements were repeated several times to check for reproducibility. Figure 5 reveals a very good agreement between the different runs. There are small deviations within the stall region as well as larger deviations above 140 deg.

The standard deviation (STD) of each single measurement was calculated based on the 5000 data points. Figure 6 gives further insight into the regions of larger fluctuations. A slightly larger STD is visible around the stall angle. The lift polar shows a double stall behavior. The first stall occurs when the flow separates from the suction side and the second stall is based on a change in the wake. According to Du et al. [11], this is caused when the point of separation moves from the suction to the pressure side resulting in a broadening wake with a direct change of the local wake flow angle. The second area of high STD is in the range of $\alpha \in [140\,\text{deg}, 170\,\text{deg}]$. The trailing edge is facing toward the inflow within this region. The flow keeps separated while pitch up until the flow reattaches at the suction side near the leading edge, which is visible in Fig. 7(*a*). This results in an abrupt shift toward negative c_p values and reduces the lift. Figure 7(*b*) reveals that the flow at the suction side keeps partially attached at the suction side during pitch down. This results in a further increased negative lift, because the airfoil is upside down at these angles. The STD is nearly identical for pitch up and pitch down beyond 150 deg. The hysteresis of the drag component within the stall regime is small compared to the large hysteresis loop at 145 deg. The increased drag during the pitch down is caused by the increased negative pressure at the suction side of the airfoil which is partially pointing downstream. The second hysteresis loop is also larger for the moment coefficient with a difference between pitch up and down of nearly $\Delta c_m = 0.2$. The general shape of the polars is not altered by tripping as shown by Fig. 6(*b*). The hysteresis loops have nearly the same extend compared to the baseline case and the regions of high standard deviation are also comparable.

The scan through the Reynolds numbers visualized in Fig. 8 reveals a nearly Reynolds-independent behavior. Just the Re = 100 k case behaves different. The stall angles increases with increasing Reynolds number. Nevertheless, the location and extent of the second hysteresis loop are unchanged for Re = 140 k and 180 k. The Re = 100 k polar is less stable within the post stall region and reveals an oscillating lift between 20 and 60 deg. The slope between 60 and 120 deg is steeper compared to the higher Reynolds numbers. The behavior changes if tripping is applied. There is no oscillation visible but a reduced lift up to 60 deg.

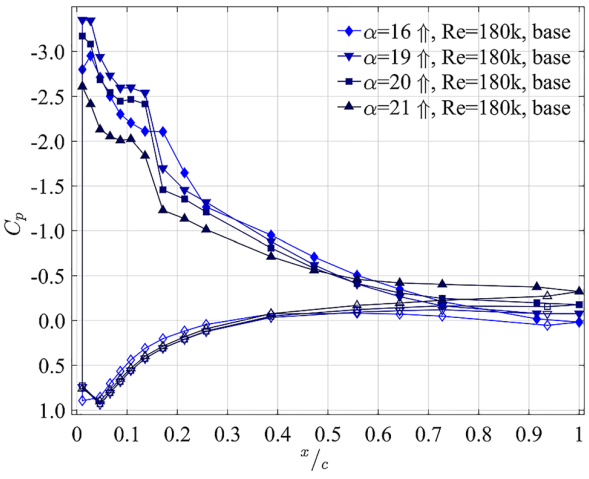

Fig. 10 Trailing edge stall during α ⇑ at Re = 180 k

Table 1 Polar data: Baseline

	$\alpha \Uparrow 100$ k			$\alpha \Downarrow 100$ k			$\alpha \Uparrow 140$ k			$\alpha \Downarrow 140$ k			$\alpha \Uparrow 180$ k			$\alpha \Downarrow 180$ k			$\alpha \Uparrow 100$ k			$\alpha \Downarrow 100$ k			$\alpha \Uparrow 140$ k			$\alpha \Downarrow 140$ k			$\alpha \Uparrow 180$ k			$\alpha \Downarrow 180$ k		
α	C_l	C_{dp}	C_m	C_l	C_{dp}	C_m	C_l	C_{dp}	C_m	C_l	C_{dp}	C_m	C_l	C_{dp}	C_m	C_l	C_{dp}	C_m	α	C_l	C_{dp}	C_m	C_l	C_{dp}	C_m	C_l	C_{dp}	C_m	C_l	C_{dp}	C_m	C_l	C_{dp}	C_m
0	0.04	0.01	−0.01	0.04	0.01	−0.01	0.03	0.00	−0.01	0.03	0.00	−0.01	0.02	0.00	0.00	0.03	0.00	0.00																	
1	0.11	0.01	−0.01	0.11	0.01	−0.01	0.07	0.00	0.00	0.07	0.00	0.00	0.08	0.00	0.00	0.08	0.00	0.00	91	0.06	0.90	−0.24	0.06	0.84	−0.22	0.06	0.87	−0.23	0.06	0.87	−0.23	0.06	0.88	−0.23
2	0.16	0.00	−0.01	0.16	0.00	−0.01	0.14	0.00	0.00	0.13	0.00	0.00	0.14	0.00	0.00	0.15	0.00	0.00	92	0.05	0.90	−0.24	0.05	0.87	−0.23	0.05	0.87	−0.23	0.05	0.88	−0.23	0.05	0.87	−0.23
3	0.23	0.01	−0.01	0.23	0.00	−0.01	0.20	0.00	0.00	0.20	0.00	0.00	0.21	0.00	0.00	0.21	0.00	0.00	93	0.04	0.90	−0.24	0.04	0.87	−0.23	0.04	0.87	−0.23	0.04	0.87	−0.23	0.04	0.88	−0.24
4	0.28	0.01	0.00	0.28	0.01	0.00	0.27	0.00	0.00	0.27	0.00	0.00	0.26	0.00	0.00	0.26	0.00	0.00	94	0.02	0.90	−0.24	0.02	0.89	−0.24	0.02	0.87	−0.24	0.03	0.87	−0.24	0.02	0.88	−0.24
5	0.34	0.01	0.00	0.33	0.01	0.00	0.32	0.01	0.00	0.32	0.01	0.00	0.33	0.00	0.00	0.33	0.00	0.00	95	0.01	0.92	−0.25	0.01	0.88	−0.24	0.01	0.87	−0.24	0.01	0.87	−0.24	0.01	0.88	−0.24
6	0.39	0.02	0.01	0.38	0.02	0.01	0.38	0.01	0.01	0.38	0.01	0.01	0.39	0.01	0.00	0.38	0.01	0.00	96	−0.01	0.90	−0.25	0.00	0.88	−0.25	0.00	0.87	−0.24	0.00	0.87	−0.24	0.00	0.87	−0.24
7	0.46	0.03	0.00	0.46	0.03	0.01	0.44	0.02	0.01	0.44	0.02	0.01	0.44	0.01	0.01	0.43	0.01	0.01	97	−0.02	0.90	−0.25	−0.02	0.90	−0.25	−0.01	0.87	−0.24	−0.01	0.87	−0.24	−0.02	0.87	−0.25
8	0.56	0.04	0.00	0.55	0.04	0.00	0.50	0.02	0.01	0.48	0.02	0.01	0.49	0.02	0.02	0.49	0.02	0.02	98	−0.04	0.92	−0.26	−0.03	0.89	−0.25	−0.03	0.86	−0.24	−0.03	0.87	−0.25	−0.03	0.87	−0.25
9	0.64	0.05	−0.01	0.64	0.05	−0.01	0.58	0.04	0.01	0.57	0.03	0.01	0.57	0.03	0.01	0.57	0.03	0.01	99	−0.05	0.92	−0.26	−0.05	0.90	−0.26	−0.04	0.86	−0.25	−0.04	0.86	−0.25	−0.04	0.87	−0.25
10	0.71	0.06	−0.02	0.57	0.07	−0.01	0.67	0.05	0.00	0.67	0.05	0.00	0.63	0.04	0.01	0.62	0.04	0.01	100	−0.06	0.92	−0.27	−0.06	0.89	−0.26	−0.05	0.85	−0.25	−0.05	0.86	−0.25	−0.05	0.86	−0.25
11	0.80	0.07	−0.03	0.11	0.10	0.00	0.72	0.06	−0.01	0.73	0.05	−0.01	0.71	0.05	0.00	0.71	0.05	0.00	101	−0.08	0.92	−0.27	−0.07	0.90	−0.26	−0.07	0.85	−0.25	−0.07	0.85	−0.25	−0.07	0.85	−0.25
12	0.84	0.08	−0.03	0.13	0.11	0.00	0.80	0.07	−0.01	0.15	0.11	0.00	0.80	0.07	−0.01	0.80	0.07	−0.01	102	−0.09	0.91	−0.27	−0.09	0.89	−0.27	−0.08	0.84	−0.25	−0.08	0.85	−0.26	−0.08	0.85	−0.26
13	0.86	0.09	−0.02	0.16	0.12	0.00	0.89	0.09	−0.02	0.16	0.12	0.00	0.89	0.08	−0.01	0.34	0.12	−0.01	103	−0.10	0.90	−0.27	−0.10	0.88	−0.26	−0.09	0.83	−0.25	−0.09	0.84	−0.26	−0.09	0.85	−0.26
14	0.87	0.10	−0.01	0.19	0.13	−0.01	0.94	0.10	−0.02	0.18	0.13	0.00	0.93	0.09	−0.01	0.19	0.13	−0.01	104	−0.12	0.90	−0.27	−0.11	0.89	−0.27	−0.10	0.84	−0.26	−0.10	0.84	−0.26	−0.10	0.84	−0.26
15	0.41	0.14	−0.01	0.21	0.14	−0.01	0.95	0.11	−0.01	0.19	0.14	0.00	0.95	0.10	−0.01	0.21	0.14	−0.01	105	−0.13	0.88	−0.27	−0.13	0.89	−0.27	−0.11	0.82	−0.26	−0.11	0.83	−0.26	−0.12	0.84	−0.26
16	0.25	0.16	−0.01	0.24	0.16	−0.01	0.93	0.11	0.01	0.23	0.16	−0.01	0.96	0.10	0.00	0.22	0.15	−0.01	106	−0.14	0.87	−0.27	−0.14	0.88	−0.27	−0.13	0.82	−0.26	−0.13	0.83	−0.26	−0.13	0.83	−0.26
17	0.28	0.18	−0.02	0.29	0.18	−0.02	0.93	0.11	0.02	0.27	0.18	−0.02	0.96	0.11	0.02	0.26	0.17	−0.01	107	−0.15	0.85	−0.27	−0.16	0.87	−0.28	−0.14	0.82	−0.26	−0.14	0.81	−0.26	−0.14	0.82	−0.26
18	0.33	0.21	−0.03	0.32	0.20	−0.03	0.92	0.12	0.03	0.31	0.20	−0.02	0.97	0.11	0.03	0.29	0.19	−0.02	108	−0.16	0.85	−0.27	−0.17	0.86	−0.28	−0.15	0.80	−0.26	−0.15	0.81	−0.26	−0.15	0.82	−0.26
19	0.36	0.23	−0.03	0.36	0.23	−0.03	0.65	0.17	0.00	0.34	0.22	−0.03	0.97	0.12	0.03	0.33	0.21	−0.03	109	−0.18	0.85	−0.28	−0.18	0.86	−0.28	−0.16	0.79	−0.26	−0.16	0.81	−0.27	−0.16	0.81	−0.27
20	0.42	0.26	−0.05	0.41	0.25	−0.04	0.37	0.24	−0.03	0.38	0.24	−0.04	0.90	0.15	0.03	0.35	0.23	−0.03	110	−0.19	0.84	−0.28	−0.20	0.86	−0.28	−0.17	0.79	−0.26	−0.17	0.79	−0.26	−0.18	0.80	−0.27
21	0.44	0.27	−0.05	0.44	0.28	−0.05	0.41	0.26	−0.04	0.42	0.27	−0.04	0.77	0.20	0.00	0.39	0.26	−0.04	111	−0.20	0.83	−0.28	−0.21	0.84	−0.28	−0.18	0.79	−0.27	−0.18	0.78	−0.26	−0.19	0.79	−0.27
22	0.46	0.29	−0.05	0.47	0.30	−0.05	0.42	0.28	−0.04	0.44	0.28	−0.05	0.42	0.28	−0.04	0.42	0.28	−0.04	112	−0.22	0.84	−0.28	−0.22	0.83	−0.28	−0.19	0.77	−0.26	−0.20	0.78	−0.27	−0.20	0.79	−0.27
23	0.47	0.31	−0.05	0.49	0.32	−0.06	0.44	0.30	−0.05	0.45	0.30	−0.05	0.44	0.30	−0.05	0.44	0.30	−0.05	113	−0.23	0.82	−0.28	−0.24	0.84	−0.28	−0.21	0.77	−0.27	−0.21	0.77	−0.27	−0.21	0.78	−0.27
24	0.49	0.33	−0.06	0.51	0.34	−0.06	0.44	0.31	−0.05	0.46	0.32	−0.05	0.45	0.31	−0.05	0.46	0.32	−0.05	114	−0.24	0.81	−0.28	−0.25	0.83	−0.29	−0.22	0.76	−0.27	−0.22	0.76	−0.27	−0.22	0.77	−0.27
25	0.50	0.35	−0.06	0.51	0.35	−0.06	0.47	0.33	−0.05	0.48	0.34	−0.05	0.46	0.33	−0.05	0.46	0.33	−0.05	115	−0.26	0.82	−0.29	−0.28	0.86	−0.30	−0.23	0.75	−0.27	−0.23	0.76	−0.27	−0.23	0.76	−0.27
26	0.48	0.35	−0.06	0.45	0.33	−0.05	0.48	0.35	−0.05	0.48	0.35	−0.05	0.47	0.35	−0.05	0.48	0.35	−0.05	116	−0.27	0.81	−0.29	−0.29	0.85	−0.30	−0.24	0.74	−0.27	−0.24	0.76	−0.28	−0.24	0.75	−0.27
27	0.51	0.38	−0.06	0.35	0.29	−0.03	0.42	0.33	−0.04	0.31	0.27	−0.02	0.44	0.34	−0.04	0.35	0.29	−0.03	117	−0.30	0.83	−0.30	−0.30	0.85	−0.30	−0.25	0.73	−0.27	−0.25	0.74	−0.27	−0.25	0.74	−0.27
28	0.40	0.33	−0.04	0.35	0.30	−0.03	0.36	0.30	−0.03	0.28	0.26	−0.01	0.41	0.33	−0.04	0.33	0.29	−0.02	118	−0.32	0.84	−0.30	−0.32	0.84	−0.30	−0.26	0.72	−0.27	−0.26	0.73	−0.28	−0.26	0.73	−0.27
29	0.34	0.30	−0.03	0.37	0.32	−0.04	0.31	0.29	−0.02	0.28	0.27	−0.02	0.31	0.29	−0.02	0.28	0.27	−0.02	119	−0.33	0.83	−0.30	−0.33	0.82	−0.30	−0.27	0.71	−0.27	−0.27	0.72	−0.27	−0.27	0.72	−0.27
30	0.34	0.31	−0.03	0.38	0.33	−0.04	0.32	0.30	−0.02	0.29	0.28	−0.02	0.29	0.28	−0.02	0.28	0.28	−0.02	120	−0.34	0.81	−0.30	−0.34	0.82	−0.30	−0.28	0.71	−0.27	−0.28	0.71	−0.27	−0.28	0.71	−0.28
31	0.36	0.33	−0.04	0.38	0.34	−0.04	0.32	0.31	−0.03	0.28	0.28	−0.02	0.29	0.29	−0.02	0.29	0.29	−0.02	121	−0.35	0.81	−0.30	−0.35	0.80	−0.30	−0.29	0.70	−0.27	−0.29	0.70	−0.27	−0.29	0.70	−0.27
32	0.37	0.34	−0.04	0.40	0.36	−0.05	0.29	0.29	−0.02	0.29	0.29	−0.02	0.30	0.30	−0.02	0.30	0.30	−0.02	122	−0.37	0.80	−0.31	−0.36	0.80	−0.30	−0.30	0.69	−0.27	−0.29	0.68	−0.27	−0.29	0.69	−0.27
33	0.38	0.36	−0.05	0.40	0.37	−0.05	0.29	0.30	−0.02	0.29	0.30	−0.02	0.30	0.31	−0.02	0.30	0.31	−0.02	123	−0.38	0.79	−0.31	−0.37	0.78	−0.30	−0.30	0.67	−0.27	−0.30	0.67	−0.27	−0.30	0.67	−0.27
34	0.41	0.39	−0.06	0.41	0.39	−0.06	0.30	0.31	−0.02	0.30	0.31	−0.02	0.30	0.32	−0.03	0.30	0.32	−0.02	124	−0.39	0.78	−0.31	−0.39	0.78	−0.31	−0.31	0.66	−0.27	−0.30	0.65	−0.27	−0.31	0.66	−0.27
35	0.43	0.41	−0.06	0.40	0.39	−0.06	0.30	0.32	−0.03	0.31	0.32	−0.03	0.31	0.33	−0.03	0.31	0.33	−0.03	125	−0.40	0.77	−0.31	−0.41	0.77	−0.31	−0.31	0.65	−0.27	−0.31	0.64	−0.27	−0.32	0.65	−0.27
36	0.44	0.42	−0.07	0.37	0.38	−0.05	0.30	0.32	−0.03	0.31	0.33	−0.03	0.32	0.34	−0.03	0.32	0.34	−0.03	126	−0.42	0.76	−0.31	−0.41	0.76	−0.31	−0.32	0.63	−0.27	−0.32	0.63	−0.27	−0.32	0.63	−0.27
37	0.44	0.44	−0.07	0.35	0.37	−0.04	0.31	0.34	−0.03	0.31	0.34	−0.03	0.33	0.35	−0.03	0.32	0.35	−0.03	127	−0.43	0.76	−0.31	−0.41	0.73	−0.30	−0.33	0.62	−0.27	−0.32	0.62	−0.27	−0.33	0.62	−0.27
38	0.45	0.45	−0.07	0.35	0.38	−0.05	0.32	0.35	−0.03	0.30	0.34	−0.03	0.33	0.36	−0.04	0.33	0.36	−0.04	128	−0.43	0.74	−0.30	−0.43	0.73	−0.30	−0.33	0.61	−0.27	−0.33	0.61	−0.27	−0.33	0.61	−0.27
39	0.45	0.47	−0.08	0.36	0.39	−0.05	0.33	0.37	−0.04	0.31	0.35	−0.03	0.34	0.38	−0.04	0.34	0.38	−0.04	129	−0.44	0.72	−0.31	−0.43	0.71	−0.30	−0.34	0.59	−0.27	−0.34	0.59	−0.26	−0.33	0.59	−0.26
40	0.46	0.48	−0.08	0.36	0.40	−0.05	0.34	0.39	−0.04	0.31	0.36	−0.04	0.35	0.39	−0.04	0.35	0.39	−0.04	130	−0.44	0.70	−0.30	−0.42	0.67	−0.29	−0.34	0.58	−0.26	−0.34	0.57	−0.26	−0.34	0.58	−0.26
41	0.45	0.49	−0.08	0.35	0.40	−0.05	0.34	0.39	−0.04	0.32	0.37	−0.04	0.35	0.40	−0.05	0.36	0.40	−0.05	131	−0.44	0.67	−0.30	−0.41	0.63	−0.28	−0.34	0.56	−0.26	−0.35	0.56	−0.26	−0.35	0.57	−0.26
42	0.43	0.48	−0.08	0.37	0.43	−0.06	0.34	0.40	−0.05	0.32	0.38	−0.04	0.36	0.41	−0.05	0.36	0.41	−0.05	132	−0.44	0.65	−0.29	−0.40	0.60	−0.27	−0.35	0.55	−0.26	−0.35	0.55	−0.26	−0.35	0.55	−0.26
43	0.43	0.49	−0.08	0.37	0.44	−0.06	0.35	0.41	−0.05	0.33	0.40	−0.05	0.36	0.42	−0.05	0.36	0.43	−0.05	133	−0.43	0.61	−0.28	−0.39	0.58	−0.27	−0.35	0.53	−0.26	−0.35	0.54	−0.26	−0.35	0.54	−0.26
44	0.42	0.49	−0.08	0.38	0.45	−0.06	0.34	0.41	−0.05	0.34	0.41	−0.05	0.37	0.44	−0.06	0.36	0.43	−0.05	134	−0.41	0.58	−0.27	−0.39	0.56	−0.27	−0.35	0.52	−0.25	−0.35	0.52	−0.25	−0.36	0.53	−0.26
45	0.40	0.48	−0.07	0.38	0.47	−0.07	0.34	0.42	−0.05	0.34	0.43	−0.05	0.37	0.45	−0.06	0.36	0.45	−0.06	135	−0.41	0.56	−0.27	−0.40	0.54	−0.26	−0.35	0.50	−0.25	−0.36	0.51	−0.25	−0.36	0.51	−0.25
46	0.40	0.49	−0.07	0.38	0.47	−0.07	0.35	0.44	−0.06	0.35	0.44	−0.06	0.36	0.46	−0.06	0.36	0.46	−0.06	136	−0.41	0.54	−0.26	−0.41	0.53	−0.26	−0.36	0.49	−0.25	−0.36	0.49	−0.25	−0.36	0.50	−0.25
47	0.40	0.51	−0.08	0.40	0.50	−0.08	0.35	0.45	−0.06	0.36	0.46	−0.06	0.37	0.47	−0.07	0.37	0.47	−0.06	137	−0.40	0.52	−0.26	−0.46	0.58	−0.28	−0.36	0.48	−0.25	−0.36	0.48	−0.25	−0.36	0.48	−0.25
48	0.41	0.53	−0.09	0.40	0.52	−0.08	0.36	0.47	−0.07	0.36	0.47	−0.07	0.38	0.49	−0.07	0.38	0.49	−0.07	138	−0.42	0.51	−0.26	−0.52	0.63	−0.31	−0.36	0.47	−0.25	−0.43	0.55	−0.28	−0.36	0.47	−0.25
49	0.43	0.57	−0.10	0.42	0.55	−0.09	0.36	0.48	−0.07	0.37	0.49	−0.07	0.38	0.50	−0.07	0.38	0.51	−0.08	139	−0.41	0.49	−0.26	−0.74	0.85	−0.40	−0.37	0.46	−0.25	−0.50	0.61	−0.31	−0.37	0.46	−0.24
50	0.43	0.57	−0.10	0.44	0.59	−0.10	0.37	0.50	−0.07	0.38	0.52	−0.08	0.39	0.53	−0.08	0.39	0.53	−0.08	140	−0.41	0.47	−0.25	−0.90	1.00	−0.46	−0.37	0.44	−0.24	−0.60	0.70	−0.35	−0.38	0.45	−0.25
51	0.45	0.61	−0.11	0.46	0.62	−0.11	0.38	0.53	−0.08	0.38	0.53	−0.08	0.39	0.55	−0.09	0.40	0.55	−0.09	141	−0.41	0.46	−0.25	−0.91	0.97	−0.46	−0.36	0.42	−0.24	−0.78	0.86	−0.41	−0.38	0.43	−0.24
52	0.45	0.63	−0.11	0.45	0.63	−0.11	0.39	0.55	−0.09	0.39	0.55	−0.09	0.40	0.56	−0.09	0.40	0.57	−0.09	142	−0.42	0.45	−0.25	−0.96	0.99	−0.47	−0.37	0.42	−0.24	−0.78	0.83	−0.40	−0.37	0.42	−0.24
53	0.45	0.65	−0.12	0.45	0.65	−0.12	0.39	0.57	−0.09	0.39	0.57	−0.09	0.40	0.58	−0.10	0.40	0.58	−0.10	143	−0.42	0.44	−0.25	−0.98	0.98	−0.46	−0.37	0.40	−0.24	−0.91	0.92	−0.44	−0.37	0.41	−0.24
54	0.47	0.68	−0.13	0.46	0.67	−0.12	0.40	0.59	−0.10	0.40	0.59	−0.10	0.40	0.59	−0.10	0.40	0.59	−0.10	144	−0.46	0.45	−0.26	−1.06	1.00	−0.48	−0.37	0.39	−0.23	−0.84	0.84	−0.42	−0.37	0.39	−0.23
55	0.48	0.72	−0.14	0.46	0.69	−0.13	0.40	0.60	−0.10	0.40	0.60	−0.10	0.40	0.61	−0.10	0.40	0.61	−0.10	145	−0.47	0.45	−0.26	−1.03	0.95	−0.46	−0.37	0.38	−0.23	−0.89	0.86	−0.42	−0.37	0.38	−0.23
56	0.47	0.73	−0.14	0.45	0.70	−0.13	0.39	0.62	−0.11	0.40	0.62	−0.11	0.40	0.62	−0.11	0.40	0.62	−0.11	146	−0.49	0.45	−0.26	−1.03	0.92	−0.46	−0.37	0.36	−0.23	−0.91	0.84	−0.42	−0.37	0.37	−0.23
57	0.47	0.75	−0.15	0.45	0.71	−0.13	0.39	0.63	−0.11	0.39	0.63	−0.11	0.39	0.63	−0.11	0.39	0.63	−0.11	147	−0.50	0.43	−0.26	−1.01	0.87	−0.45	−0.37	0.35	−0.23	−0.88	0.80	−0.41	−0.37	0.35	−0.23
58	0.47	0.76	−0.15	0.45	0.74	−0.14	0.39	0.64	−0.11	0.39	0.64	−0.12	0.39	0.64	−0.12	0.39	0.65	−0.12	148	−0.50	0.42	−0.26	−0.94	0.80	−0.43	−0.37	0.34	−0.22	−0.80	0.71	−0.39	−0.38	0.35	−0.23
59	0.46	0.78	−0.16	0.43	0.73	−0.14	0.39	0.66	−0.12	0.39	0.66	−0.12	0.39	0.66	−0.12	0.39	0.66	−0.12	149	−0.50	0.40	−0.26	−0.85	0.72	−0.40	−0.42	0.37	−0.24	−0.82	0.70	−0.39	−0.45	0.40	−0.25
60	0.45	0.79	−0.16	0.42	0.72	−0.14	0.38	0.67	−0.12	0.38	0.66	−0.12	0.38	0.67	−0.12	0.38	0.67	−0.12	150	−0.58	0.46	−0.29	−0.74	0.60	−0.37	−0.53	0.45	−0.29	−0.78	0.65	−0.37	−0.64	0.54	−0.33
61	0.44	0.80	−0.16	0.39	0.71	−0.13	0.38	0.68	−0.13	0.37	0.66	−0.12	0.38	0.67	−0.13	0.38	0.68	−0.13	151	−0.66	0.52	−0.33	−0.68	0.53	−0.34	−0.61	0.50	−0.32	−0.65	0.54	−0.34	−0.63	0.52	−0.33

Table 1 (continued)

	α ⇑ 100 k			α ⇓ 100 k			α ⇑ 140 k			α ⇓ 140 k			α ⇑ 180 k			α ⇓ 180 k			α	α ⇑ 100 k			α ⇓ 100 k			α ⇑ 140 k			α ⇓ 140 k			α ⇑ 180 k			α ⇓ 180 k		
	C_l	C_{dp}	C_m	C_l	C_{dp}	C_m	C_l	C_{dp}	C_m	C_l	C_{dp}	C_m	C_l	C_{dp}	C_m	C_l	C_{dp}	C_m		C_l	C_{dp}	C_m	C_l	C_{dp}	C_m	C_l	C_{dp}	C_m	C_l	C_{dp}	C_m	C_l	C_{dp}	C_m	C_l	C_{dp}	C_m
62	0.42	0.78	−0.16	0.38	0.70	−0.13	0.37	0.69	−0.13	0.36	0.67	−0.13	0.37	0.69	−0.13	0.37	0.69	−0.13	152	−0.67	0.50	−0.34	−0.63	0.48	−0.33	−0.60	0.47	−0.32	−0.59	0.46	−0.31	−0.62	0.49	−0.32	−0.59	0.47	−0.32
63	0.41	0.78	−0.16	0.37	0.70	−0.14	0.35	0.68	−0.13	0.36	0.68	−0.13	0.37	0.70	−0.13	0.37	0.70	−0.13	153	−0.63	0.46	−0.32	−0.60	0.45	−0.31	−0.57	0.44	−0.30	−0.56	0.42	−0.30	−0.57	0.44	−0.31	−0.56	0.43	−0.30
64	0.39	0.77	−0.15	0.36	0.71	−0.14	0.35	0.69	−0.13	0.35	0.69	−0.13	0.36	0.71	−0.14	0.35	0.70	−0.13	154	−0.62	0.43	−0.31	−0.59	0.42	−0.30	−0.55	0.40	−0.29	−0.54	0.40	−0.29	−0.55	0.41	−0.29	−0.55	0.40	−0.29
65	0.38	0.77	−0.15	0.35	0.71	−0.14	0.34	0.69	−0.13	0.34	0.70	−0.14	0.35	0.71	−0.14	0.35	0.71	−0.14	155	−0.61	0.41	−0.30	−0.57	0.40	−0.29	−0.54	0.38	−0.28	−0.53	0.38	−0.28	−0.53	0.38	−0.28	−0.53	0.38	−0.28
66	0.36	0.77	−0.16	0.34	0.71	−0.14	0.34	0.71	−0.14	0.34	0.71	−0.14	0.34	0.72	−0.14	0.34	0.72	−0.14	156	−0.61	0.40	−0.30	−0.57	0.38	−0.29	−0.53	0.36	−0.28	−0.53	0.36	−0.28	−0.53	0.36	−0.28	−0.53	0.36	−0.28
67	0.35	0.77	−0.16	0.33	0.71	−0.14	0.33	0.72	−0.14	0.33	0.72	−0.14	0.33	0.73	−0.15	0.33	0.73	−0.15	157	−0.61	0.38	−0.29	−0.58	0.37	−0.28	−0.54	0.35	−0.27	−0.53	0.35	−0.27	−0.53	0.35	−0.27	−0.53	0.35	−0.27
68	0.34	0.77	−0.16	0.32	0.71	−0.14	0.32	0.73	−0.15	0.32	0.74	−0.15	0.32	0.74	−0.15	0.32	0.74	−0.15	158	−0.62	0.37	−0.29	−0.60	0.36	−0.29	−0.56	0.35	−0.28	−0.55	0.34	−0.27	−0.54	0.34	−0.27	−0.55	0.34	−0.27
69	0.33	0.78	−0.16	0.30	0.69	−0.14	0.31	0.74	−0.15	0.32	0.75	−0.15	0.32	0.75	−0.15	0.32	0.75	−0.15	159	−0.65	0.37	−0.29	−0.61	0.35	−0.28	−0.58	0.34	−0.28	−0.58	0.34	−0.27	−0.61	0.35	−0.28	−0.58	0.34	−0.27
70	0.31	0.77	−0.16	0.29	0.70	−0.14	0.30	0.74	−0.15	0.31	0.76	−0.16	0.30	0.75	−0.15	0.31	0.75	−0.15	160	−0.64	0.34	−0.29	−0.62	0.33	−0.28	−0.59	0.32	−0.27	−0.58	0.32	−0.27	−0.59	0.32	−0.27	−0.57	0.32	−0.27
71	0.31	0.79	−0.16	0.28	0.70	−0.14	0.30	0.76	−0.16	0.30	0.77	−0.16	0.30	0.76	−0.16	0.30	0.76	−0.16	161	−0.67	0.33	−0.29	−0.65	0.32	−0.28	−0.60	0.31	−0.27	−0.60	0.31	−0.27	−0.60	0.31	−0.27	−0.59	0.31	−0.27
72	0.30	0.79	−0.17	0.27	0.72	−0.15	0.29	0.77	−0.16	0.29	0.77	−0.16	0.29	0.77	−0.16	0.29	0.77	−0.16	162	−0.68	0.32	−0.29	−0.65	0.30	−0.28	−0.62	0.29	−0.27	−0.60	0.29	−0.27	−0.62	0.29	−0.27	−0.62	0.29	−0.27
73	0.28	0.78	−0.17	0.26	0.72	−0.15	0.28	0.78	−0.17	0.28	0.78	−0.17	0.28	0.78	−0.17	0.28	0.78	−0.17	163	−0.67	0.29	−0.28	−0.62	0.27	−0.27	−0.62	0.27	−0.27	−0.62	0.27	−0.27	−0.62	0.27	−0.27	−0.61	0.27	−0.27
74	0.27	0.80	−0.17	0.25	0.73	−0.16	0.27	0.79	−0.17	0.27	0.79	−0.17	0.27	0.79	−0.17	0.27	0.79	−0.17	164	−0.64	0.25	−0.28	−0.63	0.24	−0.27	−0.59	0.24	−0.26	−0.61	0.24	−0.27	−0.61	0.24	−0.27	−0.61	0.24	−0.27
75	0.26	0.80	−0.18	0.24	0.74	−0.16	0.26	0.80	−0.17	0.26	0.80	−0.17	0.26	0.80	−0.17	0.26	0.80	−0.17	165	−0.69	0.23	−0.30	−0.71	0.22	−0.31	−0.66	0.22	−0.29	−0.71	0.21	−0.31	−0.68	0.22	−0.30	−0.71	0.21	−0.31
76	0.24	0.78	−0.17	0.24	0.75	−0.16	0.25	0.81	−0.18	0.25	0.81	−0.18	0.25	0.81	−0.18	0.25	0.81	−0.18	166	−0.79	0.20	−0.34	−0.78	0.19	−0.35	−0.76	0.19	−0.34	−0.78	0.19	−0.35	−0.78	0.19	−0.34	−0.79	0.18	−0.35
77	0.24	0.81	−0.18	0.23	0.77	−0.17	0.24	0.81	−0.18	0.24	0.82	−0.18	0.24	0.81	−0.18	0.24	0.82	−0.18	167	−0.79	0.16	−0.36	−0.77	0.16	−0.36	−0.77	0.16	−0.35	−0.77	0.15	−0.35	−0.79	0.16	−0.36	−0.78	0.15	−0.36
78	0.23	0.82	−0.18	0.22	0.77	−0.17	0.23	0.82	−0.19	0.23	0.82	−0.19	0.23	0.83	−0.19	0.23	0.83	−0.19	168	−0.76	0.14	−0.35	−0.73	0.14	−0.34	−0.74	0.13	−0.35	−0.73	0.13	−0.35	−0.75	0.13	−0.35	−0.75	0.13	−0.34
79	0.22	0.83	−0.19	0.21	0.78	−0.18	0.22	0.83	−0.19	0.21	0.83	−0.19	0.22	0.83	−0.19	0.22	0.83	−0.19	169	−0.71	0.12	−0.33	−0.69	0.12	−0.32	−0.70	0.12	−0.32	−0.68	0.11	−0.31	−0.71	0.12	−0.33	−0.70	0.12	−0.32
80	0.20	0.84	−0.19	0.19	0.77	−0.18	0.20	0.83	−0.19	0.20	0.83	−0.19	0.20	0.84	−0.19	0.20	0.84	−0.19	170	−0.67	0.11	−0.30	−0.65	0.11	−0.29	−0.66	0.10	−0.30	−0.65	0.10	−0.29	−0.67	0.10	−0.30	−0.66	0.10	−0.29
81	0.19	0.84	−0.19	0.18	0.78	−0.18	0.19	0.84	−0.20	0.19	0.84	−0.19	0.19	0.84	−0.19	0.19	0.84	−0.19	171	−0.64	0.10	−0.27	−0.61	0.09	−0.26	−0.62	0.09	−0.27	−0.61	0.09	−0.26	−0.63	0.09	−0.27	−0.61	0.09	−0.26
82	0.18	0.84	−0.20	0.17	0.77	−0.18	0.18	0.85	−0.20	0.18	0.85	−0.20	0.18	0.85	−0.20	0.18	0.85	−0.20	172	−0.60	0.08	−0.25	−0.57	0.08	−0.23	−0.59	0.08	−0.24	−0.57	0.08	−0.23	−0.60	0.08	−0.24	−0.58	0.08	−0.23
83	0.17	0.84	−0.20	0.16	0.77	−0.18	0.17	0.85	−0.20	0.17	0.86	−0.20	0.17	0.85	−0.20	0.17	0.85	−0.20	173	−0.54	0.08	−0.21	−0.50	0.08	−0.19	−0.53	0.07	−0.20	−0.51	0.08	−0.19	−0.56	0.08	−0.21	−0.53	0.08	−0.20
84	0.15	0.85	−0.20	0.15	0.80	−0.19	0.16	0.86	−0.21	0.15	0.86	−0.21	0.15	0.86	−0.21	0.15	0.86	−0.21	174	−0.47	0.07	−0.17	−0.43	0.07	−0.15	−0.47	0.07	−0.16	−0.44	0.07	−0.15	−0.49	0.07	−0.17	−0.47	0.08	−0.15
85	0.14	0.86	−0.21	0.14	0.78	−0.19	0.14	0.86	−0.21	0.14	0.86	−0.21	0.14	0.86	−0.21	0.14	0.87	−0.21	175	−0.40	0.07	−0.13	−0.36	0.07	−0.13	−0.41	0.07	−0.13	−0.40	0.07	−0.12	−0.43	0.07	−0.13	−0.42	0.07	−0.13
86	0.13	0.86	−0.21	0.13	0.81	−0.20	0.13	0.87	−0.21	0.13	0.86	−0.21	0.13	0.87	−0.21	0.13	0.87	−0.21	176	−0.33	0.06	−0.10	−0.29	0.06	−0.09	−0.37	0.06	−0.11	−0.36	0.06	−0.10	−0.40	0.06	−0.12	−0.39	0.06	−0.11
87	0.12	0.86	−0.21	0.11	0.81	−0.20	0.12	0.87	−0.22	0.12	0.86	−0.21	0.12	0.87	−0.22	0.12	0.87	−0.22	177	−0.19	0.06	−0.07	−0.13	0.06	−0.06	−0.32	0.05	−0.09	−0.30	0.05	−0.08	−0.37	0.05	−0.10	−0.35	0.05	−0.09
88	0.10	0.89	−0.22	0.10	0.83	−0.21	0.10	0.88	−0.22	0.10	0.86	−0.22	0.10	0.88	−0.22	0.10	0.87	−0.22	178	−0.10	0.05	−0.05	−0.08	0.05	−0.04	−0.10	0.05	−0.05	−0.07	0.05	−0.04	−0.32	0.05	−0.08	−0.20	0.05	−0.06
89	0.09	0.87	−0.22	0.09	0.84	−0.21	0.09	0.87	−0.22	0.09	0.87	−0.22	0.09	0.88	−0.22	0.09	0.87	−0.22	179	−0.06	0.05	−0.03	−0.04	0.05	−0.02	−0.05	0.05	−0.02	−0.03	0.05	−0.02	−0.05	0.05	−0.03	−0.03	0.05	−0.02
90	0.08	0.89	−0.23	0.08	0.83	−0.21	0.08	0.87	−0.22	0.08	0.87	−0.22	0.08	0.87	−0.22	0.08	0.87	−0.22	180	−0.03	0.04	−0.01	0.00	0.04	0.00	−0.01	0.05	0.00	−0.01	0.05	0.00	−0.01	0.05	0.00	0.01	0.05	0.00

Table 2 Polar data: tripped

	⇑ 100 k			⇓ 100 k			⇑ 140 k			⇓ 140 k			⇑ 180 k			⇓ 180 k			⇑ 100 k			⇓ 100 k			⇑ 140 k			⇓ 140 k			⇑ 180 k			⇓ 180 k		
α	C_l	C_{dp}	C_m	C_l	C_{dp}	C_m	C_l	C_{dp}	C_m	C_l	C_{dp}	C_m	C_l	C_{dp}	C_m	C_l	C_{dp}	C_m	α	C_l	C_{dp}	C_m	C_l	C_{dp}	C_m	C_l	C_{dp}	C_m	C_l	C_{dp}	C_m	C_l	C_{dp}	C_m	C_l	C_{dp}	C_m
0	−0.03	0.01	0.01	−0.03	0.01	0.01	−0.03	0.00	0.01	−0.03	0.00	0.01	−0.03	0.00	0.00	−0.02	0.00	0.01																		
1	0.03	0.00	0.01	0.02	0.00	0.01	0.02	0.00	0.01	0.03	0.00	0.01	0.03	0.00	0.01	0.04	0.00	0.01	91	0.07	0.94	−0.25	0.07	0.95	−0.26	0.07	0.88	−0.24	0.07	0.89	−0.24	0.07	0.89	−0.24	0.07	0.89	−0.24
2	0.09	0.00	0.01	0.08	0.00	0.02	0.08	0.00	0.01	0.09	0.00	0.01	0.09	0.00	0.02	0.08	0.00	0.02	92	0.05	0.95	−0.26	0.05	0.93	−0.25	0.05	0.88	−0.24	0.05	0.89	−0.24	0.05	0.89	−0.24	0.05	0.89	−0.24
3	0.14	0.00	0.02	0.13	0.00	0.02	0.16	0.00	0.01	0.16	0.00	0.01	0.15	0.00	0.01	0.16	0.00	0.01	93	0.04	0.94	−0.26	0.04	0.94	−0.26	0.04	0.88	−0.24	0.04	0.89	−0.24	0.04	0.89	−0.25	0.04	0.88	−0.25
4	0.17	0.00	0.03	0.17	0.00	0.04	0.22	0.00	0.01	0.22	0.00	0.01	0.22	0.00	0.01	0.23	0.00	0.01	94	0.02	0.94	−0.26	0.02	0.94	−0.26	0.03	0.88	−0.24	0.03	0.89	−0.25	0.03	0.89	−0.25	0.03	0.88	−0.25
5	0.23	0.01	0.03	0.23	0.01	0.04	0.27	0.00	0.01	0.27	0.00	0.02	0.28	0.00	0.01	0.29	0.00	0.01	95	0.01	0.95	−0.27	0.01	0.95	−0.27	0.01	0.88	−0.25	0.01	0.89	−0.25	0.01	0.88	−0.25	0.01	0.88	−0.25
6	0.30	0.01	0.03	0.31	0.01	0.03	0.32	0.01	0.02	0.33	0.01	0.02	0.33	0.01	0.02	0.34	0.01	0.02	96	−0.01	0.94	−0.27	−0.01	0.95	−0.27	0.00	0.87	−0.25	0.00	0.88	−0.25	0.00	0.88	−0.25	0.00	0.88	−0.25
7	0.39	0.02	0.02	0.40	0.02	0.02	0.39	0.02	0.02	0.39	0.02	0.02	0.40	0.02	0.02	0.40	0.02	0.02	97	−0.02	0.94	−0.27	−0.02	0.95	−0.27	−0.01	0.87	−0.25	−0.01	0.88	−0.25	−0.01	0.88	−0.25	−0.01	0.88	−0.25
8	0.48	0.03	0.01	0.49	0.03	0.01	0.47	0.02	0.02	0.48	0.02	0.02	0.44	0.02	0.02	0.45	0.02	0.02	98	−0.03	0.93	−0.27	−0.03	0.95	−0.27	−0.02	0.87	−0.25	−0.03	0.88	−0.26	−0.03	0.88	−0.26	−0.03	0.87	−0.26
9	0.59	0.04	0.00	0.59	0.04	0.00	0.52	0.03	0.02	0.53	0.03	0.02	0.51	0.02	0.02	0.51	0.02	0.02	99	−0.05	0.94	−0.28	−0.05	0.93	−0.27	−0.04	0.87	−0.25	−0.04	0.87	−0.26	−0.04	0.87	−0.26	−0.04	0.87	−0.26
10	0.67	0.05	−0.01	0.67	0.05	0.01	0.59	0.04	0.01	0.60	0.04	0.01	0.59	0.03	0.02	0.60	0.03	0.02	100	−0.06	0.93	−0.28	−0.06	0.92	−0.28	−0.05	0.86	−0.26	−0.05	0.86	−0.26	−0.05	0.87	−0.26	−0.05	0.86	−0.26
11	0.69	0.05	−0.01	0.68	0.05	0.00	0.68	0.05	0.00	0.68	0.05	0.00	0.68	0.05	0.01	0.70	0.05	0.01	101	−0.08	0.93	−0.28	−0.08	0.92	−0.28	−0.06	0.86	−0.26	−0.06	0.86	−0.26	−0.07	0.86	−0.26	−0.06	0.86	−0.26
12	0.75	0.07	−0.01	0.76	0.07	0.00	0.76	0.07	0.00	0.74	0.06	0.01	0.74	0.06	0.01	0.74	0.06	0.01	102	−0.09	0.92	−0.28	−0.09	0.92	−0.28	−0.08	0.85	−0.26	−0.08	0.86	−0.26	−0.08	0.86	−0.26	−0.08	0.86	−0.26
13	0.78	0.08	0.00	0.78	0.08	0.00	0.77	0.08	−0.01	0.75	0.07	0.00	0.75	0.07	0.00	0.75	0.07	0.00	103	−0.11	0.92	−0.28	−0.11	0.92	−0.28	−0.09	0.85	−0.26	−0.09	0.85	−0.26	−0.09	0.85	−0.26	−0.09	0.85	−0.27
14	0.34	0.11	0.01	0.34	0.11	0.01	0.34	0.11	0.01	0.34	0.11	0.01	0.34	0.11	0.01	0.34	0.11	0.01	104	−0.12	0.91	−0.28	−0.12	0.91	−0.28	−0.10	0.84	−0.26	−0.10	0.84	−0.26	−0.10	0.84	−0.26	−0.10	0.84	−0.27
15	0.15	0.13	0.00	0.15	0.13	0.00	0.15	0.12	0.00	0.16	0.13	0.00	0.16	0.12	0.00	0.16	0.12	0.00	105	−0.13	0.90	−0.28	−0.13	0.90	−0.28	−0.11	0.84	−0.26	−0.11	0.84	−0.27	−0.11	0.84	−0.27	−0.11	0.84	−0.27
16	0.20	0.15	0.00	0.20	0.15	0.00	0.18	0.14	0.00	0.18	0.14	0.00	0.18	0.14	0.00	0.19	0.14	−0.01	106	−0.15	0.90	−0.29	−0.14	0.89	−0.28	−0.13	0.83	−0.27	−0.13	0.83	−0.27	−0.12	0.84	−0.27	−0.12	0.84	−0.27
17	0.22	0.17	−0.01	0.22	0.16	0.00	0.22	0.16	−0.01	0.22	0.16	−0.01	0.22	0.16	−0.01	0.22	0.16	−0.01	107	−0.16	0.89	−0.29	−0.16	0.88	−0.28	−0.14	0.82	−0.27	−0.14	0.82	−0.27	−0.13	0.83	−0.27	−0.13	0.83	−0.27
18	0.26	0.18	−0.01	0.27	0.19	−0.01	0.26	0.18	−0.01	0.26	0.18	−0.01	0.26	0.18	−0.01	0.26	0.18	−0.01	108	−0.17	0.87	−0.29	−0.17	0.86	−0.28	−0.15	0.81	−0.27	−0.15	0.81	−0.27	−0.15	0.82	−0.27	−0.14	0.82	−0.27
19	0.31	0.21	−0.02	0.31	0.21	−0.02	0.31	0.21	−0.02	0.31	0.21	−0.02	0.31	0.21	−0.02	0.32	0.21	−0.02	109	−0.19	0.89	−0.29	−0.18	0.85	−0.28	−0.16	0.80	−0.27	−0.16	0.80	−0.27	−0.16	0.81	−0.27	−0.16	0.81	−0.27
20	0.32	0.22	−0.02	0.32	0.22	−0.02	0.32	0.22	−0.02	0.32	0.22	−0.02	0.32	0.22	−0.02	0.32	0.22	−0.02	110	−0.20	0.88	−0.29	−0.19	0.85	−0.28	−0.17	0.79	−0.27	−0.17	0.79	−0.27	−0.17	0.80	−0.27	−0.17	0.80	−0.27
21	0.34	0.24	−0.02	0.36	0.25	−0.03	0.37	0.25	−0.03	0.37	0.24	−0.03	0.38	0.25	−0.03	0.39	0.26	−0.04	111	−0.22	0.87	−0.29	−0.20	0.83	−0.28	−0.18	0.78	−0.27	−0.18	0.78	−0.27	−0.19	0.79	−0.27	−0.19	0.79	−0.27
22	0.38	0.26	−0.03	0.39	0.26	−0.03	0.40	0.27	−0.04	0.40	0.27	−0.04	0.41	0.27	−0.04	0.41	0.28	−0.04	112	−0.23	0.86	−0.29	−0.21	0.81	−0.28	−0.20	0.78	−0.27	−0.19	0.78	−0.27	−0.20	0.78	−0.28	−0.20	0.78	−0.27
23	0.39	0.27	−0.03	0.39	0.28	−0.03	0.43	0.29	−0.04	0.43	0.29	−0.04	0.42	0.29	−0.04	0.42	0.29	−0.04	113	−0.24	0.84	−0.29	−0.20	0.76	−0.27	−0.20	0.77	−0.27	−0.21	0.77	−0.28	−0.21	0.77	−0.28	−0.21	0.77	−0.28
24	0.39	0.28	−0.03	0.41	0.29	−0.03	0.45	0.31	−0.05	0.45	0.31	−0.05	0.44	0.31	−0.04	0.44	0.31	−0.04	114	−0.25	0.82	−0.29	−0.21	0.74	−0.27	−0.22	0.76	−0.27	−0.22	0.77	−0.28	−0.22	0.77	−0.28	−0.22	0.76	−0.28
25	0.39	0.29	−0.03	0.40	0.30	−0.03	0.44	0.32	−0.05	0.47	0.34	−0.05	0.45	0.33	−0.05	0.45	0.33	−0.05	115	−0.26	0.81	−0.29	−0.22	0.73	−0.27	−0.22	0.75	−0.27	−0.23	0.75	−0.28	−0.23	0.76	−0.28	−0.23	0.75	−0.27
26	0.37	0.29	−0.03	0.19	0.20	0.01	0.44	0.33	−0.05	0.31	0.26	−0.02	0.43	0.33	−0.04	0.41	0.31	−0.04	116	−0.27	0.80	−0.29	−0.22	0.71	−0.27	−0.24	0.74	−0.27	−0.24	0.74	−0.28	−0.24	0.75	−0.28	−0.24	0.75	−0.28
27	0.21	0.22	0.00	0.18	0.20	0.01	0.28	0.26	−0.01	0.28	0.25	−0.01	0.36	0.30	−0.03	0.32	0.28	−0.02	117	−0.27	0.77	−0.29	−0.23	0.69	−0.27	−0.25	0.73	−0.27	−0.25	0.73	−0.28	−0.25	0.74	−0.28	−0.25	0.74	−0.28
28	0.18	0.21	0.01	0.17	0.20	0.01	0.27	0.26	−0.01	0.28	0.26	−0.01	0.31	0.28	−0.02	0.29	0.27	−0.02	118	−0.27	0.74	−0.28	−0.24	0.68	−0.27	−0.26	0.72	−0.28	−0.26	0.72	−0.28	−0.26	0.73	−0.28	−0.26	0.73	−0.28
29	0.16	0.20	0.02	0.16	0.20	0.02	0.28	0.27	−0.02	0.28	0.27	−0.01	0.29	0.27	−0.02	0.29	0.27	−0.02	119	−0.27	0.72	−0.28	−0.24	0.67	−0.26	−0.27	0.72	−0.28	−0.27	0.72	−0.28	−0.27	0.72	−0.28	−0.27	0.72	−0.28
30	0.14	0.20	0.02	0.17	0.21	0.01	0.29	0.28	−0.02	0.28	0.28	−0.02	0.29	0.28	−0.02	0.30	0.29	−0.02	120	−0.27	0.70	−0.27	−0.25	0.66	−0.26	−0.27	0.70	−0.28	−0.27	0.70	−0.28	−0.28	0.71	−0.28	−0.28	0.71	−0.28
31	0.15	0.21	0.02	0.17	0.21	0.01	0.30	0.30	−0.02	0.29	0.29	−0.02	0.30	0.29	−0.02	0.30	0.29	−0.02	121	−0.27	0.68	−0.27	−0.26	0.65	−0.26	−0.28	0.69	−0.27	−0.28	0.69	−0.28	−0.29	0.70	−0.28	−0.29	0.70	−0.28
32	0.16	0.21	0.02	0.17	0.22	0.01	0.31	0.30	−0.02	0.30	0.30	−0.02	0.30	0.30	−0.02	0.30	0.30	−0.02	122	−0.28	0.66	−0.27	−0.27	0.64	−0.26	−0.29	0.68	−0.28	−0.29	0.68	−0.28	−0.29	0.68	−0.28	−0.29	0.68	−0.28
33	0.16	0.22	0.02	0.17	0.22	0.01	0.31	0.31	−0.03	0.30	0.31	−0.02	0.31	0.31	−0.03	0.31	0.31	−0.03	123	−0.28	0.65	−0.27	−0.27	0.62	−0.26	−0.30	0.67	−0.28	−0.30	0.67	−0.28	−0.30	0.67	−0.28	−0.30	0.67	−0.28
34	0.17	0.22	0.01	0.18	0.23	0.01	0.32	0.33	−0.03	0.32	0.33	−0.02	0.32	0.33	−0.03	0.32	0.33	−0.03	124	−0.29	0.63	−0.27	−0.27	0.60	−0.26	−0.31	0.66	−0.27	−0.30	0.64	−0.27	−0.31	0.66	−0.27	−0.31	0.66	−0.27
35	0.18	0.23	0.01	0.19	0.24	0.01	0.33	0.34	−0.03	0.31	0.32	−0.03	0.33	0.34	−0.03	0.33	0.34	−0.03	125	−0.30	0.62	−0.27	−0.28	0.59	−0.26	−0.31	0.64	−0.27	−0.31	0.63	−0.27	−0.31	0.64	−0.27	−0.31	0.64	−0.27
36	0.19	0.24	0.01	0.19	0.25	0.01	0.33	0.35	−0.03	0.31	0.33	−0.03	0.34	0.35	−0.04	0.33	0.35	−0.04	126	−0.30	0.61	−0.26	−0.29	0.58	−0.26	−0.32	0.63	−0.27	−0.32	0.63	−0.27	−0.32	0.63	−0.27	−0.32	0.63	−0.27
37	0.20	0.25	0.00	0.21	0.26	0.00	0.34	0.36	−0.04	0.32	0.35	−0.03	0.35	0.37	−0.04	0.34	0.36	−0.04	127	−0.32	0.61	−0.27	−0.29	0.56	−0.25	−0.32	0.61	−0.27	−0.32	0.60	−0.26	−0.32	0.62	−0.27	−0.32	0.61	−0.27
38	0.21	0.26	0.00	0.22	0.27	0.00	0.35	0.37	−0.04	0.33	0.36	−0.04	0.35	0.38	−0.04	0.35	0.38	−0.04	128	−0.32	0.58	−0.26	−0.29	0.54	−0.25	−0.33	0.60	−0.27	−0.32	0.59	−0.27	−0.33	0.60	−0.27	−0.33	0.60	−0.27
39	0.22	0.28	0.00	0.22	0.28	−0.01	0.35	0.38	−0.04	0.34	0.37	−0.04	0.36	0.39	−0.05	0.36	0.39	−0.05	129	−0.31	0.56	−0.26	−0.29	0.53	−0.25	−0.33	0.58	−0.26	−0.33	0.59	−0.27	−0.33	0.58	−0.26	−0.33	0.58	−0.26
40	0.23	0.29	−0.01	0.24	0.29	−0.01	0.36	0.40	−0.05	0.35	0.39	−0.04	0.37	0.41	−0.05	0.37	0.41	−0.05	130	−0.31	0.53	−0.25	−0.30	0.52	−0.25	−0.33	0.56	−0.26	−0.33	0.56	−0.26	−0.34	0.57	−0.26	−0.33	0.57	−0.26
41	0.24	0.30	−0.01	0.25	0.31	−0.02	0.37	0.41	−0.05	0.35	0.39	−0.05	0.38	0.42	−0.05	0.38	0.42	−0.05	131	−0.31	0.52	−0.25	−0.30	0.50	−0.24	−0.33	0.55	−0.26	−0.33	0.54	−0.26	−0.34	0.56	−0.26	−0.34	0.56	−0.26
42	0.25	0.31	−0.02	0.26	0.32	−0.02	0.38	0.43	−0.06	0.36	0.42	−0.05	0.38	0.43	−0.06	0.38	0.43	−0.06	132	−0.32	0.51	−0.25	−0.30	0.49	−0.24	−0.34	0.53	−0.25	−0.33	0.52	−0.25	−0.35	0.55	−0.26	−0.34	0.54	−0.26
43	0.26	0.33	−0.02	0.26	0.33	−0.02	0.38	0.44	−0.06	0.37	0.43	−0.05	0.38	0.44	−0.06	0.39	0.45	−0.06	133	−0.32	0.49	−0.24	−0.30	0.47	−0.24	−0.34	0.52	−0.25	−0.33	0.51	−0.25	−0.34	0.53	−0.26	−0.34	0.52	−0.26
44	0.27	0.35	−0.03	0.27	0.35	−0.03	0.38	0.45	−0.06	0.37	0.44	−0.06	0.39	0.46	−0.06	0.39	0.46	−0.06	134	−0.31	0.47	−0.24	−0.30	0.46	−0.24	−0.34	0.50	−0.25	−0.34	0.50	−0.25	−0.35	0.51	−0.25	−0.34	0.51	−0.25
45	0.28	0.36	−0.03	0.28	0.36	−0.03	0.40	0.47	−0.07	0.38	0.46	−0.06	0.40	0.48	−0.07	0.40	0.48	−0.07	135	−0.32	0.46	−0.24	−0.30	0.44	−0.23	−0.34	0.48	−0.24	−0.34	0.48	−0.24	−0.35	0.50	−0.25	−0.35	0.49	−0.25
46	0.29	0.38	−0.04	0.29	0.37	−0.04	0.40	0.49	−0.07	0.38	0.47	−0.07	0.40	0.49	−0.07	0.40	0.49	−0.07	136	−0.32	0.45	−0.24	−0.30	0.43	−0.23	−0.34	0.47	−0.24	−0.34	0.47	−0.24	−0.35	0.48	−0.25	−0.35	0.48	−0.25
47	0.30	0.39	−0.04	0.29	0.39	−0.04	0.40	0.50	−0.08	0.39	0.49	−0.07	0.41	0.51	−0.08	0.41	0.51	−0.08	137	−0.32	0.43	−0.23	−0.29	0.40	−0.22	−0.34	0.45	−0.24	−0.34	0.46	−0.24	−0.35	0.47	−0.25	−0.35	0.46	−0.24
48	0.30	0.40	−0.05	0.30	0.40	−0.04	0.41	0.52	−0.08	0.40	0.51	−0.08	0.41	0.52	−0.08	0.41	0.52	−0.08	138	−0.32	0.41	−0.23	−0.29	0.39	−0.22	−0.35	0.45	−0.25	−0.35	0.45	−0.25	−0.35	0.45	−0.25	−0.35	0.45	−0.25
49	0.31	0.42	−0.05	0.30	0.41	−0.05	0.41	0.53	−0.09	0.40	0.52	−0.08	0.41	0.53	−0.09	0.41	0.53	−0.09	139	−0.31	0.40	−0.22	−0.62	0.75	−0.36	−0.34	0.42	−0.23	−0.51	0.61	−0.30	−0.36	0.44	−0.24	−0.59	0.70	−0.34
50	0.32	0.44	−0.06	0.31	0.43	−0.05	0.41	0.55	−0.09	0.40	0.53	−0.08	0.41	0.55	−0.09	0.42	0.55	−0.09	140	−0.32	0.39	−0.22	−0.78	0.89	−0.41	−0.35	0.42	−0.23	−0.65	0.75	−0.36	−0.36	0.43	−0.24	−0.67	0.76	−0.37
51	0.32	0.45	−0.06	0.32	0.44	−0.06	0.41	0.56	−0.09	0.40	0.54	−0.09	0.42	0.56	−0.09	0.42	0.57	−0.10	141	−0.32	0.38	−0.22	−0.74	0.82	−0.39	−0.35	0.41	−0.23	−0.80	0.89	−0.42	−0.36	0.42	−0.24	−0.80	0.88	−0.42
52	0.33	0.47	−0.07	0.32	0.46	−0.06	0.42	0.58	−0.10	0.40	0.56	−0.09	0.42	0.58	−0.10	0.42	0.58	−0.10	142	−0.31	0.36	−0.21	−0.79	0.84	−0.40	−0.35	0.39	−0.22	−0.84	0.89	−0.43	−0.36	0.40	−0.23	−0.88	0.92	−0.43
53	0.33	0.48	−0.07	0.33	0.47	−0.07	0.42	0.59	−0.10	0.41	0.58	−0.10	0.42	0.59	−0.10	0.42	0.60	−0.10	143	−0.31	0.35	−0.21	−0.80	0.82	−0.40	−0.35	0.38	−0.22	−0.90	0.91	−0.43	−0.36	0.39	−0.23	−0.89	0.90	−0.43
54	0.34	0.50	−0.08	0.33	0.49	−0.07	0.42	0.61	−0.11	0.41	0.60	−0.10	0.42	0.61	−0.11	0.41	0.60	−0.11	144	−0.31	0.34	−0.21	−0.89	0.88	−0.42	−0.35	0.37	−0.22	−0.87	0.87	−0.42	−0.36	0.37	−0.23	−0.90	0.88	−0.43
55	0.34	0.52	−0.08	0.33	0.50	−0.08	0.42	0.62	−0.11	0.41	0.61	−0.11	0.41	0.62	−0.11	0.41	0.62	−0.11	145	−0.31	0.32	−0.20	−0.89	0.85	−0.41	−0.35	0.35	−0.22	−0.91	0.87	−0.42	−0.35	0.36	−0.22	−0.84	0.81	−0.41
56	0.35	0.53	−0.09	0.33	0.52	−0.08	0.41	0.64	−0.12	0.41	0.62	−0.11	0.41	0.63	−0.12	0.41	0.63	−0.12	146	−0.30	0.31	−0.20	−0.79	0.76	−0.39	−0.35	0.34	−0.22	−0.90	0.83	−0.42	−0.36	0.35	−0.22	−0.88	0.81	−0.41
57	0.35	0.55	−0.09	0.34	0.53	−0.09	0.41	0.65	−0.12	0.40	0.64	−0.12	0.41	0.65	−0.12	0.41	0.65	−0.12	147	−0.29	0.29	−0.19	−0.88	0.79	−0.40	−0.36	0.34	−0.22	−0.86	0.77	−0.40	−0.36	0.34	−0.22	−0.88	0.79	−0.41
58	0.34	0.56	−0.10	0.34	0.55	−0.09	0.41	0.66	−0.12	0.40	0.65	−0.12	0.41	0.66	−0.12	0.41	0.66	−0.12	148	−0.30	0.28	−0.19	−0.83	0.73	−0.39	−0.41	0.37	−0.24	−0.80	0.70	−0.38	−0.36	0.33	−0.21	−0.84	0.74	−0.39
59	0.35	0.58	−0.10	0.34	0.57	−0.10	0.40	0.67	−0.13	0.40	0.66	−0.13	0.40	0.67	−0.13	0.41	0.68	−0.13	149	−0.27	0.26	−0.19	−0.78	0.66	−0.37	−0.42	0.36	−0.23	−0.79	0.67	−0.38	−0.39	0.34	−0.22	−0.77	0.66	−0.37
60	0.35	0.60	−0.11	0.34	0.58	−0.10	0.40	0.69	−0.13	0.39	0.68	−0.13	0.40	0.69	−0.13	0.40	0.69	−0.13	150	−0.42	0.37	−0.25	−0.61	0.51	−0.33	−0.54	0.46	−0.29	−0.71	0.60	−0.36	−0.60	0.51	−0.31	−0.72	0.60	−0.35
61	0.35	0.62	−0.12	0.34	0.60	−0.11	0.40	0.70	−0.14	0.39	0.69	−0.13	0.40	0.70	−0.14	0.40	0.70	−0.14	151	−0.52	0.43	−0.30	−0.56	0.46	−0.31	−0.59	0.48	−0.32	−0.60	0.49	−0.32	−0.59	0.48	−0.32	−0.59	0.48	−0.32

Table 2 (continued)

α	$\alpha \Uparrow 100$ k			$\alpha \Downarrow 100$ k			$\alpha \Uparrow 140$ k			$\alpha \Downarrow 140$ k			$\alpha \Uparrow 180$ k			$\alpha \Downarrow 180$ k			α	$\alpha \Uparrow 100$ k			$\alpha \Downarrow 100$ k			$\alpha \Uparrow 140$ k			$\alpha \Downarrow 140$ k			$\alpha \Uparrow 180$ k			$\alpha \Downarrow 180$ k		
	C_l	C_{dp}	C_m	C_l	C_{dp}	C_m	C_l	C_{dp}	C_m	C_l	C_{dp}	C_m	C_l	C_{dp}	C_m	C_l	C_{dp}	C_m		C_l	C_{dp}	C_m	C_l	C_{dp}	C_m	C_l	C_{dp}	C_m	C_l	C_{dp}	C_m	C_l	C_{dp}	C_m	C_l	C_{dp}	C_m
62	0.35	0.63	−0.12	0.34	0.62	−0.12	0.39	0.71	−0.14	0.38	0.70	−0.14	0.39	0.71	−0.14	0.39	0.71	−0.14	152	−0.51	0.41	−0.29	−0.52	0.42	−0.29	−0.56	0.44	−0.30	−0.56	0.44	−0.30	−0.56	0.44	−0.30	−0.56	0.44	−0.30
63	0.35	0.65	−0.13	0.34	0.64	−0.12	0.38	0.72	−0.14	0.38	0.71	−0.14	0.38	0.72	−0.15	0.39	0.73	−0.15	153	−0.50	0.39	−0.28	−0.50	0.39	−0.28	−0.54	0.41	−0.29	−0.54	0.41	−0.29	−0.54	0.41	−0.29	−0.54	0.41	−0.29
64	0.34	0.66	−0.13	0.34	0.66	−0.13	0.37	0.71	−0.14	0.36	0.71	−0.14	0.38	0.73	−0.15	0.38	0.74	−0.15	154	−0.49	0.37	−0.27	−0.50	0.37	−0.27	−0.52	0.38	−0.28	−0.52	0.38	−0.28	−0.52	0.38	−0.28	−0.52	0.38	−0.28
65	0.34	0.68	−0.14	0.34	0.68	−0.14	0.36	0.73	−0.15	0.36	0.72	−0.15	0.37	0.74	−0.15	0.37	0.75	−0.15	155	−0.49	0.35	−0.26	−0.49	0.35	−0.26	−0.51	0.36	−0.27	−0.51	0.36	−0.27	−0.51	0.36	−0.27	−0.51	0.36	−0.27
66	0.34	0.70	−0.14	0.33	0.69	−0.14	0.35	0.74	−0.15	0.35	0.73	−0.15	0.36	0.76	−0.16	0.36	0.75	−0.16	156	−0.50	0.34	−0.26	−0.49	0.34	−0.26	−0.51	0.34	−0.26	−0.51	0.34	−0.26	−0.50	0.34	−0.26	−0.50	0.34	−0.26
67	0.33	0.71	−0.15	0.33	0.71	−0.15	0.35	0.75	−0.16	0.34	0.74	−0.16	0.35	0.75	−0.16	0.35	0.75	−0.16	157	−0.50	0.33	−0.26	−0.49	0.32	−0.26	−0.51	0.33	−0.26	−0.50	0.33	−0.26	−0.51	0.33	−0.26	−0.51	0.33	−0.26
68	0.32	0.72	−0.15	0.32	0.72	−0.15	0.34	0.76	−0.16	0.34	0.75	−0.16	0.34	0.76	−0.16	0.34	0.76	−0.16	158	−0.50	0.31	−0.26	−0.53	0.33	−0.26	−0.54	0.33	−0.26	−0.50	0.32	−0.26	−0.51	0.32	−0.26	−0.51	0.32	−0.26
69	0.32	0.74	−0.16	0.32	0.74	−0.16	0.33	0.76	−0.16	0.33	0.77	−0.16	0.33	0.77	−0.17	0.33	0.77	−0.17	159	−0.54	0.31	−0.26	−0.54	0.32	−0.26	−0.57	0.33	−0.27	−0.55	0.32	−0.26	−0.54	0.32	−0.26	−0.54	0.32	−0.26
70	0.31	0.75	−0.16	0.31	0.76	−0.16	0.32	0.78	−0.17	0.32	0.77	−0.17	0.32	0.78	−0.17	0.32	0.78	−0.17	160	−0.54	0.30	−0.26	−0.55	0.30	−0.26	−0.56	0.31	−0.26	−0.55	0.31	−0.26	−0.55	0.31	−0.26	−0.55	0.30	−0.26
71	0.31	0.77	−0.17	0.31	0.77	−0.17	0.31	0.78	−0.17	0.31	0.78	−0.17	0.31	0.79	−0.17	0.31	0.79	−0.17	161	−0.56	0.29	−0.26	−0.56	0.29	−0.26	−0.58	0.30	−0.26	−0.57	0.29	−0.26	−0.56	0.29	−0.26	−0.57	0.29	−0.26
72	0.30	0.79	−0.18	0.29	0.77	−0.17	0.30	0.79	−0.17	0.30	0.79	−0.18	0.30	0.80	−0.18	0.30	0.80	−0.18	162	−0.59	0.28	−0.26	−0.59	0.27	−0.26	−0.58	0.28	−0.26	−0.57	0.27	−0.25	−0.58	0.28	−0.25	−0.58	0.28	−0.25
73	0.29	0.81	−0.18	0.29	0.79	−0.18	0.29	0.80	−0.18	0.29	0.80	−0.18	0.29	0.81	−0.18	0.29	0.80	−0.18	163	−0.57	0.25	−0.25	−0.55	0.24	−0.25	−0.58	0.25	−0.26	−0.58	0.25	−0.25	−0.57	0.25	−0.25	−0.56	0.25	−0.25
74	0.29	0.83	−0.19	0.28	0.81	−0.18	0.28	0.81	−0.18	0.28	0.81	−0.18	0.28	0.82	−0.18	0.28	0.81	−0.18	164	−0.56	0.22	−0.25	−0.57	0.22	−0.26	−0.57	0.22	−0.25	−0.57	0.23	−0.25	−0.57	0.22	−0.25	−0.57	0.22	−0.25
75	0.27	0.84	−0.19	0.27	0.83	−0.19	0.27	0.82	−0.19	0.27	0.82	−0.19	0.27	0.83	−0.19	0.27	0.82	−0.19	165	−0.63	0.20	−0.28	−0.65	0.19	−0.29	−0.65	0.20	−0.29	−0.68	0.20	−0.28	−0.65	0.20	−0.28	−0.68	0.20	−0.30
76	0.26	0.85	−0.20	0.26	0.83	−0.19	0.26	0.82	−0.19	0.26	0.82	−0.19	0.26	0.83	−0.19	0.26	0.83	−0.19	166	−0.74	0.17	−0.33	−0.74	0.16	−0.34	−0.78	0.17	−0.35	−0.77	0.18	−0.34	−0.77	0.18	−0.34	−0.79	0.17	−0.35
77	0.25	0.86	−0.20	0.25	0.84	−0.20	0.25	0.83	−0.19	0.25	0.83	−0.19	0.25	0.84	−0.20	0.25	0.84	−0.20	167	−0.74	0.14	−0.35	−0.73	0.14	−0.34	−0.79	0.15	−0.36	−0.78	0.14	−0.36	−0.80	0.15	−0.36	−0.80	0.15	−0.36
78	0.24	0.87	−0.21	0.24	0.86	−0.20	0.23	0.83	−0.20	0.23	0.84	−0.20	0.24	0.85	−0.20	0.24	0.85	−0.20	168	−0.71	0.12	−0.33	−0.69	0.12	−0.32	−0.75	0.12	−0.34	−0.74	0.12	−0.33	−0.77	0.13	−0.35	−0.76	0.13	−0.34
79	0.23	0.88	−0.21	0.23	0.87	−0.21	0.22	0.84	−0.20	0.22	0.84	−0.20	0.22	0.85	−0.20	0.22	0.85	−0.20	169	−0.66	0.11	−0.30	−0.65	0.10	−0.30	−0.70	0.11	−0.31	−0.69	0.11	−0.30	−0.72	0.11	−0.32	−0.71	0.11	−0.31
80	0.22	0.88	−0.21	0.22	0.87	−0.21	0.21	0.85	−0.20	0.21	0.85	−0.20	0.21	0.86	−0.21	0.21	0.86	−0.21	170	−0.62	0.09	−0.27	−0.60	0.09	−0.27	−0.64	0.10	−0.28	−0.64	0.10	−0.27	−0.66	0.10	−0.29	−0.65	0.10	−0.28
81	0.21	0.92	−0.22	0.21	0.89	−0.22	0.20	0.85	−0.21	0.20	0.85	−0.21	0.20	0.86	−0.21	0.20	0.86	−0.21	171	−0.59	0.08	−0.25	−0.58	0.08	−0.25	−0.61	0.08	−0.26	−0.61	0.08	−0.25	−0.62	0.09	−0.26	−0.61	0.09	−0.25
82	0.19	0.91	−0.22	0.19	0.90	−0.22	0.18	0.85	−0.21	0.19	0.86	−0.21	0.19	0.87	−0.21	0.19	0.86	−0.21	172	−0.57	0.07	−0.23	−0.56	0.07	−0.23	−0.60	0.07	−0.24	−0.59	0.07	−0.24	−0.60	0.08	−0.24	−0.60	0.07	−0.24
83	0.18	0.91	−0.23	0.18	0.91	−0.23	0.17	0.86	−0.21	0.17	0.86	−0.21	0.17	0.87	−0.22	0.17	0.87	−0.22	173	−0.55	0.06	−0.22	−0.53	0.06	−0.21	−0.58	0.06	−0.23	−0.56	0.06	−0.22	−0.58	0.07	−0.23	−0.57	0.07	−0.22
84	0.17	0.91	−0.23	0.17	0.91	−0.23	0.16	0.86	−0.22	0.16	0.87	−0.22	0.16	0.87	−0.22	0.16	0.87	−0.22	174	−0.51	0.05	−0.20	−0.49	0.05	−0.19	−0.52	0.06	−0.19	−0.51	0.06	−0.18	−0.53	0.06	−0.19	−0.50	0.07	−0.17
85	0.15	0.93	−0.24	0.15	0.92	−0.23	0.15	0.87	−0.22	0.15	0.88	−0.22	0.15	0.88	−0.22	0.15	0.88	−0.22	175	−0.46	0.05	−0.17	−0.43	0.05	−0.16	−0.44	0.06	−0.15	−0.41	0.06	−0.13	−0.45	0.06	−0.14	−0.42	0.06	−0.13
86	0.14	0.94	−0.24	0.14	0.92	−0.24	0.13	0.87	−0.22	0.14	0.88	−0.22	0.14	0.88	−0.23	0.14	0.88	−0.23	176	−0.37	0.04	−0.13	−0.32	0.05	−0.11	−0.37	0.06	−0.11	−0.35	0.06	−0.10	−0.38	0.06	−0.11	−0.37	0.06	−0.10
87	0.12	0.94	−0.24	0.12	0.92	−0.24	0.12	0.88	−0.23	0.12	0.88	−0.23	0.12	0.88	−0.23	0.12	0.88	−0.23	177	−0.16	0.05	−0.06	−0.10	0.05	−0.05	−0.32	0.05	−0.08	−0.30	0.05	−0.08	−0.35	0.05	−0.09	−0.33	0.05	−0.08
88	0.11	0.94	−0.25	0.11	0.93	−0.24	0.11	0.88	−0.23	0.11	0.88	−0.23	0.11	0.89	−0.23	0.11	0.89	−0.23	178	−0.08	0.05	−0.04	−0.05	0.04	−0.03	−0.12	0.05	−0.05	−0.07	0.05	−0.04	−0.31	0.05	−0.07	−0.17	0.05	−0.05
89	0.10	0.95	−0.25	0.10	0.93	−0.25	0.10	0.88	−0.23	0.10	0.89	−0.23	0.09	0.89	−0.24	0.10	0.89	−0.24	179	−0.04	0.04	−0.02	−0.02	0.04	−0.01	−0.05	0.05	−0.02	−0.03	0.05	−0.02	−0.05	0.05	−0.02	−0.03	0.05	−0.01
90	0.08	0.95	−0.25	0.08	0.94	−0.25	0.08	0.88	−0.23	0.08	0.89	−0.24	0.08	0.89	−0.24	0.08	0.89	−0.24	180	0.00	0.04	0.00	0.03	0.04	0.01	0.00	0.05	0.00	0.01	0.05	0.00	−0.01	0.05	0.00	0.01	0.05	0.01

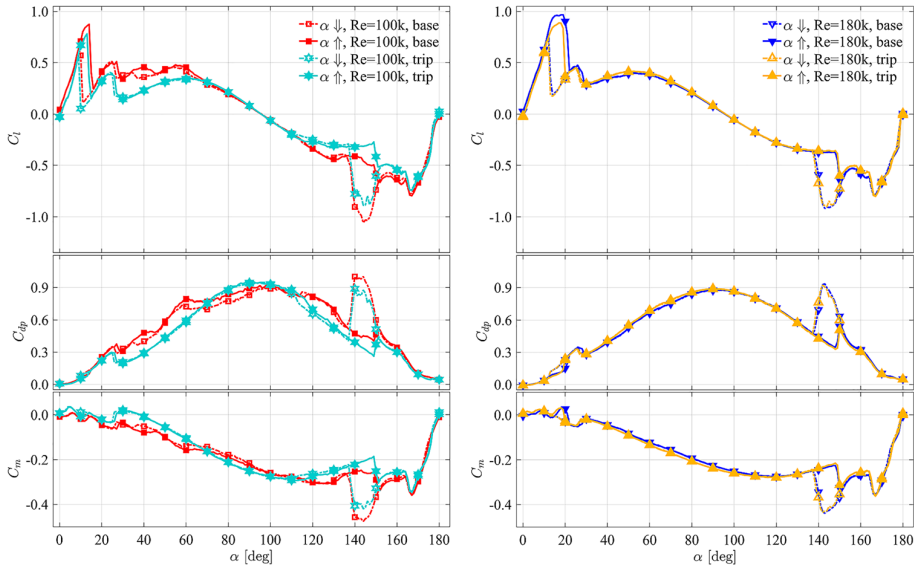

Fig. 11 NACA 0021: Comparison between baseline and tripped configuration for Re = 100 k and 180 k: (*a*) Re = 100 k and (*b*) Re = 180 k

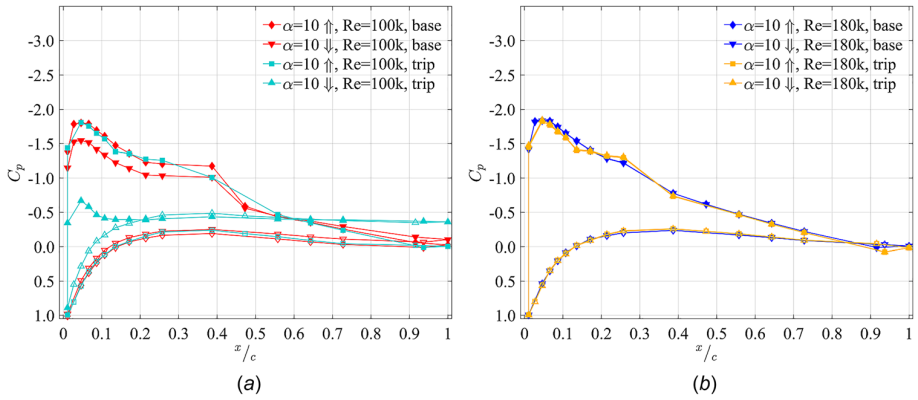

Fig. 12 NACA 0021: Effect of tripping on c_p distribution for Re = 100 k and 180 k: (*a*) Re = 100 k and (*b*) Re = 180 k

Figure 8(*b*) reveals a Reynolds independent lift polar beyond 60 deg. The polar data shown in Fig. 8 are additionally summarized within Tables 1 and 2. The measured polars have to be validated before discussing the Reynolds number differences in further detail.

Well-documented low Reynolds data for the thick NACA 0021 airfoil are rare and this is even worse for 180 deg polars. Therefore, Fig. 9 summarizes different data sets. The graph in Fig. 9(*a*) compares the data for the NACA 0021 at lower angles of attack up to 20 deg. The literature data are taken out of the works of Sheldahl and Klimas [6], the NACA technical note of Stack [17], and the NACA technical report of Jacobs [18]. The measurements agree with the data of Stack and Jacobs. The slope of the Re = 100 k polar is steeper than the slope of the higher Reynolds numbers. This behavior is also visible within the data of Jacobs. The stall angle is represented well while the maximum lift is smaller than in literature. This might be caused by the different setups or inflow conditions. The data of Sheldahl and Klimas do not seem to be representative for a NACA 0021 airfoil. Slope, stall angle, and maximum lift are completely off.

The graphs in Fig. 9(*b*) visualize the full 180 deg polars compared to the NACA 0021 data of Sheldahl and Klimas [6] as well as to data sets of Rainbird et al. [13] and Du et al. [12]. The Sheldahl and Klimas data, which are fully calculated using the PROFILE code, do not represent the measurements. The measurements of Rainbird match well the NACA 0021 data even though the Rainbird data are based on NACA 0015 and NACA 0018. The NACA 0021 drag values match well with the literature data of the open-loop configuration but are lower than the values of Rainbird. This shift within drag is known in literature [11,12,14] and is caused by the different wind tunnel configurations. Rainbird's data are based on a wind tunnel with reduced blockage but still a contained test section. The present study is based on an open jet configuration, which results in smaller drag coefficients [11,12].

Figure 8(*a*) and the detail plot in Fig. 9(*a*) visualize a nearly constant lift between 15 and 19 deg for the NACA 0021 at Re = 180 k. This is caused by a continuous trailing edge stall whose c_p distribution is shown in Fig. 10. The increase of the angle of attack from 16 deg to 19 deg results in a larger suction peak but c_p starts shifting toward negative values. The suction peak decreases but the pressure within the trailing edge region is reduced. This compensates the reduced suction peak in the overall integration but results, nevertheless, in a sign change of moment coefficient visible in Fig. 8(*a*). The stall behavior of the tripped

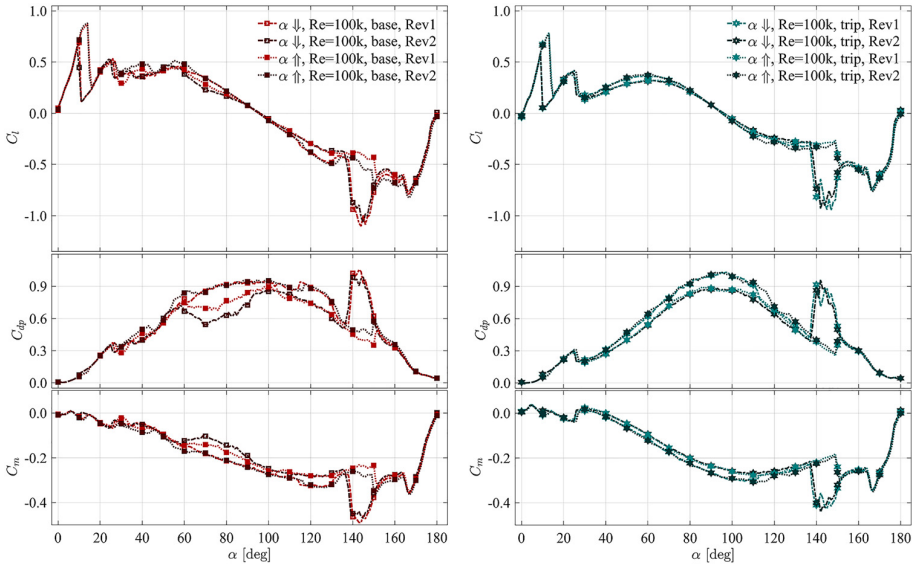

Fig. 13 NACA 0021: Effect of movement history on polars: (*a*) baseline and (*b*) tripped

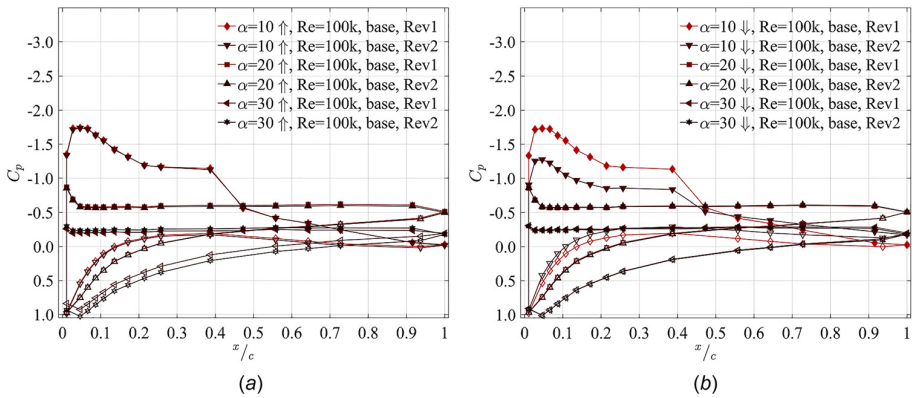

Fig. 14 NACA 0021: Effect of movement history on c_p distribution: (*a*) pitch up and (*b*) pitch down

configuration is slightly different because the trailing edge stall is not as pronounced but still partially visible in Fig. 8(*b*).

Figure 11 compares baseline and tripped conditions for Re = 100 k and 180 k. The maximum lift and the stall angle are reduced for each Reynolds number. While the tripping has no further effect at Re = 180 k in the post stall region, the flow is more sensitive to the tripping at the lower Reynolds number. Tripping reduces the lift in the post stall region between 20 deg and 70 deg and shifts the lift polar toward higher lift values in the range of 120 – 170 deg. This results in a nearly Reynolds-independent behavior beyond 70 deg compared to the other Reynolds numbers visible in Fig. 8(*b*). The standard deviation of all coefficients, which was calculated but is not shown within this paper, was reduced by applying the tripping. Figure 12(*a*) reveals the separation bubble for the baseline at $\alpha = 10$ deg, which is approximately located between $x/c \in [0.2, 0.5]$. The trip nearly eliminates this bubble but prevents a reattachment during pitch down. The tripped configuration is still stalled at 10 deg during pitch down while the flow of the baseline case is attached with a slight trailing edge separation. The NACA 0021 airfoil has also a separation bubble at Re = 180 k, which is less pronounced and located further upstream as visualized in Fig. 12(*b*). The tripping at $x/c \approx 0.15$ could not prevent the formation of a separation bubble.

Further analyses of the data were done because of the oscillating lift polar in the post stall region. The evaluation of each single run revealed a different behavior depending on the history of movement. The flow around the airfoil behaves different during the first revolution after a direction change compared to the second revolution, which continues with the movement of the first. Figure 13 shows the different behavior of both revolutions. This is especially visible within the drag component which deviates by up to $\Delta c_{dp} \approx 0.15$. The influence of movement history is also visible for the tripped configuration, nevertheless with less deviations and fluctuations. Figure 14 gives further insight into the pressure distribution of different revolutions at selected angles. Both revolutions are identical during the pitch up for $\alpha = 10$ and 20 deg, shown in Fig. 14(*a*). The higher lift at $\alpha = 30$ deg of the second revolution is a result of an increased pressure on the pressure side and an enhanced suction on the suction side. If this is based on changes within the wake or caused by other effects, it cannot be clarified in further detail. Therefore, a more detailed study is necessary to validate and understand this behavior. Nonetheless, a

comparable behavior is depicted in Fig. 14(*b*). The two revolutions of $\alpha = 20$ and 30 deg are identical in the pitch down case. The first revolution deviates at 10 deg from the second. While the flow is fully attached in the first rotation, it is partially stalled in the second resulting in a reduced suction peak and a decreased pressure at the trailing edge. This deviation was not clearly visible within the lift polars. It seems that the decreased pressure alleviates the reduction of the suction peak.

Conclusion and Future Work

An experimental study was carried out to analyze the airfoil performance of a NACA 0021 airfoil over the full range of incidence at several Reynolds numbers. The measurements revealed a second hysteresis loop at angles above 140 deg with significantly increased deviations. The hysteresis effects in lift are nearly comparable to the area around the stall angle but the changes in drag and moment are more pronounced in the deep stall region resulting in a difference of $\Delta c_m \approx 0.2$ and $\Delta c_l \approx 0.5$. The phenomenon of this second loop was accessed in more detail by analyzing the surface pressure distribution. A local reattachment near to the leading edge leads to this enhanced negative lift. The influence of tripping was investigated and the data set at $\mathrm{Re} = 100$ k was most sensible to tripping. A dependency to the history of movement was revealed as the airfoil showed a different behavior during two continuous revolutions in the same direction but further investigations are necessary to validate and analyze this effect.

The experimental setup will be extended in future by an additional wake rake. Load cells for synchronous acquisition of lift and drag will complete the setup, which will be finally able to measure lift and drag each in two independent ways synchronous to the surface pressure measurement. The experiments will focus on the effect of tripping and passive flow control on the performance of several airfoils.

Nomenclature

Latin letters

a_{ips} = static calibration factor of ith sensor
b = span of wing
c = chord length
c_l = lift coefficient
c_d = drag coefficient
c_{dp} = pressure drag coefficient
c_m = moment coefficient
c_n = normal force coefficient
c_t = tangential force coefficient
c_{dp} = pressure drag coefficient
c_p = pressure coefficient
d = nozzle diameter
p_i = pressure of ith sensor
p_{ia} = AoA specific corr. of ith sensor
p_{io} = offset of ith sensor
p_{dyn} = dynamic pressure of inflow u_∞
Re = Reynolds number
u_∞ = inflow velocity
x = chord wise coordinate
y = normal coordinate

Greek Symbols

α = angle of attack
σ = standard deviation

Acronyms

AoA = angle of attack
AR = aspect ratio
STD = standard deviation
VAWT = vertical axis wind turbine

References

[1] Selig, M. S., Donovan, J., and Fraser, D., 1989, *Airfoils at Low Speeds (SoarTech 8)*, SoarTech Aero Publications, Virginia Beach, VA.
[2] Selig, M. S., Guglielmo, J. J., Broeren, A. P., and Giguère, P., 1995, *Summary of Low-Speed Airfoil Data*, Vol. 1, SoarTech Publications, Virginia Beach, VA.
[3] Selig, M. S., Lyon, C., Giguère, P., Ninham, C. P., and Guglielmo, J. J., 1996, *Summary of Low-Speed Airfoil Data*, Vol. 2, SoarTech Publications, Virginia Beach, VA.
[4] Dominy, R., Lunt, P., Bickerdyke, A., and Dominy, J., 2007, "Self-Starting Capability of a Darrieus Turbine," Proc. Inst. Mech. Eng., Part A, **221**(1), pp. 111–120.
[5] Worasinchai, S., Ingram, G. L., and Dominy, R. G., 2012, "Effects of Wind Turbine Starting Capability on Energy Yield," ASME J. Eng. Gas Turbines Power, **134**(4), p. 042603.
[6] Sheldahl, R. E., and Klimas, P. C., 1981, "Aerodynamic Characteristics of Seven Symmetrical Airfoil Sections Through 180-Degree Angle of Attack for Use in Aerodynamic Analysis of Vertical Axis Wind Turbines," Sandia National Laboratories, Albuquerque, NM, Technical Report No. SAND-80-2114.
[7] Dossena, V., Persico, G., Paradiso, B., Battisti, L., Dell'Anna, S., Brighenti, A., and Benini, E., 2015, "An Experimental Study of the Aerodynamics and Performance of a Vertical Axis Wind Turbine in a Confined and Unconfined Environment," ASME J. Energy Resour. Technol., **137**(5), p. 051207.
[8] Bianchini, A., Balduzzi, F., Rainbird, J. M., Peiro, J., Graham, J. M. R., Ferrara, G., and Ferrari, L., 2015, "An Experimental and Numerical Assessment of Airfoil Polars for Use in Darrieus Wind Turbines—Part II: Post-Stall Data Extrapolation Methods," ASME J. Eng. Gas Turbines Power, **138**(3), p. 032603.
[9] Worasinchai, S., Ingram, G. L., and Dominy, R. G., 2011, "A Low-Reynolds-Number, High-Angle-of-Attack Investigation of Wind Turbine Aerofoils," Proc. Inst. Mech. Eng., Part A, **225**(6), pp. 748–763.
[10] Worasinchai, S., 2012, "Small Wind Turbine Starting Behaviour," Ph.D. thesis, University of Durham, Durham, UK.
[11] Du, L., Berson, A., and Dominy, R. G., 2014, "Aerofoil Behaviour at High Angles of Attack and at Reynolds Numbers Appropriate for Small Wind Turbines," Proc. Inst. Mech. Eng., Part C: J. Mech. Eng. Sci., **229**(11), pp. 2007–2022.
[12] Du, L., Berson, A., and Dominy, R. G., 2014, "NACA0018 Behaviour at High Angles of Attack and at Reynolds Numbers Appropriate for Small Wind Turbines," Durham University, Durham, UK, Report No. ECS-TR 2014/08.
[13] Rainbird, J., 2007, "The Aerodynamic Development of a Vertical Axis Wind Turbine," Master's thesis, University of Durham, Durham, UK.
[14] Rainbird, J. M., Peirá, J., and Graham, J. M. R., 2015, "Blockage-Tolerant Wind Tunnel Measurements for a NACA 0012 at High Angles of Attack," J. Wind Eng. Ind. Aerodyn., **145**, pp. 209–218.
[15] Holst, D., Balduzzi, F., Bianchini, A., Church, B., Wegner, F., Pechlivanoglou, G., Ferrari, L., Ferrara, G., Nayeri, C. N., and Paschereit, C. O., 2018, "Static and Dynamic Analysis of a NACA 0021 Airfoil Section at Low Reynolds Numbers Based on Experiments and CFD," ASME J. Eng. Gas Turbines Power (accepted).
[16] Holst, D., Church, B., Wegner, F., Pechlivanoglou, G., Nayeri, C. N., and Paschereit, C. O., 2018, "Experimental Analysis of a NACA 0021 Airfoil Under Dynamic Angle of Attack Variation and Low Reynolds Numbers," ASME J. Eng. Gas Turbines Power (accepted).
[17] Stack, J., 1931, "Tests in the Variable Density Wind Tunnel to Investigate the Effects of Scale and Turbulence on Airfoil Characteristics," National Advisory Committee for Aeronautics, Washington, DC, Technical Report No. NACA-TN-364.
[18] Jacobs, E. N., 1932, "The Aerodynamic Characteristics of Eight Very Thick Airfoils From Tests in the Variable Density Wind Tunnel," National Advisory Committee for Aeronautics. Langley Aeronautical Laboratory, Langley Field, VA, Technical Report No. NACA-TR-391.

D. Holst[1]
Chair of Fluid Dynamics,
Hermann-Föttinger-Institut,
Technische Universität Berlin,
Müller-Breslau-Straße 8,
Berlin 10623, Germany
e-mail: David.Holst@TU-Berlin.de

B. Church
Chair of Fluid Dynamics,
Hermann-Föttinger-Institut,
Technische Universität Berlin,
Müller-Breslau-Straße 8,
Berlin 10623, Germany

F. Wegner
Chair of Fluid Dynamics,
Hermann-Föttinger-Institut,
Technische Universität Berlin,
Müller-Breslau-Straße 8,
Berlin 10623, Germany

G. Pechlivanoglou
Chair of Fluid Dynamics,
Hermann-Föttinger-Institut,
Technische Universität Berlin,
Müller-Breslau-Straße 8,
Berlin 10623, Germany

C. N. Nayeri
Chair of Fluid Dynamics,
Hermann-Föttinger-Institut,
Technische Universität Berlin,
Müller-Breslau-Straße 8,
Berlin 10623, Germany

C. O. Paschereit
Chair of Fluid Dynamics,
Hermann-Föttinger-Institut,
Technische Universität Berlin,
Müller-Breslau-Straße 8,
Berlin 10623, Germany

Experimental Analysis of a NACA 0021 Airfoil Under Dynamic Angle of Attack Variation and Low Reynolds Numbers

The wind industry needs reliable and accurate airfoil polars to properly predict wind turbine performance, especially during the initial design phase. Medium- and low-fidelity simulations directly depend on the accuracy of the airfoil data and even more so if, e.g., dynamic effects are modeled. This becomes crucial if the blades of a turbine operate under stalled conditions for a significant part of the turbine's lifetime. In addition, the design process of vertical axis wind turbines needs data across the full range of angles of attack between 0 and 180 deg. Lift, drag, and surface pressure distributions of a NACA 0021 airfoil equipped with surface pressure taps were investigated based on time-resolved pressure measurements. The present study discusses full range static polars and several dynamic sinusoidal pitching configurations covering two Reynolds numbers Re = 140k and 180k, and different incidence ranges: near stall, poststall, and deep stall. Various bistable flow phenomena are discussed based on high frequency measurements revealing large lift-fluctuations in the post and deep stall regime that exceed the maximum lift of the static polars and are not captured by averaged measurements. Detailed surface pressure distributions are discussed to provide further insight into the flow conditions and pressure development during dynamic motion. The experimental data provided within the present paper are dedicated to the scientific community for calibration and reference purposes, which in the future may lead to higher accuracy in performance predictions during the design process of wind turbines. [DOI: 10.1115/1.4041146]

Introduction

The market of small wind turbines is growing, yet economically difficult. Many turbines do not perform the way the manufacturer promised. Several cases are due to their design being based on wrong power curves [1], but another problem is that small turbines are often situated in regions of lower wind speeds and experience unsteady conditions. This can result in poor performance or reduced lifetime of the entire turbine. Obstacles as well as gusts or yaw-misalignment can cause the unsteadiness, which leads to changes in the local angle of attack (AoA).

Engineers often use low- or medium-fidelity models like QBLADE [2,3] during the design process of a turbine, especially during the first design phase, as fast simulation times are essential for a short design phase. However, at the same time, detailed knowledge of the airfoil performance is crucial for a good prediction [4–7]. Darrieus vertical axis wind turbines are even more sensitive to airfoil polars, as their blades operate in stalled conditions for a significant part of their life [7,8]. They experience many dynamic effects, i.e., dynamic stall, which is largely present in their rotational motion [9,10]. Low- or medium-fidelity simulations mainly model these dynamic effects, which are also significantly polar dependent [11]. The blades of Darrieus vertical axis wind turbines operate under higher AoA than those typically investigated in the aircraft-industry. The literature lacks of high quality experimental data concerning AoAs reaching beyond the classic stall regime of up to around 25 deg. There are studies of symmetric airfoils that investigate thinner airfoils like the NACA 0012 [12,13] and NACA 0015 [13,14], but data of thicker airfoils, especially at lower Reynolds numbers, are rare. There are experimental studies of a NACA 0018 airfoil done by Rainbird et al. [15,16] and Du et al. [17,18] but the present study investigates the NACA 0021, providing additional data referring to the existing work of Holst et al. [8,19]. This paper concentrates on experiments with dynamic AoA changes at two different Reynolds numbers of Re = 140 k and 180 k.

[1]Corresponding author.

Manuscript received July 3, 2018; final manuscript received July 20, 2018; published online October 17, 2018. Editor: Jerzy T. Sawicki.

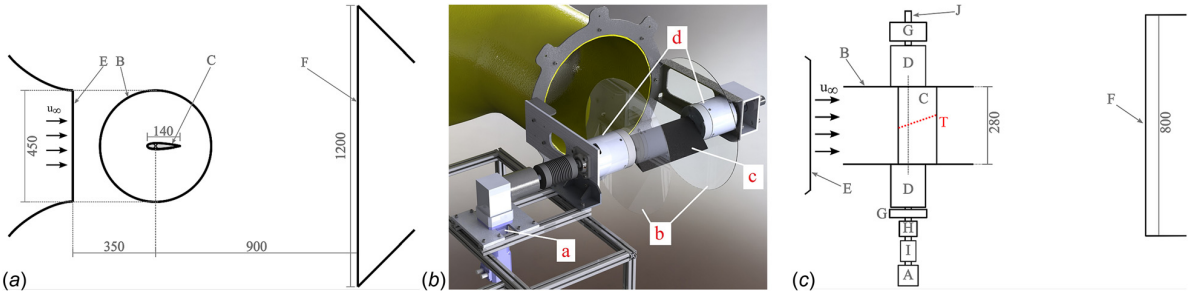

Fig. 1 Setup for dynamic and static measurements including A—motor, B—splitter plates, C—NACA 0021 airfoil with pressure taps, D—hollow shaft with room to connect time resolved pressure sensors, E—nozzle, F—collector, G—bearings, H—flexible coupling, I—1:10 angular gearbox, J—shaft, T—staggered surface pressure taps: (*a*) side view, (*b*) wind tunnel setup [8], and (*c*) top view

Experimental Configuration

The experiments were conducted at the Herman-Föttinger-Institute's laminar wind tunnel. The Göttinger type tunnel was modified to include an open test section. Details of the setup will be discussed in the setup section, followed by a description of the experimental procedure and validation.

Setup. The NACA 0021 airfoil is mounted directly in front of a nozzle with a circular cross section ($d = 0.45$ m). The nozzle has no aerodynamic lip, but the flow quality was validated by additional measurements that indicated that the turbulence level never exceeded 1.0% in the potential core. The entire setup, which is shown in Fig. 1, allows for dynamic AoA changes within a range of $\alpha = \pm 360$ deg and a maximum inflow velocity of $u_{\infty,\max} = 20$ m/s.

Figure 1(*a*) presents a side view sketch of the experimental setup, including the nozzle, test section, and collector. The latter has a contraction ratio of 6 and is not fully optimized, but manages to cover the wake area downstream of the airfoil. The dynamic movements are driven by a servomotor able to ensure positioning within an error margin of less than 0.05 deg. A custom made control program, developed using LabVIEW, controls the setup using an embedded controller and several 16-bit analog digitizers [20]. The entire setup is optimized for the acquisition of time-resolved surface pressures. The setup provides dedicated mounting room for up to 64 pressure sensors, marked with d in Fig. 1(*b*). Figure 2 shows the sensors mounted in the hollow shaft. In the present experiments, 32 high frequency pressure sensors were used to acquire the surface pressure of the NACA 0021 airfoil. The model was equipped with 32 pressure taps, which are 0.5 mm diameter holes through the surface and a metal tube in the inner part of the airfoil. The position of the pressure taps is sketched in Fig. 3. The metal tube and the respective pressure sensor are connected by a flexible tube. The regions of larger pressure gradients have a higher spatial resolution to resolve, i.e., the suction peak.

The short distance between the airfoil's pressure taps and the sensors in the mounting room ensures reduced damping. The 1000 Pa sensors have an accuracy of 0.1%FS and were calibrated in situ against a reference pressure covering the full range of ± 1000 Pa and using the same values for each sensor, allowing for a sensor specific gain. The sensor-offsets depend on the AoA and were determined by no-flow measurements. The resulting angle-dependent offsets were subtracted during the postprocessing. At high angles of incidence, the inflow velocity is affected by the airfoil downstream and was, therefore, monitored using a Prandtl probe connected to a differential pressure transducer that has an identical accuracy as the high frequency sensors. Each of the experiments was repeated multiple times to ensure repeatability and to gain further insights into the statistics.

The NACA 0021 airfoil was mounted between two splitter plates in order to avoid tip vortexes as well as to achieve 2D flow around the airfoil with minimal wall influence. The profile has a chord of $c = 0.14$ m, a span of $b = 0.28$ m, and therefore, an aspect ration of AR = 2. The model was 3D printed and the surface refined using 280 grit sanding paper. Thus, the surface is not polished but smooth, which is closer to real conditions of a wind turbine.

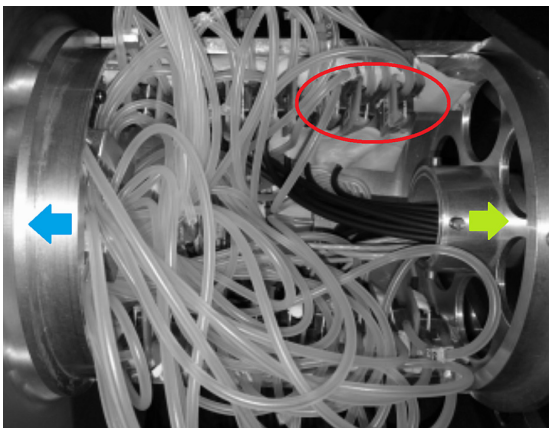

Fig. 2 Pressure sensors (circled) in the hollow shaft on the opposite side of the motor. Flexible tubing connection to the airfoil's pressure taps (left arrow) and electrical connection to the amplifier (right arrow).

Experimental Procedure and Validation. The present study is based on two different experimental procedures. The static polars were acquired by moving the airfoil to the selected AoA, waiting 1 s for the flow to stabilize and start the acquisition for 1 s at a sampling rate of 5 kHz. Afterward, a time-based average is done for each angle of the static polars. All static data sets presented are an average out of at least four repetitions. During the dynamic measurements, the pressure signals are continuously recorded, while the airfoil is performing a sinusoidal movement between the maximal and minimal angles. The sampling rate is

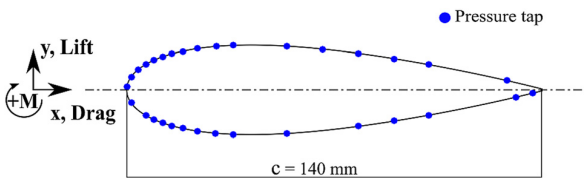

Fig. 3 Pressure tap location

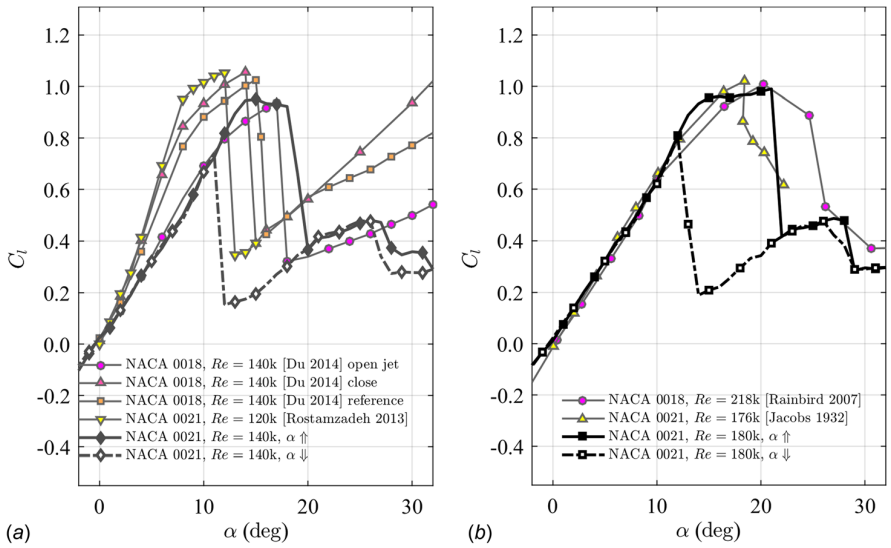

Fig. 4 Literature validation in the stall range: (*a*) Re = 140 k and (*b*) Re = 180 k

also set to 5 kHz. Lift and drag coefficients are calculated using the surface pressure distribution. The resulting drag coefficient only includes the pressure drag as contributions from skin friction are inherently missing. This affects the region of small AoA where skin friction is dominant. In these regions, the drag is underestimated. The pressure coefficient c_p is calculated for each sample using the according value of the time-resolved dynamic pressure of the inflow, thus minimizing the influence of sudden inflow fluctuations. The frequency of the sinusoidal AoA movement is represented by using the reduced frequency k, defined as

$$k = \frac{\omega}{u_\infty} \cdot \frac{c}{2} \tag{1}$$

$$= \frac{\pi f c}{u_\infty} \tag{2}$$

Movements with $0 < k \leq 0.05$ are regarded as quasi-steady aerodynamics, everything above $k > 0.05$ as unsteady. The dynamic changes we present within this paper represent a range of $0 < k \leq 0.05$.

A short validation of the experimental setup has to be done in advance of the discussion of the dynamic results. As discussed before, the literature providing validation data is rare and is even more limited for the combination of a thick NACA 0021 airfoil at low Reynolds numbers in an open test section. Therefore, Fig. 4(*a*), therefore, also shows data of a NACA 0018, taken from the work of Du et al. [18]. They showed that the form of the test section has a direct influence on the shape of the polars. However, the NACA 0021 static polar at Re = 140 k matches the shape of the open jet polar from Du et al. even though it is not the same airfoil, while the data of Rostamzadeh et al. [21] match Du's closed test-section data. Therefore, the authors are confident that the differences between, e.g., Rostamzadeh's data and the data presented within this paper are due to different types of test section. A very good agreement of the author's experimental data can be found in Fig. 4(*b*) in a comparison to data sets taken out of the NACA technical report of Jacobs [22] and the work of Rainbird [15] at a Reynolds number of Re = 180 k. Rainbird is using a test section with slitted side walls to reduce the wall influence of their closed test section. The experimental polar in Fig. 4(*b*) also reveals the occurrence of a second stall in the region of $\alpha = 28$ deg. This double stall is known to the literature and is caused when the point of separation moves from the suction to the pressure side. According to Du et al. [17], this results in a broadened wake and a direct change of the local wake flow angle.

The differences between different test sections can be minimized using appropriate correction methods to take care of blockage and buoyancy effects in a closed test section, or curvature and downwash corrections for open sections. Nevertheless, Du et al. [17] have shown that the existing open jet wind tunnel corrections exceed their limits in deep stall conditions. The authors decided to provide uncorrected experimental data as a reference for future

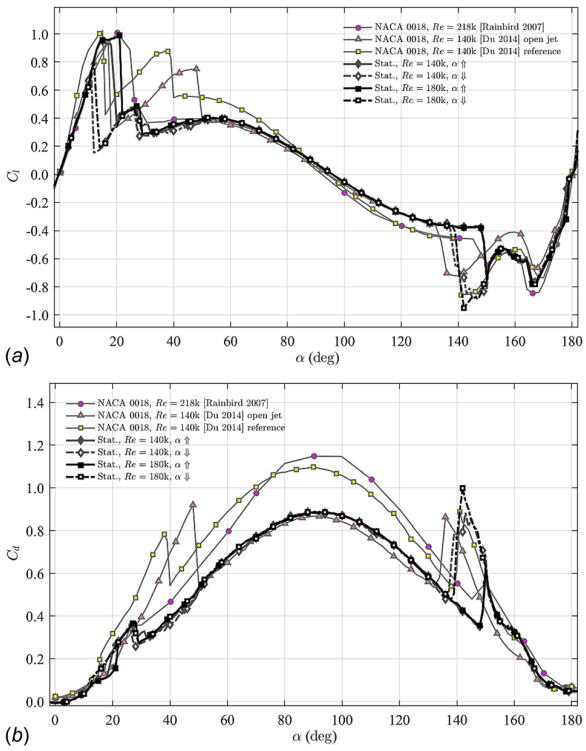

Fig. 5 Literature validation in the full 180 deg range: (*a*) lift coefficient and (*b*) drag coefficient

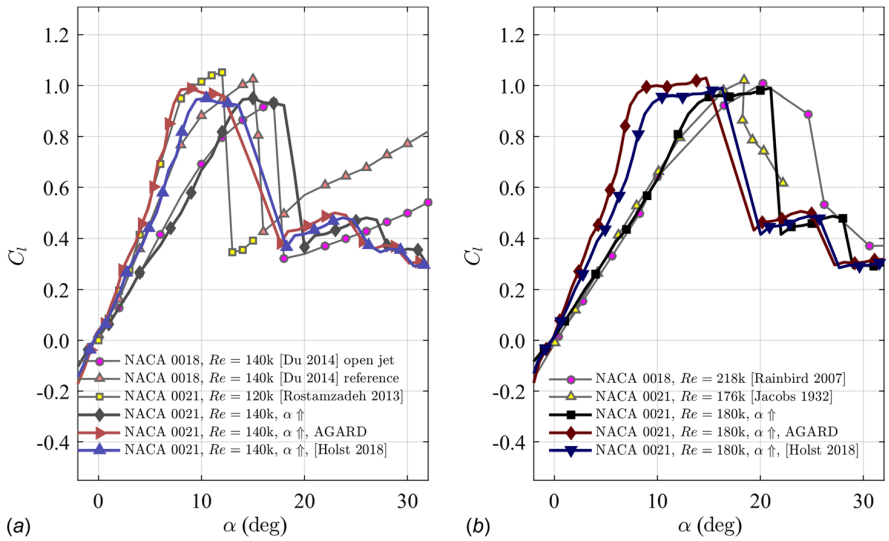

Fig. 6 Effect of correction methods in the stall range including corrections proposed by the NATO-AGARD [23,24] and a correction proposed by Holst et al. [19]: (*a*) Re = 140 k and (*b*) Re = 180 k

correction methods. Deep stall is not reached in Fig. 4 but the investigations shown in Fig. 5 cover the full range of incidence.

The open jet and the reference wind tunnel configurations of Du et al. [17] as well as Rainbird's data [15] are shown in comparison to the experimental results in Fig. 5(*a*). Rainbird's polar does not indicate the second stall, but the overall agreement is very good, even within the region beyond 140 deg. The polars of the open jet and reference wind tunnel show the phenomenon of second stall, but at different AoAs. The open jet data of Du et al. [17] match the best. The drag coefficients shown in Fig. 5(*b*) again reveal a difference between open and closed test sections. While Rainbird's polar matches Du's reference wind tunnel polar, the experimental data match Du's open jet data. The differences at $30 \leq \alpha \leq 50$ deg are based on a different behavior during the second stall.

The present shift in drag is known to the literature [12,17,18] and caused by different wind tunnel configurations. Rainbird's data are based on a wind tunnel with reduced blockage, but still represents a contained test section. The present study is based on an open jet configuration, which results in smaller drag coefficients [17,18].

For the sake of completeness, even though the paper presents uncorrected data, Figs. 6 and 7 visualize the effects of the correction methods suggested by Du et al. [17] which are based on the AGARD [23,24], as well as a correction method suggested by Holst et al. [19]. Du's corrections are based on the below equations:

$$C_{l,\mathrm{corr}} = C_l + C_l \frac{\pi^2}{24}\left(\frac{c}{\beta h}\right) \tag{3}$$

$$\beta = \sqrt{|1 - Ma^2|} \approx 1 \tag{4}$$

$$C_{d,\mathrm{corr}} = C_d - \frac{1}{2\pi}\left(\frac{L_0}{L} - 1\right)C_l^2 \tag{5}$$

$$\alpha_{\mathrm{corr}} = \alpha - \frac{1}{2\pi}\left(\frac{L_0}{L} - 1\right)C_l \tag{6}$$

L_0/L is a function which depends on the wind tunnel specific chord to tunnel height ratio c/h, a value that can be looked up in the AGARDograph 109 [23]. Additionally, the function depends on further factors, such as the form of the nozzle: square, rectangular, or circular. β is the Prandtl–Glauert factor, which is set to 1, because of the very low inflow velocities of $u_\infty \leq 20\,\mathrm{m/s}$, resulting in a Mach number $\mathrm{Ma} \leq 0.06$.

The other shown correction method originates from the work of Holst et al. [19]. Their correction is based on numerical simulations of the open test section wind tunnel setup in comparison to a

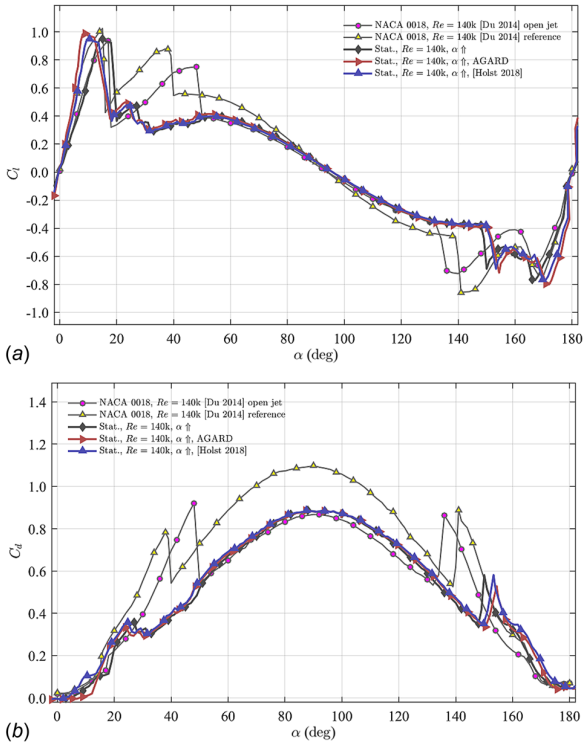

Fig. 7 Effect of correction methods in the full 180 deg range proposed by the NATO-AGARD [23,24] and a correction proposed by Holst et al. [19]: (*a*) lift coefficient and (*b*) drag coefficient

free inflow. It simply corrects the AoA in such a way that it diminishes the effect of flow deflection behind the airfoil

$$\alpha_{\text{corr}} = \alpha - a_l C_l \tag{7}$$

$$a_l = 4.762 \tag{8}$$

In contrast to the formula in Holst et al. [19], Eq. (7) subtracts the correction term instead of adding it up. This is due to the direction of the correction, in this case going from the open jet to the open field configuration.

Figure 6 confirms the assumption that the difference between the data of Rostamzadeh et al. [21] and the present data are caused by different forms of test sections. The polars based on the AGARD corrections show very good agreement with this set of data. The correction proposed by Holst et al. [19] results in a polar that matches the reference case of Du et al. [17], and therefore, reproduces the shift from their open to their reference configuration. The graphs in Fig. 7 reveal that none of the two corrections methods have an effect on the polars in the deep and poststall region, thus reinforcing the authors' decision to present fully uncorrected data in the present study.

Experimental Results

The experiments presented within this study focus on three different AoA ranges. The first covers the near stall area, starting in the linear region of the polar at $\alpha = 0$ deg and going up to the angles just behind stall at $\alpha = 20$ deg. The second extends from $\alpha = 10$ deg to 30 deg, covering the region in which the static polar encounters the second stall. Finally, deep stall investigations are conducted, covering the full range of $0 \leq \alpha \leq 180$ deg, or a limited range up to 90 deg. Each of the dynamic movements was repeated for 40 repetitions to achieve a well-grounded statistical basis. The experimental results section will be concluded by an analysis of the surface pressure coefficients for selected dynamic configurations.

Lift Under Dynamic Angle of Attack Changes at Near Stall. Static lift and drag polars have shown a good agreement in comparison to literature data, but none of the literature known to the authors provided full hysteresis investigations consisting of pitch up and down in the range of $0 \leq \alpha \leq 180$ deg, whose results were also shown within Figs. 4 and 5. The first dynamic AoA movement covers the range up to stall angle. The reader should keep in mind that the airfoil moves sinusoidal between the minimal and the maximal angle of the defined range for multiple repetitions at a given reduced frequency k, defined by Eq. (1).

Figure 8 visualizes the results of a near stall investigation at Re = 140 k between 0 and 20 deg for $k = 0.0500$ and 0.0250. The dynamic hysteresis loop differs from the static one in both cases. The higher frequency results in a higher $c_{l,\max}$ but reattachment during the pitch down phase is less stable compared to the configuration shown in Fig. 8(*b*), which nearly follows the static stall. However, the lower frequency flow stays detached until 5 deg during pitch down, while the static flow reattaches at $\alpha = 12$ deg.

The faster movement at $k = 0.0500$ causes a bistable behavior during pitch down. An average over all repetitions is shown in Fig. 8(*a*) but a closer look at the repetitions reveals that a general average is not suitable. Therefore, a binning method is used to define two different states. Figure 9 visualizes the binning method in more detail. The repetitions shown in Fig. 9(*a*) are divided into two different categories. The selection rule was defined by the authors and is a simple limit test of the lift coefficient at $\alpha = 10$ deg during pitch down described by the below equations:

$$c_l(\alpha \Downarrow = 10\,\text{deg}) \geq 0.5 \rightarrow \text{bin1} \tag{9}$$

$$c_l(\alpha \Downarrow = 10\,\text{deg}) < 0.5 \rightarrow \text{bin2} \tag{10}$$

The binned repetitions, shown in Fig. 9(*b*), are used to calculate a separate mean value for each bin, which leads to the additional plots in Fig. 9(*c*). Both curves depict a possible mode in the dynamic hysteresis loop. The flow of the repetitions in the first bin reattaches early during pitch down movement and suffers no full stall compared to the cases in the second bin. In the second bin, the flow fully detaches and stays stalled up until $\alpha = 4$ deg. The analysis of this bistable behavior illustrates that an automated averaging process can create data sets that do not represent the reality. Figure 9(*c*) visualizes that the mean of all repetitions actually represents none of the single repetitions, while the binned averages represent the main trends of the bistable behavior. This regime will be analyzed in more detail later on in this paper. For now, the focus will stay on the stall region, but with the incidence range shifting to higher angles into the poststall region.

The authors would like to emphasize that this binning method is simply based on a manual selection of a limit value in order to

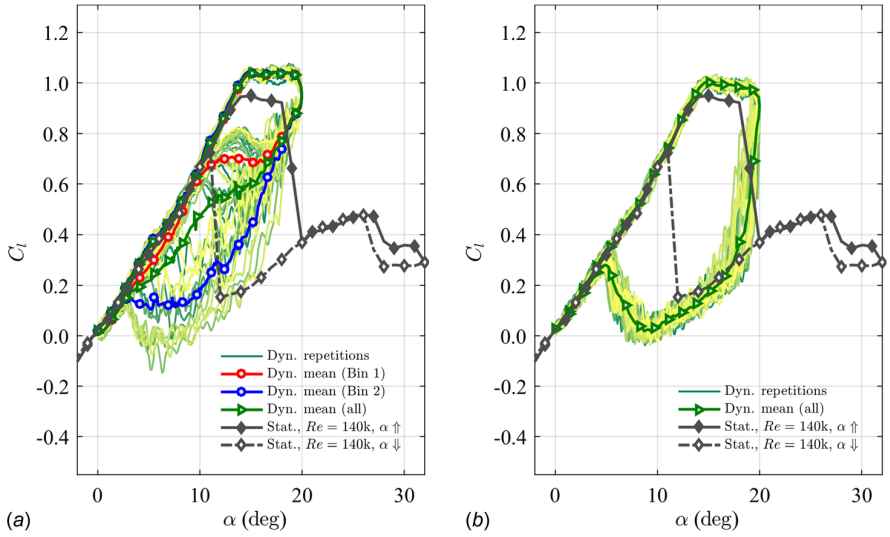

Fig. 8 Near stall investigation between 0 and 20 deg at Re = 140 k for different reduced frequencies *k*: (*a*) *k* = 0.0500 and (*b*) *k* = 0.0250

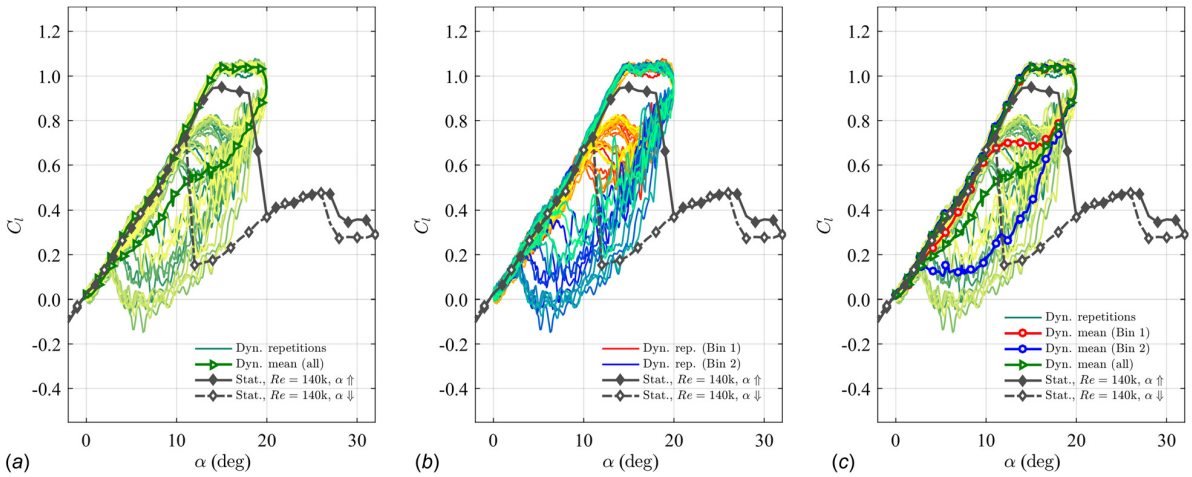

Fig. 9 Binning method for bistable configurations: (*a*) using all repetitions, (*b*) binning the repetitions, and (*c*) calculating mean of binned repetitions

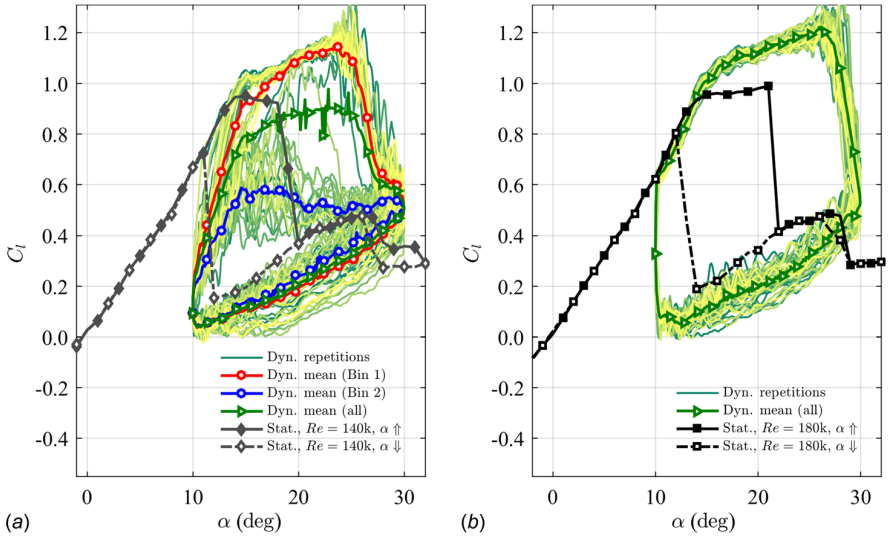

Fig. 10 Poststall investigation between 10 and 30 deg for a reduced frequency of $k = 0.0500$ at various Reynolds numbers Re: (*a*) Re = 140 k and (*b*) Re = 180 k

separate the 40 repetitions into two bins. Typically, a conditional sampling method would be used for continuous measurements at fixed positions. That means that the time-resolved data are split into certain parts using conditions. This would also result into different polars based on the according parts. In the present experiment, the airfoil is continuously moving, thus making it difficult to apply such a method. A selection of bins using automated algorithms that could, e.g., check for a variable number of bins could be more precise and flexible than the chosen manual selection. Nevertheless, implementing such methods was beyond the scope of the present study, which rather aims to focus on general effects.

Lift Under Dynamic Angle of Attack Changes in Poststall. This section concentrates on the phenomena occurring, when the airfoil oscillates between 10 and 30 deg. This region covers the static reattachment angle during pitch down at $\alpha \approx 11$ deg and the angle of second static stall at $\alpha \approx 27$ deg. Figure 10 directly visualizes a more stable behavior for the higher Reynolds number Re = 180 k, while the reattachment process at the lower Reynolds number is not stable. Here, the repetitions reveal two different modes during pitch up movement. While cases in bin 1 stay fully attached until $c_{l,\max}$, the repetitions in the second bin are not able to reach static lift values at all and are limited to a lift level roughly around that of the second static stall. All different averages converge during pitch down.

A variation in reduced frequency was performed to analyze the bistable behavior at Re = 140 k, shown in Fig. 11. Unlike Fig. 10, which only showed results for $k = 0.0500$, Fig. 11 visualizes polars for multiple frequencies $k = 0.0500$, 0.0250, and 0.0100. The decrease in frequency allows the flow more time to reattach during pitch up, which is visible in the graphs in Figs. 11(*b*) and 11(*c*). The reattachment process is stable for those smaller reduced frequencies, but dynamic effects, that stabilize the flow toward higher stall angles, are reduced as well, thus leading to an earlier stall and a reduced dynamic $c_{l,\max}$. Furthermore, the

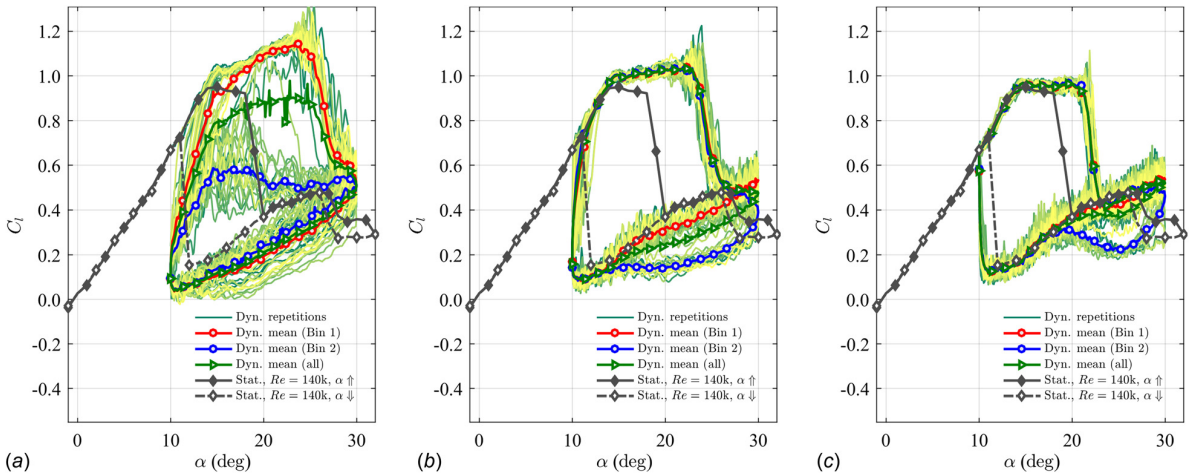

Fig. 11 Poststall investigation between 10 and 30 deg at Re = 140 k for various reduced frequencies *k*: (*a*) *k* = 0.0500, (*b*) *k* = 0.0250, and (*c*) *k* = 0.0100

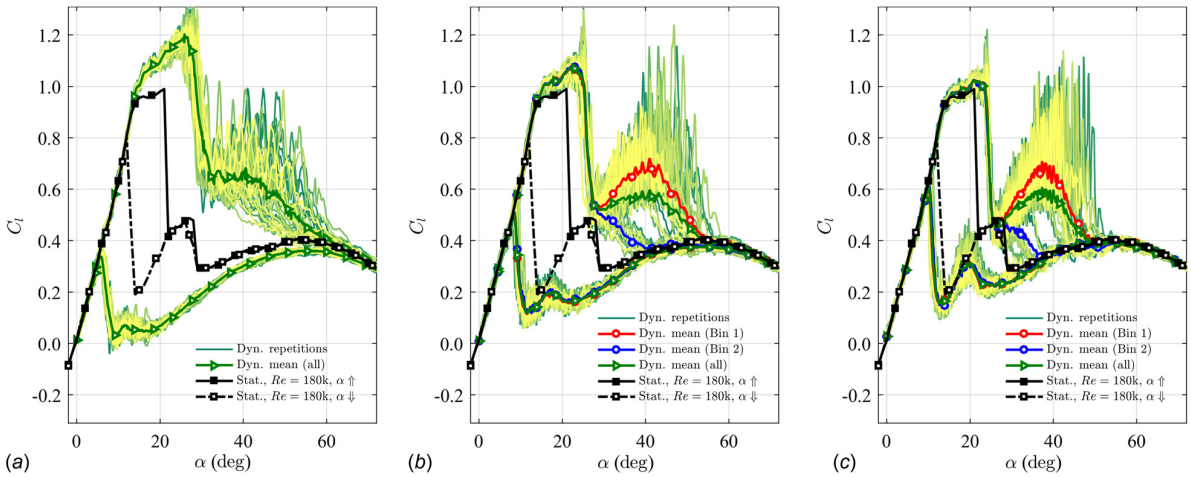

Fig. 12 Deep stall investigation between 0 and 90 deg (0 to 70 deg shown) at Re = 180 k for various reduced frequencies *k*: (*a*) *k* = 0.0100, (*b*) *k* = 0.0050, and (*c*) *k* = 0.0025

reduced frequencies cause unstable flow behavior during pitch down.

At $k = 0.0250$, the first bin does not stall a second time during pitch up, while also not reaching the pitch down lift levels of the static polar. The second bin stalls a second time but does not recover until all repetitions converge at approximately 14 deg during pitch down. A further decrease in frequency leads to a more defined behavior around the region of second stall. The first bin follows the static polar rather precisely without stalling a second time. The second bin again reveals a second hysteresis, stalling at 28 deg and recovering earlier than the $k = 0.0250$ case during pitch down. The variation of reduced frequency revealed that at each stall region of the static polar, the flow is prone to instability during dynamic movements.

Lift Under Dynamic Angle of Attack Changes in Deep Stall. In this section, the AoA range is increased beyond poststall to cover the deep stall region. The sinusoidal movements presented so far covered the regions of the first or second static stall. The experiments to be discussed within this section investigate the full range from 0 to 90 deg or even to 180 deg. The results of movements beyond the second stall until 90 deg are shown in Fig. 12 for different reduced frequencies.

The lift curve of each repetition becomes more volatile once exceeding the angle of second static stall. All repetitions of $k = 0.0100$ converge during the entire pitch down and the pitch up until 30 deg. Once surpassing 30 deg at pitch up, the lift is oscillating. As to be expected, the averaged curves do not oscillate, as averaging operates as a low pass filter as long as the repetitions are not in phase. The lift gradually declines after the first stall and converges to the static polar at $\alpha = 60$ deg.

A reduction in frequency to $k = 0.0050$ leads to a larger drop of $\Delta c_l \approx 0.55$ during the first stall, nearly reaching the level of the static polar. The continuous pitch up can cause two different flow modes. The first (bin 1) causes a new increase in lift of $\Delta c_l \approx 0.2$ with the lift gradually decreasing again afterward. In contrast to this mode, the lift of the second mode (bin 2) decreases directly after the first stall and reaches the static polar level at 40 deg. Both modes have a maximum lift difference of $\Delta c_l \approx 0.3$ to each other. This behavior is also visible for the smallest reduced frequency $k = 0.0025$, except that the dynamic polars converge to the static polar earlier. For all displayed reduced frequencies, the fluctuations in the deep stall region are large and their maximum lift is in

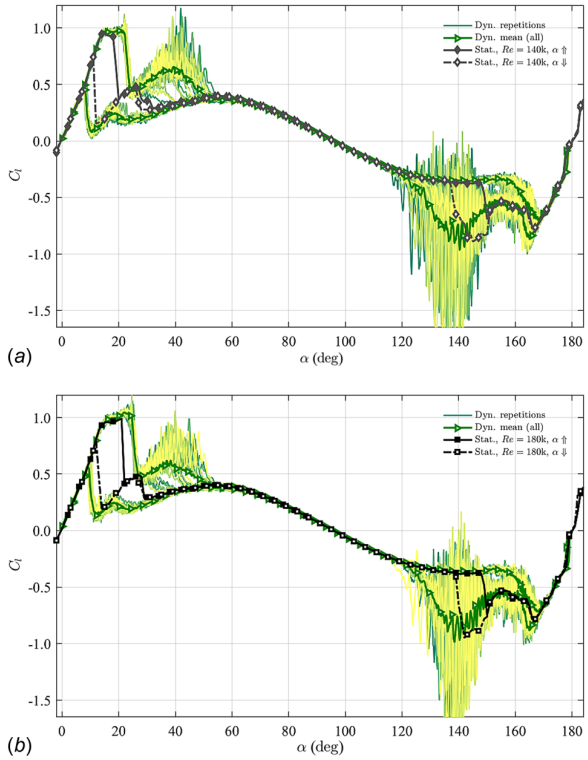

Fig. 13 Full range dynamic investigation between 0 and 180 deg for a reduced frequency of $k = 0.0025$ at various Reynolds numbers Re: (*a*) Re = 140 k and (*b*) Re = 180 k

the same range as $c_{l,\max}$ of the static polar, or even exceeds this value at lower k. The large c_l fluctuations could be explained by vortexes that are washed downstream and induce additional lift. A more detailed analysis is necessary to gain further insights. Unfortunately, this is beyond the scope of this paper.

The variation of k in deep stall reveals a single hysteresis loop for fast movements, ranging from 7 to 60 deg, while the static hysteresis loop is between 12 and 21 deg. The dynamic hysteresis loop shrinks for smaller k and develops into the shape of two overlapping loops, one for each static stall area.

The first and second stalls of the static polars, as well as their according hysteresis, are known to the literature. Holst et al. [8] showed a hysteresis loop at very high angles in a full range investigation between 0 and 180 deg. This loop is also visible in the full range static polars shown in Figs. 5(*a*) and 13 for two different Reynolds numbers Re = 140 k and 180 k. The dynamic full range investigations shown in Fig. 13 reveal extreme oscillations in the range of 120–165 deg. In this range, the average over all repetitions reveals a dynamic hysteresis loop, but the lift fluctuates in a range of more than $\Delta c_l = 1.6$, which is 60% larger than the static $c_{l,\max}$. The airfoil's trailing edge is pointing upstream, making a highly unsteady flow likely, e.g., switching between a fully separated flow and formation of a closed separation bubble on the suction side (which is pointing downwards at these AoAs), and resulting in large lift variations. An analysis of surface pressure distributions at this range is very comprehensive and will be an own study. Nevertheless, a few of the unsteady or bistable configurations will be discussed in the Analysis of C_p During Bistable Behavior section.

Analysis of C_p During Bistable Behavior. During the analysis of the lift polars in the last sections, multiple configurations showed a bistable behavior. This section will focus on three selected configurations, one out of each section, to analyze the surface pressure distributions in detail to gain further insights. The first dynamic test of interest covers the near stall range between 0 and 20 deg at Re = 140k and a reduced frequency of $k = 0.0500$. Figure 14(*a*) shows two modes during pitch down. To the right, Figs. 14(*b*)–14(*d*) visualize the surface pressure at selected AoAs during pitch. The graphs in Fig. 14(*b*) reveal a pronounced suction peak for all AoAs except 10 deg. At this angle, the repetitions of bin 1 converge to the static polar. A stable separation bubble is visible between $x/c = 0.05$ and 0.2. The same bubble is visible in the plots of bin 2 in Fig. 14(*d*). The repetitions in bin 2 undergo a complete stall during the pitch down movement, resulting in a pressure difference of $\Delta c_p \approx 2$ between 20 and 17 deg. For the sake of completeness, the average plots over all repetitions are shown in Fig. 14(*c*). It shows which phenomena can be identified by using a general average approach without any detailed analysis of single repetitions or binning. The general average covers the gradual reduction of the suction peak with decreasing angle and is able to locate the separation bubble correctly, but entirely misses the fully stalled case. The two bins represent different types of dynamic stall. The first one is a light stall and the second one a full stall. Which one occurs is hard to determine. Small changes in the flow can modify the form of the separation bubble, resulting in a completely different flow field. Van Dyken et al. [25] have analyzed the influence of transition on the light dynamic stall. Their surface pressure distributions showed a comparable behavior, even if they investigated a slim NACA 0012 airfoil at transitional Reynolds numbers at a Mach number of 0.3.

The analysis of dynamic movements in the poststall region between 10 and 30 deg revealed an unstable behavior during pitch

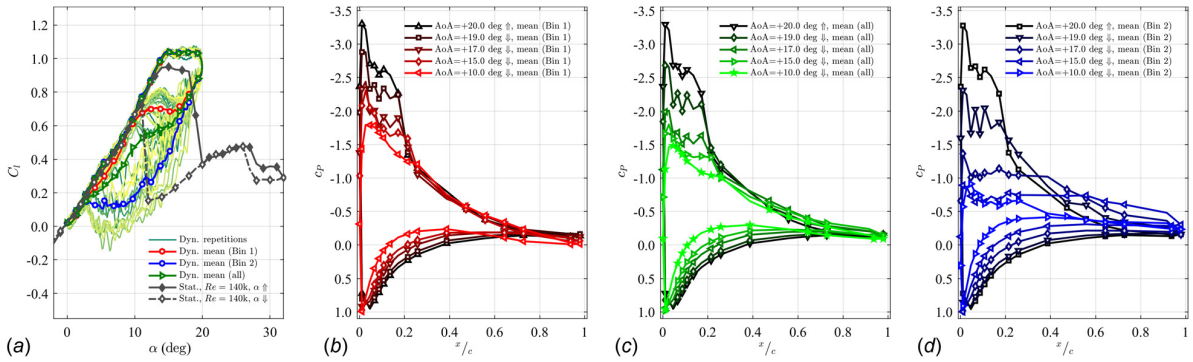

Fig. 14 Near stall investigation of c_p between 0 and 20 deg at Re = 140 k for various angles of attack during pitch down: (*a*) c_l for $k = 0.0500$, (*b*) c_p: mean of repetitions in bin 1, (*c*) c_p: mean of all repetitions, and (*d*) c_p: mean of repetitions in bin 2

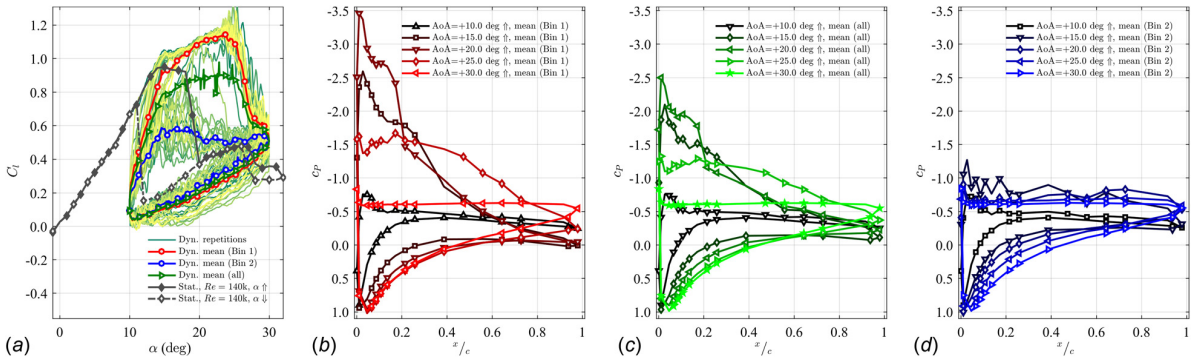

Fig. 15 Poststall investigation of c_p between 10 and 30 deg at Re = 140 k for various angles of attack during pitch up: (*a*) c_l for $k = 0.0500$, (*b*) c_p: mean of repetitions in bin 1, (*c*) c_p: mean of all repetitions, and (*d*) c_p: mean of repetitions in bin 2

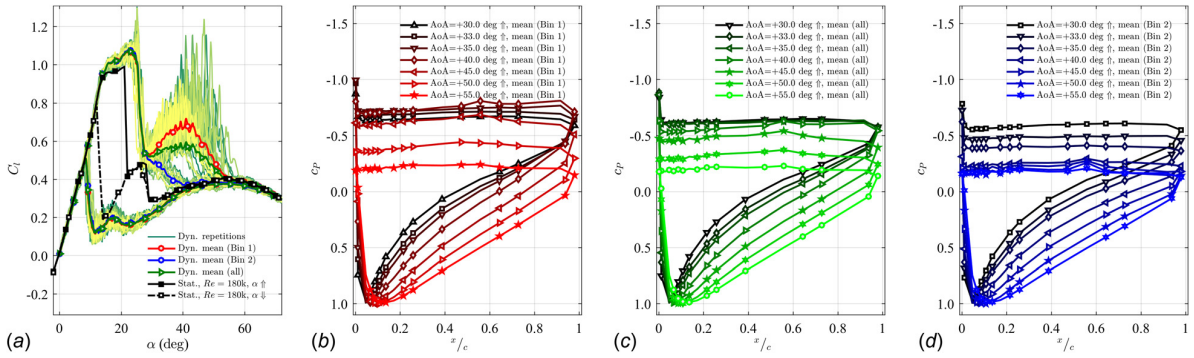

Fig. 16 Deep stall investigation of c_p between 0 and 90 deg at Re = 180 k for various angles of attack during pitch up: (*a*) c_l for $k = 0.0050$, (*b*) c_p: mean of repetitions in bin 1, (*c*) c_p: mean of all repetitions, and (*d*) c_p: mean of repetitions in bin 2

up at Re = 140 k and the airfoil oscillating at $k = 0.0500$. The reattachment process during pitch up was either quite fast (bin 1) or did not occur at all (bin 2), resulting in a nearly flat c_l curve until pitch down. This behavior can be recapitulated in Fig. 15(*a*). The selected angles in the c_p plots cover the entire pitch up cycle. While the flow is separated at 10 deg for all shown cases, an increase from 10 to 20 deg in bin 1, Fig. 15(*b*), shows the process of reattachment, and the formation of a suction peak as well as a separation bubble. The bubble is shifted upstream with increasing AoA. The suction peak, as well as the well-defined bubble, disappears at $\alpha \approx 25$ deg and the entire suction side is under low pressure, which is expected to be caused by dynamic effects, i.e., a dynamic stall vortex traveling downstream. An identical behavior is visible for the general average case in Fig. 15(*c*) for 25 deg, but due to the bi-modality of the flow none of the c_p distributions, except starting and final angles, provide meaningful information. Hence, the resulting lift polar does not match any repetition at any angle during pitch up. Repetitions in bin 2 do not form a proper suction peak during pitch up movement, which is visible in Fig. 15(*d*). The suction side undergoes a slight pressure reduction, but the pressure is unstable, and therefore, the flow keeps stalled.

A final analysis was conducted to gain further insight into the second hysteresis located in the deep stall regime. The airfoil was oscillating at $k = 0.0050$ between 0 and 90 deg at a Reynolds number of Re = 180 k. The two modes visible in Fig. 16(*a*) show either an increase in lift (bin 1) or a complete second stall (bin 2). The analysis of the surface pressure distribution in Fig. 16(*b*) reveals that the increase in lift is a combination of a slight but continuous decrease of pressure over the entire suction side and an increase of pressure on the pressure side, the latter of which is due to the increasing angle of attack. The pressure at the aft of the airfoil is especially reduced, which could be caused by a closed separation bubble starting at the leading edge, covering the entire suction side and reattaching toward the trailing edge. This behavior is stable until 40 deg. Afterward, the pressure on the suction side increases again, but the additional increase of pressure on the pressure side mitigates the loss in lift.

The decrease of pressure on the suction side is not visible in Fig. 16(*d*), which represents the stalling case. In fact, the pressure starts increasing faster than it does on the pressure side of the airfoil, resulting in the loss of lift also visible in the lift polars. The lift difference is roughly $\Delta c_{l,\max} \approx 0.3$.

Conclusion and Future Work

An experimental study was conducted to investigate the performance of a NACA 0021 airfoil under dynamic AoA changes. The present paper focused on three ranges: near stall, poststall, and deep stall. The dynamic movements showed bistable behavior at each of the ranges, either during pitch down in the near stall region, during pitch up in the poststall region, or frequency-dependent during pitch up or down. The present study used a simple binning method to analyze the bistability in comparison to a general averaging method using all repetitions at once.

The high resolution of the dynamic experiments revealed extreme fluctuations of the lift that exceeded $c_{l,\max}$ of the static polar in the poststall regime. Even larger fluctuations were found in the range beyond 120 deg, an AoA range not likely to occur during the operation of a wind turbine, but may trigger oscillations during stand still at changing wind directions. Furthermore, surface pressure distributions were analyzed to gain deeper knowledge of the local flow-phenomena at selected AoA.

Acknowledgment

The authors would like to thank Frank Stanton for helping with the images of the experimental setup.

Nomenclature

Latin Letters

a_l = correction factor for lift
b = span of wing
c = chord length
d = nozzle diameter
c_l = lift coefficient
c_d = drag coefficient
c_p = pressure coefficient
f = frequency
h = height
k = reduced frequency
Ma = Mach number
Re = Reynolds number
u_∞ = inflow velocity
x = chordwise coordinate
y = normal coordinate

Greek Symbols

α = angle of attack
β = Prandtl–Glauert factor
ω = angular frequency

Subscripts

corr = corrected value
max = maximum value

Acronyms

AoA = angle of attack
AR = aspect ratio
FS = full scale

References

[1] Simic, Z., Havelka, J. G., and Vrhovcak, M. B., 2013, "Small Wind Turbines—A Unique Segment of the Wind Power Market," Renewable Energy, **50**(50), pp. 1027–1036.
[2] Marten, D., Wendler, J., Pechlivanoglou, G., Nayeri, C. N., and Paschereit, C. O., 2013, "QBlade: An Open Source Tool for Design and Simulation of Horizontal and Vertical Axis Wind Turbines," Int. J. Emerging Technol. Adv. Eng., **3**(3), pp. 264–269.
[3] Marten, D., 2014, "QBlade," Chair of Fluid Dynamics, Technical University of Berlin, Berlin, Germany, accessed Feb. 19, 2018, http://fd.tu-berlin.de/en/research/projects/wind-energy/qblade/
[4] Bianchini, A., Balduzzi, F., Rainbird, J. M., Peiro, J., Graham, J. M. R., Ferrara, G., and Ferrari, L., 2015, "An Experimental and Numerical Assessment of Airfoil Polars for Use in Darrieus Wind Turbines—Part I: Flow Curvature Effects," ASME J. Eng. Gas Turbines Power, **138**(3), p. 032602.
[5] Bianchini, A., Balduzzi, F., Rainbird, J. M., Peiro, J., Graham, J. M. R., Ferrara, G., and Ferrari, L., 2015, "An Experimental and Numerical Assessment of Airfoil Polars for Use in Darrieus Wind Turbines—Part II: Post-Stall Data Extrapolation Methods," ASME J. Eng. Gas Turbines Power, **138**(3), p. 032603.
[6] Marten, D., Bianchini, A., Pechlivanoglou, G., Balduzzi, F., Nayeri, C. N., Ferrara, G., Paschereit, C. O., and Ferrari, L., 2016, "Effects of Airfoil's Polar Data in the Stall Region on the Estimation of Darrieus Wind Turbine Performance," ASME J. Eng. Gas Turbines Power, **139**(2), p. 022606.
[7] Lennie, M., Pechlivanoglou, G., Marten, D., Nayeri, C. N., and Paschereit, C. O., 2015, "A Review of Wind Turbine Polar Data and Its Effect on Fatigue Loads Simulation Accuracy," ASME Paper No. GT2015-43249.
[8] Holst, D., Church, B., Pechlivanoglou, G., Tüzüner, E., Saverin, J., Nayeri, C. N., and Paschereit, C. O., 2018, "Experimental Analysis of a NACA 0021 Airfoil Section Through 180-Degree Angle of Attack at Low Reynolds Numbers for Use in Wind Turbine Analysis," ASME J. Eng. Gas Turbines Power (accepted).
[9] Fujisawa, N., and Shibuya, S., 2001, "Observations of Dynamic Stall on Darrieus Wind Turbine Blades," J. Wind Eng. Ind. Aerodyn., **89**(2), pp. 201–214.
[10] Laneville, A., and Vittecoq, P., 1986, "Dynamic Stall: The Case of the Vertical Axis Wind Turbine," ASME J. Sol. Energy Eng., **108**(2), pp. 140–145.
[11] Bianchini, A., Balduzzi, F., Ferrara, G., and Ferrari, L., 2016, "Critical Analysis of Dynamic Stall Models in Low-Order Simulation Models for Vertical-Axis Wind Turbines," Energy Procedia, **101**(Suppl. C), pp. 488–495.
[12] Rainbird, J. M., Peirá, J., and Graham, J. M. R., 2015, "Blockage-Tolerant Wind Tunnel Measurements for a NACA 0012 at High Angles of Attack," J. Wind Eng. Ind. Aerodyn., **145**, pp. 209–218.
[13] Sheldahl, R. E., and Klimas, P. C., 1981, "Aerodynamic Characteristics of Seven Symmetrical Airfoil Sections Through 180-Degree Angle of Attack for Use in Aerodynamic Analysis of Vertical Axis Wind Turbines," Sandia National Laboratories, Albuquerque, NM, Report No. SAND-80-2114.
[14] Rainbird, J. M., Peiro, J., and Graham, J. M. R., 2015, "Post-Stall Airfoil Performance and Vertical-Axis Wind Turbines," AIAA Paper No. AIAA 2015-0720.
[15] Rainbird, J., 2007, "The Aerodynamic Development of a Vertical Axis Wind Turbine," Master's thesis, University of Durham, Durham, UK.
[16] Rainbird, J. M., Bianchini, A., Balduzzi, F., Peir, J., Graham, J. M. R., Ferrara, G., and Ferrari, L., 2015, "On the Influence of Virtual Camber Effect on Airfoil Polars for Use in Simulations of Darrieus Wind Turbines," Energy Convers. Manage., **106**(Suppl. C), pp. 373–384.
[17] Du, L., Berson, A., and Dominy, R. G., 2014, "Aerofoil Behaviour at High Angles of Attack and at Reynolds Numbers Appropriate for Small Wind Turbines," Proc. Inst. Mech. Eng., Part C, **229**(11), pp. 2007–2022.
[18] Du, L., Berson, A., and Dominy, R. G., 2014, "NACA0018 Behaviour at High Angles of Attack and at Reynolds Numbers Appropriate for Small Wind Turbines," School of Engineering and Computing Sciences, Durham University, Durham, UK, Report No. ECS-TR 2014/08.
[19] Holst, D., Balduzzi, F., Bianchini, A., Church, B., Wegner, F., Pechlivanoglou, G., Ferrari, L., Ferrara, G., Nayeri, C. N., and Paschereit, C. O., 2018, "Static and Dynamic Analysis of a NACA 0021 Airfoil Section at Low Reynolds Numbers Based on Experiments and CFD," ASME J. Eng. Gas Turbines Power (accepted).
[20] Holst, D., Thommes, K., Schönlau, M., Nayeri, C. N., and Paschereit, C. O., 2016, "Entwicklung eines aerodynamischen Prüfstands zur Flügelprofiluntersuchung von Kleinwindkraftanlagen unter dynamischen Winkeländerungen auf Basis eines cRIO-9068," *Virtuelle Instrumente in der Praxis* (Mess-, Prüf- und Regelungstechnik), VDE VERLAG, Berlin, Germany, pp. 54–57.
[21] Rostamzadeh, N., Kelso, R. M., Dally, B. B., and Hansen, K. L., 2013, "The Effect of Undulating Leading-Edge Modifications on NACA 0021 Airfoil Characteristics," Phys. Fluids, **25**(11), p. 117101.
[22] Jacobs, E. N., 1932, "The Aerodynamic Characteristics of Eight Very Thick Airfoils From Tests in the Variable Density Wind Tunnel," National Advisory Committee for Aeronautics, Langley Aeronautical Laboratory, Langley Field, VA, Report No. NACA-TR-391.
[23] Garner, H. C., ed., 1966, *AGARDograph 109—Subsonic Wind Tunnel Wall Corrections*, NATO-Advisory Group for Aerospace Research and Development, Paris, France.
[24] Ewald, B. F. R., ed., 1998, *AGARDograph 336—Wind Tunnel Wall Corrections*, NATO-Advisory Group for Aerospace Research and Development, Neuilly-sur-Seine Cedex, France.
[25] Van Dyken, R. D., Ekaterinaris, J. A., Chandrasekhara, M. S., and Platzer, M. F., 1996, "Analysis of Compressible Light Dynamic Stall Flow at Transitional Reynolds Numbers," AIAA J., **34**(7), pp. 1420–1427.

David Holst[1]
Mem. ASME
Chair of Fluid Dynamics
Hermann-Föttinger-Institut,
Technische Universität Berlin,
Müller-Breslau-Str. 8,
Berlin 10623, Germany
e-mail: david.holst@tu-berlin.de

Francesco Balduzzi
Department of Industrial Engineering,
Università degli Studi di Firenze,
Via di Santa Marta 3,
Italy 50139, Firenze
e-mail: francesco.balduzzi@unifi.it

Alessandro Bianchini
Mem. ASME
Department of Industrial Engineering,
Università degli Studi di Firenze,
Via di Santa Marta 3,
Italy 50139, Firenze

Benjamin Church
Chair of Fluid Dynamics
Hermann-Föttinger-Institut,
Technische Universität Berlin,
Müller-Breslau-Str. 8,
Berlin 10623, Germany

Felix Wegner
Chair of Fluid Dynamics
Hermann-Föttinger-Institut,
Technische Universität Berlin,
Müller-Breslau-Str. 8,
Berlin 10623, Germany

Georgios Pechlivanoglou
Chair of Fluid Dynamics
Hermann-Föttinger-Institut,
Technische Universität Berlin,
Müller-Breslau-Str. 8,
Berlin 10623, Germany

Lorenzo Ferrari
Mem. ASME
DESTEC,
Università di Pisa,
Largo Lucio Lazzarino,
Pisa 56122, Italy
e-mail: lorenzo.ferrari@unipi.it

Giovanni Ferrara
Department of Industrial Engineering,
Università degli Studi di Firenze,
Via di Santa Marta 3,
Italy 50139, Firenze

Christian Navid Nayeri
Chair of Fluid Dynamics
Hermann-Föttinger-Institut,
Technische Universität Berlin,
Müller-Breslau-Str. 8,
Berlin 10623, Germany

Christian Oliver Paschereit
Mem. ASME
Chair of Fluid Dynamics
Hermann-Föttinger-Institut,
Technische Universität Berlin,
Müller-Breslau-Str. 8,
Berlin 10623, Germany

Static and Dynamic Analysis of a NACA 0021 Airfoil Section at Low Reynolds Numbers Based on Experiments and Computational Fluid Dynamics

The wind industry needs airfoil data for ranges of angle of attack (AoA) much wider than those of aviation applications, since large portions of the blades may operate in stalled conditions for a significant part of their lives. Vertical axis wind turbines (VAWTs) are even more affected by this need, since data sets across the full incidence range of 180 deg are necessary for a correct performance prediction at different tip-speed ratios. However, the relevant technical literature lacks data in deep and poststall regions for nearly every airfoil. Within this context, the present study shows experimental and numerical results for the well-known NACA 0021 airfoil, which is often used for Darrieus VAWT design. Experimental data were obtained through dedicated wind tunnel measurements of a NACA 0021 airfoil with surface pressure taps, which provided further insight into the pressure coefficient distribution across a wide range of AoAs. The measurements were conducted at two different Reynolds numbers ($Re = 140\,k$ and $Re = 180\,k$): each experiment was performed multiple times to ensure repeatability. Dynamic AoA changes were also investigated at multiple reduced frequencies. Moreover, dedicated unsteady numerical simulations were carried out on the same airfoil shape to reproduce both the static polars of the airfoil and some relevant dynamic AoA variation cycles tested in the experiments. The solved flow field was then exploited both to get further insight into the flow mechanisms highlighted by the wind tunnel tests and to provide correction factors to discard the influence of the experimental apparatus, making experiments representative of open-field behavior. The present study is then thought to provide the scientific community with high quality, low-Reynolds airfoil data, which may enable in the near future a more effective design of Darrieus VAWTs. [DOI: 10.1115/1.4041150]

[1]Corresponding author.
Manuscript received July 3, 2018; final manuscript received July 20, 2018; published online January 8, 2019. Editor: Jerzy T. Sawicki.

Introduction

A continuous improvement of numerical simulation models is thought to represent the pivotal step toward a wider take up of wind turbine design. Most design tools used in the analysis of industrial turbines (especially in the first design phase) indeed are still based on low- or medium-fidelity models [1–3] for which the accuracy of the input airfoils polars becomes crucial to ensure reliable predictions of turbines performance [4–7]. The wind industry generally needs airfoil data for ranges of angle of attack (AoA) much wider than those of aviation applications, since large portions of the blades may operate in stalled conditions for a significant part of their lives [4,8]. Darrieus vertical axis wind turbines (VAWTs) are even more affected by this need, since the continuous variation of the AoA during the revolution and in dependence on the tip-speed ratio makes them experiencing almost all the angles in the full incidence range of 180 deg [9,10]. In addition, the IEC 61400 standard defines special load cases beyond the standard operation (e.g., parking and fault conditions, or extreme direction changes) during which the local AoA can assume any value. However, the relevant technical literature lacks data in deep and poststall regions for nearly every airfoil, except very few studies NACA 0015 [11], the NACA 0018 [12–14], or for cambered ones, like the NACA 44XX family [15].

In addition, airfoils for use in Darrieus VAWTs are also subject to additional issues, since they experience a progressive variation of the incidence during time. Under these conditions, which resemble those of pitching wings, recent studies (e.g., see Ref. [16]) showed a lack of that abrupt performance drop in the lift coefficient that is typically found in static polars just after the stall angle. In particular, these studies showed that, whenever the airfoil just passes through the static stall angle without remaining in that condition for a sufficiently long time, the large performance drop measured in the time-averaged tests in the wind tunnel is bypassed [5]. Superimposed to this effect, dynamic stall is also largely present in airfoils in cycloidal motion [17,18], introducing even large hysteresis cycles into the lift and drag forces produced by the airfoils. Again, even though several models do exist to account for dynamic stall in low-fidelity models [19], they are even more sensitive to the quality of tabulated polars, making the need for detailed measurements more and more urgent.

Moving from the above, the present study reports detailed static and dynamic wind tunnel measurements on a NACA 0021 airfoil, which is quite often used in the design of medium and small VAWTs (e.g., see Ref. [20]). The measurements were carried out at two different Reynolds numbers (Re = 140 k and Re = 180 k), providing both the description of the pressure over the airfoil through pressure taps and the dynamic behavior of the same under different reduced frequencies. Experimental results were then complemented with those coming from dedicated high fidelity computational fluid dynamics (CFD) simulations. CFD analyses were carried out using both a numerical setup able to reproduce the tunnel and one typical of an open-field behavior: proper corrections were found to correct experiments from any bias due to wind tunnel effects, making them fully representative of the undisturbed behavior of the airfoil for this low Reynolds numbers and then of practical use for the scientific community.

Experiments

The experiments were conducted in the Hermann-Föttinger-Institute's laminar wind tunnel. The formerly closed test section of the closed-loop wind tunnel was modified to operate openly. Details on the measurement equipment are discussed within the "Experimental Setup" section, followed by the discussion of the acquired data within the "Experimental Results" section.

Experimental Setup. The Göttinger type wind tunnel has an open test section with a circular jet, shown in Fig. 1, and a collector 90 cm downstream of the airfoil, having a contraction ratio of

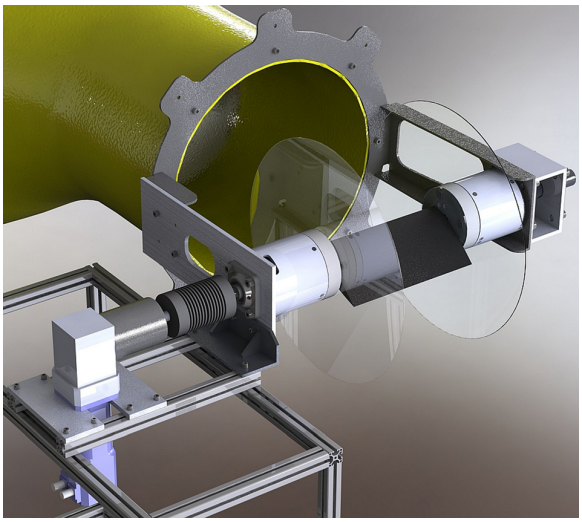

Fig. 1 Experimental wind tunnel setup

six. The inflow characteristics downstream of the nozzle with a circular cross section of $d = 0.45$ m were analyzed and the turbulence level did not exceed 1.0% up to the maximal velocity of 20 m/s within the potential core of the jet. The results of the power spectrum density (PSD) analysis of the velocity measurements are shown in Fig. 2 for the Re = 140 k case, where $y/c = 0$ defines the center of the nozzle. The PSD reveals no dominant frequencies and an evenly distributed spectrum within the area of interest. At the top of the same picture, it can be also noticed that the Reynolds number is constant over the entire core. The airfoil section was mounted between two splitter plates to improve the flow around the airfoil. Figure 1 shows the setup mounted directly to the nozzle. The 32 high frequency pressure sensors were mounted within the barrels next to the splitter plates using short flexible tubing. A servomotor drove the entire setup using a 1:10 gearbox to ensure an incidence error of less than 0.05 deg. The motor was able to reach new positions every 20 ms. Further details on the setup can be found in Holst et al. [8,21]. For completeness, the setup and measurement equipment are described briefly below.

The 32 time-resolving pressure sensors acquired synchronized the surface pressure of the airfoil through 32 pressure taps, as shown in Fig. 3. The sensors are mounted next to the airfoil to reduce the tubing length, and hence, ensure the best accuracy. The sensors were calibrated in situ against the same reference

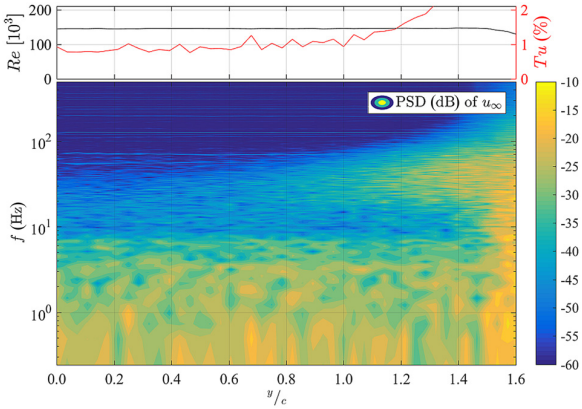

Fig. 2 Inflow velocity: Reynolds number, turbulence level, and PSD analysis starting at the center of the nozzle toward the outer edge for Re = 140 k at the LE position of the airfoil

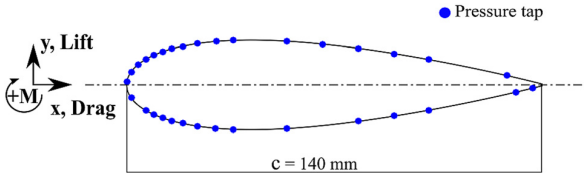

Fig. 3 Pressure tap locations

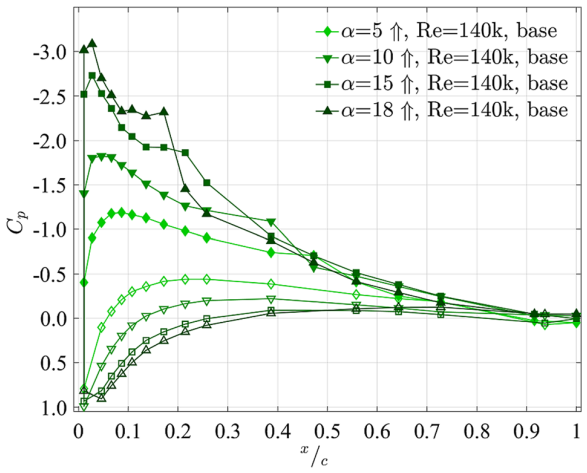

Fig. 4 Experimental c_p distribution during pitch up. Filled markers define the suction side, while empty markers define the pressure side. The darker, the higher the AoA.

pressure. The angle dependency of the sensors was removed in postprocessing using no-flow measurements. All analog signals were digitized using 16-bit input modules and a custom-made control and acquisition program written in LabVIEW™ [22]. All experimental measurements presented within this paper are based on a sample rate of 5000 Hz and a measurement time of 1.0 s per degree for the static measurements or acquired continuously during the dynamic measurements.

The postprocessing included a calculation of the pressure coefficient for each single sample of the time-resolved measurements. This removes the influence of the airfoil onto the inflow, which exists during the experiments using the open jet configuration. Nevertheless, differences compared to the uncontained inflow were expected because of the limited dimension of the jet. The comparison between CFD and experiments provided a suitable correction method to mitigate this influence.

Experimental Results. The experimental results presented within this paper are based on surface pressure measurements at two different Reynolds numbers, i.e., Re = 140 k and 180 k, respectively. Figure 4 reveals that the spatial distribution of pressure taps is appropriate to capture the stagnation point as well as the position of the separation bubble. The single plots in Fig. 4 show that the laminar separation bubble moves toward the leading edge with increasing angle of attack. The flow is still attached until 18 deg and separated afterward. The NACA 0021 undergoes a trailing edge stall until the flow fully separates [8]. The flow stays detached until approximately 10 deg during the pitch down motion.

Figure 5 shows the result of the hysteresis based on the pressure distribution. All aerodynamic coefficients are calculated based on the local pressure distributions.

The full range of 180 deg incidence was analyzed with a 1 deg resolution and Fig. 6 summarizes the polars of lift, drag, and moment coefficients for the two Reynolds numbers of interest.

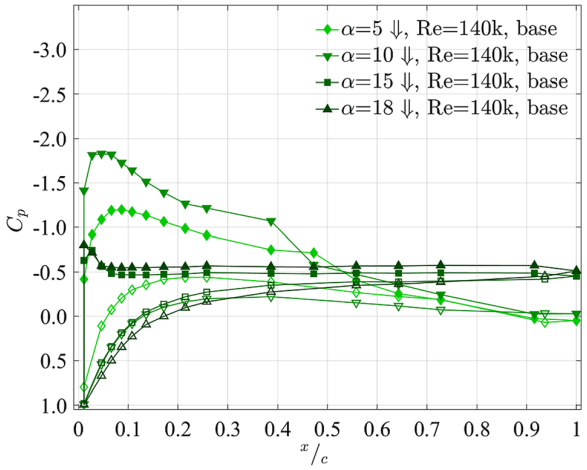

Fig. 5 Experimental c_p distribution during pitch down. Filled markers define the suction side, while empty markers define the pressure side. The darker, the higher the AoA.

The detailed analysis was performed within the work of Holst et al. [8], but some of the key findings have to be further addressed within this paper.

The complete polars reported in Fig. 6 for the whole 180 deg range revealed two hysteresis loops. The first cycle, located between 12 deg and 20 deg, is well known and it is based on the delayed reattachment during the pitch down process. The corresponding c_p distributions are shown in Figs. 4 and 5. The second hysteresis loop between 135 deg and 150 deg is less known and is caused by the formation of a closed separation bubble when the trailing edge is facing the flow [8]. This first comparison between CFD and experiment focuses on the range of 0 deg to 30 deg

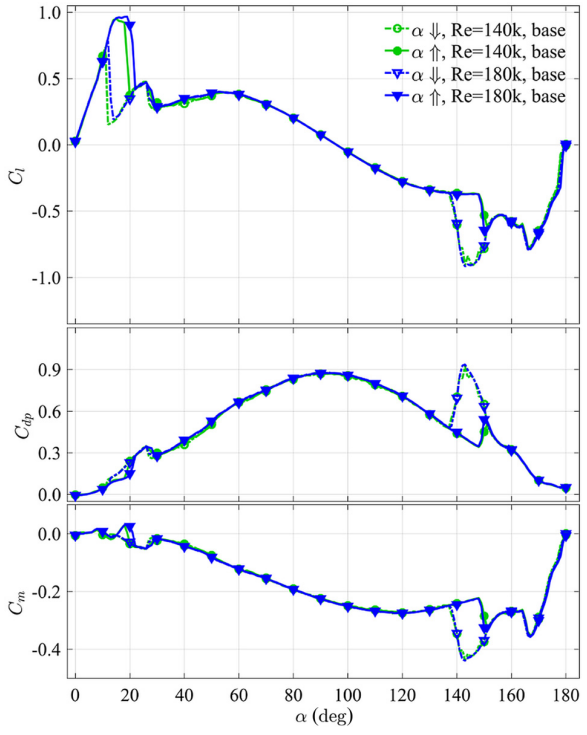

Fig. 6 Experimental c_l, c_{dp}, and c_m at Re = 140 k and 180 k. Markers are displayed every ten samples only for better readability.

incidence. Fine resolved simulations can be done within the region of attached flow to capture low Reynolds effects like laminar separation bubbles or local phenomena like trailing edge stall.

The dynamic sinusoidal pitching movements are not analyzed within this paper in detail. Selected measurements are used for comparison between CFD and experiment. A more detailed analysis is provided within the paper of Holst et al. [21] and it is not included for the sake of brevity.

Computational Fluid Dynamics Simulations

In the second part of the study, the authors performed a cross-comparison between wind tunnel experiments and CFD simulations for the static polars of the airfoil and for some relevant dynamic AoA variation cycles. This step was thought to provide a valuable contribution to the study, since numerical model predictions can be verified in comparison with experimental data, which in turn can be improved or corrected.

A detailed description of the numerical settings cannot be provided in this paper for reasons of brevity. Indeed, some of the authors have already assessed and validated the main settings for a proper numerical setup for the CFD analysis on different airfoils over a full range of incidences from −180 deg to +180 deg in Refs. [6,7], and [13]. The accuracy of the proposed CFD approach has also been successfully verified by means of experimental wind tunnel measurements both in the prestall region [6,13] of the polars and in the poststall one [7]. For completeness, however, the simulation model is briefly described below.

Numerical Setup. The two-dimensional CFD simulations presented in this paper were carried out with the commercial solver ANSYS® FLUENT. The unsteady Reynolds-averaged Navier–Stokes approach (U-RANS) was adopted using a pressure-based formulation.

Turbulence closure is achieved by means of the κ–ω SST (shear stress transport) model. Since an accurate prediction of the transition from laminar to turbulent flow is necessary at low Reynolds number, the γ-Re_θ transition model (developed by Menter and Langtry starting from the SST model [23]) was adopted, despite its increased computational cost. The model constants were selected after a dedicated sensitivity analysis, with the goal of minimizing the differences between numerical and experimental pressure distributions at four different AoAs.

The coupling between the pressure and velocity fields was achieved with the *Coupled* algorithm. The governing equations were discretized by a second-order upwind scheme for the spatial discretization and the bounded second-order scheme for the time differencing.

Computational fluid dynamics analyses for both static polars and dynamic cycles were performed by means of unsteady calculations using a very small timestep, due to the complex phenomena occurring at high AoAs. The aerodynamic conditions of the airfoil can be thought to present an oscillatory pattern, similar to the von Karman vortex street in the wake of a bluff body. Based on the typical Strouhal number correlations for the flow over a circular cylinder at Reynolds number of 10^5, a frequency of almost 20 Hz was estimated. The simulation timestep was therefore chosen such as to guarantee 500 steps per shedding cycle.

Two different computational domains were considered for the analysis, as shown in Fig. 7:

- a "wind tunnel" domain (Fig. 7(*a*)) featuring an inlet nozzle with the same width d of the experimental wind tunnel and a circular outlet boundary placed at a distance $R = 60c$;
- an "open field" domain (Fig. 7(*b*)) of rectangular shape having a length of $L = 60c$ and width of $W = 40c$.

Both CFD domains were split into two subdomains in order to allow the rotation of the airfoil: an inner circular zone (rotating region) having a diameter of $D_R = 7c$, and a fixed outer zone

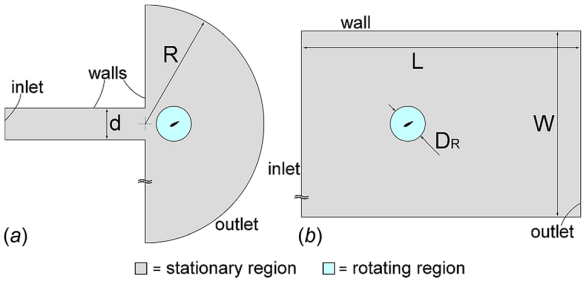

Fig. 7 Computational fluid dynamics domain: (*a*) wind tunnel domain and (*b*) open field domain

(stationary region), determining the overall domain extent. The two regions communicate by means of a sliding interface.

The undisturbed wind speed was imposed at the inlet boundary, while the ambient pressure was imposed at the outlet boundary. Blade and tunnel walls were treated as smooth nonslip walls.

The use of two different simulation domains was in fact needed in order to identify the influence of the wind tunnel configuration on the collected data. The present study shows that a proper correction of the experimental measurements was found; this correction made them fully representative of an undisturbed flow condition.

As an example, Fig. 8 depicts the streamlines of the velocity field and the contour plots of the x-component of velocity (u) in a dimensionless form with respect to the inlet wind speed (u_0) for the static simulations of the airfoil at Re = 140 k with an incidence of $\alpha = 10$ deg. In the case of an open-field-like domain, although the streamlines impacting on the blade surface are forced to follow the direction imposed by the blade angle, the flow is almost undisturbed away from the wall (Fig. 8(*b*)). Indeed, the flow can be considered straight at a distance greater than $2c$ from the airfoil wall, since the deflection of the velocity vectors is lower than 1 deg.

Conversely, a change in the direction of the jet exiting the nozzle is apparent when simulating the configuration that replicates the wind tunnel section (Fig. 8(*a*)). The streamlines are forced to deflect downward, with a steering effect in the wake region of about 5 deg. This behavior is related to the blade size, whose chord was 30% of the nozzle diameter.

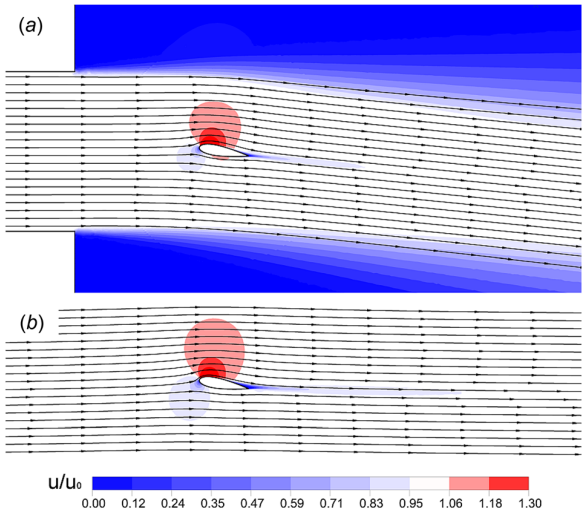

Fig. 8 Streamlines and axial velocity contours for the NACA 0021 airfoil at $\alpha = 10$ deg and Re = 140 k: (*a*) wind tunnel domain and (*b*) open field domain

It is worth pointing out that the local fluid velocity impacting on the blade in the wind tunnel domain is not decelerated. The blade is sufficiently close to the jet exiting from the nozzle and the actual velocity "seen" from the airfoil is the undisturbed one, i.e., the inlet wind speed u_0. Therefore, only a correction of the incidence was thought to be necessary in the postprocessing of experimental data.

Computational Grid. For the core region of the fluid domain, the grid discretization required the use of a triangular element mesh, which allowed localized grid refinement to capture efficiently the complex flow structure. Quadrilateral elements were used in the near-wall regions for the discretization of the boundary layer. In detail, a structured O-grid was used on the airfoil surface with a row of 40 nodes inside the boundary layer. The distance of the first mesh node to the wall was chosen in order to guarantee the dimensionless wall distance (y^+) values not exceeding the limit of ∼1, which is recommended for a proper resolution of the boundary layer with the SST turbulence model.

A partial view of the computational grid employed in the simulations, in the region close to the blade, is shown in Fig. 9. According to the results of the mesh sensitivity analyses reported in Ref. [13], a very refined discretization level was adopted on the airfoil surface. The details of the unstructured grid close to the blade are shown in Fig. 9(*a*).

A mesh featuring 750 nodes on the blade wall boundary was used, leading to a mesh size of the rotating region of 1.5×10^5 elements (Fig. 9(*b*)).

A clustering of the nodes in both the leading edge (Fig. 9(*c*)) and the trailing edge regions was also performed to ensure an adequate solution of the gradients due to the high curvature of the surface.

For an effective control of the element size in the region closer to the blade, an expansion ratio lower than 1.1 was used for the growth of the elements off of the blade wall. The sliding interface between the rotating region and the stationary region was discretized with 400 nodes. The meshes of the stationary region were created with 6.0×10^4 and 7.0×10^4 elements for the wind tunnel and the open field configurations, respectively.

Results

The experimental and computational data are compared within this section. The first focus is on the validation of CFD and experiments using static polars and c_p distributions. The sinusoidal pitching until and beyond stall becomes of interest afterward.

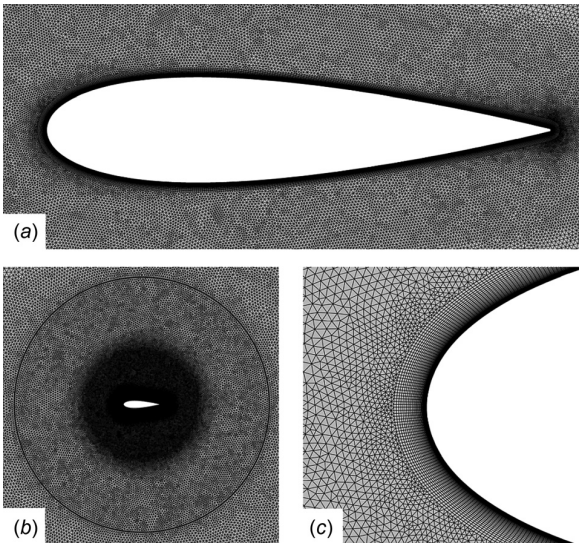

Fig. 9 Computational grid: (*a*) airfoil, (*b*) rotating domain, and (*c*) boundary layer at the leading edge

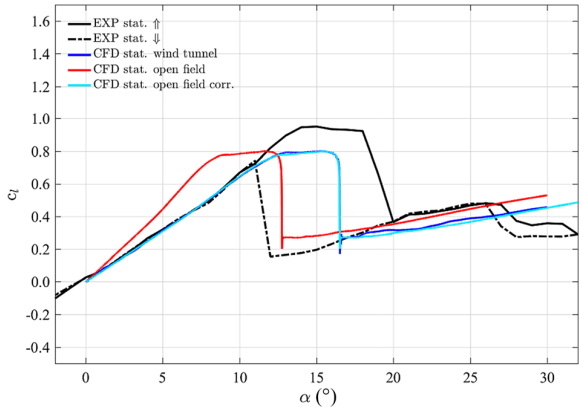

Fig. 10 Experimental and CFD lift polars for different domains at Re = 140 k

Static Polars. Figure 10 shows the experimental and numerical static polars at a Reynolds number of Re = 140 k. The experimental curves shown in black are a part out of the full 180 deg polar presented in Fig. 6. It is worth noticing that in the range between 0 deg and 30 deg, the time-dependent and averaged data are equivalent. Indeed, the onset of highly unsteady phenomena, like vortex shedding, occurs for higher AoAs.

As mentioned earlier, the simulations presented within this paper are based on two different domains described earlier. The wind tunnel (WT) domain simulates the full wind tunnel configuration including the free jet. The resulting lift polar matches the experiment very good within the linear region below stall but the CFD underestimates the maximum lift coefficient. The simulated airfoil stalls earlier compared to the experiment. Globally, a suitable matching between CFD results and measured data was obtained. However, a good agreement within the values of lift coefficient is not necessarily representative of the same flow field around an airfoil. To this purpose, in addition to the analysis of aggregate parameters, the experimental and numerical c_p distributions at various incidences before the stall were also investigated. Figure 11 reveals very good matching also in terms of spatial quantities. In particular, the c_p distributions at 5 deg and 10 deg incidence match the experiments almost perfectly. The simulation captured the general shape as well as the location of the laminar

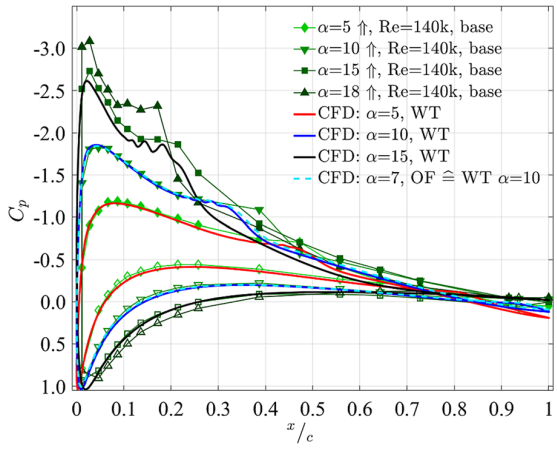

Fig. 11 Comparison of experimental and CFD pressure distributions at Re = 140 k

separation bubble. The length of the bubble, representing the location of reattachment, deviates if compared to the experimental data. This was in fact expected because the numerical model has its limitations in the prediction of the transition from laminar to turbulent flow. It can be noticed that the simulation becomes less accurate with increasing angle. The results at $\alpha = 15$ deg show an oscillating behavior in the area of the laminar separation bubble and c_p is lower toward the trailing edge. The less stable behavior matches the earlier stall of the simulated airfoil within the wind tunnel domain.

In contrast to the WT simulations, the lift polar of the open field domain (OF) simulation does not match the experiments. Figure 10 shows that neither the linear slope nor the stall angle agrees with experiments. Nevertheless, the maximum lift is exactly the same using anyone of the two computational domains. The numerical flow field analysis of Fig. 8 already revealed a deviation of the incidence experienced by the blade when comparing the open field and the wind tunnel domains. According to Newton's laws of conservation of momentum, the lift force is caused by the turning of the flow. Therefore, the downward deflection of the local flow around the airfoil surface can be thought to depend directly on the lift itself. A more detailed analysis of the slope differences—confirmed by the analysis of CFD data—revealed that the open field CFD data can be in fact corrected by accounting for an angular shift proportional to the lift coefficient to match the experiments.

The corrected lift curve shown in Fig. 10 is obtained by applying the correction based on the following equations:

$$\mathrm{AoA}_{\mathrm{OF,corr}} = \mathrm{AoA}_{\mathrm{OF}} + a_1 c_{l,\mathrm{OF}} \tag{1}$$

$$c_{l,\mathrm{OF,corr}}(\mathrm{AoA}_{\mathrm{OF,corr}}) = c_{l,\mathrm{OF}}(\mathrm{AoA}_{\mathrm{OF}}) \tag{2}$$

where a_1 is a constant. In the present case, the best matching was obtained for $a_1 = 4.762$, i.e., the inverse of the thickness to chord ratio of the airfoil (0.21). This conclusion, however, cannot be generalized, since it was based on a single case only but it will be further verified by future studies.

It is worth noticing that, especially under low Reynolds conditions, the airfoil can exhibit multiple discontinuities along the entire 180 deg polars. The standard static stall is clearly visible in Fig. 6, occurring when the boundary layer becomes detached from the suction side of the airfoil surface. Moreover, the polars show additional drops in the lift at higher incidence angles during both pitch up and pitch down, as it happens in the case of reattachment of the boundary layer. In this case, the direct application of Eq. (1) could lead to unphysical discontinuities in the correction term $a_1 c_{l,\mathrm{OF}}$. Therefore, the authors suggest the use of appropriate blending functions in order to ensure a monotonic trend of $\mathrm{AoA}_{\mathrm{OF,corr}}$.

The corrected open field simulation matches the simulations using the wind tunnel domain almost exactly, both in the prestall and poststall regions, confirming the validity of the proposed approach. As a further demonstration, Fig. 11 also shows the c_p distribution at $\alpha = 7$ deg for the open field domain. According to Eq. (1), the angular shift based on the lift ($c_l = 0.65$) is approximately 3 deg. The nearly perfect match between the 7 deg OF plot and the 10 deg WT graph implies that the two considered cases are equivalent and the applicability of the correction method is verified. Multiple simulations were then carried out using the open field domain. The lift polars at a Reynolds number of $\mathrm{Re} = 180$ k are visualized in Fig. 12. Analogous to the results at $\mathrm{Re} = 140$ k, the correction of the simulation data by applying Eqs. (1) and (2) allowed to reproduce accurately the linear slope as well as the stall angle compared to the experiments. The maximum lift coefficient is slightly underestimated, although the matching is better than the $\mathrm{Re} = 140$ k case shown in Fig. 10. This behavior is related to the superior prediction capability of the turbulence model when the regions characterized by laminar flow are narrower.

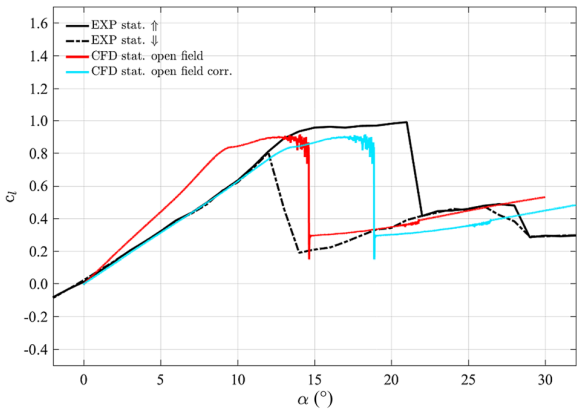

Fig. 12 Experimental and CFD lift polars including the correction method at Re = 180 k

Dynamic Pitching Movement Up to Stall. The dynamic movement of the airfoil was one focus of the experimental investigation as well as of the simulations. The behavior of a sinusoidal pitching airfoil for an incidence range up to the stall limit at $\mathrm{Re} = 140$ k with a reduced frequency of $k = 0.05$ is first analyzed; k is defined according to the below equation:

$$k = \frac{\omega}{u_0} \cdot \frac{c}{2} = \frac{\pi f c}{u_0} \tag{3}$$

Since the analysis aims to be representative of VAWTs applications, a large AoA variation during the rotation is experienced at low tip-speed ratios, where stall occurs for a large portion of the revolution. Moreover, a low Reynolds value is associated with a small turbine. Therefore, a low reduced frequency is representative of such operating conditions.

The experimental investigation relies on 40 repetitions. The according data points are always shown in shades of gray with thin lines (shades of yellow to green within the online version) within the following figures to highlight the dispersion of measured data.

Concerning numerical simulations, only 3–4 repetitions of the sinusoidal movement were needed to guarantee a periodic solution, since the data dispersion over different cycles was significantly lower. Analogous to the analysis of static polars, both computational domains are investigated to get further insight into their influence. Figure 13 shows the results of a sinusoidal movement between 0 deg and 20 deg of incidence. This range

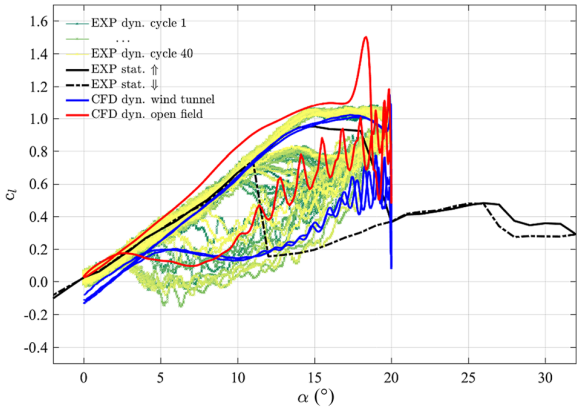

Fig. 13 Sinusoidal movement between 0 deg and 20 deg by CFD and experiment (thin lines represent 40 experimental repetitions) at Re = 140 k and $k = 0.05$

represents the full linear slope of the lift polar as well as the full static hysteresis loop. The experimental static polars in pitch-up and pitch-down motion are also shown in the figure.

None of the curves referring to dynamic pitching cases was averaged over the repetition cycles in order to emphasize the different cycle-to-cycle variation between experiments and simulations.

Focusing on the comparison between static and dynamic experimental data, an almost analogous behavior can be observed during the pitch up motion. Conversely, the experimental data reveal a bistable behavior during the pitch down motion for the dynamic case. The reattachment during pitch down can occur earlier in a range between 9 deg and 11 deg or later in between 3 deg and 6 deg, while the reattachment occurs at 11 deg for the static polar. The detailed analysis of the experimental data is provided within the paper of Holst et al. [21].

As discussed, the cycle-to-cycle variation is substantially lower for the CFD results, especially in the case of the open field computational domain, where the subsequent cycles are almost superimposed. This behavior is due to the time-average process of the RANS approach, which produces a deterministic solution of the Navier–Stokes equations. The results of the CFD simulation with the wind tunnel domain capture the form of the hysteresis loop quite well, especially within the larger angles. Nevertheless, a slight deviation from the experimental data in the linear region between 0 deg and 10 deg can be observed. A bistable behavior is not visible within the simulations but the simulation of multiple cycles ensured a proper repeatability. The same movement between 0 deg and 20 deg incidence was also performed with the open field computational domain. The resulting loop matches neither the experimental nor the simulated WT data. Just the point of reattachment matches the cluster of experimental cases undergoing a late reattachment. The large lift overshoot seems to be based on dynamic stall, but is located too early. Furthermore, the hysteresis loop is not wide enough. In this case, the correction method presented for the static polars is not directly applicable because this would result in a simulated movement between 0 deg and 24.2 deg.

In order to apply a transformation of the open field CFD results using a consistent approach with respect to the static polar case, an additional simulation was necessary. Indeed, from the static polar analysis, it was found that an incidence of $\alpha = 20$ deg for the wind tunnel domain corresponds to $\alpha = 15.4$ deg for the open field domain. Therefore, the angular range of sinusoidal movement was reduced to 0–15.4 deg. By doing so, the results can be plotted by scaling the angular values proportionally to the instantaneous lift to revert to the 0–20 deg range. The corrected and uncorrected simulation results are shown in Fig. 14. The corrected open field

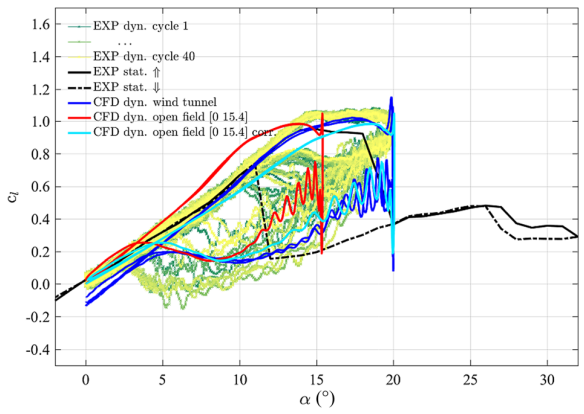

Fig. 14 Sinusoidal movement between 0 deg and 20 deg within CFD using the proposed correction and experiment (thin lines represent 40 experimental repetitions) at Re = 140 k and *k* = 0.05

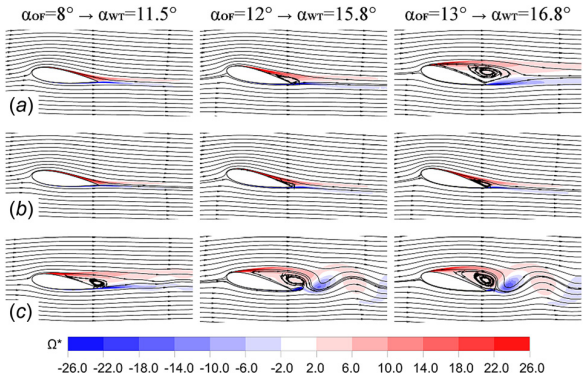

Fig. 15 Computational fluid dynamics vorticity contours and streamlines at different angular positions at Re = 140 k in open field domain: static polar (*a*), dynamic polar between 0 deg and 15.4 deg at *k* = 0.05 during pitch up (*b*) and pitch down (*c*)

data match the experiments very well within the linear slope as well as in terms of both size and shape of the loop.

Each of the simulations shown in Figs. 13 and 14 reveals an oscillating behavior during the first phase of pitch down. The numerical model seems not to be fully stable when considering fast pitch changes within the region of separated flow. Nevertheless, the experimental data also show oscillations within the pitch down movement. The lift overshoot at 20 deg is not directly visible in the experimental data but was experimentally observed under other conditions, which will be shown later in the paper.

The resulting CFD flow fields under both static and dynamic conditions are shown in Fig. 15 for three relevant angular positions. The contours of the vorticity field are reported in a dimensionless form (Ω*) according to the below equation:

$$\Omega* = \frac{\Omega}{u_0/c} \tag{4}$$

where Ω is the vorticity and c is the blade chord. Positive vorticity is clockwise.

In the figure, the incidence angles of the open field simulations are shown, along with the corresponding angular values for the wind tunnel case. Starting from the static case (Fig. 15(*a*)), the sudden change in the flow field between $\alpha = 12$ deg and $\alpha = 13$ deg due to the stall occurrence can be observed.

The region of detached flow covers the entire suction side at $\alpha = 13$ deg, while only a small recirculation area is present at $\alpha = 12$ deg. At $\alpha = 8$ deg, the flow is completely attached.

Focusing the attention on the dynamic case, the hysteresis cycle is clearly visible. During the pitch up positions of Fig. 15(*b*), the flow field is definitely similar to the static case for the angular positions below the static stall value, while the profile does not exhibit any stall at $\alpha = 13$ deg. Conversely, during the pitch down motion (Fig. 15(*c*)), the flow is never attached to the blade and vortices are detached from both the leading and the trailing edges. At $\alpha = 8$ deg, the detached region is still marked.

Dynamic Pitching Movement Beyond Stall. After analyzing the dynamic behavior up to the stall region, this section focuses on movements beyond the static stall AoA. It is worth pointing out that the flow in the poststall regime is extremely complex and the chosen CFD approach could be considered not enough accurate for such a highly unsteady low-Re condition. However, the simulations provide further insights into both the limits of the simulation setup and the suitability of the proposed correction of the measured data.

The behavior of a sinusoidal pitching airfoil for an incidence range up between 5 deg and 25 deg is first analyzed. The selected

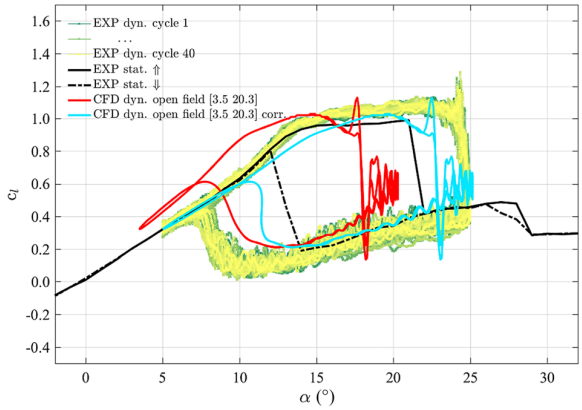

Fig. 16 Sinusoidal movement between 5 deg and 25 deg within CFD and experiment (thin lines represent 40 experimental repetitions) at Re = 180 k and $k = 0.025$

case is characterized by a reduced frequency of $k = 0.025$ and Re = 180 k to guarantee more stable results, thanks to the higher Reynolds and slower frequency of oscillation. Figure 16 shows the comparison between the measured data and the CFD results for the open field domain considering the scaled angular range between 3.5 deg and 20.3 deg. Numerical simulations were not carried out for the theoretical 5–25 deg range, as they were deemed not to guarantee consistent results with respect to the experiments. The increase of Reynolds number led to a more stable behavior of both the experimental and numerical curves. The results are similar to what was already observed in Fig. 14: the corrected CFD hysteresis cycle shows a satisfactorily matching with the experiments, especially during the pitch up and the first part of the pitch down phase. Analogous to all previous results, the maximum lift is slightly underestimated but the width of the hysteresis loop is correctly predicted. In this case, the reattachment is predicted too in advance, being similar to the one of the static polar. Moreover, it can be noticed that the location of the lift overshoot and the subsequent stall occur slightly in advance. Again, the simulation becomes modestly unstable when getting close to the maximum angles.

Figure 17 reports the results of the 10–30 deg movement, with a reduced frequency of $k = 0.05$ and Re = 180 k. Under these conditions, the simulation becomes unstable and the results are not satisfactorily in agreement with the experiments. The corrected lift curve matches the experiments roughly during pitch up movement. It has to be noticed that the location of stall is delayed of

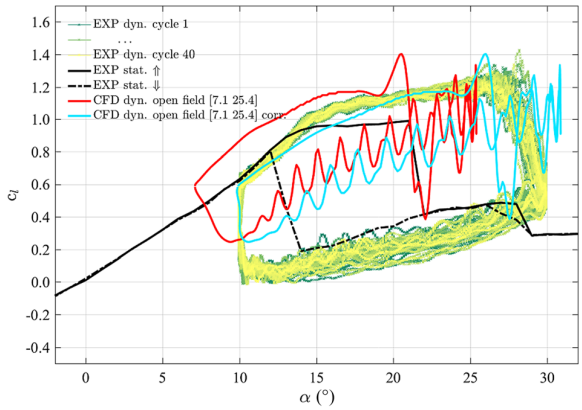

Fig. 17 Sinusoidal movement between 10 deg and 30 deg within CFD using the proposed correction and experiment (thin lines represent 40 experimental repetitions) at Re = 180 k and $k = 0.05$

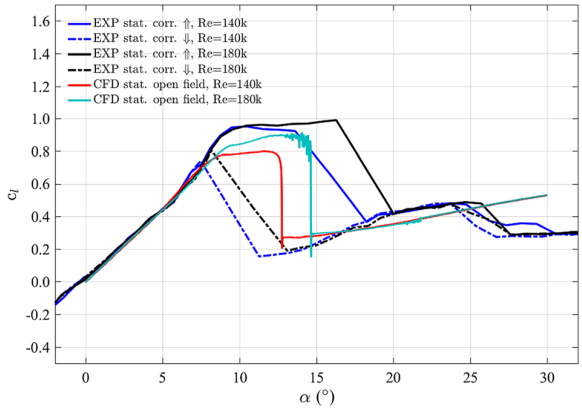

Fig. 18 Corrected experimental lift polars for the NACA 0021 airfoil at Re = 140 k and Re = 180 k

roughly 8 deg with respect to the static stall for both experiments and corrected CFD data. In terms of absolute location, the numerical stall occurs in advance with respect to the experiments, in agreement with the static case.

This leads to an earlier drop of the lift during pitch up, with a subsequent instability due to the formation of vortices. The onset of such instability also affects the results during pitch down, with a too fluctuating pattern and a reduced amplitude of the hysteresis loop. Nevertheless, even if the poststall flow is borderline and demanding for the selected U-RANS approach, a well-designed simulation setup is at least able to provide a rough estimation of the location of the maximum lift.

Corrected NACA 0021 Polars in Open Field. The possibility of having accurate polars for the NACA 0021 airfoil in open field condition at low Reynolds number to be used as a literature reference can be considered of great value. Therefore, the corrected experimental lift polars within the investigated range are finally reported in Fig. 18 in comparison to the open field CFD simulations.

The correction method used and presented is applicable for the full range of incidence. In addition, for the sake of completeness, a table is presented in the Appendix containing the corrected experimental data purged by the effect of the wind tunnel configuration. In detail, the table contains the pitch up polars at Re = 140 k that can be used as a benchmark for the calibration of numerical tools, such as CFD models and low order models for the performance prediction and aero-elastic analysis. If the reader is interested in additional data, they can refer to the complete table of the full uncorrected 180 deg polars at three different Reynolds numbers (i.e., Re = 100 k, Re = 140 k, and Re = 180 k) reported in Ref. [8].

Conclusions

An experimental as well as numerical study was carried out to investigate the static and dynamic performance of a NACA 0021 airfoil. The experimental setup was numerically replicated using a U-RANS simulation approach, which was used to validate and correct the chosen experimental setup. The dimension of the wind tunnel as well as the location of the airfoil in front of the jet allow experiments with minimized upstream influences. The existing influences during the experiment were mitigated using a proper postprocessing and a fully time-resolved c_p calculation.

The CFD simulation of the same airfoil with two different computational domains, the full wind tunnel and the open field, provided a deep insight into the impact of the experimental setup onto the measurement data. It was proven that the lift force is responsible for the deflection of the local flow around the blade in the wind tunnel configuration. A correction method was proposed to alleviate these influences. The actual incidence seen by the

blade can be computed by accounting for an angular shift proportional to the lift coefficient.

The comparison between simulation results and experiments both in static and in dynamic conditions confirmed the validity of the method, at least for the data sets investigated within this paper. Further studies on other airfoils have to be conducted to validate the correction method and to generalize it. As a final remark, within the present study, the authors have confirmed that CFD and experiments can match extremely well if the respective datasets are of highest quality and external influences are reduced as far as possible by means of calibrations and corrections.

Acknowledgment

Thanks are due to Professor Ennio A. Carnevale of the Università degli Studi di Firenze for supporting this study.

Nomenclature

AoA = angle of attack, deg
c = blade chord, m
c_{dp} = drag coefficient based on surface pressure
c_l = lift coefficient
c_m = moment coefficient
c_p = pressure coefficient
d = nozzle diameter, m
D_R = rotating region diameter, m
k = reduced frequency
L = open field domain length, m
R = wind tunnel domain outer radius, m
Re = Reynolds number
Re_θ = momentum thickness Reynolds number
u = absolute wind speed, m s^{-1}
W = open field domain width, m
y^+ = dimensionless wall distance

Greek Symbols

α = incidence angle (in formulas), deg
γ = intermittency
κ = turbulent kinetic energy, $m^2\ s^{-2}$
ω = specific turbulent dissipation rate, s^{-1}
Ω = vorticity, s^{-1}
Ω^* = dimensionless vorticity

Subscripts

corr = corrected
OF = open field domain
WT = wind tunnel domain
0 = value at infinity

Acronyms

CFD = computational fluid dynamics
OF = open field
PSD = power spectrum density
RANS = Reynolds-averaged Navier–Stokes
SST = shear stress transport
VAWT = vertical axis wind turbines
WT = wind tunnel

Appendix: Aerodynamic Coefficients (Lift, Drag Based on Surface Pressure, Moment) at Re=140 k During Static Pitch Up in 1 deg Steps

α_{exp}	α_{corr}	c_l	c_{dp}	c_m	α_{exp}	α_{corr}	c_l	c_{dp}	c_m	α_{exp}	α_{corr}	c_l	c_{dp}	c_m
0.0	−0.1	0.03	0.00	−0.01										
1.0	0.7	0.07	0.00	0.00	61.0	59.2	0.38	0.68	−0.13	121.0	122.4	−0.29	0.70	−0.27
2.0	1.4	0.14	0.00	0.00	62.0	60.2	0.37	0.69	−0.13	122.0	123.4	−0.30	0.69	−0.27
3.0	2.1	0.20	0.00	0.00	63.0	61.3	0.35	0.68	−0.13	123.0	124.4	−0.30	0.67	−0.27
4.0	2.7	0.27	0.00	0.00	64.0	62.3	0.35	0.69	−0.13	124.0	125.5	−0.31	0.66	−0.27
5.0	3.5	0.32	0.01	0.00	65.0	63.4	0.34	0.69	−0.13	125.0	126.5	−0.31	0.65	−0.27
6.0	4.2	0.38	0.01	0.01	66.0	64.4	0.34	0.71	−0.14	126.0	127.5	−0.32	0.63	−0.27
7.0	4.9	0.44	0.02	0.01	67.0	65.4	0.33	0.72	−0.14	127.0	128.6	−0.33	0.62	−0.27
8.0	5.6	0.50	0.02	0.01	68.0	66.5	0.32	0.73	−0.15	128.0	129.6	−0.33	0.61	−0.27
9.0	6.2	0.58	0.04	0.01	69.0	67.5	0.31	0.74	−0.15	129.0	130.6	−0.34	0.59	−0.27
10.0	6.8	0.67	0.05	0.00	70.0	68.6	0.30	0.74	−0.15	130.0	131.6	−0.34	0.58	−0.26
11.0	7.6	0.72	0.06	−0.01	71.0	69.6	0.30	0.76	−0.16	131.0	132.6	−0.34	0.56	−0.26
12.0	8.2	0.80	0.07	−0.01	72.0	70.6	0.29	0.77	−0.16	132.0	133.7	−0.35	0.55	−0.26
13.0	8.8	0.89	0.09	−0.02	73.0	71.7	0.28	0.78	−0.17	133.0	134.7	−0.35	0.53	−0.26
14.0	9.5	0.94	0.10	−0.02	74.0	72.7	0.27	0.79	−0.17	134.0	135.7	−0.35	0.52	−0.25
15.0	10.5	0.95	0.11	−0.01	75.0	73.8	0.26	0.80	−0.17	135.0	136.7	−0.35	0.50	−0.25
16.0	11.6	0.93	0.11	0.01	76.0	74.8	0.25	0.81	−0.18	136.0	137.7	−0.36	0.49	−0.25
17.0	12.6	0.93	0.11	0.02	77.0	75.9	0.24	0.81	−0.18	137.0	138.7	−0.36	0.48	−0.25
18.0	13.6	0.92	0.12	0.03	78.0	76.9	0.23	0.82	−0.19	138.0	139.7	−0.36	0.47	−0.25
19.0	15.9	0.65	0.17	0.00	79.0	78.0	0.22	0.83	−0.19	139.0	140.8	−0.37	0.46	−0.25
20.0	18.2	0.37	0.24	−0.03	80.0	79.0	0.20	0.83	−0.19	140.0	141.7	−0.37	0.44	−0.24
21.0	19.1	0.41	0.26	−0.04	81.0	80.1	0.19	0.84	−0.20	141.0	142.7	−0.36	0.42	−0.24
22.0	20.0	0.42	0.28	−0.04	82.0	81.1	0.18	0.85	−0.20	142.0	143.8	−0.37	0.42	−0.24
23.0	20.9	0.44	0.30	−0.05	83.0	82.2	0.17	0.85	−0.20	143.0	144.8	−0.37	0.40	−0.24
24.0	21.9	0.44	0.31	−0.05	84.0	83.3	0.16	0.86	−0.21	144.0	145.8	−0.37	0.39	−0.23
25.0	22.8	0.47	0.33	−0.05	85.0	84.3	0.14	0.86	−0.21	145.0	146.8	−0.37	0.38	−0.23
26.0	23.7	0.48	0.35	−0.05	86.0	85.4	0.13	0.87	−0.21	146.0	147.7	−0.37	0.36	−0.23
27.0	25.0	0.42	0.33	−0.04	87.0	86.4	0.12	0.87	−0.22	147.0	148.8	−0.37	0.35	−0.23
28.0	26.3	0.36	0.30	−0.03	88.0	87.5	0.10	0.88	−0.22	148.0	149.8	−0.37	0.34	−0.22
29.0	27.5	0.31	0.29	−0.02	89.0	88.6	0.09	0.87	−0.22	149.0	151.0	−0.42	0.37	−0.24
30.0	28.5	0.32	0.30	−0.02	90.0	89.6	0.08	0.87	−0.22	150.0	152.5	−0.53	0.45	−0.29
31.0	29.5	0.32	0.31	−0.03	91.0	90.7	0.06	0.87	−0.23	151.0	153.9	−0.61	0.50	−0.32
32.0	30.6	0.29	0.29	−0.02	92.0	91.8	0.05	0.87	−0.23	152.0	154.8	−0.60	0.47	−0.32
33.0	31.6	0.29	0.30	−0.02	93.0	92.8	0.04	0.87	−0.23	153.0	155.7	−0.57	0.44	−0.31
34.0	32.6	0.30	0.31	−0.02	94.0	93.9	0.02	0.87	−0.24	154.0	156.6	−0.55	0.40	−0.29

(continued)

α_{exp}	α_{corr}	c_l	c_{dp}	c_m	α_{exp}	α_{corr}	c_l	c_{dp}	c_m	α_{exp}	α_{corr}	c_l	c_{dp}	c_m
35.0	33.6	0.30	0.32	−0.03	95.0	94.9	0.01	0.87	−0.24	155.0	157.6	−0.54	0.38	−0.28
36.0	34.6	0.30	0.32	−0.03	96.0	96.0	0.00	0.87	−0.24	156.0	158.5	−0.53	0.36	−0.28
37.0	35.5	0.31	0.34	−0.03	97.0	97.1	−0.01	0.87	−0.24	157.0	159.6	−0.54	0.35	−0.27
38.0	36.5	0.32	0.35	−0.03	98.0	98.1	−0.03	0.86	−0.24	158.0	160.7	−0.56	0.35	−0.28
39.0	37.4	0.33	0.37	−0.04	99.0	99.2	−0.04	0.86	−0.25	159.0	161.8	−0.58	0.34	−0.28
40.0	38.4	0.34	0.39	−0.04	100.0	100.3	−0.05	0.85	−0.25	160.0	162.8	−0.59	0.32	−0.27
41.0	39.4	0.34	0.39	−0.04	101.0	101.3	−0.07	0.85	−0.25	161.0	163.9	−0.60	0.31	−0.27
42.0	40.4	0.34	0.40	−0.05	102.0	102.4	−0.08	0.84	−0.25	162.0	164.9	−0.62	0.29	−0.27
43.0	41.3	0.35	0.41	−0.05	103.0	103.4	−0.09	0.83	−0.25	163.0	165.9	−0.62	0.27	−0.27
44.0	42.4	0.34	0.41	−0.05	104.0	104.5	−0.10	0.84	−0.26	164.0	166.8	−0.59	0.24	−0.26
45.0	43.4	0.34	0.42	−0.05	105.0	105.5	−0.11	0.82	−0.26	165.0	168.2	−0.66	0.22	−0.29
46.0	44.3	0.35	0.44	−0.06	106.0	106.6	−0.13	0.82	−0.26	166.0	169.6	−0.76	0.19	−0.34
47.0	45.3	0.35	0.45	−0.06	107.0	107.7	−0.14	0.82	−0.26	167.0	170.7	−0.77	0.16	−0.35
48.0	46.3	0.36	0.47	−0.07	108.0	108.7	−0.15	0.80	−0.26	168.0	171.5	−0.74	0.13	−0.35
49.0	47.3	0.36	0.48	−0.07	109.0	109.8	−0.16	0.79	−0.26	169.0	172.3	−0.70	0.12	−0.32
50.0	48.2	0.37	0.50	−0.07	110.0	110.8	−0.17	0.79	−0.26	170.0	173.1	−0.66	0.10	−0.30
51.0	49.2	0.38	0.53	−0.08	111.0	111.9	−0.18	0.79	−0.27	171.0	173.9	−0.62	0.09	−0.27
52.0	50.1	0.39	0.55	−0.09	112.0	112.9	−0.19	0.77	−0.26	172.0	174.8	−0.59	0.08	−0.24
53.0	51.1	0.39	0.57	−0.09	113.0	114.0	−0.21	0.77	−0.27	173.0	175.5	−0.53	0.07	−0.20
54.0	52.1	0.40	0.59	−0.10	114.0	115.0	−0.22	0.76	−0.27	174.0	176.2	−0.47	0.07	−0.16
55.0	53.1	0.40	0.60	−0.10	115.0	116.1	−0.23	0.75	−0.27	175.0	177.0	−0.41	0.07	−0.13
56.0	54.1	0.39	0.62	−0.11	116.0	117.1	−0.24	0.74	−0.27	176.0	177.8	−0.37	0.06	−0.11
57.0	55.1	0.39	0.63	−0.11	117.0	118.2	−0.25	0.73	−0.27	177.0	178.5	−0.32	0.05	−0.09
58.0	56.1	0.39	0.64	−0.11	118.0	119.2	−0.26	0.72	−0.27	178.0	178.5	−0.10	0.05	−0.05
59.0	57.2	0.39	0.66	−0.12	119.0	120.3	−0.27	0.71	−0.27	179.0	179.2	−0.05	0.05	−0.03
60.0	58.2	0.38	0.67	−0.12	120.0	121.3	−0.28	0.71	−0.27	180.0	180.0	−0.01	0.05	0.00

References

[1] Manwell, J. F., McGowan, J. G., and Rogers, A. L., 2009, *Wind Energy Explained*, 2nd ed., Wiley, Chichester, UK.

[2] Simão Ferreira, C., Aagaard Madsen, H., Barone, M., Roscher, B., Deglaire, P., and Arduin, I., 2014, "Comparison of Aerodynamic Models for Vertical Axis Wind Turbines," J. Phys.: Conf. Ser., **524**, p. 012125.

[3] Marten, D., Wendler, J., Pechlivanoglou, G., Nayeri, C. N., and Paschereit, C. O., 2013, "QBlade: An Open Source Tool for Design and Simulation of Horizontal and Vertical Axis Wind Turbines," Int. J. Emerging Technol. Adv. Eng., **3**(SI 3), pp. 264–269.

[4] Lennie, M., Pechlivanoglou, G., Marten, D., Nayeri, C., and Paschereit, C. O., 2015, "A Review of Wind Turbine Polar Data and Its Effect on Fatigue Loads Simulation Accuracy," ASME Paper No. GT2015-43249.

[5] Marten, D., Bianchini, A., Pechlivanoglou, G., Balduzzi, F., Nayeri, C. N., Ferrara, G., Paschereit, C. O., and Ferrari, L., 2016, "Effects of Airfoil's Polar Data in the Stall Region on the Estimation of Darrieus Wind Turbines Performance," ASME J. Eng. Gas Turbines Power, **139**(2), p. 0226069.

[6] Bianchini, A., Balduzzi, F., Rainbird, J., Peiro, J., Graham, J. M. R., Ferrara, G., and Ferrari, L., 2015, "An Experimental and Numerical Assessment of Airfoil Polars for Use in Darrieus Wind Turbines—Part 1: Flow Curvature Effects," ASME J. Eng. Gas Turbines Power, **138**(3), p. 032602.

[7] Bianchini, A., Balduzzi, F., Rainbird, J., Peiro, J., Graham, J. M. R., Ferrara, G., and Ferrari, L., 2015, "An Experimental and Numerical Assessment of Airfoil Polars for Use in Darrieus Wind Turbines—Part 2: Post-Stall Data Extrapolation Methods," ASME Paper No. GT2015-42285.

[8] Holst, D., Church, B., Pechlivanoglou, G., Tüzüner, E., Saverin, J., Nayeri, C. N., and Paschereit, C. O., 2018, "Experimental Analysis of a NACA 0021 Airfoil Section Through 180-Degree Angle of Attack at Low Reynolds Numbers for Use in Wind Turbine Analysis," ASME J. Eng. Gas Turbines Power (accepted).

[9] Paraschivoiu, I., 2002, *Wind Turbine Design With Emphasis on Darrieus Concept*, Polytechnic International Press, Montreal, QC, Canada.

[10] Dominy, R., Lunt, P., Bickerdyke, A., and Dominy, J., 2007, "Self-Starting Capability of a Darrieus Turbine," Proc. Inst. Mech. Eng., Part A, **221**(1), pp. 111–120.

[11] Sheldahl, R. E., and Klimas, P. C., 1981, "Aerodynamic Characteristics of Seven Symmetrical Airfoil Sections Through 180-Degree Angle of Attack for Use in Aerodynamic Analysis of Vertical Axis Wind Turbines," National Renewable Energy Laboratory, Golden, CO, Technical Report No. SAND80-2114.

[12] Rainbird, J., Peiro, J., and Graham, J. M. R., 2015, "Post-Stall Airfoil Performance and Vertical-Axis Wind Turbines," AIAA Paper No. 2015-0720.

[13] Rainbird, J., Bianchini, A., Balduzzi, F., Peiro, J., Graham, J. M. R., Ferrara, G., and Ferrari, L., 2015, "On the Influence of Virtual Camber Effect on Airfoil Polars for Use in Simulations of Darrieus Wind Turbines," Energy Convers. Manage., **106**, pp. 373–384.

[14] Du, L., Berson, A., and Dominy, R. G., 2014, "NACA0018 Behaviour at High Angles of Attack and at Reynolds Numbers Appropriate for Small Wind Turbines," School of Engineering and Computing Sciences, Durham University, Durham, UK, ECS Technical Report No. 2014/08.

[15] Ostowari, C., and Naik, D., 1984, "Post-Stall Wind Tunnel Data for NACA 44XX Series Airfoil Sections," Solar Energy Research Institute, Golden, CO, Technical Report No. SERI/STR-217-2559.

[16] Linn, A. B., 1999, "Determination of Average Lift of a Rapidly Pitching Airfoil," M.Sc. thesis, Worcester Polytechnic Institute, Worcester, MA.

[17] Fujisawa, N., and Shibuya, S., 2001, "Observations of Dynamic Stall on Darrieus Wind Turbine Blades," J. Wind Eng. Ind. Aerodyn., **84**(2), pp. 201–214.

[18] Laneville, A., and Vittecoq, P., 1986, "Dynamic Stall; the Case of the Vertical Axis Wind Turbine," ASME J. Sol. Energy Eng., **108**, pp. 140–145.

[19] Bianchini, A., Balduzzi, F., Ferrara, G., and Ferrari, L., 2016, "Critical Analysis of Dynamic Stall Models in Low-Order Simulation Models for Vertical-Axis Wind Turbines," Energy Procedia, **101**, pp. 488–495.

[20] Dossena, V., Persico, G., Paradiso, B., Battisti, L., Dell'Anna, S., Brighenti, A., and Benini, E., 2015, "An Experimental Study of the Aerodynamics and Performance of a Vertical Axis Wind Turbine in a Confined and Unconfined Environment," ASME J. Energy Resour. Technol., **137**(5), p. 051207.

[21] Holst, D., Church, B., Wegner, F., Pechlivanoglou, G., Nayeri, C. N., and Paschereit, C. O., 2018, "Experimental Analysis of a NACA 0021 Airfoil Under Dynamic Angle of Attack Variation and Low Reynolds Numbers," ASME J. Eng. Gas Turbines Power (accepted).

[22] Holst, D., Thommes, K., Schönlau, M., Nayeri, C. N., and Paschereit, C. O., 2016, "Entwicklung eines aerodynamischen Prüfstands zur Flügelprofiluntersuchung von Kleinwindkraftanlagen unter dynamischen Winkeländerungen auf Basis eines cRIO-9068," R. Jamal and R. Heinze, eds., VDE VERLAG, Berlin, Germany, pp. 54–57.

[23] Langtry, R. B., and Menter, F. R., 2009, "Correlation-Based Transition Modeling for Unstructured Parallelized Computational Fluid Dynamics Codes," AIAA J., **47**(12), pp. 2894–2906.

Proceedings of ASME Turbo Expo 2019: Turbomachinery Technical Conference and Exposition
GT2019
June 17-21, 2019, Phoenix AZ, USA

GT2019-90500

STATIC AND DYNAMIC ANALYSIS OF A NACA 0021 AIRFOIL SECTION AT LOW REYNOLDS NUMBERS: DRAG AND MOMENT COEFFICIENTS

David Holst [1) †*], Francesco Balduzzi [2)], Alessandro Bianchini [2) †], Christian Navid Nayeri [1)], Christian Oliver Paschereit [1) †], Giovanni Ferrara [2)]

[1)] Chair of Fluid Dynamics
Hermann-Föttinger-Institut,
Technische Universität Berlin,
Müller-Breslau-Str. 8,
10623, Berlin, Germany
Tel. +49 30 314 27489
Fax +49 30 314 21101
david.holst@tu-berlin.de

[2)] Department of Industrial Engineering
Università degli Studi di Firenze
Via di Santa Marta 3
50139, Firenze, Italy
Tel. +39 055 275 8797
Fax +39 055 275 8755
francesco.balduzzi@unifi.it

ABSTRACT

Wind industry needs high quality airfoil data for a range of the angle of attack (AoA) much wider than that often provided by the technical literature, which often lacks data i.e. in deep- and post-stall region. Especially in case of vertical axis wind turbines (VAWTs), the blades operate at very large AoAs, which exceed the range of typical aviation application. In a previous study, some of the authors analyzed the trend of the lift coefficient of a NACA 0021 airfoil, using the suggestions provided by detailed CFD analyses to correct experimental data at low Reynolds numbers collected in an open-jet tunnel. In the present study, the correction method is extended in order to analyze even the drag and moment coefficients over a wide range of AoAs for two different Reynolds numbers (Re=140k and Re=180k) of particular interest for small wind turbines. The utility of these data is again specifically high in case of VAWTs, in which both the drag and the moment coefficient largely contribute to the torque. The investigation involves tunnel data regarding both static polars and dynamic sinusoidal pitching movements at multiple reduced frequencies. Concerning the numerical simulations, two different computational domains were considered, i.e. the full wind tunnel and the open field. Once experimental data have been purged by the influence of the wind tunnel by means of the proposed correction method, they were compared to existing data for similar Reynolds both for the NACA0021 and for similar airfoils. By doing so, some differences in the static stall angle and the extent of the hysteresis cycle are discussed. Overall, the present paper provides the scientific community with detailed analysis of low-Reynolds NACA 0021 data in multiple variations, which may enable, inter alia, a more effective VAWT design in the near future.

INTRODUCTION

An improvement of the accuracy of airfoils polars has long been recognized as fundamental for the development and the predictability of design tools used in the analysis of industrial wind turbines based on low- or medium-fidelity models [1-5]. Such traditional tools and techniques, combined with existing airfoil data, are often insufficient for the required challenges of ensuring reliable predictions of turbines performance and effective energy conversion. Another important aspect is related to the fact that wind turbine blades operate over a much wider range of incidence with respect to aircraft blades, often extending deep into stall conditions [2,6]. In case of horizontal axis wind turbines (HAWTs) this occurs especially in proximity of the root region of the blade. In case of Darrieus vertical axis wind turbines (VAWTs), the operating conditions are even worse, due to both the continuous variation of the AoA during the revolution and the strong dependence of the AoA history on the tip-speed ratio (TSR). As a result, all the angles in the full incidence range of 180 degree can be experienced by such machines [7,8].

In addition, a correct estimation of the pitching moment coefficient is pivotal for an accurate prediction of the aerodynamic forces acting on the blade of Darrieus turbines [9]. It has to be noticed that the effect of the pitching moment is usually neglected in lumped parameters models, probably due to the fact that the pitching moment is applied about an axis

∗ Address all correspondence to this author.
† ASME Member.

orthogonal to the rotation axis for a conventional HAWT, causing only a torsional stress on the blades. Conversely, in case of a VAWT blade, the pitching moment has a direct impact on the aerodynamic torque. The turbine torque coefficient (C_T) can be indeed expressed in terms of the two contributions coming from the tangential force (vector sum of lift and drag) and the pitching moment coefficient c_m, as shown in Eq. (1):

$$C_T = \frac{1}{2}\frac{c}{r}\left((c_l(\alpha)\sin\alpha - c_d(\alpha)\cos\alpha) + \frac{c}{r}c_m(\alpha) \right) \qquad (1)$$

where c is the blade chord, r is the turbine radius and α is the incidence (or AoA).

The pitching moment can rise significantly for high AoAs and it is strongly related to the choice of the blade-spoke connection point, as it increases as a function of the distance from the aerodynamic center of the airfoil itself. As an example, Fig. 1 shows the decomposition of the overall torque coefficient into the two contributions coming from the tangential force and the pitching moment for two turbines featuring a different blade-spoke connection point [9]. The pitching moment can have a major impact on the aerodynamic performance of the blade and therefore it cannot be neglected in the design phase of the rotor. Literature lacks reliable moment data within the extended AoA regime necessary for VAWT application. To this purpose, a combined use of wind tunnel measurements and high-fidelity numerical simulation models, such as CFD, is surely one the most valuable solution for providing reliable deep and post stall data to the technical literature.

In a previous paper [10], some of the authors showed the results of a combined experimental-numerical study on the static and dynamic performance of a NACA 0021 airfoil at two different low Reynolds numbers (Re=140 k and Re=180 k). The wind tunnel setup was numerically replicated using a U-RANS approach with the goal of validating and correcting the chosen experimental setup. In particular, two different computational domains were considered for the CFD computations, i.e. a full wind tunnel and an open field domain, showing the presence of a deflection of the local flow around the blade when simulating the configuration that replicates the wind tunnel section (Fig. 2a). Conversely, in case of an open-field-like domain, the flow is almost undisturbed away from the blade wall (Fig. 2b). The numerical results provided a deep insight into the impact of the experimental setup onto the measurements, since it was proven that the lift force is responsible for the change in the direction of the jet exiting the wind tunnel nozzle. Therefore, a proper correction for the lift polar was proposed to correct measurements from any bias due to wind tunnel effects, making them representative of the undisturbed behavior of the airfoil at low Reynolds numbers. The present study refines and extends the correction method to drag and moment coefficients, analogous to what was already shown in [10] for the analysis of lift polars.

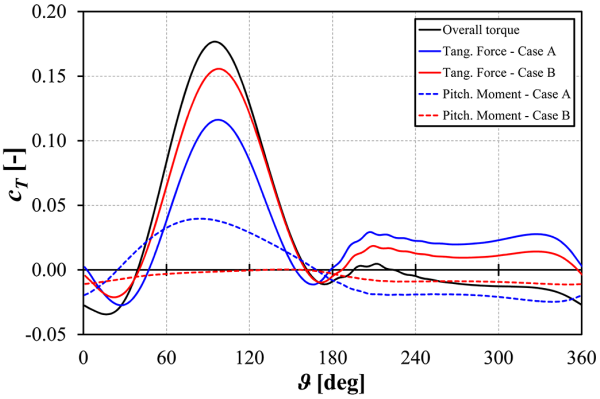

FIGURE 1. TORQUE CONTRIBUTIONS OF THE TANGENTIAL FORCE AND THE PITCHING MOMENT [9].

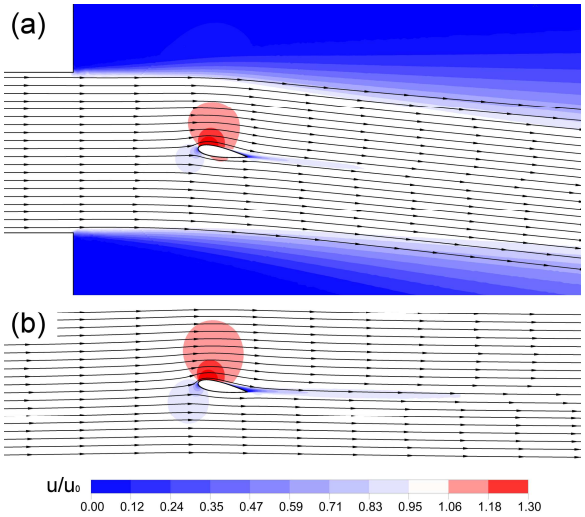

FIGURE 2. STREAMLINES AND VELOCITY CONTOURS AT α=10 DEG AND Re=140 K: (a) WIND TUNNEL DOMAIN, (b) OPEN FIELD DOMAIN [10].

The simulation results presented in [10] revealed that a deep knowledge of the experimental setup improves the numerical results. Figure 3 visualizes the very good agreement of CFD and experiment. The linear region is optimal, nevertheless, the maximum lift as well as the stall angle are underestimated. Literature provides another comparison study between CFD and experiment [11], which is also based on the NACA 0021 airfoil. They achieved a better agreement regarding $C_{l,max}$ and the stall angle but the results do not match the post stall lift properly. The present simulation, which uses a γ-Re_θ model, shows a very good agreement within this region, which is crucial if the resulting polar data is used for VAWT design. However, if own experimental data sets are not available, polar data can be either found in the technical literature [11-18] or computed by means of well-known tools as XFOIL [19]. Figure 4 and Fig. 5 summarize the literature

results of NACA 0021 polar data for lift and drag, respectively. Starting from the lift coefficient curves, Fig. 4 reveals large deviations between the data sets. In particular, three different groups are visible. The data of Stack et al. [12] and Jacobs et al. [13] belong to the first group, since they are both based on an open jet configuration. The poor coherence of the curves' slope is related to the fact that the authors did not correct the results. The second group is built by the data of Raghunathan et al. [17] and Swalwell et al. [18], which was acquired in large test sections resulting in very low blockage and minimized wall influences. Finally the third group consists of the remaining data sets, especially the XFOIL data overestimates the maximal lift as well as the stall angle. The data of Sheldahl et al. [16] is the only data set which is completely inconsistent. The data set is computed and extrapolated based on NACA 0009, NACA 0012, NACA 0015 experiments, which may explain the deviations.

The literature drag polars presented in Fig. 5 show consequently comparable differences, although the drag data provided are lesser if compared to the corresponding lift data. The experimental results reveal the increased post stall drag. As XFOIL predicts stall at larger AoA the drag stays at lower values. At low AoAs the drag of the Swalwell data is about zero [18], which is significantly lower if compared to the other references. Nonetheless, this results from the chosen acquisition system. Swalwell et al. use surface pressure measurements to calculate lift and drag. Therefore, the presented drag is just pressure drag missing the friction drag, which is dominant within low AoA region.

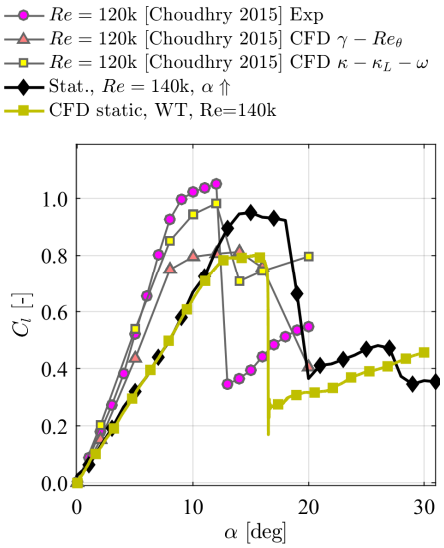

FIGURE 3. PRESENT CFD RESULTS OF A NACA 0021 COMPARED TO LITERATURE [11].

The influence of the experimental setup was investigated by Du et al. [20,21], who analyzed the same NACA 0018 airfoil in different setups for the full 180 deg range. The resulting lift and drag polars are shown in Fig. 6 and Fig. 7 and additionally the data set of Sheldahl et al. [16] was included. A significant disagreement can be observed, with a maximum difference of roughly one in the post-stall region. The open as well as the closed test section results of Du et al [20,21] were measured in a setup with 5% to 28% blockage ratio between 0 deg and 90 deg of incidence. Nearly 30% blockage is too much for closed test sections. Additionally, the reference setup is nearly optimal by using a large wind tunnel resulting in a blockage ratio of 0.5% to 3%. The open jet as well as the reference configuration reveal the phenomenon of a second stall while this is not visible for the closed test section with higher blockage ratio. The calculated polar of Sheldahl et al [16] is based on measurements collected by means of a setup with a blockage ratio between 1% to 7%, which still could be to large at higher AoA.

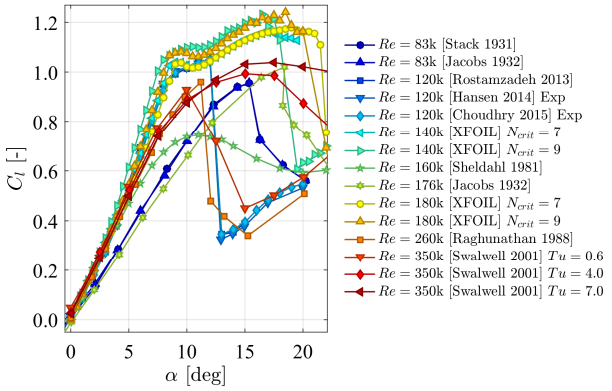

FIGURE 4. NACA 0021 LITERATURE LIFT DATA. [11 - 18]

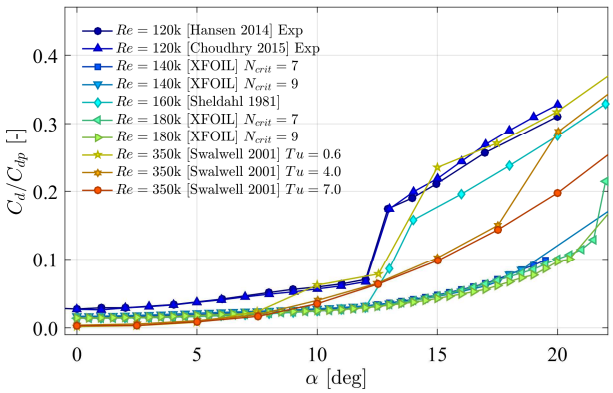

FIGURE 5. NACA 0021 LITERATURE DRAG DATA. [11, 15, 16, 18]

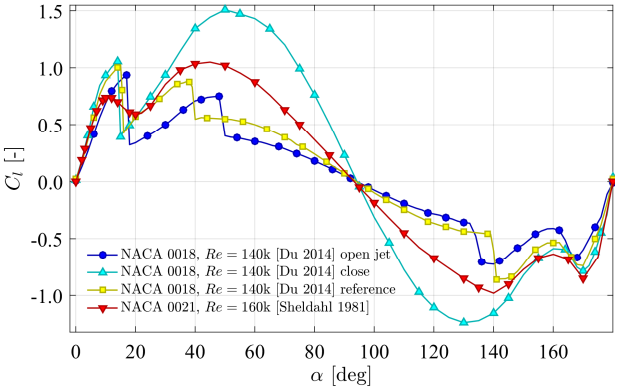

FIGURE 6. LITERATURE 180 LIFT DATA FOR DIFFERENT TUNNEL SETUPS. [DU 2014] DATA UNCORRECTED AND 28% BLOCKAGE AT 90 DEG IN CLOSED TUNNEL [20,21].

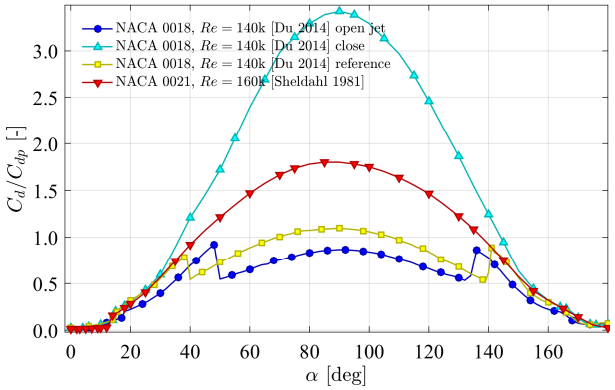

FIGURE 7. LITERATURE 180 LIFT DATA FOR DIFFERENT TUNNEL SETUPS. [DU 2014] DATA UNCORRECTED AND 28% BLOCKAGE AT 90 DEG IN CLOSED TUNNEL [20,21].

Because Du et al [20,21] present uncorrected data for the full 180 degree range, their data will be used to compare and validate the setup of the present study. Even though the investigated airfoil is not exactly the same (i.e. NACA 0018), the data can be reasonably considered valid for benchmarking since, especially in the post-stall region, all existing models [5] and experimental data sets [16] agree that a small variation in the thickness-to-chord ratio is supposed to have a negligible effect.

The influence of the experimental apparatus can be removed if a proper correction is applied. However, most of the corrections include assumptions as thin airfoil theory or others. Sometimes it is not possible to apply multiple corrections because different methods can be based on assumptions that are not valid at the same time. Literature provides numerous references for correction methods. The NATO Advisory Group for Aerospace Research and Development (AGARD) provided one of the most extensive compositions of wind tunnel corrections [22,23]. Additional publications, i.e. of Barlow et al. [24], or correction methods defined by D. Althaus for the laminar wind tunnel of Stuttgart [25,26] are also known. The reader is referred to these works in case of further interest because the analysis of the different methods is beyond the scope of this paper.

The investigation presented in this paper was carried out for both static polars and dynamic sinusoidal pitching movements at multiple reduced frequencies.

EXPERIMENTS

The experiments presented in this paper were conducted at the Hermann-Föttinger-Institute (HFI) of the TU Berlin. The *Experimental setup* section will present some details of the data acquisition as well as of the general wind tunnel layout. The *Experimental Validation* section concentrates only on general experimental outcomes in preparation of the final comparisons in the *Results* section.

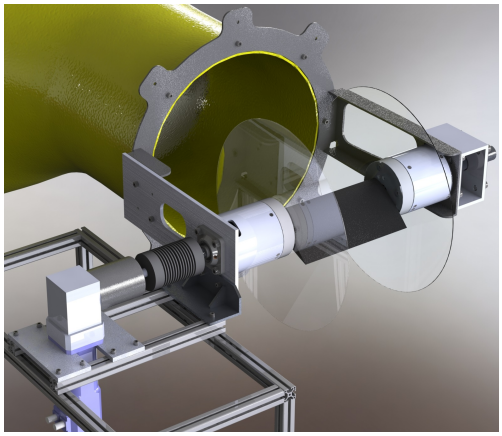

FIGURE 8. 3D CAD MODEL OF THE EXPERIMENTAL WIND TUNNEL SETUP [6].

Experimental setup

The experimental wind tunnel setup for the present study is schematized by its 3D CAD model in Fig. 8. The setup is part of the Hermann-Föttinger-Institute's laminar wind tunnel. The closed loop tunnel was modified to include an open test section. The airfoil of interest was directly mounted in front of the nozzle which has a circular cross section (d=0.45 m). The turbulence level does not exceed 1.0% in the potential core at the maximum inflow velocity of 20 m/s, even without an aerodynamic lip. The AoA of the airfoil can be set automatically by a servomotor within a range of α=±360 deg. An embedded controller and a custom-made program, developed using LabVIEW ™, control the motor position within a margin of less than 0.05 deg. A full description of the mechanical setup as well as of the software and data acquisition is already published by Holst et al. [6,10,27] and it is therefore not presented in full detail. The setup is optimized for the acquisition of time-resolved surface pressures. The present experiment used 32 high-frequency pressure transducers with a range of 1000 Pa

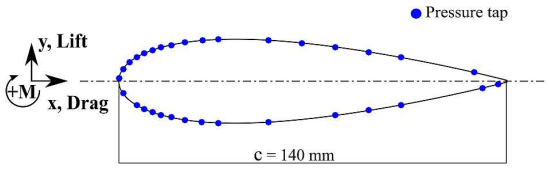

FIGURE 9. PRESSURE TAP LOCATIONS.

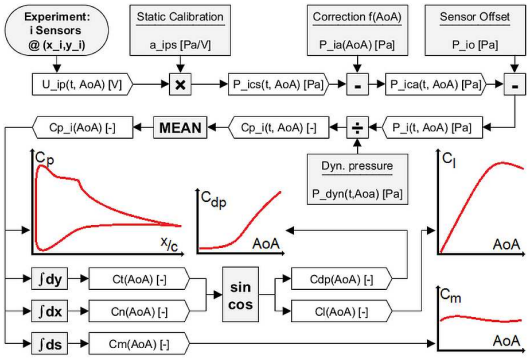

FIGURE 10. DATA PROCESSING ANALOGUE TO Holst et al. [6].

and an accuracy of ±1 Pa. All signals were converted using several 16-bit analog digitizers. The corresponding pressure tap locations are sketched in Fig. 9. The spatial resolution was higher within the regions of large pressure gradients, i.e. the leading edge, where the suction peak occurs. The NACA 0021 profile section had a chord of c=0.14 m and an aspect ratio of AR=2. Splitter plates at each end of the airfoil reduced the tip influence resulting in a 2D flow around the airfoil.

The final analysis of the pressure signals incorporated multiple calibrations and corrections. Figure 10 summarizes the entire data processing chain. All sensors were calibrated in situ against a reference pressure. Subtracting no-flow measurements in the post-processing removed the AoA dependency of the sensor signals. Finally, the resulting pressure coefficient was used to calculate all experimental aerodynamic coefficients presented in this paper. Readers, who are interested in a more detailed discussion of the data processing, are referred to the papers of Holst et al. [6,27].

Experimental validation

The procedure presented is well established and was verified in earlier publications by some of the authors [6,10,27]. The measurements are reproducible and validated by comparisons with literature data. However, the available literature lacks reliable full range data sets of thick airfoils at low Reynolds numbers up to 180 deg AoA. Well known experiments are provided e.g. by Rainbird et al. [28], as well as Du et al. [20,21], which were already introduced. Both of them also discuss the influence of the experimental setup onto

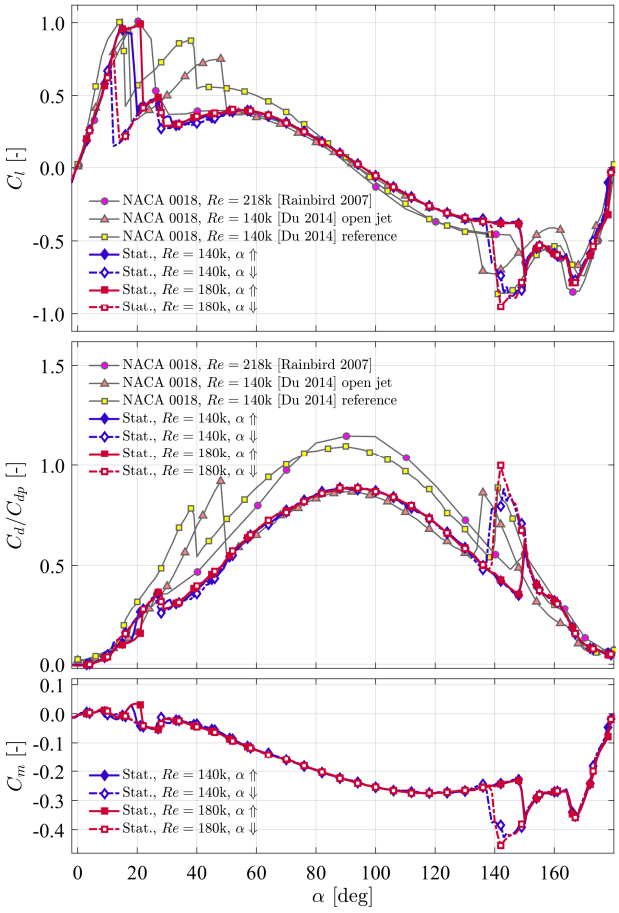

FIGURE 11. EXPERIMENTAL C_L, C_{DP} AND C_M IN COMPARISON TO LITERATURE DATA REPRESENTING DIFFERENT EXPERIMENTAL SETUPS [20,21,28].

the results. Du et al. investigated a NACA 0018 in different wind tunnels to provide further insights.

Comparable NACA 0021 data is not available and therefore, Fig. 11 includes the polars of Rainbird et al., as well as those of Du et al. even if it represents the NACA 0018 airfoil. Again, it should be noticed that all existing models and data (e.g. [5]) do confirm that these data can be considered relevant, especially in the post-stall region, where the two airfoils are expected to work similarly. The comparison between the current experiments and the polars of Du's open jet configuration reveals a good agreement. All lift polars increase again after the first stall and each of them has a second stall in the range of 25 deg-40 deg. The angle, as well as the strength of the second stall, depend on the wind tunnel configuration and the experimental setup. The second stall is caused by a change of the wake state [20,21]. The point of flow detachment travels towards the leading edge and jumps to the pressure side.

The experimental drag coefficients plotted in Fig. 11 are

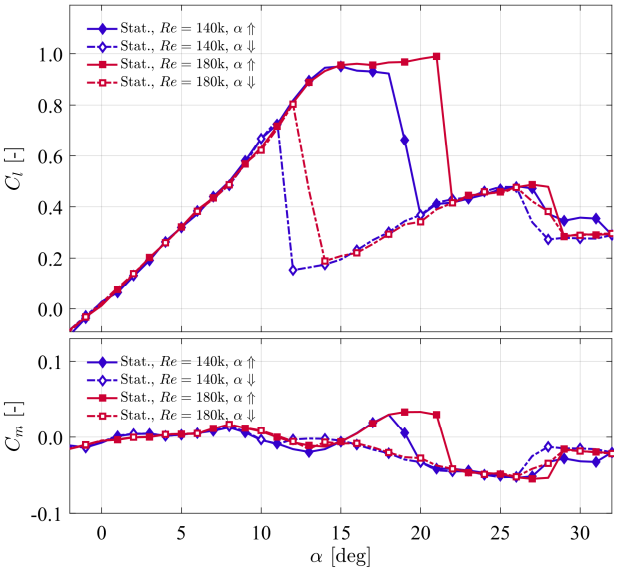

FIGURE 12. LIFT AND MOMENT COEFFICIENTS IN THE LINEAR AND NEAR-STALL REGION.

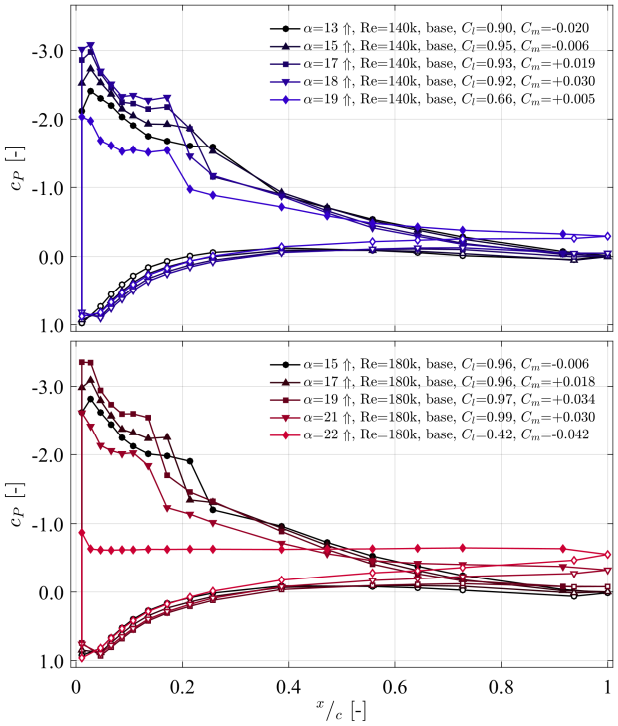

FIGURE 13. PRESSURE COEFFICIENTS FOR *RE*=140 K AND *RE*=180 K FOR VARIOUS AOA UP TO STALL.

based on the integration of surface pressure coefficients. Hence, they do not include skin friction, which can be neglected at high AoA but not at low incidence, where the friction drag is dominant. As a result, the pressure based drag, c_{dp} has to be always smaller than the total drag c_d of comparable literature data within this range. The hysteresis behavior of the airfoil was discussed over the full 180 degree range in literature for lift and drag coefficients [6,10,27]. Figure 11 additionally presents the quarter-chord moment coefficient. The moment polar has a small hysteresis in the range of the first stall, but a large one at 145 deg with a $\Delta c_m \approx 0.15$. The quarter chord moment is very sensitive to the surface pressure distribution. Figure 12 visualizes the lift and moment coefficients in the linear and near-stall region, while Fig. 13 shows the according pressure distribution for selected incidences. The lift coefficient of the *Re*=180 k polar is nearly constant between 15 deg and 21 deg, while the moment coefficient shows a significant change. Figure 13 reveals that the increasing suction peak, as well as the shift of the separation bubble towards the leading edge, result in an increasing pitch up moment until 19 deg. The onset of trailing edge stall causes a stagnating, and afterwards decreasing, moment coefficient. The moment switches the sign during stall from pitch up to pitch down.

The present paper focuses on the comparison between experiment and CFD. A previous study [10] has proven a good agreement regarding c_l as well as the c_p distributions. Nevertheless, differences in the length of the separation bubble were visible as well as some limitations in the stall regime. Hence, a comparison of c_m should reveal some differences.

CFD SIMULATIONS

The numerical solutions of the compressible unsteady Reynolds-Averaged Navier-Stokes equations (U-RANS) in a two-dimensional form were computed by employing the commercial CFD solver ANSYS® FLUENT®. The *κ-ω SST (Shear Stress Transport)* turbulence model was used, coupled with the *γ-Re*$_\theta$ transition model for predicting the laminar-turbulent transition in the boundary layer.

In the present section, a brief description regarding the most relevant settings used for the definition of the numerical model is provided. A more complete and general description is given in [4,5], where the CFD results were validated by comparing the simulations with experimental data on different airfoils over the entire range of AoAs. The validity of the proposed setup for the present case study of a NACA 0021 airfoil was previously discussed in [10], where the comparisons revealed that numerical and experimental pressure coefficient distributions were both qualitatively and quantitatively comparable after a calibration of the *γ-Re*$_\theta$ model constants. In particular, both the boundary layer transition location and the extent of the transition region were correctly predicted. The *Coupled* algorithm of the pressure-based approach was applied to solve the mass and momentum balance equations. The second-order upwind differencing scheme and the bounded second order scheme were used for the spatial and temporal

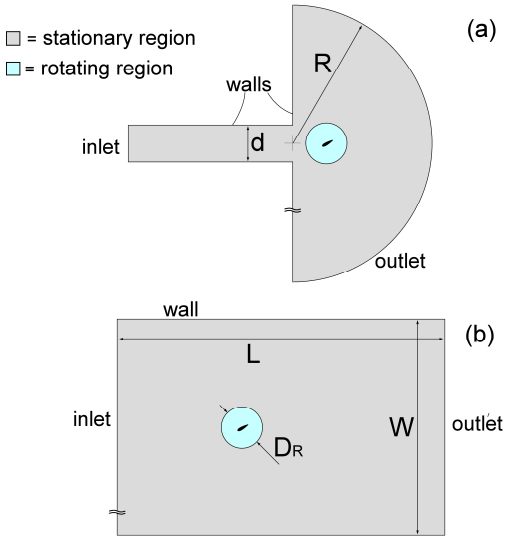

FIGURE 14. CFD DOMAINS: (a) WIND TUNNEL, (b) OPEN FIELD.

discretization, respectively. Both static polars and dynamic cycles were performed by means of unsteady calculations using small angular timesteps, ranging between 0.01 deg and 0.1 deg, due to the very complex phenomena occurring at high AoAs.

The CFD domain was split into two communicating sub-domains for the rotation of the blade: a circular rotating region defined by a diameter of D_R=7c and a stationary outer region defined depending on the analyzed configuration. In particular, the two analyzed cases are reported in Fig. 14:

- a "wind tunnel" domain (Fig. 14a) in which the blade is placed in front of a nozzle (having the same width d of the wind tunnel section) and surrounded by a semi-circular outlet boundary characterized by a radius of R=60c;
- an "open field" rectangular domain (Fig. 14b) characterized by a width of W=40c to avoid blockage effects and an overall length of L=60c.

For both CFD domains, the freestream wind speed u_0 and the ambient pressure were imposed at the inlet and outlet boundaries, respectively. A non-slip condition is imposed on the solid walls of blade and tunnel boundaries.

The flow domain under investigation was discretized using a triangular mesh in interior of the domain and a quadrilateral mesh in the boundary layer regions. An O-grid was used on the blade surface featuring a row of 40 layers, with a distance of the first mesh node to the wall able to guarantee a value of the dimensionless wall distance (y^+) lower than ~1. The size and number of mesh elements have a strong influence on the accuracy of the solution. In earlier studies [4,5], some of the authorsinvestigated extensively the sensitivity of the solution to the mesh density. According to previous experiences, similar

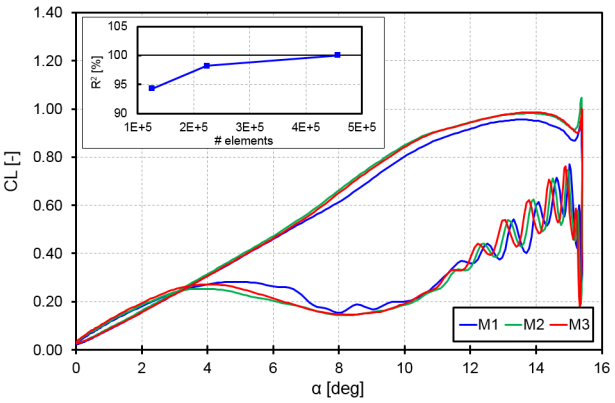

FIGURE 15. GRID INDEPENDENCY TEST.

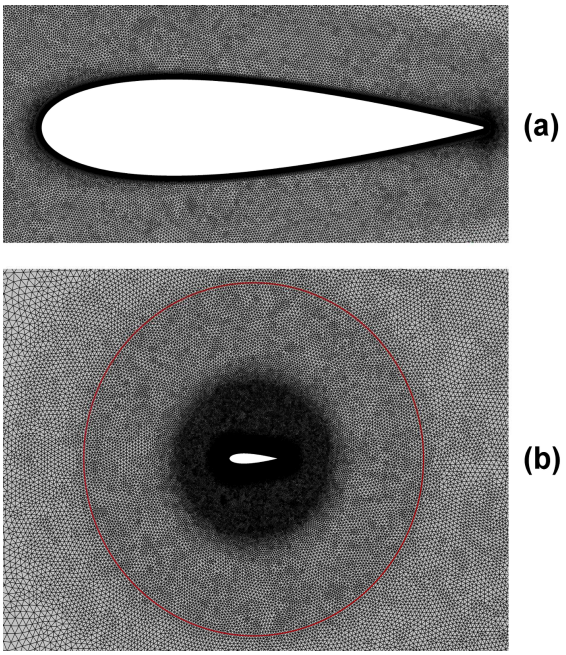

FIGURE 16. MESH DETAILS: (a) AIRFOIL, (b) ROTATING DOMAIN.

mesh refinement levels were also tested in the present case for a dynamic pitching movement to validate the grid independency test also for sinusoidal changes of AoA. Three meshes were defined by progressively increasing the number of nodes on the airfoil wall boundary. The coarse mesh (*M1)* features 500 nodes around the blade and a total cell count of $1.2 \cdot 10^5$ elements. The intermediate mesh (*M2)* features 750 nodes on the blade and $2.2 \cdot 10^5$ elements. The finest mesh (*M3)* features 120 nodes on the blade and $4.5 \cdot 10^5$ elements. The results for a sinusoidal movement in the AoA range $\alpha \in$ [0 deg, 15.4 deg] at Re=140 k and k=0.05 in open field are shown in Fig. 15. The solution from the *M2* grid was considered to be grid-independent since

no significant variation in the lift coefficient cycle was observed with the *M3* refinement. The independency was also quantified in terms of similarity of the curves by means of the coefficient of determination R^2. A value of 98.2% between the *M2* and *M3* curves implies a satisfactory matching.

The details of the final mesh are shown in Fig. 16. A very fine mesh is used (Fig. 16a) with a higher density of nodes in the leading and trailing edges of the airfoil, leading to a mesh size of the rotating region of $1.5 \cdot 10^5$ elements (Fig. 16b). The stationary domains are discretized with $6.0 \cdot 10^4$ cells for the wind tunnel configuration and $7.0 \cdot 10^4$ cells for the open field configuration.

RESULTS

The detailed comparison between experiments and CFD consists of two different sections. *Static polars* focuses on the discussion of correction methods and on their effect on the data. The following section *Dynamic pitching movement* analyses the capability of high-fidelity CFD to simulate sinusoidal changes of AoA.

Static polars

As already pointed out from the analysis of Fig. 2 reported by Holst et al. [10], the comparison between wind tunnel and open field simulations was helpful to quantify the impact of the experimental setup onto the measurements. The proposed correction method was based on the addition of an angular shift (ΔAoA) proportional to the lift coefficient to the actual angle of attack "seen" by the blade in order to make the open field results equivalent to the wind tunnel results. The relationship between the deflection of the local flow around the airfoil surface and the lift itself was indeed expressed according to Eq. (1) and Eq. (2):

$$\Delta AoA = a_1 \cdot c_{l,OF} = {}^{1}\!/_{T_{\max}} \cdot c_{l,OF} \tag{1}$$

$$AoA_{OF,corr} = AoA_{OF} + \Delta AoA \tag{2}$$

where T_{max}=0.21 is the thickness-to-chord ratio of the airfoil. It was shown that, when correcting the open field CFD lift polars by considering the transformation applied to the AoA values as reported in Eq. (3), a suitable matching with the experiments was achieved:

$$c_{l,OF,corr}(AoA_{OF,corr}) = c_{l,OF}(AoA_{OF}) \tag{3}$$

An analogous correction was then postulated also for the drag and moment polars, as expressed in Eq. (4) and Eq. (5):

$$c_{d,OF,corr}(AoA_{OF,corr}) = c_{d,OF}(AoA_{OF}) \tag{4}$$

$$c_{m,OF,corr}(AoA_{OF,corr}) = c_{m,OF}(AoA_{OF}) \tag{5}$$

The analysis of drag and moment coefficients over a wide range of AoAs is the focus of the present investigation. Starting from the static data, Fig. 17 shows the experimental and numerical moment polars at a Reynolds number of *Re*=140 k.

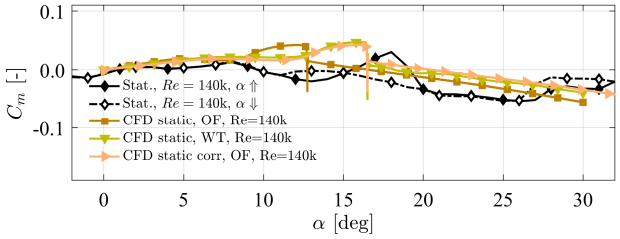

FIGURE 17. EXPERIMENTAL AND CFD PITCHING MOMENT POLARS FOR DIFFERENT DOMAINS AT *Re*=140 K.

The experimental curves shown in black are a part out of the full 180-degree polar presented in Fig. 11. Focusing the attention on the comparison between the measured data and the results of the wind tunnel domain (WT) simulations, the matching between the curves is not completely acceptable. For low incidences, i.e. up to roughly α=10 deg, the moment is almost null in both cases.

Conversely, for incidence values beyond the linear region of lift, the curves show different trends, since the numerical values are slightly positive and tend to increase, while the measured values show an oscillating behavior. Notwithstanding this, the location of the simulated airfoil stall is just slightly advanced with respect to the experiments. The aforementioned discrepancies were expected since the solution is strongly sensitive to the exact location of the separation point and to the extension of the transition region from laminar to turbulent flow, when the flow starts to separate on the suction side. The 2D U-RANS approach has some limits in correctly predicting the aerodynamic behavior within stall and, as a consequence, the pitching moment is the most sensitive parameter suffering from such inaccuracy.

The pitching moment polar of the open field domain (OF) simulation does not match the experiments, since a difference of roughly 5 deg can also be noticed in the prediction of the stall angle. When applying the correction proposed in Eq. (2) and Eq. (5), the shifted open field curve matches almost exactly with the wind tunnel CFD curve in both the pre-stall and post-stall regions, as a confirmation that accounting for an angular shift is valid for the moment correction.

The drag polars at a Reynolds number of *Re*=140 k are reported in Fig. 18. From a perusal of the figure, it can be readily noticed that the results of the wind tunnel simulations are in very good agreement with measured data for the whole range of analyzed incidences. This result is a further evidence that the full wind tunnel CFD configuration including the free jet is suitable for reproducing the experimental setup. On the other hand, the open field simulation does not match the experiments once again.

Moreover, in contrast to the lift and moment polars, no matching can be obtained between the corrected open field and the wind tunnel polars applying the proposed pure AoA correction to drag data (◀). Therefore, the original correction

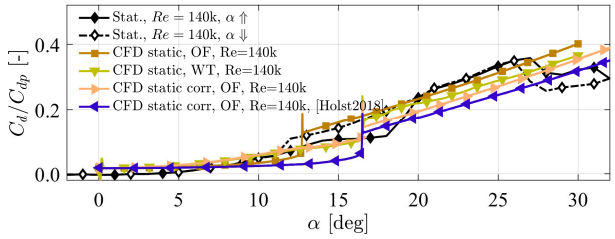

FIGURE 18. EXPERIMENTAL AND CFD DRAG POLARS FOR DIFFERENT DOMAINS AT *Re*=140 k.

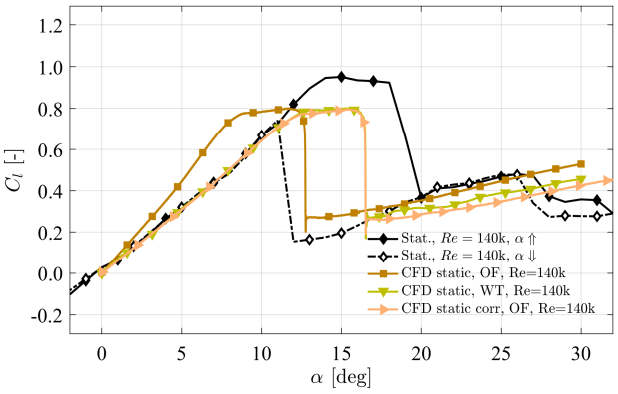

FIGURE 19. EXPERIMENTAL AND CFD LIFT POLARS FOR DIFFERENT DOMAINS AT *Re*=140 k.

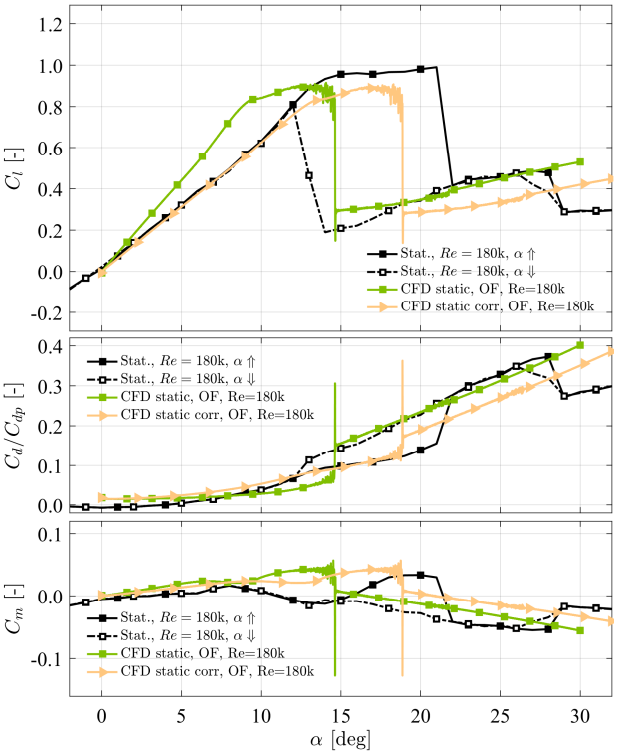

FIGURE 20. LIFT, DRAG AND MOMENT POLARS: COMPARISON BETWEEN EXPERIMENTS AND CFD AT *Re*=180 k.

based only on the angular shift for the AoA values fails for the evaluation of drag.

The following explanation is proposed: the forces measured in the *x*-*y* reference frame directly correspond to drag and lift forces, respectively, only in case of an open field flow, such as the one shown in Fig. 2b. Conversely, when the flow around the blade is deflected by an angle ΔAoA, *x* and *y* directions do not correspond anymore to drag and lift directions, since they are rotated by the same angle. Therefore, the forces measured in the *x* and *y* directions must be projected onto the new reference frame to obtain the actual drag and lift forces.

Thus, in the present paper, an additional correction is proposed for lift and drag coefficients, according to Eq. (6) and Eq. (7):

$$c_{l,OF,corr}(AoA_{OF,corr}) = c_{l,OF}(AoA_{OF}) \times \cos(\Delta AoA) - c_{d,OF}(AoA_{OF}) \times \sin(\Delta AoA) \quad (6)$$

$$c_{d,OF,corr}(AoA_{OF,corr}) = c_{d,OF}(AoA_{OF}) \times \cos(\Delta AoA) + c_{l,OF}(AoA_{OF}) \times \sin(\Delta AoA) \quad (7)$$

The new correction must be applied to the open field CFD data (►) in order to guarantee the equivalence with the wind tunnel conditions, as it can be clearly observed in Fig. 18. In particular, the angular shift ΔAoA of the jet causes a large increase in the measured drag, especially at high incidence, due to the additional contribution of lift, which must be accounted for when correcting the open field data.

Conversely, the subsequent reduction of measured lift is less sensible since the contribution of the drag term in Eq. (6) is one order of magnitude smaller. As a result, the corrected lift polar using Eq. (6) for calculating the lift coefficient is almost coincident with the results shown in [10].

For completeness, Fig. 19 reports the experimental and numerical static lift polars at *Re*=140 k. The open field curve corrected using Eq. (6) is again superimposed with the one resulting from the simulation with the wind tunnel domain.

Finally, the lift, drag and moment polars at a Reynolds number of *Re*=180 k are visualized in Fig. 20. In this case, the CFD simulations were performed only for the open field configuration. The correction of numerical data by applying Eq. (2) for the AoA values and Eq. (5), Eq. (6) and Eq. (7) for the coefficient values is shown in the figure. The slope of the corrected lift and drag curves matches almost perfectly the experiments up to the stall angle. Analogous to the results at *Re*=140 k, the agreement between the numerical and

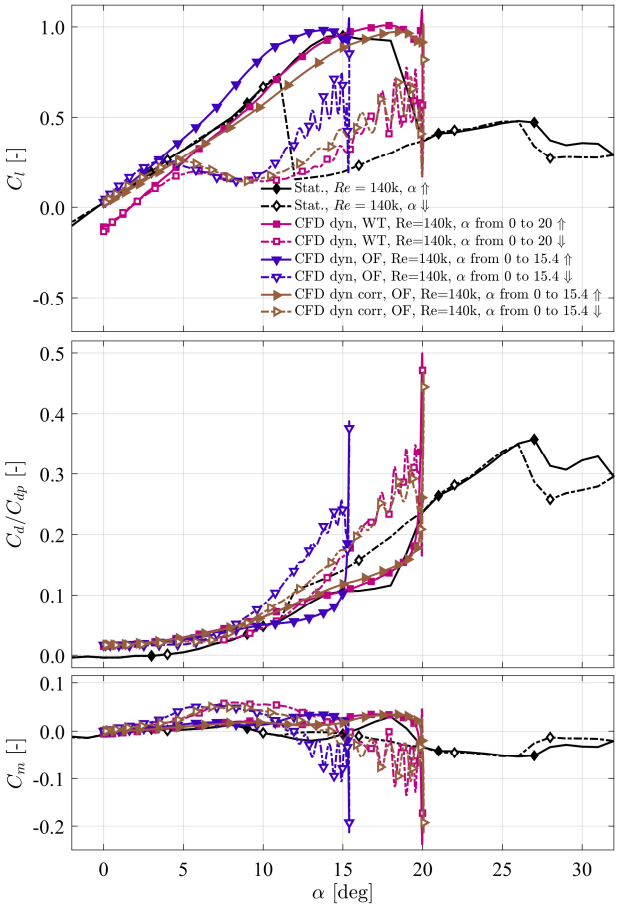

FIGURE 21. SINUSOIDAL MOVEMENT BETWEEN 0 AND 20 DEGREE BY CFD AT *Re*=140 k AND *k*=0.05.

experimental trends of moment coefficient is poor for the incidence range between 10 deg and 20 deg.

As a final remark, the extension of the correction method proposed in [10] to drag and moment coefficients revealed that a modification of the proposed correction was necessary to account for the projection of the lift and drag forces on the actual flow direction "seen" by the airfoil. Therefore, the equations for computing lift and drag coefficients were refined to correlate more accurately wind tunnel experiments with CFD. Conversely, the equation for computing the moment coefficient was unaltered.

Dynamic pitching movement

The corrections based on Eq. (6) and (7) are not limited to static polars. The previous methods of Holst et al. [10] were also successfully applied to the results of dynamic pitching movements CFD simulations. The sinusoidal movement is characterized by the reduced frequency k, which is defined according to Eq. (8).

$$k = \frac{\omega}{u_0} \cdot \frac{c}{2} = \frac{\pi f c}{u_0}. \tag{8}$$

First, the validity of the newly-proposed correction is checked for the dynamic conditions by focusing on the results of multiple CFD simulations representing the open field (OF) as well as the wind tunnel (WT) configurations. The results of a sinusoidal movement in the AoA range $\alpha \in$ [0 deg, 20 deg] at *Re*=140 k and k=0.05 are shown in Fig. 21. The open field simulation was limited to $\alpha \in$ [0 deg, 15.4 deg] range because the subsequent correction applied to the AoAs values (Eq. (2)) increases the range to the full extent of $\alpha \in$ [0 deg, 20 deg]. It can be readily noticed that the new correction allows obtaining a good agreement between the corrected OF and the WT results for all of the three analyzed aerodynamic coefficients. In particular, drag and moment loops are almost superimposed.

The black curves marked with diamonds representing the static baseline curves without any movement are also shown in the graphs, revealing that the WT configuration does not match the slope of the lift polar in the linear region, but captures the stall properly. The corrected OF simulation has the proper stall angle and a better agreement within the linear part of the polar. Nevertheless, the slope diverges a bit with increasing AoA. Corrected OF, as well as WT configurations, are nearly congruent with the static drag during pitch up movement. The simulated moment coefficients show small discrepancies compared to the experiment. However, these are expected because a U-RANS simulation cannot reproduce the experimental conditions and small differences in the c_p distribution can result in large deviations of c_m. The fluctuations during the pitch down phase are based on the U-RANS simulation because of the known limitations in stalled flows, which was already discussed in a previous paper [10].

Previous work of Holst et al. [27] experimentally investigated dynamic AoA changes in the near stall region. They showed an at least bi-stable behavior of the dynamic polars by analyzing 40 repetitions of the same movement. The resulting dynamic polars are shown in Fig. 22, labeled with Bin 1 and 2. They represent two different stall types. While Bin 1 stalls just slightly, a full stall is visible within Bin 2. The corrected OF simulation already shown in Fig. 21 is additionally plotted in Fig. 22.

The comparison reveals very good agreement with the second bin of the experimental data. The drag polar is nearly identical beyond the known differences between c_{dp} and c_d at small AoA. The lift is underestimated, but the stall angle is predicted properly and the size of the hysteresis loop is comparable.

The general trends of the moment polar are captured by the CFD. Nonetheless, the agreement is not as good as in lift and drag. The CFD based c_m is constantly positive during the pitch up, while the experimental coefficients are partially negative. During pitch down, CFD captures the general effects very well in relation to the according pitch up values. The pitch down moment is smaller than the pitch up between 20 deg and 13 deg.

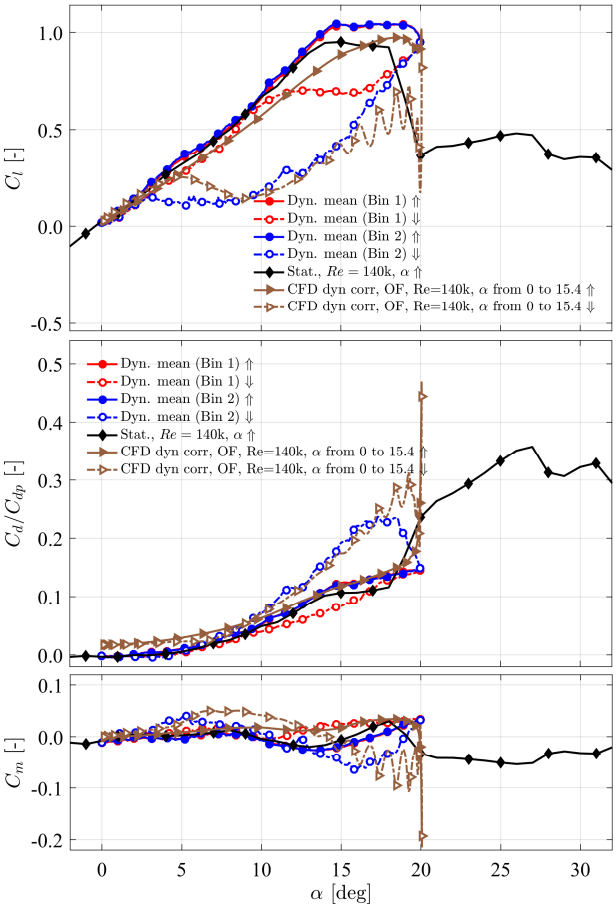

FIGURE 22. SINUSOIDAL MOVEMENT BETWEEN 0 AND 20 DEGREE AT *Re*=140 k AND *k*=0.05: CORRECTED CFD AND EXPERIMENTS.

It switches at lower AoAs and becomes greater than the c_m for increasing incidence. An identical behavior was captured in the experiments for Bin 2 shown in Fig. 22.

The good agreement between measurements and numerical results continues even with increasing Reynolds number (*Re*=180 k) and increasing dynamic AoAs regime, i.e. $\alpha \in$ [5 deg, 25 deg]. The CFD polars are based on an open field simulation between 3.5 deg and 20.3 deg, which represents the requested AoA regime after the correction. Figure 23 summarizes the drag and moment curves for CFD and experimental results. A previous work [10] already discussed the according lift polars and revealed no bi-stable behavior, which was prominent in Fig. 22. CFD generally matches the experimental drag polar of Fig. 23, and it shows an identical overshoot during the stall. Nevertheless, the simulation overestimates the dimension of this overshoot and it is located at a smaller AoA compared to the experiments. The CFD based c_m curve is mostly shifted towards positive coefficients, thus

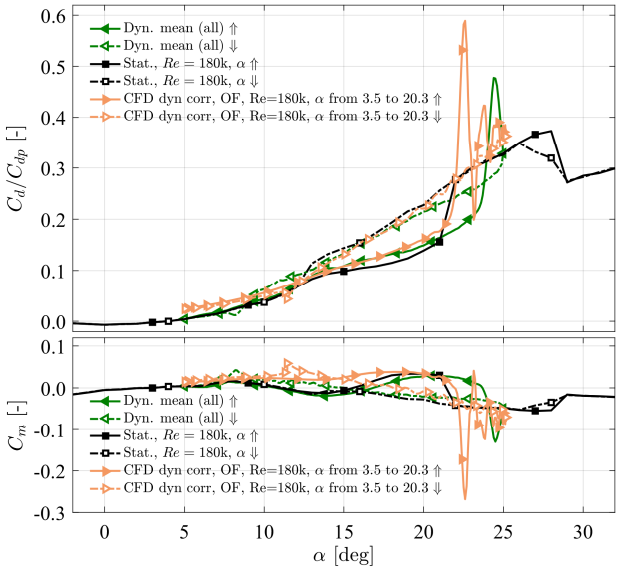

FIGURE 23. DRAG AND MOMENT COEFFICIENTS FOR A SINUSOIDAL MOVEMENT BETWEEN 5 AND 25 DEGREE AT *Re*=180 k AND *k*=0.025: CORRECTED CFD AND EXPERIMENTS.

CFD tends to predict a greater c_m. U-RANS captures the general trend and the form of the resulting hysteresis loops.

The correction methods provided within this paper have proven their suitability to match CFD and experimental results. The open field simulations were corrected so far to represent the wind tunnel configuration. Nevertheless, the corrections can also be used to correct the experimental polars to represent an open field configuration, thus purging the measurements from the influence of the setup. The following section *Literature comparison* analyzes the effect of the provided correction method in comparison to methods known by literature.

Literature comparison

The comparison with the relevant literature has to involve the influences of different experimental setups. Correction methods try to remove the influence of the setup from the real measurement. Some of the most reputed methods are the NATO Advisory Group for Aerospace Research and Development (AGARD) compositions of wind tunnel corrections [22,23], the work Barlow et al. [24], or the correction methods by D. Althaus for the laminar wind tunnel of Stuttgart [25,26]. Figure 24 and Fig. 25 visualize the effect of different correction methods for a selected range of incidence starting at 0 deg up to 30 deg for a Reynolds number of *Re*=140 k and *Re*=180 k, respectively. The authors decided to include the correction based on AGARD (▶) because this is one of the core references also used by Barlow and Althaus. The extended correction presented within this paper (◀) is shown as well as the version of the preceding publication [10] (▲).

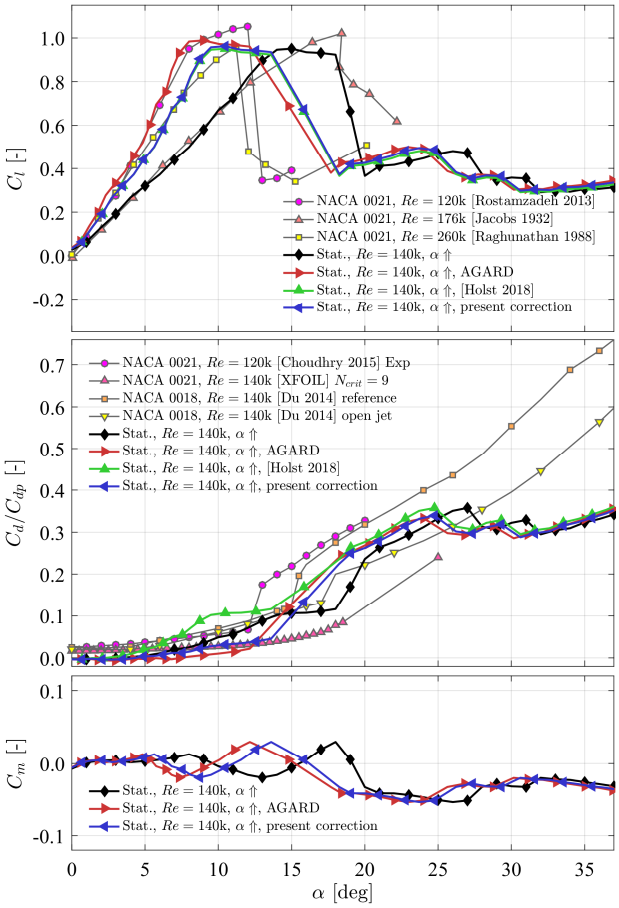

FIGURE 24. CORRECTED EXPERIMENTAL POLARS AT *Re*=140 k COMPARED WITH LITERATURE DATA [4,14,20,21] AND CORRECTION METHODS BASED ON NATO AGARD [22,23] AND HOLST ET AL. [10].

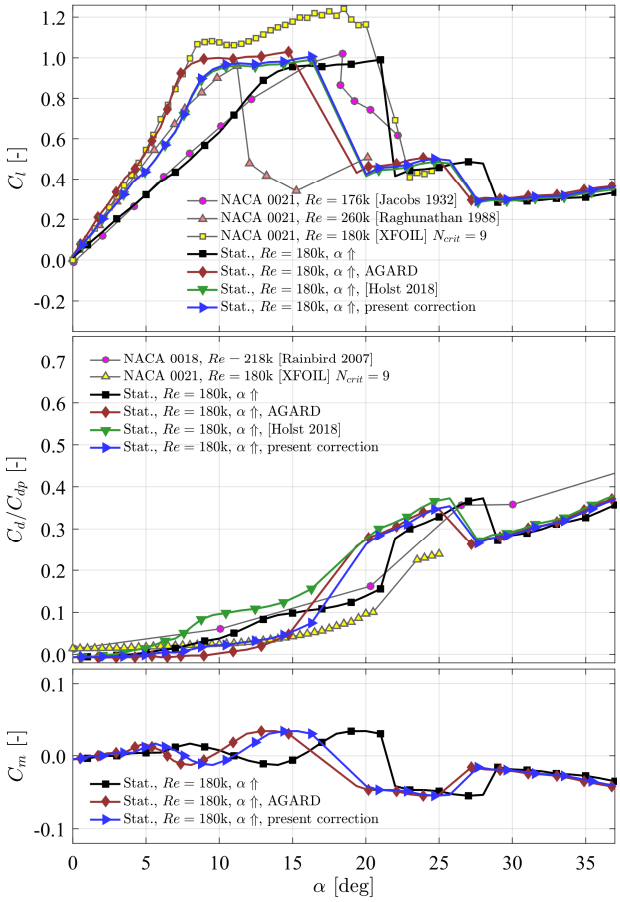

FIGURE 25. CORRECTED EXPERIMENTAL POLARS AT *Re*=180 k COMPARED WITH LITERATURE DATA [28] AND CORRECTION METHODS BASED ON NATO AGARD [22,23] AND HOLST ET AL. [10].

Experimental results are plotted together with literature data sets of known wind tunnel configuration. Du et al. [20,21] provide reference data for an open wind tunnel configuration and a very low blockage reference wind tunnel.

Rostamzadeh et al. [14] acquired their data in a closed test section. Comparison between all data sets reveals that the AGARD correction (►) results in polars representing a closed test section. The detailed AGARD calculation for this setup is published [27]. The uncorrected data matches Du's open configuration until stall, which was already discussed for the full 180 deg range in the *Experimental validation* section.

The extended correction method of the present paper (◄) and of the preceding paper (▲) reveal their difference if applied to the drag data. The current extension removes the predecessor's drag over-prediction for smaller AoAs and improves the drag prediction in deep stall region. Nevertheless, none of the correction methods works properly for incidence angles beyond 30 deg.

The c_m plot includes only the actual correction (◄) and as it is identical to the previous version. To the author's knowledge, literature provides no moment data for the NACA 0021 airfoil within the Reynolds number regime. Therefore, Fig. 24 and Fig. 25 do not include c_m literature data for comparison but both figures reveal a massive impact of the correction methods to the shape of the c_m polars. It is obvious that the pitching moment has direct impact on the turbines torque coefficient of a VAWT, which was discussed in the *Introduction* section. Thus, the knowledge of the influencing factors on c_m is crucial for proper load predictions as shown by Bianchini et al. [9] and consequently one factor could be the choice of the correction method.

CONCLUSIONS

A combined numerical and experimental study was carried out to get further insights into the performance of the NACA 0021 airfoil section at low Reynolds numbers. The influence of the experimental setup was numerically investigated by comparing an open field U-RANS simulation with a full wind tunnel configuration. The detailed simulations revealed very good agreement with experimental data, i.e. a better agreement than those presented in literature using a comparable simulation setup. The experimental data itself was compared to numerous literature data revealing large differences within the available polar data for a NACA 0021 airfoil. The differences were analyzed and a proper set of data for comparison was chosen accordingly.

The analysis presented in this paper focuses specifically on drag and moment coefficients, which lead to an extension of a correction method, which was previously only based on lift coefficients. The simulation of dynamic sinusoidal movement represented properly the experiments even if it is based on U-RANS. The deviations in moment coefficient were in fact expected, because of differences in separation bubble position and length, nonetheless the main trends were captured properly.

Once the correction between wind tunnel and open field configuration was assessed, it was possible to correct the experimental measurements in order to obtain polar curves for an undisturbed profile. The correction method is not based on any assumptions and may be used with other corrections from literature. The polars were compared to literature data and other correction methods as a further validation of the approach. The results are very promising. However, studies on other airfoils have to be conducted to be able to optimize and validate the proposed correction method in general.

NOMENCLATURE

Acronyms

CFD	computational fluid dynamics.
HFI	Hermann-Föttinger-Institute
OF	open field.
RANS	Reynolds-averaged Navier-Stokes.
SST	shear stress transport.
TSR	tip speed ratio.
VAWT	vertical axis wind turbines.
WT	wind tunnel.

Latin letters

AoA	angle of attack, deg.
c	blade chord, m.
c_{dp}	drag coefficient based on surface pressure.
c_l	lift coefficient.
c_m	moment coefficient.
C_P	pressure coefficient.
C_T	turbine's torque coefficient.
d	nozzle diameter, m.
D_R	rotating region diameter, m.
k	reduced frequency.
L	open field domain length, m.
r	turbine radius, m.
R	wind tunnel domain outer radius, m.
Re	Reynolds number.
Re_θ	momentum thickness Reynolds number.
y^+	dimensionless wall distance.
u	absolute wind speed, m s^{-1}.
W	open field domain width, m.

Greek letters

α	incidence angle (in formulas), deg.
γ	intermittency.
κ	turbulent kinetic energy, m^2 s^{-2}.
ω	specific turbulent dissipation rate, s^{-1}.
Ω	vorticity, s^{-1}.
Ω^*	dimensionless vorticity.

Subscripts

0	value at infinity.
corr	corrected.
OF	open field domain.
WT	wind tunnel domain.

REFERENCES

[1] Simão Ferreira, C., Aagaard Madsen, H., Barone, M., Roscher, B., Deglaire, P., and Arduin, I., 2014, "Comparison of aerodynamic models for Vertical Axis Wind Turbines," *Journal of Physics: Conference Series*, **524**(Conference 1), pp. 012125-10.

[2] Lennie, M., Pechlivanoglou, G., Marten, D., Nayeri, C. and Paschereit, C.O., 2015, "A Review of Wind Turbine Polar Data and its Effect on Fatigue Loads Simulation Accuracy," *Proc. of the ASME Turbo Expo 2015*, Montreal, Canada, June 15-19, 2015.

[3] Marten, D., Bianchini, A., Pechlivanoglou, G., Balduzzi, F., Nayeri, C.N., Ferrara, G., Paschereit, C.O. and Ferrari, L., 2016, "Effects of airfoil's polar data in the stall region on the estimation of Darrieus wind turbines performance," *J. Eng. Gas Turbines Power*, **139**(2), pp. 022606-9.

[4] Bianchini, A., Balduzzi, F., Rainbird, J., Peiro, J., Graham, J. M. R., Ferrara, G. and Ferrari, L., 2015, "An Experimental and Numerical Assessment of Airfoil Polars for Use in Darrieus Wind Turbines. Part 1 - Flow Curvature Effects," *J. Eng. Gas Turbines and Power*, **138**(3), pp.032602-1 - 032602-10.

[5] Bianchini, A., Balduzzi, F., Rainbird, J., Peiro, J., Graham, J. M. R., Ferrara, G. and Ferrari, L., 2015, "An Experimental and Numerical Assessment of Airfoil Polars for Use in Darrieus Wind Turbines. Part 2 - Post-Stall Data Extrapolation Methods," *J. Eng. Gas Turbines and Power*, **138**(3), pp.032603-1 - 032603-10.

[6] Holst, D., Church, B., Pechlivanoglou, G., Tüzüner, E., Saverin, J., Nayeri, C.N., and Paschereit, C. O., 2018, "Experimental Analysis of a NACA 0021 Airfoil Section Through 180-Degree Angle of Attack at Low Reynolds Numbers for Use in Wind Turbine Analysis," *J. Eng. Gas Turbines and Power*, **141**, pp. 041012-1 – 041012-10

[7] Paraschivoiu, I., 2002, *Wind turbine design with emphasis on Darrieus concept*, Polytechnic International Press, Montreal, Canada.

[8] Dominy, R., Lunt, P., Bickerdyke, A. and Dominy, J., 2007, "Self-starting capability of a Darrieus turbine," *Proceedings of the Institution of Mechanical Engineers, Part A: Journal of Power and Energy*, **221**, pp. 111-120.

[9] Bianchini, A., Balduzzi, F., Ferrara, G. and Ferrari, L., 2016, "Aerodynamics of Darrieus Wind Turbines Airfoils: The Impact of Pitching Moment," *J. Eng. Gas Turbines and Power*, **139**(4), pp.042602-1 - 042602-12.

[10] Holst, D., Balduzzi, F., Bianchini, A., Church, B., Wegner, F., Pechlivanoglou, G., Ferrari, L., Ferrara, G., Nayeri, C.N. and Paschereit, C.O., 2018, "Static and Dynamic Analysis of a NACA 0021 Airfoil Section at Low Reynolds Numbers Based on Experiments and Computational Fluid Dynamics," *J. Eng. Gas Turbines and Power*, **141**, pp. 051015-1 – 051015-10

[11] Choudhry, A., Arjomandi, M., and Kelso, R. M., 2015, "A Study of Long Separation Bubble on Thick Airfoils and Its Consequent Effects," International Journal of Heat and Fluid Flow, **52**, pp. 84–96.

[12] Stack, J., 1931, "Tests in the Variable Density Wind Tunnel to Investigate the Effects of Scale and Turbulence on Airfoil Characteristics," NACA-TN-364, NACA, Washington, USA.

[13] Jacobs, E. N., 1932, "The Aerodynamic Characteristics of Eight Very Thick Airfoils from Tests in the Variable Density Wind Tunnel," NACA-TR-391, National Advisory Committee for Aeronautics. Langley Aeronautical Lab.; Langley Field, VA, United States.

[14] Rostamzadeh, N., Kelso, R. M., Dally, B. B., and Hansen, K. L., 2013, "The Effect of Undulating Leading-Edge Modifications on NACA 0021 Airfoil Characteristics," *Physics of Fluids*, **25**(11), p. 117101

[15] Hansen, K. L., Kelso, R. M., Choudhry, A., and Arjomandi, M., 2014, "Laminar Separation Bubble Effect on the Lift Curve Slope of an Airfoil," *Proceedings of the19th Australasian Fluid Mechanics Conference*, H. Chowdhury, and F. Alam, eds., RMIT University, Melbourne Vic, Australia.

[16] Sheldahl, R. E., and Klimas, P. C., 1981, "Aerodynamic Characteristics of Seven Symmetrical Airfoil Sections through 180-Degree Angle of Attack for Use in Aerodynamic Analysis of Vertical Axis Wind Turbines," SAND-80-2114, Sandia National Laboratories, Albuquerque, NM (USA).

[17] Raghunathan, S., Harrison, J. R., and Hawkins, B. D., 1988, "Thick Airfoil at Low Reynolds Number and High Incidence," *Journal of Aircraft*, **25** (7), pp. 669–671.

[18] Swalwell, K. E., Sheridian, J., and Melbourne, W. H., 2001, "The Effect of Turbulence Intensity on Stall of the NACA 0021 Aerofoil," *Proceedings of the14th Australasian Fluid Mechanics Conference*, B.B. Dally, ed., Adelaide University, Adelaide SA, Australia, pp. 941–944.

[19] Drela, M., 1989, "XFOIL: An Analysis and Design System for Low Reynolds Number Airfoils," *Low Reynolds Number Aerodynamics*, T. Mueller, ed., Springer Berlin Heidelberg, pp. 1–12.

[20] Du, L., Berson, A., and Dominy, R. G., 2014, "Aerofoil Behaviour at High Angles of Attack and at Reynolds Numbers Appropriate for Small Wind Turbines," Proceedings of the Institution of Mechanical Engineers, Part C: *Journal of Mechanical Engineering Science*, **229**(11), pp. 2007–2022.

[21] Du, L., Berson, A., and Dominy, R. G., 2014, "NACA0018 Behaviour at High Angles of Attack and at Reynolds Numbers Appropriate for Small Wind Turbines," ECS-TR 2014/08, School of Engineering and Computing Sciences, Durham University, Durham, UK.

[22] Garner, H. C., ed., 1966, "AGARDograph 109 - Subsonic Wind Tunnel Wall Corrections," NATO - AGARD, Paris, France.

[23] Ewald, B. F. R., ed., 1998, "AGARDograph 336 - Wind Tunnel Wall Corrections," NATO - AGARD, Neuilly-sur-Seine Cedex, France.

[24] Barlow, J. B., Rae Jr., W. H., and Pope, A., 1999, "Low-Speed Wind Tunnel Testing," John Wiley & Sons, Ltd - New York.

[25] Althaus, D., "Tunnel-Wall Corrections at the Laminar Wind Tunnel," (https://www.iag.uni-stuttgart.de/dateien/pdf/laminarwindkanal_messtechniken/ althaus_1.pdf)

[26] Althaus, D., "Measurement of Lift and Drag in the Laminar Wind Tunnel," (https://www.iag.uni-stuttgart.de/dateien/pdf/laminarwindkanal_messtechniken/ althaus_2.pdf)

[27] Holst, D., Church, B., Wegner, F., Pechlivanoglou, G., Nayeri, C. N., and Paschereit, C. O., 2018, "Experimental Analysis of a NACA 0021 Airfoil Under Dynamic Angle of Attack Variation and Low Reynolds Numbers," J Eng Gas Turb Power, **141**(3), pp. 031020-1 - 031020-10

[28] Rainbird, J. M., 2007, "The Aerodynamic Development of a Vertical Axis Wind Turbine," University of Durham, Durham, UK.

4 Clustering for dynamic analysis

The publications 3.2 to 3.4 use a simplified binning concept based on a manual selected limit dividing the data set into two different groups. Paper 3.2 already sketched the idea of an automated algorithm to divide cycles into bins. The following section introduces the method of clustering to build groups out of measurement data, which is known in literature [40–42]. The concept is applied to two selected test cases to demonstrate chances and challenges.

4.1 Clustering – The basic concept

A human is capable to identify groups or similarities quite easy by looking at data points but an algorithm needs rules and definitions to decide which data point belongs to a certain group. Figure 8 depicts random data on the left side which may be interpreted by a human into three groups. The clustering algorithm was configured to build three clusters and the result is shown on the right side of figure 8. The centroid of a cluster (**X**) is the mean of all data points (x) within the cluster and may be used for data reduction in later analysis.

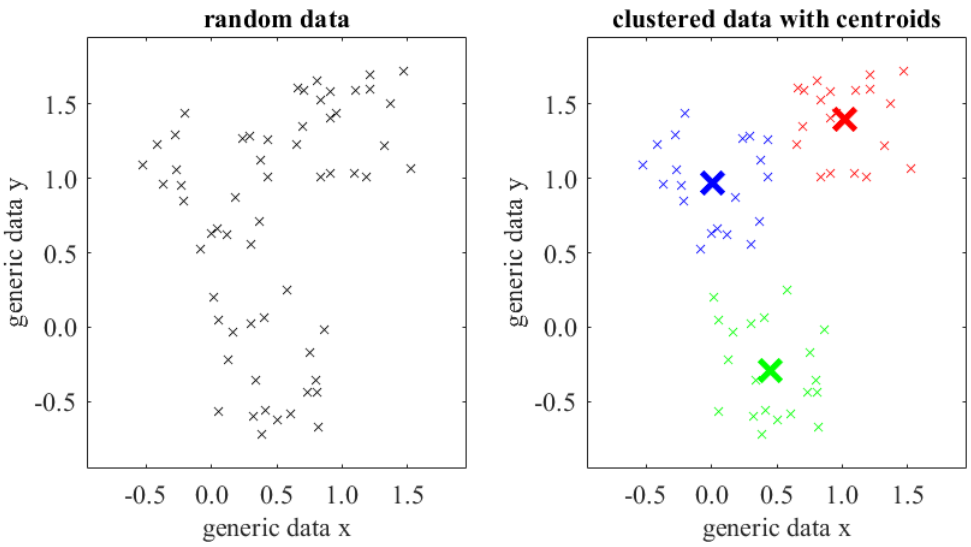

Figure 8: Concept of data clustering. Left: random data. Right: clustered data points (x) and according centroids (**X**)

The `k-means` clustering method is also known as Lloyd's algorithm [43] and analyzes a feature space s which is used to group the data points. The method analyzes the distance between the data point in s and the according cluster centroid which should be minimal while the distance between cluster centroids should be maximized. In general the squared euclidean distance is used. Lloyd's algorithm was significantly improved by Arthur and Vassilvitskii regarding running time and the quality of the final solution, which results in the `k-means++` algorithm [44]. This algorithm is a part of the *Statistics and Machine Learning Toolbox* in Matlab and can be called by `kmeans`, eq. (4-1).

$$\{\mathbf{c}_k\}_{k=1}^{K} = \texttt{kmeans}\,(s, K, \texttt{'Replicates'}, 500) \tag{4-1}$$

$$(\mathbf{c}_1, \ldots, \mathbf{c}_k) = \arg\min_{\mathcal{C}} J_w \tag{4-2}$$

Each of the N measurements in the feature space s is sorted into one of K clusters $\mathcal{C} = \{\mathcal{C}_1, \cdots, \mathcal{C}_K\}$ represented by their according centroids $\mathbf{c}_1, \ldots, \mathbf{c}_K$. The algorithm solves the minimization problem (4-2). The distances d defined by eq. (4-4) are summed up over all clusters and all elements within each cluster, and divided by the total number of elements N to define J_w in eq. (4-3).

$$J_w = \frac{1}{N} \sum_{k=1}^{K} \sum_{s \in \mathcal{C}_k} d(s, \mathbf{c}_k) \tag{4-3}$$

$$d(s, \mathbf{c}_k) = \|s - \mathbf{c}_k\|^2 = (s - \mathbf{c}_k)(s - \mathbf{c}_k)' \tag{4-4}$$

The entire process in (4-1) is configured to test 500 replicates using different initial starting centroids for grouping. This ensures that the process is able to 'escape' a local minimum and find the global minimum instead. Rerunning the algorithm will lead to the same clusters but the numbering may change. Within the results discussed in this chapter, the clusters are additionally ordered by number of elements and re-labeled. The cluster containing the most elements is the first cluster and thus the most dominant within the data set. With increasing cluster number the number of elements decreases.

`k-means++` is a general algorithm which is adopted to the actual application by defining the relevant feature space s. Different definitions of s lead to different results. Paper 3.2 introduced the binning based on a sinusoidal movement between 0 deg to 20 deg at $Re = 140\,\text{k}$. Figure 9 summarizes the results for c_l, $c_{d,p}$ and c_m for 40 cycles. While paper 3.2 focused only on lift coefficients the following clustering process additionally includes drag and moment data. The feature space includes lift, drag and moment data of the full cycle for each of the 40 repetitions, which results in eq. 4-5.

$$s = \{\vec{c}_l;\ \vec{c}_{d,p};\ \vec{c}_m\} \tag{4-5}$$

This definition of feature space is used for the following sections. The number of clusters K is set to two in figure 10 to compare the automated binning with the manual version

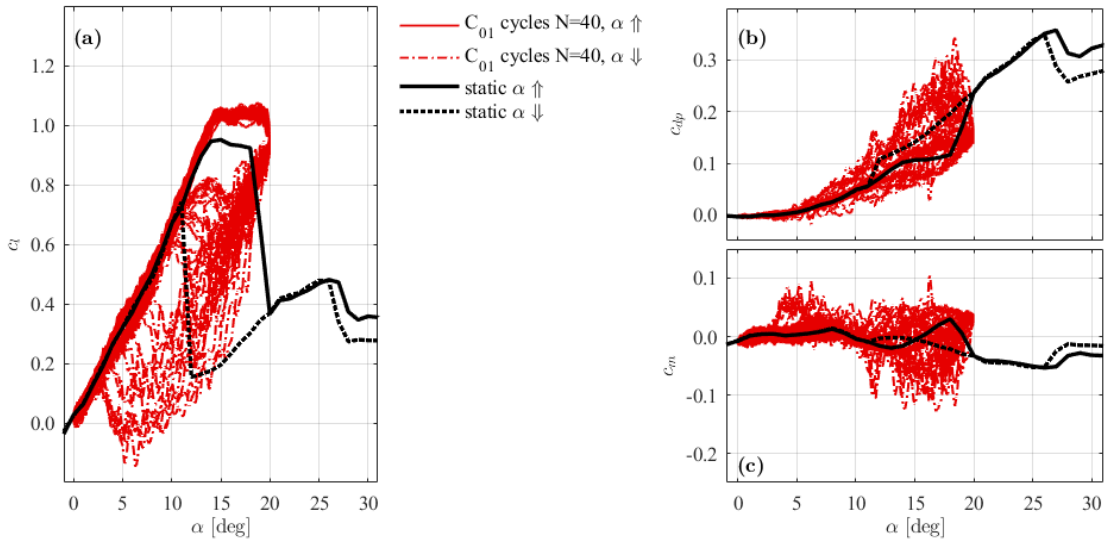

Figure 9: 40 repetitions of sinusoidal airfoil movement between 0 deg to 20 deg at $Re = 140\,\text{k}$ and $k = 0.05$

in the publications. The result is nearly identical to the publications only one cycle is put to a different bin. The deviation might be related to drag and moment data which were not part of the binning process in paper 3.2. The associated centroids are visualized in figure 11 and reveal a different aerodynamic behavior in pitch down movement. The first centroid $\mathbf{c}_1$ represents a light stall with fast reattachment. The moment stays nearly constant during the first phase of pitch down while drag is even lower than the pitch up values. The second cluster represents the fully stalled cycle with very late reattachment. The drag raises fast during the first phase of pitch down and the moment becomes negative very fast which indicates a fast collapsing suction peak in the pressure distribution of the airfoil.

Further details are revealed by the surface plot in figure 12a which visualizes the pressure coefficient relative to the cycle's phase φ (left to right) and to the normalized chord x/c

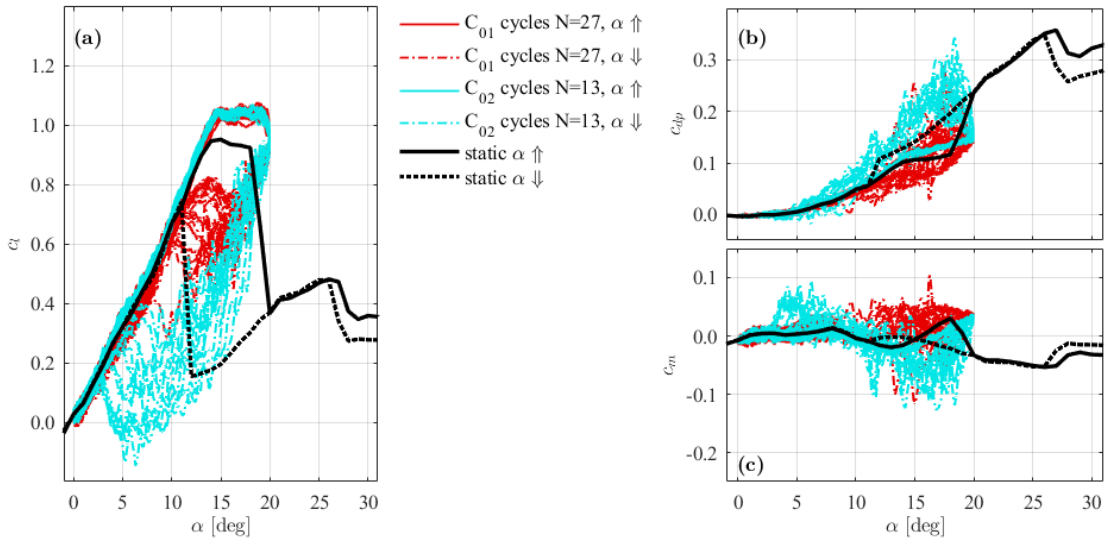

Figure 10: 40 repetitions of sinusoidal airfoil movement between 0 deg to 20 deg at $Re = 140\,\mathrm{k}$ and $k = 0.05$ separated into two clusters

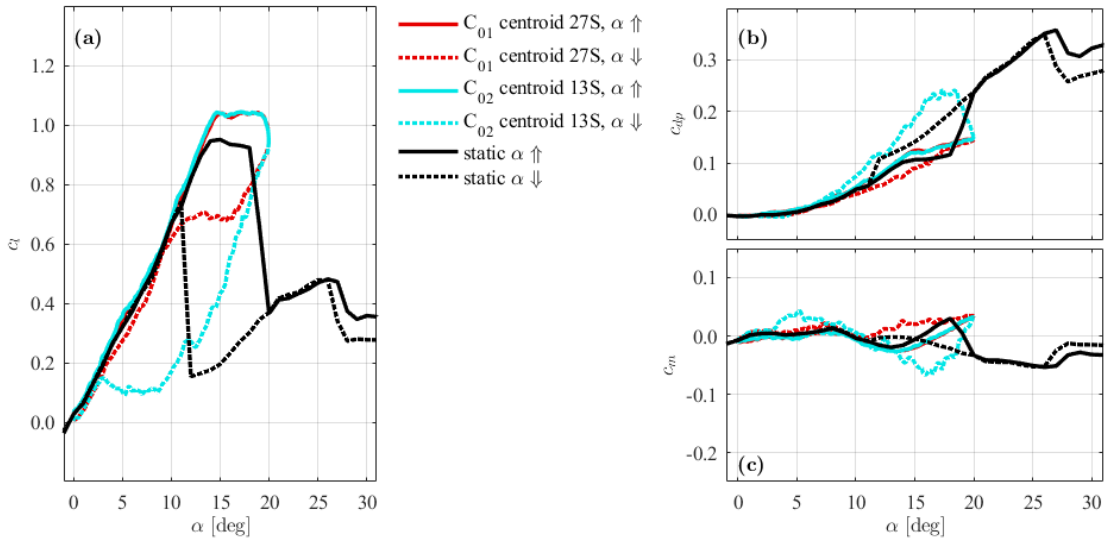

Figure 11: Two cluster centroids of sinusoidal airfoil movement between 0 deg to 20 deg at $Re = 140\,\mathrm{k}$ and $k = 0.05$

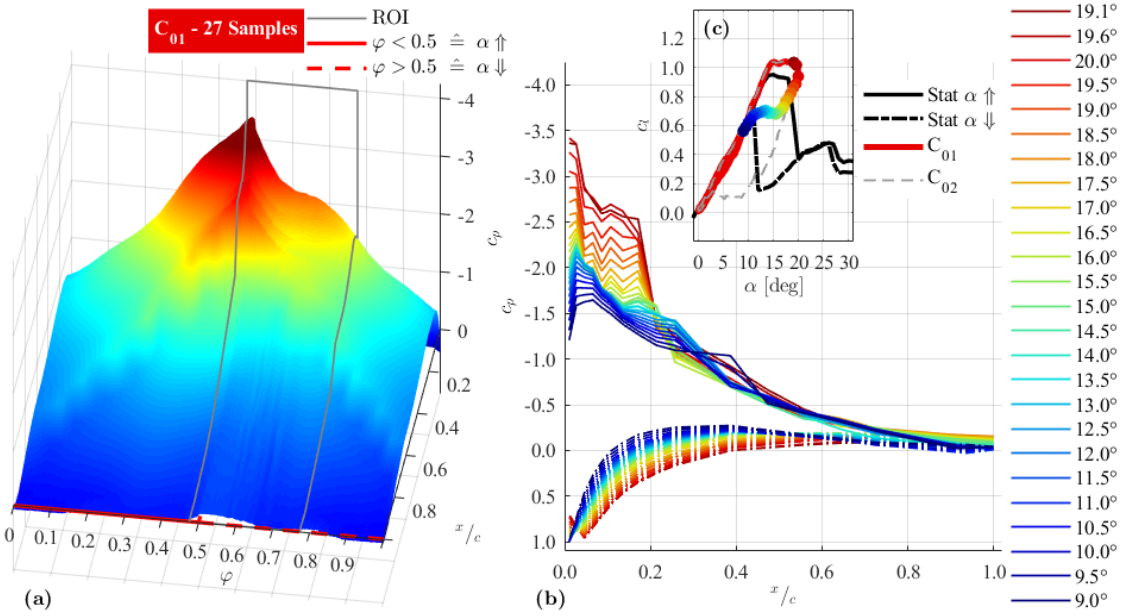

Figure 12: Cluster 1 of 2: Pressure coefficient distribution of sinusoidal airfoil movement between 0 deg to 20 deg at $Re = 140\,\text{k}$ and $k = 0.05$. **(a)** - surface plot of c_p over phase φ and x/c; **(b)** - c_p distribution over x/c; **(c)** - c_l over α with color marked angles shown in (b)

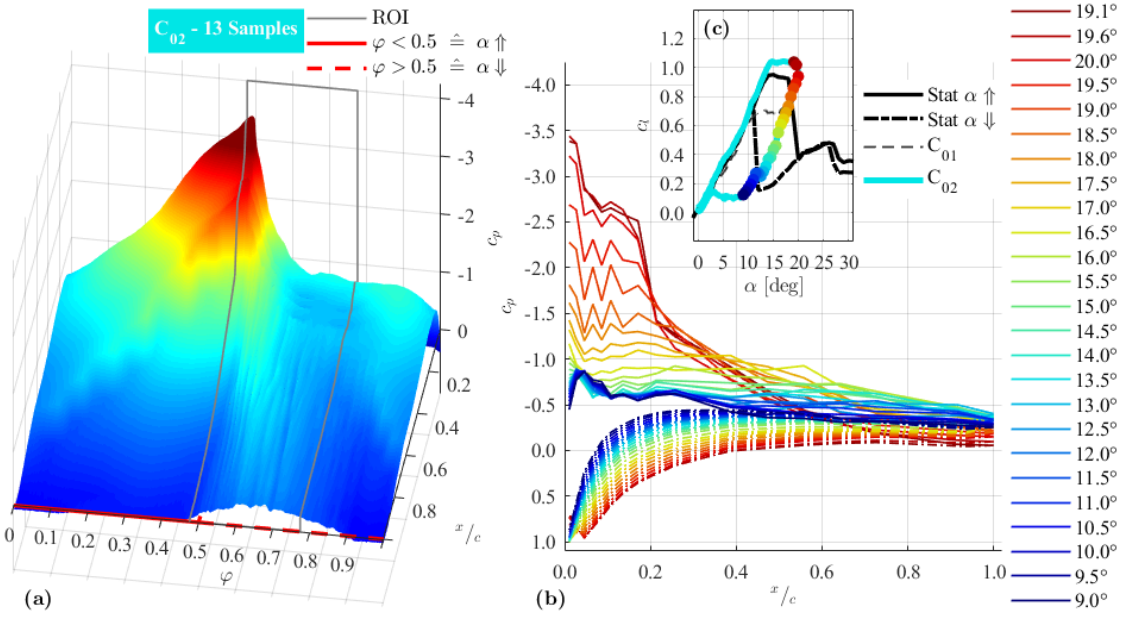

Figure 13: Cluster 2 of 2: Pressure coefficient distribution of sinusoidal airfoil movement between 0 deg to 20 deg at $Re = 140\,\text{k}$ and $k = 0.05$. **(a)** - surface plot of c_p over phase φ and x/c; **(b)** - c_p distribution over x/c; **(c)** - c_l over α with color marked angles shown in (b)

(back to front) at the same time. The leading edge is at $x/c = 0$ and the trailing edge at $x/c = 1$. This way of plotting enables the reader to identify even small changes in the TE area. The phase includes pitch up ($\varphi < 0.5$) as well as pitch down ($\varphi > 0.5$) and may be interpreted as a kind of 'time'. The section labeled ROI (region of interest) in figure 12a marks the part of phase investigated in figure 12b in more detail. The plot shows the classical pressure distribution over x/c for selected incidences in the ROI. The data points are marked at the corresponding angles with identical colors in the additional lift polar in figure 12c. The entire figure 12 provides insights into the data of the centroid $\mathbf{c}_1$ which is an average of 27 cycles belonging to cluster $\mathcal{C}_1$. The light stall with fast reattachment of centroid $\mathbf{c}_1$, which was mentioned earlier, is caused by a gradually reduced suction peak near LE during pitch down. Nonetheless, a suction peak is always present. The separation bubble visible in figure 12b moves towards TE but does not burst. A light TE-stall is detectable in figure 12a which may have been missed in 12b.

The second centroid's $\mathbf{c}_2$ data are depicted in figure 13 and multiple differences become obvious if compared to figure 12. The suction peak breaks down and a TE stall starts. The separation bubble moves downstream until the bubble bursts finally potentially triggered by the TE stall moving upstream. Consequentially the airfoil fully stalls and the flow does not reattach within the region of interest.

Manual binning was used within the publications in chapter 3 and the proposed automated solution in this chapter works to reproduce the manual version. The real advantage of automated solutions can be used by analyzing the same data set with different numbers of clusters.

The 40 repetitions previously shown in figure 9 indicate that intermediate flow conditions between light and full stall could be revealed if the repetitions are divided into more than just two clusters. Increasing the number of clusters K diminishes the statistical significance of each cluster if the number of included elements is reduced. Thus, the number of clusters K should be at least an order of magnitude lower than the number of elements N to be binned. The 40 repetitions available are not enough to analyze multiple clusters with full statistical significance but sufficient to show the capabilities of the method. The results to be discussed in the test cases have to be validated in future rerunning the experiments with an increased number of cycles.

4.2 Test case: Separate intermediate flow cases

The data was previously divided into groups of 27 and 13 cycles with just two clusters. Nonetheless, more than just two groups may be identified in figure 9a by concentrating on the reattachment angles. The former cluster $\mathbf{c}_1$ in figure 10 could be divided into three subgroups and $\mathbf{c}_2$ in up to four, which results in up to six or seven different flow states in total.

The binning method is expected to put six or seven elements in each cluster if the data of 40 repetitions is evenly distributed but the previous clustering indicated quite the contrary. Figure 14 visualizes the result of a `k-means++` clustering with $K = 7$. The first two clusters incorporate more than half of the cycles. The remaining clusters contain two to five cycles each, which is obviously not enough to be statistically valid as previously discussed. However, this is not relevant to test if `k-means++` is capable of separating intermediate flow cases. The centroids in figure 15 represent clearly seven different cases. The previous chapter's light stall case is substituted by three clusters $\mathbf{c}_1$, $\mathbf{c}_2$ and $\mathbf{c}_5$. The reader should keep in mind that the cluster sorting bases on the number of elements included. The algorithm divided the former full stall case into four subgroups. Centroids $\mathbf{c}_6$, $\mathbf{c}_3$ and $\mathbf{c}_7$ represent different angles of reattachment. The last centroid $\mathbf{c}_4$ is quite

similar to $\mathbf{c}_7$ but with a different size of hysteresis loop. The differences in lift polar are more pronounced than in drag and moment for all four full stall cases. The three light stall centroids show clear differences in drag and moment during pitch down. $\mathbf{c}_1$ has a reduced drag and increased moment compared to pitch up during the first 30 % of pitch down. The second centroid $\mathbf{c}_2$ represents a case that follows the pitch up polar first but after three degrees of pitch down movement the drag decreases and moment increases comparable to $\mathbf{c}_1$ but with delay. The last light stall centroid $\mathbf{c}_5$ has increased drag during the first five degrees of pitch down but decreases afterward compared to the pitch up values. The moment polar show a converse development: A decrease first and an increase afterward.

The pressure surface plots provide information for a more detailed discussion. Cluster centroid's $\mathbf{c}_1$ pressure data in figure 16 reveals that the flow is attached during the entire pitch down phase. Obviously the separation bubble is present all the time but this is

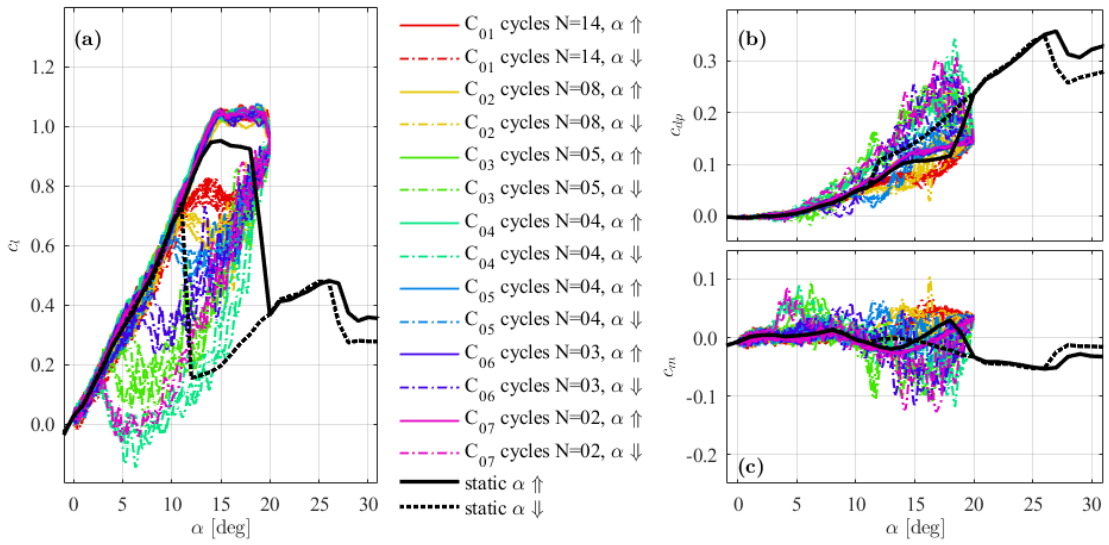

Figure 14: 40 repetitions of sinusoidal airfoil movement between 0 deg to 20 deg at $Re = 140\,\text{k}$ and $k = 0.05$ separated into seven clusters

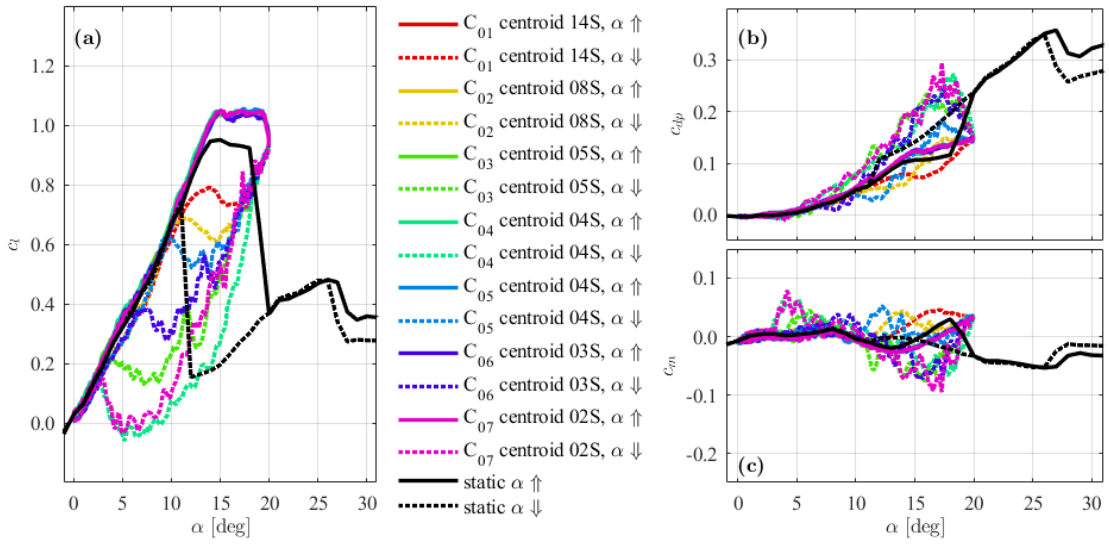

Figure 15: Seven cluster centroids of sinusoidal airfoil movement between 0 deg to 20 deg at $Re = 140\,\text{k}$ and $k = 0.05$

typical for thick airfoils [22]. The suction peak is continuously reduced during pitch down but always present and without abrupt changes. A light TE stall is visible in figure 16a but the flow reattaches quickly during the pitch down movement. $\mathbf{c}_1$ differs from the more general two cluster approach in figure 12 showing the light stall. However, the second cluster $\mathbf{c}_2$ data shown in figure 17 represent the flow situation already discussed in the previous section. An abrupt drop in the suction peak is apparent but the peak does not

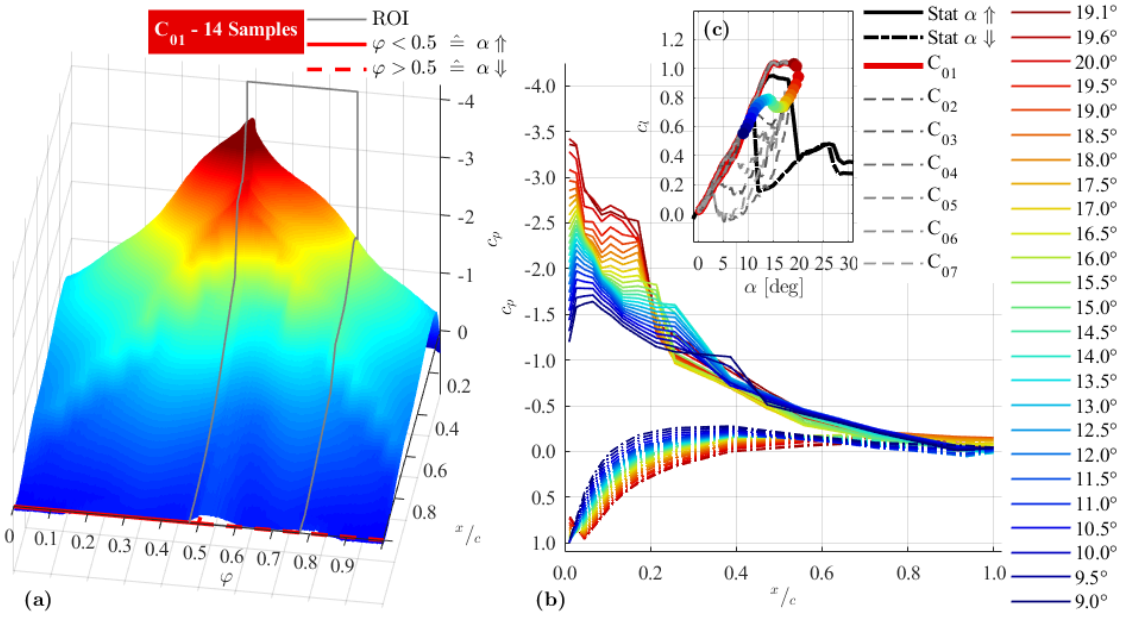

Figure 16: Cluster centroid 1 of 7: Pressure coefficient distribution of sinusoidal airfoil movement between 0 deg to 20 deg at $Re = 140\,\text{k}$ and $k = 0.05$. **(a)** - surface plot of $c_p(\varphi, x/c)$; **(b)** - $c_p(x/c)$ distribution; **(c)** - $c_l(\alpha)$ with color marked angles shown in (b)

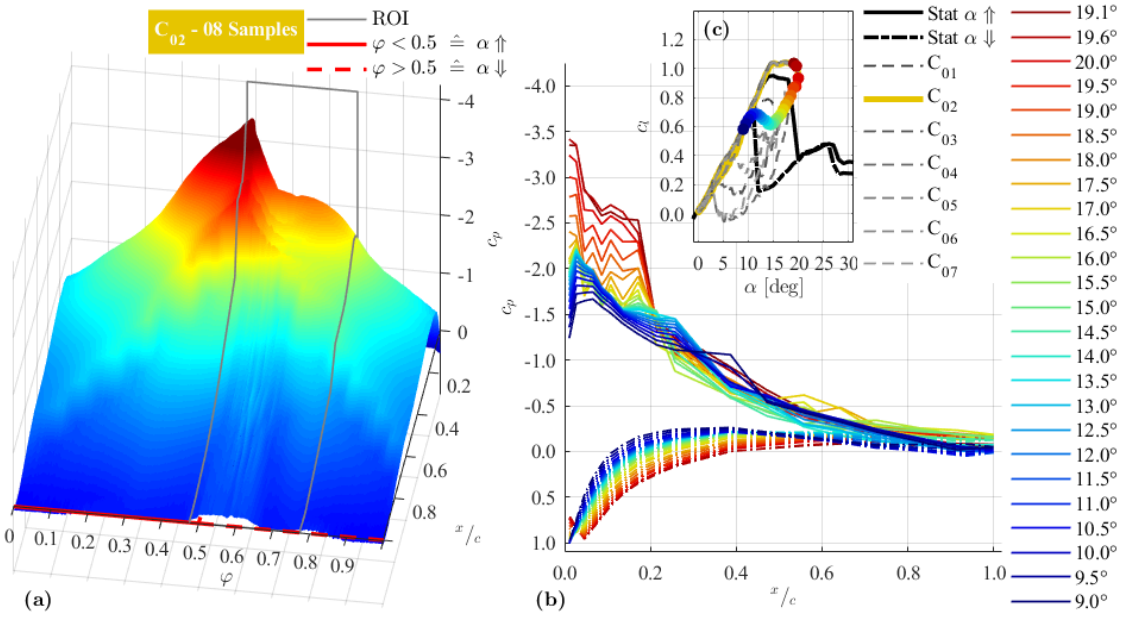

Figure 17: Cluster centroid 2 of 7: Pressure coefficient distribution of sinusoidal airfoil movement between 0 deg to 20 deg at $Re = 140\,\text{k}$ and $k = 0.05$. **(a)** - surface plot of $c_p(\varphi, x/c)$; **(b)** - $c_p(x/c)$ distribution; **(c)** - $c_l(\alpha)$ with color marked angles shown in (b)

fully disappear. The TE separation is more pronounced compared to $\mathbf{c}_1$ and first signs of vortices traveling downstream are visible in the range of $\varphi \in [0.5, 0.6]$ and $x/c > 0.6$. The streaks of lighter blue indicate areas of less pressure which may be pressure footprints induced by vortices [22]. This is even more pronounced in figure 18a which belongs to centroid $\mathbf{c}_5$. This phase range with high pressure fluctuations matches the range of higher drag discussed previously in figure 15. The drop of the suction peak is more severe for $\mathbf{c}_5$

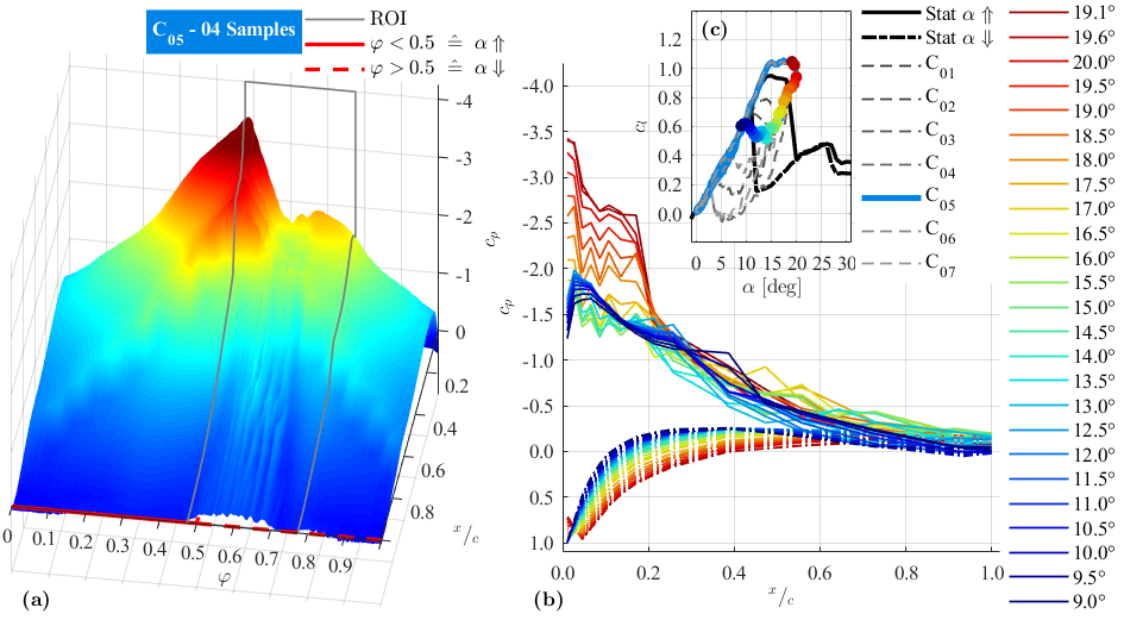

Figure 18: Cluster centroid 5 of 7: Pressure coefficient distribution of sinusoidal airfoil movement between 0 deg to 20 deg at $Re = 140\,\text{k}$ and $k = 0.05$. **(a)** - surface plot of $c_p(\varphi, x/c)$; **(b)** - $c_p(x/c)$ distribution; **(c)** - $c_l(\alpha)$ with color marked angles shown in (b)

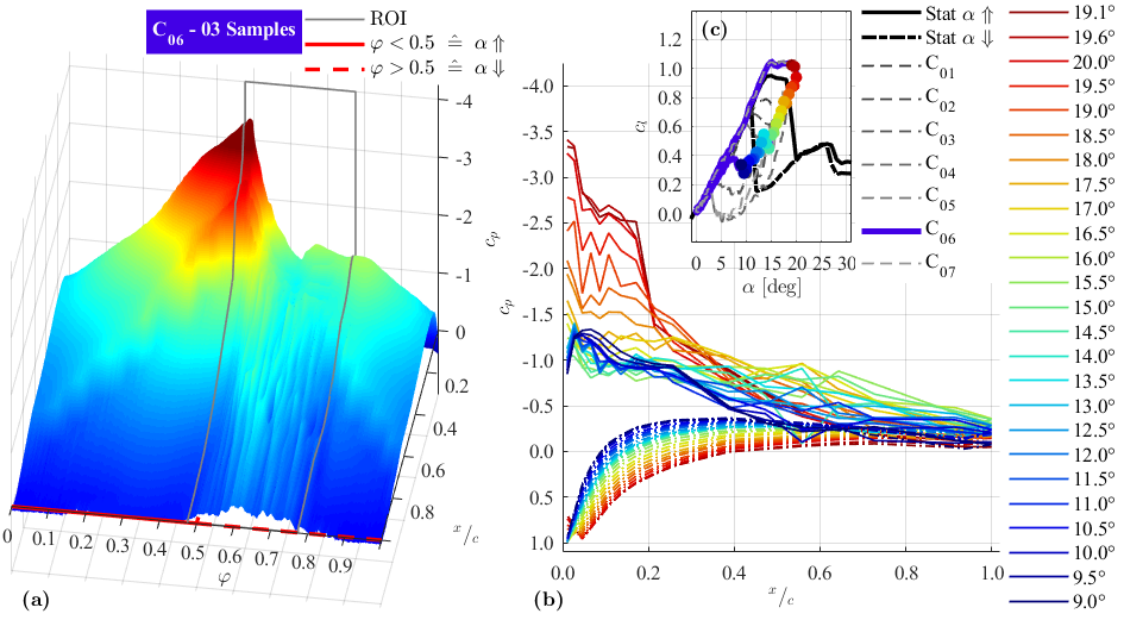

Figure 19: Cluster centroid 6 of 7: Pressure coefficient distribution of sinusoidal airfoil movement between 0 deg to 20 deg at $Re = 140\,\text{k}$ and $k = 0.05$. **(a)** - surface plot of $c_p(\varphi, x/c)$; **(b)** - $c_p(x/c)$ distribution; **(c)** - $c_l(\alpha)$ with color marked angles shown in (b)

during pitch down but recuperates in the range of $\varphi = 0.7$. This recuperation leads to a reduction in drag and results additionally in an increase in moment when combined with a flow reattachment at the trailing edge. The centroid $\mathbf{c}_5$ may be seen as a border case next to the full stall, the flow nearly detaches but re-stabilizes with further decreasing AoA.

The remaining centroids $\mathbf{c}_6$ (Fig. 19), $\mathbf{c}_3$ (Fig. 20), $\mathbf{c}_7$ (Fig. 21), and $\mathbf{c}_4$ (Fig. 22) visualize different stages of stalled flow during pitch down movement. A rest of flow re-stabilization

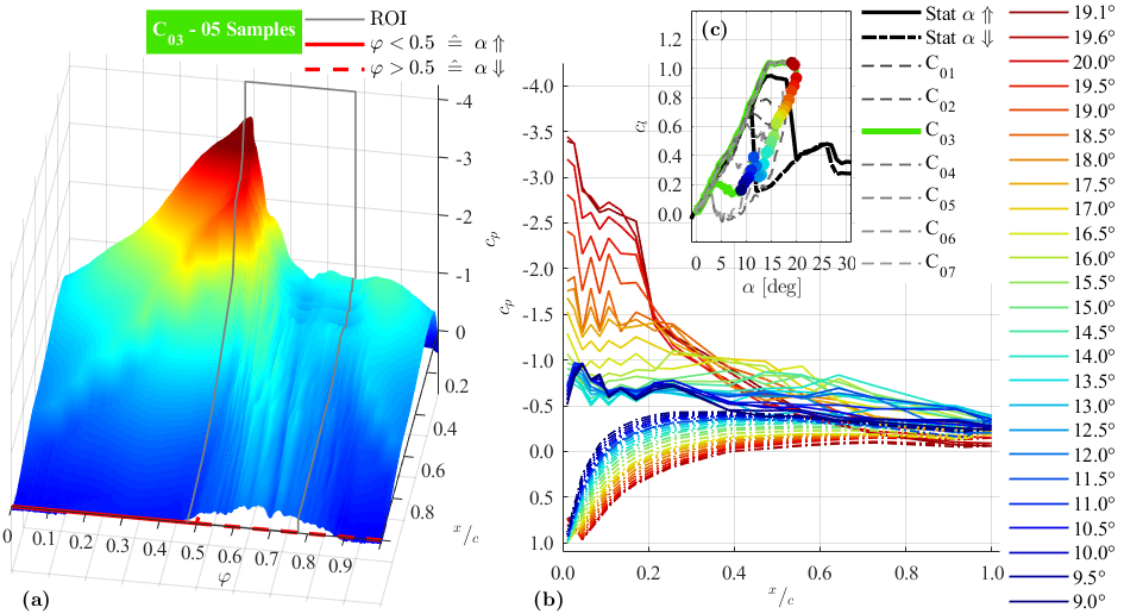

Figure 20: Cluster centroid 3 of 7: Pressure coefficient distribution of sinusoidal airfoil movement between 0 deg to 20 deg at $Re = 140\,\text{k}$ and $k = 0.05$. **(a)** - surface plot of $c_p(\varphi, x/c)$; **(b)** - $c_p(x/c)$ distribution; **(c)** - $c_l(\alpha)$ with color marked angles shown in (b)

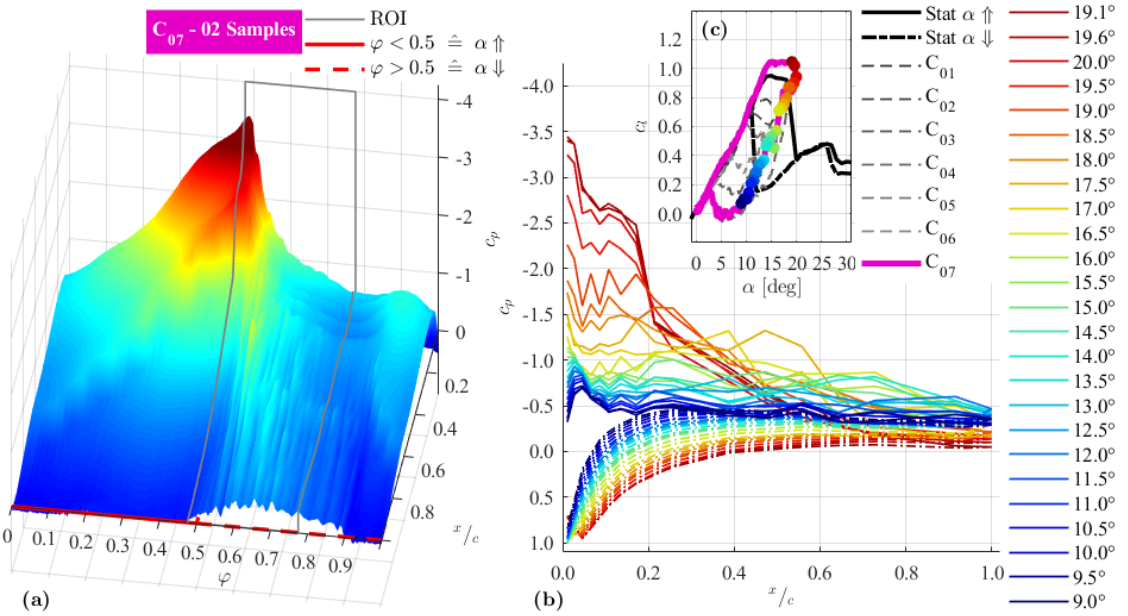

Figure 21: Cluster centroid 7 of 7: Pressure coefficient distribution of sinusoidal airfoil movement between 0 deg to 20 deg at $Re = 140\,\text{k}$ and $k = 0.05$. **(a)** - surface plot of $c_p(\varphi, x/c)$; **(b)** - $c_p(x/c)$ distribution; **(c)** - $c_l(\alpha)$ with color marked angles shown in (b)

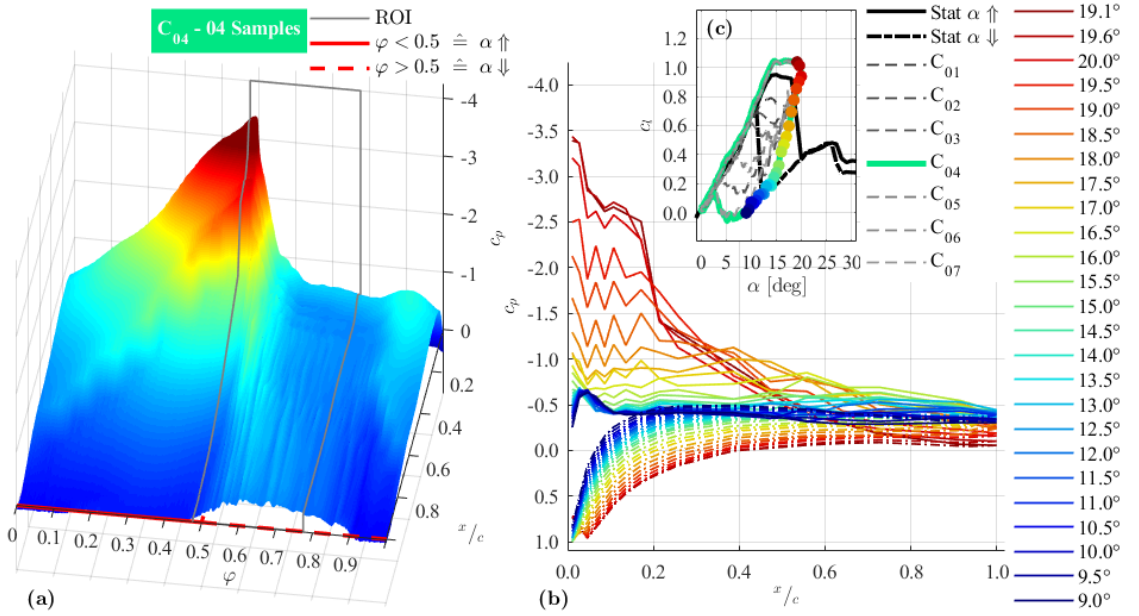

Figure 22: Cluster centroid 4 of 7: Pressure coefficient distribution of sinusoidal airfoil movement between 0 deg to 20 deg at $Re = 140\,\text{k}$ and $k = 0.05$. **(a)** - surface plot of $c_p(\varphi, {}^{x}/_{c})$; **(b)** - $c_p({}^{x}/_{c})$ distribution; **(c)** - $c_l(\alpha)$ with color marked angles shown in (b)

may be seen for $\mathbf{c}_6$ in figure 19a which is not strong enough to compensate the increased drag caused by the high pressure fluctuations. The others are dominated by separated flows and pressure fluctuations moving towards the trailing edge. The c_p curves for 19 deg to 17 deg in figure 21b illustrate the vortex induced pressures traveling downstream. The difference in lift between the centroids $\mathbf{c}_7$ and $\mathbf{c}_4$ was just a larger hysteresis loop for $\mathbf{c}_4$. The lift decreased more during pitch down. Figure 22 indicates a leading edge stall without any local reattachment while the centroid $\mathbf{c}_7$ in figure 21 represents flow cases which hold at least a small suction peak. This results in a slightly increased lift compared to $\mathbf{c}_4$.

Finally, the present test case demonstrated the capabilities of the `k-means++` algorithm to separate intermediate flow cases. Some of the clusters may represent different intermediate phases of the same flow state. The clusters have shown major differences and the resulting centroids can be used to discuss the according aerodynamics. Nonetheless, the available number of 40 cycles is not enough to get a statistical valid number of elements in each cluster. The test underlines the requirement of a number of repetitions that is adequate to the requested number of clusters.

4.3 Test case: Clustering highly fluctuating data

The previous test case analyzed a data set in which possible groups can be also identified manually. The next data set is more volatile and a binning may not be done just by setting a limit. The paper 3.1 has identified regions of very high standard deviation. Figure 23a is a reprint of an according graph showing the baseline polars. The reader should keep in mind that the single measurement at each incidence was conducted without any movement and the angle was changed between two measurements. The high standard deviation in the range of 140-160 deg during pitch down indicates a very dynamic flow. The region is additionally noteworthy because the investigation of the dynamics in publication 3.2 have revealed oscillations with an amplitude in the order of maximum lift during pitch down. Figure 23b shows 20 repetitions of full range cycles.

Both graphs in figure 23 emphasize the suitability of this AoA range for the current test case. The `k-means++` algorithm was used to divide the 20 cycles shown in figure 23b into three clusters. The resulting centroids are plotted in figure 24 but with a reduced AoA range of 90-180 deg. The first centroid $\mathbf{c}_1$ represents 14 cycles whereas $\mathbf{c}_2$ and $\mathbf{c}_3$ contain just three cycles each. Obviously cycles with high fluctuations were outsourced into these two clusters. The second centroid $\mathbf{c}_2$ has a larger drag and lower moment in the range of 120 deg compared to $\mathbf{c}_3$. Nevertheless, the graphs in figure 24 are not suitable to analyze the source of the fluctuations.

Figure 25 shows the surface plot of centroid $\mathbf{c}_1$. The reader should keep in mind that in this data set $\varphi = 0.125$ corresponds to $\alpha = 45$ deg and consequentially $\varphi = 0.5$ to

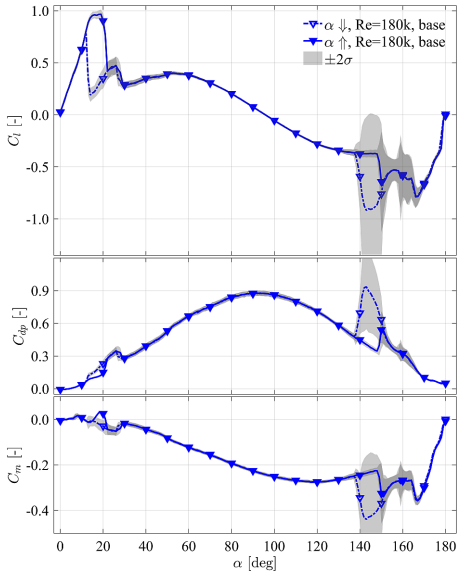

(a) Static investigation with standard deviation (figure reprint from paper 3.1)

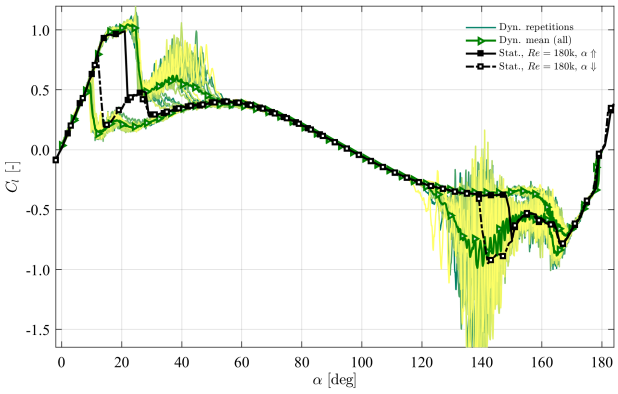

(b) Dynamic cycles at $k = 0.0025$ (figure reprint from paper 3.2)

Figure 23: Polars between 0 deg to 180 deg at $Re = 180$ k

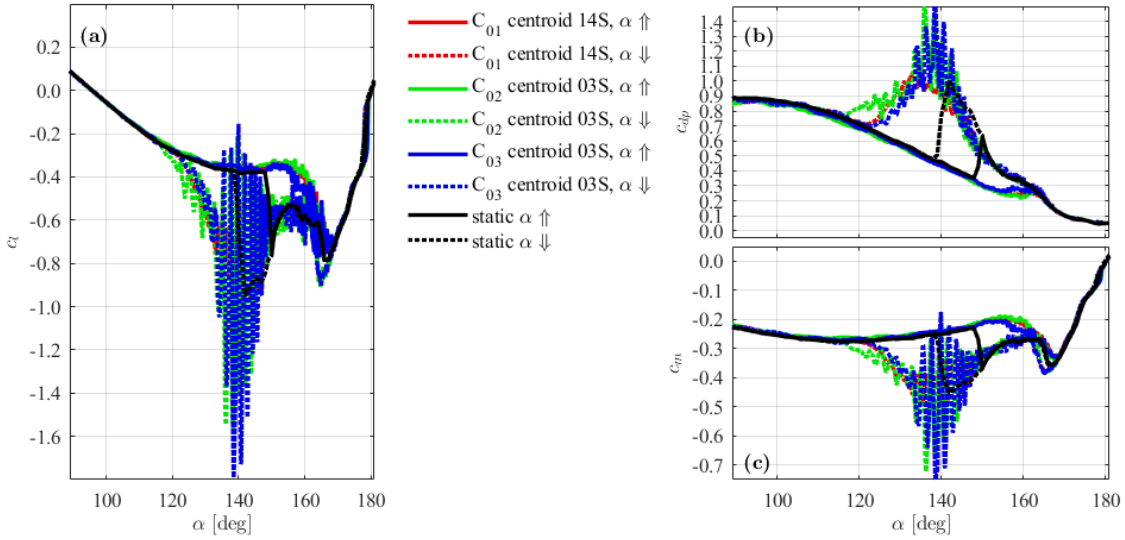

Figure 24: Three cluster centroids of sinusoidal airfoil movement between 0 deg to 180 deg (90 deg to 180 deg shown) at $Re = 180$ k and $k = 0.0025$

$\alpha = 180\,\text{deg}$. The pressure distribution during pitch up ($\varphi < 0.5$) shows the series of flow states which are expected for a full 180 deg movement: Starting with attached flow and a high suction peak ($\varphi \approx 0.06$); stalling ($\varphi \in [0.07, 0.15]$); a nearly constant pressure level over chord x/c in deep stall (e.g. $\varphi = 0.25$) and finally a small suction peak near TE ($\varphi \approx 0.47$). At this phase the airfoil is nearly upside down. The TE is pointing upstream

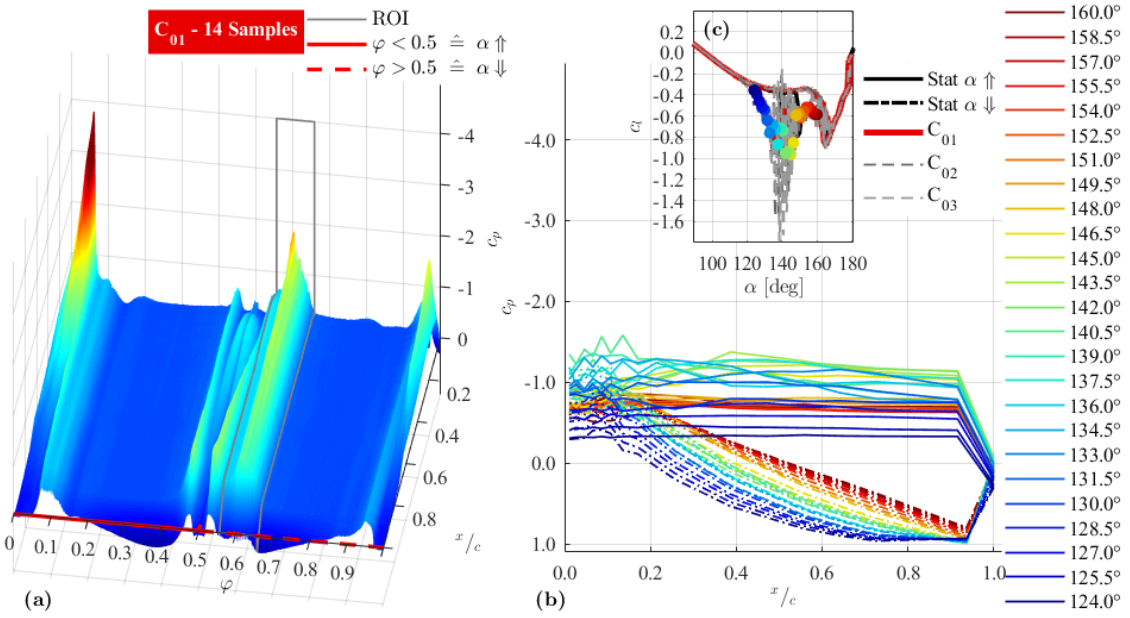

Figure 25: Cluster centroid 1 of 3: Pressure coefficient distribution of sinusoidal airfoil movement between 0 deg to 180 deg (focus on 90 deg to 180 deg) at $Re = 180\,\text{k}$ and $k = 0.0025$. **(a)** - surface plot of $c_p(\varphi, x/c)$; **(b)** - $c_p(x/c)$ distribution; **(c)** - $c_l(\alpha)$ with color marked angles shown in (b)

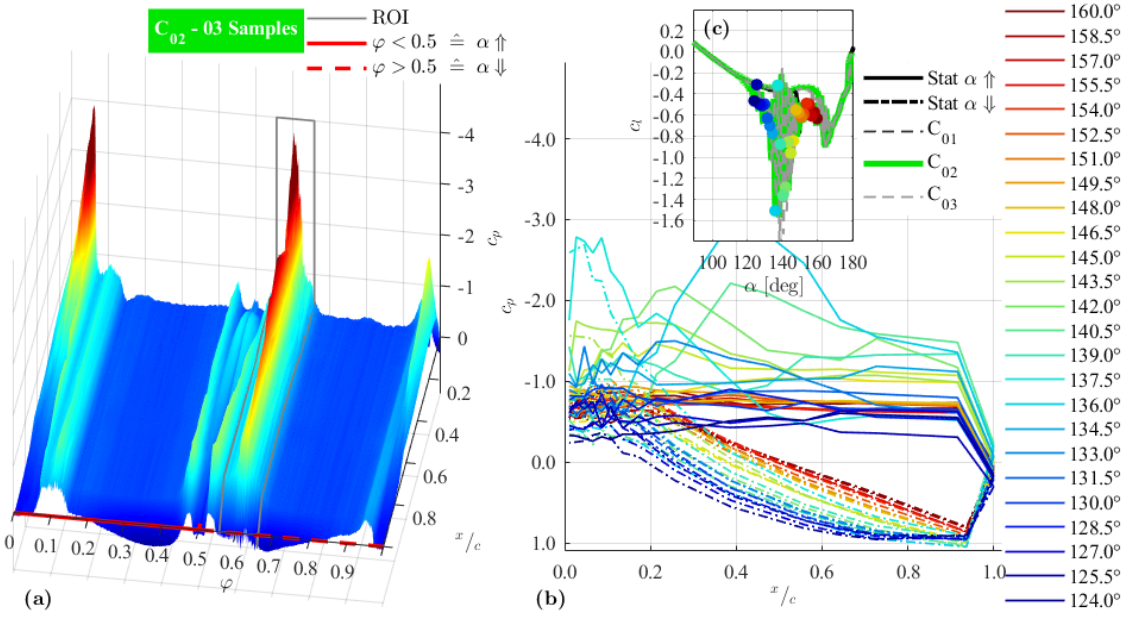

Figure 26: Cluster centroid 2 of 3: Pressure coefficient distribution of sinusoidal airfoil movement between 0 deg to 180 deg (focus on 90 deg to 180 deg) at $Re = 180\,\text{k}$ and $k = 0.0025$. **(a)** - surface plot of $c_p(\varphi, x/c)$; **(b)** - $c_p(x/c)$ distribution; **(c)** - $c_l(\alpha)$ with color marked angles shown in (b)

and may be interpreted as sharp leading edge and the airfoil's nose is pointing downstream. The first phase of pitch down ($\varphi \in [0.50, 0.55]$) is comparable to the corresponding pitch up range ($\varphi \in [0.45, 0.50]$).

The ROI marked in figure 25a covers a range of incidence $\alpha \in [160, 124]$ deg which matches the area of high fluctuations discussed in the beginning of the section. An increased suction near the airfoil's LE seems to cause the fluctuations in lift. The c_p distribution in figure 25b indicates flow structures inducing a footprint with reduced pressure which are traveling downstream. At this AoA downstream is equivalent to a flow from TE to LE. However, centroid $\mathbf{c}_1$ obviously does not include the cases with extreme fluctuations but represents the general flow. The `k-means++` algorithm built clusters two and three by grouping the cycles with more dominant fluctuations. The centroids $\mathbf{c}_2$ in figure 26 and $\mathbf{c}_3$ in figure 27 show unexpected high suction peaks during pitch down. $\mathbf{c}_2$ reaches the pressure levels of attached flow ($\varphi \approx 0.06$) and $\mathbf{c}_3$ even exceeds these values. These regions of reduced pressure are not fixed in chord wise position but continuously washed downstream. Figures 26b and 27b impressively visualize this. A detailed discussion what flow phenomenon causes these fluctuations can not be based on pressure data only and therefor needs further experiments focusing on the flow around the airfoil, e.g., particle image velocimetry. Nonetheless, it is likely that these low pressure regions are caused by strong vortices passing the airfoils surface [22].

The detailed flow analysis is not scope of this test case, however, the `k-means++` algorithm seems to be capable of analyzing highly volatile data sets. Clusters built by `k-means++` differ significantly among each other. Accordingly the algorithm is promising to contribute to future dynamic analysis but in the context of the data covered in the publications 3.1 to 3.4 the number of repetitions available is not large enough.

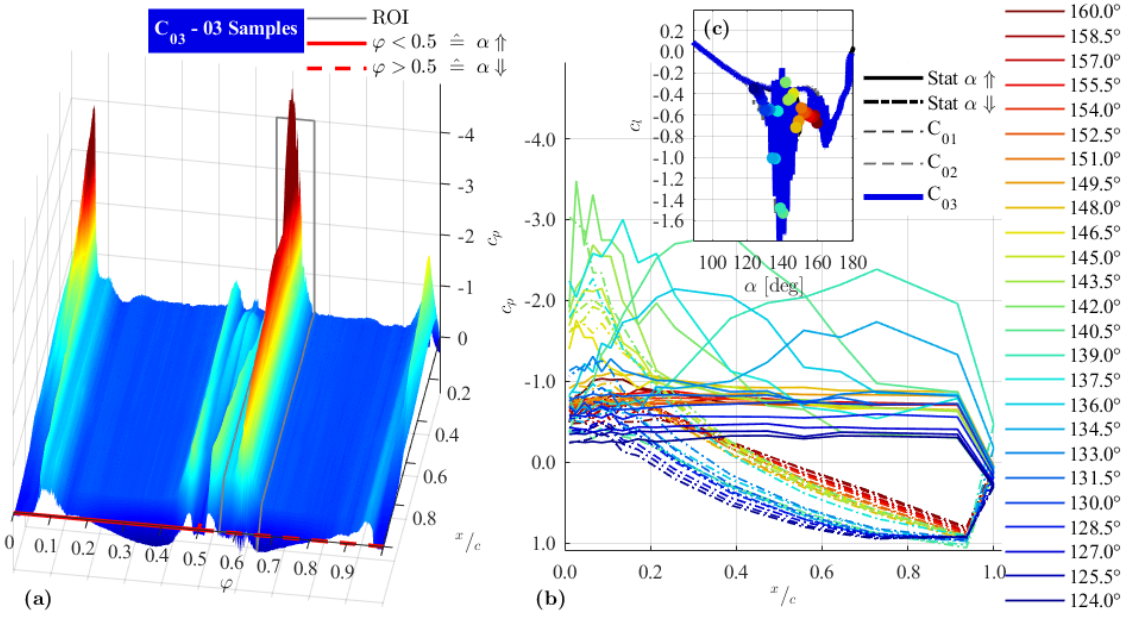

Figure 27: Cluster centroid 3 of 3: Pressure coefficient distribution of sinusoidal airfoil movement between 0 deg to 180 deg (focus on 90 deg to 180 deg) at $Re = 180\,\mathrm{k}$ and $k = 0.0025$. **(a)** - surface plot of $c_p(\varphi, x/c)$; **(b)** - $c_p(x/c)$ distribution; **(c)** - $c_l(\alpha)$ with color marked angles shown in (b)

5 Concluding discussion

Each of the publications presented in chapter 3 had their specific focus and the idea of automated binning discussed in paper 3.2 was implemented and tested in the previous chapter 4. Nonetheless, the overarching context will be given by the following chapter. In the beginning, the analysis of challenges solved on the way and possible improvements of the setup are discussed. Subsequently, a more detailed review of the selected inflow conditions for potential applications in wind energy is given and followed by the overarching discussion of results. The chapter is concluded by presenting ideas for future work and projects.

5.1 Challenges and possible improvements

Generally speaking, every experimental setup unveils its challenges only over time. The parameters, e.g., inflow conditions, may be chosen carefully and accurately in advance but some details will end up as lessons learned over time. The following section presents selected details that may be of interest for similar setups or future extensions.

Pressure calibration and measurement

The pressure sensor's accuracy is crucial to all measurements presented as all force coefficients are based on surface pressure. The differential sensors used within this thesis, contain a membrane, whose deflection creates a measure for the pressure difference. Gravity has an influence on the deflection and thus the method of mounting the sensors is of grave significance if the sensor is placed within a moving system. This gravitational influence should be minimized as much as possible. In this regard, the sensors were mounted in a fixed direction that ensures the membrane is parallel to the rotational plane. However, it is not possible to align any two sensors in exactly the same way, thus the calibration procedure needs to minimize the systematic influences of the sensor alignment. This is one of the main challenges, with typical effects to address: sensor specific gain, inertia effects in dynamic movements, and signal drift.

The sensor specific gain is checked on a daily basis using a pressure calibrator covering the full sensor range. This covers multiple aspects: firstly the gain of each sensor in $^{\mathrm{Pa}}/_{\mathrm{V}}$, secondly the daily check for linearity; and finally, the check for sensor failure. The calibration process needs to account for inertia effects in the dynamic system. Consequentially no-flow readings were acquired for each measurement. Important to note that it has to be the actual AoA profile of interest including all predefined movements. This results in a phase dependent correction representing, i.e., gravity influence caused by sensor misalignment or inertia effects on the sensor's membrane caused by different magnitudes of acceleration. This AoA based calibration is necessary at least once for every motion profile but was done in advance of every measurement series in the present experiments. Consequentially, changes in dynamic sensor behavior, e.g., loose sensors, may be detected. The impact of signal drift can be ignored for short measurements in the order of minutes if a signal offset was acquired in advance. The offset measurement was performed at no-flow conditions. Accordingly, the differential pressure of each sensor has to be zero. This series of calibrations reduce the systematical influence inherent in the final experiments.

A dynamic pressure calibration was not done because no adequate system was available. A dynamic in-situ calibration from every single pressure tap to the according sensor would be a significant improvement because the resulting transfer functions could be used to recalculate the original surface pressure signals without the system's inherent frequency dependent damping of amplitudes and phase shift. The influence on amplitude and phase

can be estimated which was previously discussed in chapter 2, i.e., in figure 4, but this estimation is not good enough to be a basis for a signal correction.

The differential sensors consequentially need a reference pressure to build the 'difference'. The inflow's static pressure was used as reference in the present studies and was provided by a Prandtl tube which was additionally used to acquire the inflow velocity. The position of the Prandtl tube is a compromise between a representative measurement and a minimized flow disturbance. This resulted in a position in the potential core of the open jet but on the pressure side of the airfoil which is less sensitive to upstream disturbances. Nonetheless, it is still a single point measurement which is sensitive to local velocity changes not representative for the entire flow field. A more integral measurement would be preferable in future. If multiple pressure taps are interconnected over the circumference each at the nozzle's inlet and outlet, the differential pressure between both positions can be used for integral velocity measurements. Prandtl tube and nozzle differential pressure could be used redundantly to detect sensor failures. Unfortunately, the implementation of such system was prevented by external constraints. Nevertheless, the implementation is recommended and should get high priority if the external restrictions are removed.

Mechanics

Even if a setup is 'only' redesigned or built from scratch, mechanical challenges will occur. The more moving parts and electric cables exist the higher the risk of failure. This is not limited to structural failure but small deviations in the setup may cause mechanical damage. The present setup is designed to coil the sensor cables on the cylinders for up to two revolutions during the dynamic tests. A misalignment in cable management resulted in squeezing some sensor cables and lead to damages of cable insulation. Squeezing is even worse, if it affects the reference pressure tubing which has to be connected to the differential sensors within the rotating system. The result is a misleading pressure signal. At first sight, the pressure distribution looks plausible and may be interpreted as an effect of 'history of movement', discussed in paper 3.1. Unfortunately, an extended data analysis has shown after publication, that the effect was caused by mechanical influences on the tubing of the reference pressure. The beginning and the end of the disturbance was identified within the data sets. Thus, the data of $Re_c = 100\,\mathrm{k}$ in paper 3.1 is, therefore, at least questionable but fortunately represents only a small part of the content presented in paper 3.1. Nonetheless, the other publications are not affected because they were limited to two Reynolds numbers excluding the faulty case.

The installation of the airfoil into the test stand is an important step and contains several challenges. The wing is a structural part of the setup. The splitter plates are screwed to the airfoil section and the cylinders left and right of the splitter plates interconnect the wing finally with the bearings and the motor. Thus, all loads are transferred through the section. This is a weakness of the setup because the airfoil model is exposed to high bending moments and torsional stresses due to the mass and mass inertia of cylinders, splitter plates, and airfoil, which is thin compared to the rest. Consequentially, a redesign of the setup should consider decoupling the airfoil from splitter plates and cylinders. The structural loads on the airfoil section would be reduced but a gap between splitter plates and airfoil is necessary if the airfoil rotates between fixed plates. The flow through the gap would influence the pressure distribution on the airfoil, which is not the case for the current setup, because the splitter plates are screwed to the airfoil without any gap. Nonetheless, the decoupling would allow an extension of the measurement setup. A balance measuring lift and drag would improve a future setup by providing integral measurements

in addition to the local pressure distributions. The drag measurement would be of interest in particular because a balance measurement would include the friction drag, which cannot be measured by surface pressure measurements.

The definition of $\alpha = 0\,\text{deg}$ is an additional challenge during the installation process of the airfoil. The coupling, which connects the motor unit with the cylinder-plate-airfoil unit, allows radial variations during the mounting process and will be fixed by tightening the clamp. The zero angle is defined manually using a spirit level and a template matching the suction side of the airfoil. However, the incidence is aerodynamically relative to the inflow and not based on the spirit level. An automated definition of $\alpha = 0\,\text{deg}$ could be of interest in the future. The AoA with zero lift could be a definition for symmetrical airfoils or if the airfoil provides two pressure taps at the same chord-wise position in the first quarter on the suction and pressure side. The differential pressure between both taps should be zero if the flow around the airfoil is identical on pressure and suction side.

Data post processing – cycle detection

The definition of $\alpha = 0\,\text{deg}$ in the previous paragraph is just the preparation for the experiments. Dynamic measurements consist of multiple continuous cycle repetitions. Accordingly, the data acquisition samples continuously and the post processing has to distinguish each cycle from another. A simple idea would be to split the samples acquired into a number of sections equal to the number of repetitions. Unfortunately, this results in a higher AoA deviation because this method does not account for small inter-cycle differences. Another idea could focus on the incidences directly and e.g., identifies the maximum or minimum angle to define a cycle. A mechanical setup may have small deviation from cycle to cycle and the resulting incidence is never fully identical. The post processing should be able to properly identify a cycle even if the AoA deviates a bit or if the number of sample differs. The method used within the publications is based on the Hilbert transform, which is commonly used in signal and data processing [45]. It is an integral transform defined by eq. (5-1) which is included in the Matlab signal processing toolbox and may be called by `hilbert` [46].

$$h_{HT}(t) = \text{HT}\left\{f(t)\right\} = \frac{1}{\pi}\int_{-\infty}^{\infty}\frac{f(\tau)}{t-\tau}\mathrm{d}\tau \tag{5-1}$$

The Hilbert transform is especially useful in cycle separation of sinusoidal cycles because the phase of $h_{HT}(t)$ is a sawtooth signal if $f(t)$ is a pure sinusoid [46]. This is used to separate the cycles in the continuous data of the present thesis. The function $f(t)$ used for the transform within the data processing is the normalized AoA, whose mean was additionally removed. Assuming a pure sinusoid, the mean α_m in eq. (5-2) and the amplitude α_amp in eq. (5-3) are applied to normalize the AoA in eq. (5-4). The resulting $f_\alpha(t)$ is used in the Hilbert transform in eq. (5-1).

$$\alpha_\text{m} = \frac{\max\left[\alpha(t)\right] + \min\left[\alpha(t)\right]}{2} \tag{5-2}$$

$$\alpha_\text{amp} = \max[\alpha\left(t\right)] - \min\left[\alpha(t)\right] \tag{5-3}$$

$$f_\alpha(t) = \frac{\alpha(t) - \alpha_\text{m}}{\alpha_\text{amp}} \tag{5-4}$$

The phase of the resulting Hilbert transform is used to identify the exact samples defining the borders between the cycles. This process is robust against deviations in incidence

as well as in sample count per cycle. If the number of samples is different within the cycles, an additional resampling step in post processing is conducted to provide all cycles with identical sample count for further analysis. This resampling does not significantly affect the accuracy but facilitates a significant speed up in further data analysis.

5.2 Review of selected inflow conditions

While the previous section concentrated on challenges of the setup, the next will discuss the experimental parameters chosen in the publications in chapter 3. The papers did not verify the selected inflow velocities u_∞, which were set to fixed values in the experiments. The purpose of the present theses is to provide reliable airfoil data at conditions relevant to small wind turbine applications. Therefore, the tip speed ratio (TSR) will be used in the following to get an idea of possible combinations of wind speed and TSR which would lead to the experimental flow velocities selected. The TSR is the ratio between the tip speed and wind speed, eq. (5-5).

$$\mathrm{TSR} = \frac{u_\mathrm{tip}}{u_\mathrm{wind}} \tag{5-5}$$

The respective wind speed u_wind may be calculated if a predefined TSR is given and assuming $u_\infty \approx u_\mathrm{tip}$. This is a simplification because the real inflow velocity is a sum of the vectors wind and tip speed and continuously changing during a full revolution of a VAWT. Nonetheless, this vector addition can result in $u_\infty = u_\mathrm{tip}$. Typical TSRs of Darrieus turbines are in the range of TSR $\in [3, 5]$ [47, 48] and table 1 summarizes the calculated wind speeds u_wind based on the given TSRs which are relevant for VAWTs. Blades are in deep stall for TSR lower than two and if higher than five to six drag becomes dominant and reduces turbine performance [48]. All Reynolds numbers shown are chord based with $c = 0.14\,\mathrm{m}$. As mentioned previously, literature assumes mean wind speeds in the range of $u_\mathrm{wind} \in [3, 5.5]\,\mathrm{m/s}$ [9, 10] for urban environment. Table 1 shows that the experimental inflow velocities match these wind speeds for Darrieus typical TSR. The experimental data can be applied even if the TSR is lower, resulting in higher calculated wind speeds which are also of interest. An environment with a mean wind speed of $5\,\mathrm{m/s}$ will have occasionally higher wind speeds, e.g., $u_\mathrm{wind} = 10\,\mathrm{m/s}$ (TSR = 2) could represent a gust during turbine start up.

The focus on two Reynolds numbers $Re_c = 140\,\mathrm{k}$ and $200\,\mathrm{k}$ covers the entire range

	TSR	2	3	4	5	6
$u_\infty = 10\,\mathrm{m/s}$ ($Re_c \approx 100\,000$) used in 3.1	$\Rightarrow u_\mathrm{wind}$ in (m/s)	5.00	3.33	2.50	2.00	1.67
$u_\infty = 15\,\mathrm{m/s}$ ($Re_c \approx 140\,000$) used in 3.1-3.4	$\Rightarrow u_\mathrm{wind}$ in (m/s)	7.50	5.00	3.75	3.00	2.50
$u_\infty = 20\,\mathrm{m/s}$ ($Re_c \approx 200\,000$) used in 3.1-3.4	$\Rightarrow u_\mathrm{wind}$ in (m/s)	10.00	6.67	5.00	4.00	3.33

Table 1: Re_c and according inflow velocity u_∞ in correlation to real wind speeds u_wind at predefined TSRs of a wind turbine

of typical wind speeds expected. Thus, it is no flaw to reduce the number of different velocities in papers 3.2 to 3.4 from three to two. The periodic AoA changes per revolution of an VAWT are TSR dependent. Oscillation amplitudes of 12 deg (TSR = 5), 30 deg (TSR = 2) or 42 deg (TSR = 1.5) may occur [48]. The sinusoidal variations in chapter 3 are mainly focused on amplitudes of 10 deg with extensions of 45 deg and the extreme case of 90 deg amplitude. This extreme is possible for VAWTs but just if TSR < 1, thus the resulting wind direction may be back to front for during some of the azimuthal positions. In conclusion of this section – the analysis of the chosen inflow conditions has proven to be a suitable setting that provides new airfoil data relevant to VAWT application. This includes the static polars as well as the investigation of dynamic AoA changes.

5.3 Discussion of the results

The aerodynamic assessment of a NACA 0021 airfoil section at low Reynolds numbers is the overarching topic of the present thesis. This includes AoAs beyond values typically found in literature as well as the sinusoidal variation of incidences. Polar measurements at fixed angles are the basis of all discussions. The static experiments, i.e., in paper 3.1, have proven a good overall repeatability even though several key findings were present. The influence of the wind tunnel was discussed and literature provided enough data representing wind tunnels with closed test sections, some of them large enough with minimal blockage and others with high blockage ratios. Additionally, some open jet data was included and the comparison showed significant differences, i.e., in drag but also in lift, which was assessed in most of the papers. The drag measured in open jet wind tunnels is significantly lower at high AoA up to 90 deg than in closed test sections. The work of Du et al. [49, 50] includes a more detailed discussion than presented in this thesis. The lift curve revealed an additional stall about eight to ten degrees after the first stall. This second abrupt decrease in lift is known in literature [14, 49–51] and e.g., Du et al. argue that the wake broadens if the point of separation moves from suction to pressure side [49]. Thus, the lift is further reduced. The second stall may not be present in data sets acquired in closed test sections with increased blockage because walls affect the expansion of the wake when separation moves to the pressure side [49].

Another key finding was revealed analyzing the hysteresis effects in static polars. Literature did not provide hysteresis data for the full range, however, comparison to open jet literature has shown a good agreement for pitch up. Consequentially the pitch down data is presumed to be valid. The experiments show a second hysteresis loop in the range of 140 deg, which has nearly the same extent as the known loop around 20 deg. The sharp trailing edge is pointing upstream at 140 deg and the delayed reattachment during pitch up and a longer attached flow during pitch down form this loop. However, the standard deviation has an order of magnitude, i.e., comparable to maximum lift, which indicates a highly dynamic flow field in this range. The increase in standard deviation in the typical stall region around 20 deg is negligible compared to $2\sigma_{C_l} \approx C_{\mathrm{l,max}}$ in the range of 140 deg. The influence of wind tunnel setups on the hysteresis loops cannot be discussed because no data for comparison is available but it would be plausible if e.g., wall effects would affect the stall behavior in this AoA regime.

Setups are known to influence airfoil measurements and literature provides numerous corrections methods [52–56]. Nonetheless, nearly all the data presented in this thesis is uncorrected. The range of incidences may not be fully covered by the theories used to develop the correction methods. Thin airfoil theory would work for thin streamlined bodies with small wakes, which allow to assume a negligible influence of thickness and that friction drag is dominant [21]. The resulting linearized correction methods could be

applied for small AoA and thin airfoils [52] but they are not valid for large AoA, i.e., not for the full range, and additionally the NACA 0021 is not a thin airfoil. The airfoil has a large wake, separated flow at larger incidences, and behaves like a bluff body [21]. The drag of bluff bodies is dominated by pressure drag and friction drag may be neglected most of the time [21]. General correction methods for bluff bodies cover effects of nozzle and collector blockage as well as an increasing pressure gradient and jet expansion [57]. However, these corrections would not fit for small AoA. The airfoil's behavior over this large range of incidences from zero to 180 deg is finally a mixture between streamlined and bluff bodies. No correction is valid over the entire range and consequentially uncorrected data is presented within this thesis. This allows an application of any correction method useful for future comparisons. The typical correction methods used for 2D airfoil measurements are listed by Barlow et al.: buoyancy, solid blockage, streamline curvature, and wake blockage [53]. A variation of static pressure along the axis of test section causes buoyancy effects, but this is not relevant for open jet measurements. The solid blockage correction would account for walls confining the flow around the model and the streamline curvature is corrected because walls prevent the curvature of free air stream around the body, which appears to have more curvature than in an unconfined surrounding. Both methods are obsolete because of missing walls in the setup. The wake blockage effect causes an over speed region outside of the wake, which is negligible for open jet configurations [53]. Thus, the four standard corrections proposed by Barlow et al. for 2D airfoil measurements may be neglected for the present setup.

However, any setup has an influence on the measurement. The present thesis uses numerical simulations to identify the difference between the open jet and a clean free stream. The wind tunnel setup and an open field were simulated using U-RANS. The cooperation between experimental and numerical investigators was beneficial for both sides. The simulation of the wind tunnel setup is validated against experimental results, which were in very good agreement. The pressure distributions of both approaches were nearly identical for AoA up to the limit of 15 deg at which the simulation deviated. The location and shape of the separation bubble were well predicted. The deviations with increasing incidence shown in paper's 3.3 figure 11 were expected because the numerical model has its limitations to predict the transition from laminar to turbulent flow. The comparison between open field and wind tunnel simulation visualized the deflection of the open jet with increasing AoA, which results in a deviation of local incidence because the surrounding flow is deflected. This is plausible and known by literature [52]. The correction methods proposed by Garner [52] for open jet airfoil measurements unfortunately assume an infinitely long jet that is undistorted by the model, which is not valid for the present setup. Thus, the numeric simulation was used to propose a correction method matching the present setup. The U-RANS simulation was performed up to 30 deg because at higher AoA the onset of highly unsteady phenomena occur, like vortex shedding which is beyond the stable applicability of U-RANS simulation. The corrections improved the comparability to literature data within this range. The present measurements coincide after correction with measurements of low blockage closed section measurements, e.g., by Raghunathan et al. [58], which were presented by paper 3.4.

The U-RANS based correction was used to compare numeric and experimental results. CFD was able to predict the slope of lift and drag polars up to the stall angle but deviates significantly for moment coefficients above 10 deg. Additionally, maximum lift and stall angle were underestimated. CFD deviates from experiment if a precise prediction of laminar-turbulent transition becomes crucial. Nonetheless, the simulation was additionally used to simulate some of the dynamic AoA variations to evaluate the limits of U-RANS in these applications. The simulation was able to predict hysteresis loops in lift and drag

adequately for dynamic near stall investigations up to 20 deg with known discrepancies in the pitching moment. Increasing the maximum AoA of variation from 20 deg to 25 deg and finally to 30 deg revealed a nearly acceptable result for 25 deg but the 30 deg simulation was not satisfactorily in agreement with the experiments. To sum up, simulations are able to capture general trends and form of hysteresis loop in dynamic variations, but the lift overshoots are over predicted and the numerical results are oscillating during pitch down. Post stall variations are not acceptable at all. However, U-RANS simulations have proven to be extremely useful to investigate the influence of the experimental setup.

Dynamic AoA variations are inherent in VAWTs and at least U-RANS simulations were not able to predict airfoil performance of dynamic cycles exceeding stall angle. The insights provided by the experiments presented in chapter 3 are therefore valuable to understand the dynamics of VAWT applications in more detail and to serve as validation data for other numeric simulations. During start-up with no or very low rotation of the turbine (TSR < 1) the incidence varies from zero to 180 deg. Static as well as dynamic full range investigations have shown, that the range of $\alpha \in [140, 160]$ deg should be investigated in more detail if the start-up behavior is of interest. The region is dominated by highly oscillating phenomena which increase drag in dynamic cycles. Even if the turbine has not started yet and the AoA variation is based on a change in wind direction, these oscillations may be a source of noise and vibration which reduces the acceptance of small wind turbines in urban environment if perceptible in the neighborhood. The range of high volatility was not affected by an increase in inflow velocity.

The parameter variation in dynamic experiments has proven that none of the sinusoidal oscillations behaved quasi-steady. Though, the reduced frequency k was within the range $0 < k \leq 0.05$ which is regarded as quasi-steady aerodynamics [14, 59]. Decreasing the frequency k was reducing the cycle to cycle variation at near stall but for deep stall the decrease lead to more variation reaching $k = 0.005$ and $k = 0.0025$. Paper 3.2 investigates oscillation ranges which are characterized by stall effects in static polar. Analysis revealed that flow stability changes if k was altered but no proper trend can be determined. Consequentially sinusoidal movements in these regions have to be regarded as unsteady within the Reynolds regime investigated even if $k < 0.05$.

The bi-stability of the flow around the NACA 0021 has not been documented yet in literature to the author's knowledge. Experiments have shown that shape and extension of the hysteresis loop may change from cycle to cycle, e.g., switching from an attached flow state to full stall and back. This behavior was documented for multiple ranges of AoAs and different reduced frequencies. Consequentially, calculating a simple average over all cycles is not applicable per default. Paper 3.2 separated the different flow states by manual binning. The existence of different flow states for the same AoA range is crucial, i.e., if the data should be used for validation of numeric results. The U-RANS simulation in paper 3.4 predicted just one state which represents just a third of cycles investigated but possibly another numerical approach may lead to the other state. Without knowledge of the second state, different results may be discarded due to the deviations to the known state.

The differentiation of states can be done manually as shown in paper 3.2 but an automated binning method was introduced in chapter 4 and has proven useful. The `k-means++` clustering algorithm was able to separate intermediate flow cases as well as highly fluctuating cases. The test cases were additionally used to discuss the aerodynamic differences of different states even if the statistical validity was not optimal due to the reduced number of cycles available. The intermediate states showed different stages: attached flow, TE stall, LE stall, and transition states between them. The cycles per bin are not consecutive or jump in a fixed order from one cluster to the next. The abrupt changes in lift, drag, and

moment while switching between flow states will lead to an increased dynamic loading of the wind turbine. If sensitive AoA ranges are known in advance of the turbine design, the planned operation point should avoid these ranges. This reinforces the opinion of Bianchini et al. [16] stating the turbine layout depends on the inflow conditions and should ensure a good energy extraction over a wider range of conditions. Profound knowledge of the airfoil's dynamic behavior is necessary before companies are able to incorporate the necessary design changes. The switching process between different states can be analyzed in more detail e.g., using cluster transition matrices which was done in literature, e.g., for shear flows [40], mixing layers [41], and separated flows [42]. This more detailed analysis could identify if several clusters represent states of the same mode or define an additional mode. Unfortunately, a comparable analysis for the present data would be beyond the scope of the thesis and requires significantly more cycles than available. Several hundred repetitions would provide a solid basis for further analysis. Nonetheless, the clustering of highly fluctuating data in chapter 4 revealed huge pressure fluctuations on the suction side during pitch down in the range of $130\,\text{deg} < \alpha < 160\,\text{deg}$ which coincides with the region of high standard deviation in the static polars. The pressure data indicate vortex structures inducing low pressures convecting over the airfoil's surface.

5.4 Concluding remarks and future work

The present work analyzes the aerodynamic performance of a NACA 0021 airfoil section at incidences and Reynolds numbers which literature is lacking. Aircraft industry dominated the historic airfoil research and thick airfoils beyond stall were not of interest. Though wind turbine industry becomes more important the present study fills a gap especially relevant for vertical axis wind turbines. The larger AoA variations of 45 deg and 90 deg are representative of the start-up phase with low TSR, which is of extremely high interest because of its significance for the economic payback period [14, 15]. The smaller variations of 20 deg are part of possible operating conditions [48] and provide insights into possible sources of vibrations that may affect the long-term reliability of the turbine. The experimental data shown and the setup used, build a basis that will eventually pave the way for further investigations to extend the parametric studies regarding velocity, reduced frequency, and AoA ranges. Although the work is only limited to few examples within the parametric room available, several key findings were found:

1. A second hysteresis loop exists $140\,\text{deg} < \alpha < 150\,\text{deg}$
   - High standard deviation in the order of $2\sigma \approx c_{\text{l,max}}$ in static measurements
   - Large pressure fluctuations in dynamic AoA variations
2. U-RANS simulation appropriate to identify the influence of setup and get an idea of correction methods
   - Well calibrated simulation able to predict dynamic hysteresis loops at least at incidences near stall
3. Sinusoidal AoA changes are not quasi-steady even if $k < 0.05$
   - Resulting flow may be at least bi-stable
   - No general trends detectable by varying k or Re
4. Automated binning using `k-means++` algorithm promising
   - Able to distinguish between different flow states
   - Good basis for further analysis if large numbers of cycles are available

Future projects are not limited to the parameters investigated in this thesis. A research work always has the side effect of developing ideas of setup extension or further research ideas. Some of them will be presented in the following paragraphs to inspire other researchers who may continue.

Setup optimization

Some challenges discussed in section 5.1 were caused by shortcomings of the setup. The major issue to be solved is the single point measurement of the inflow velocity. The measurement of the nozzle differential pressure is important and has to be realized for any future experiment. The redundancy of acquisition methods enables the researcher to identify malfunctions and inaccuracies are reduced.

A change of the airfoil mounting system would result in a larger redesign of the setup. Nonetheless, this could offer the possibility to include a balance measuring normal and tangential forces of the airfoil. The present setup prevents such installation because the balance system is sensitive to crosswise bending moments. These moments occur because the airfoil is a structural part of the setup transferring bending loads.

Different types of AoA variation

This thesis concentrates on sinusoidal AoA variations but the setup is capable of arbitrary cycle definition within the setup's limits of inertia and acceleration. Future studies may focus on any cycles, e.g., representing the tower effect, gusts, or cutting the wake of a preceding blade, as long as the phenomena may be represented by a sequence of AoA at constant inflow velocities. The AoA series can be provided by measurements of real turbines or numerical simulations. Real AoA series could lead to results 'nearer' to industry application. This may be of interest if an existing turbine experiences vibrations or issues during start-up.

A second approach would focus on cycles less complex with constant angular velocity. This would lead to more insights into the flow physics. Sinusoidal cycles are a combination of changing AoA and angular velocity. The elimination of one variable enables the investigator to differentiate between the influences.

Flow field measurements

The data presented in this work is based on surface pressure measurements which do not include any information on the flow field around the airfoil. Pressures may indicate different flow phenomena but cannot show the real flow field. A particle-image-velocimetry campaign may provide further insights into bi-modal flows and identify causes for the large fluctuations during pitch down at high incidences around 140 deg. Additionally, the field information could be used to validate the results of numeric simulations.

Passive flow control

All experiments presented in this work as well as all extensions and further parameters are based on a clean airfoil. However, any experiment could be repeated with passive flow control elements applied to the airfoil. If literature lacks baseline data the gap is even larger for flow control applications. The setup is well suited to investigate the influence of vortex generators or Gurney flaps because no setup alterations are necessary. The integration of active flow control, e.g., blowing or moving flaps, would be challenging because of limited space within the model and additional cabling or tubing connected to the rotating system.

References

[1] IEA Wind. IEA Wind 2020 Annual Report. Technical report, International Energy Agency, August 2021.

[2] Bundesministerium für Wirtschaft und Klimaschutz. Bulletin der Bundesregierung 60-1. https://www.bundesregierung.de/resource/blob/992814/2039592/1c84a75ff3d34f3267dd14b3bfc20e47/60-1-bmwk-energie-data.pdf?download=1, 2022. (Last visited 07.06.2022).

[3] IEA Wind. IEA Wind task 41 Report 2020. Technical report, International Energy Agency, 2021.

[4] Daniel Fraile, Alexander Vadnenberghe, Vasiliki Klonari, Lizet Ramirez, Ivan Pineda, Pierre Tardieu, Blandine Malvault, and Ivan Komusanac. Getting fit for 55 and set for 2050 - Electrifying Europe with wind energy. Technical report, ETIP Wind, 2021.

[5] IEA Wind. IEA Wind Task 41. https://iea-wind.org/task41/, 2022. (Last visited 07.06.2022).

[6] Stefan Gsänger and Jean Pitteloud. Small Wind World Report 2014. Technical report, World Wind Energy Association, 2014.

[7] IEA Wind. *IEA Wind Energy Annual Report 2006*. PWT Communications, 2007.

[8] Zdenko Simic, Juraj George Havelka, and Maja Bozicevic Vrhovcak. Small wind turbines - A unique segment of the wind power market. *Renewable Energy*, 50(50): 1027 – 1036, 2013. ISSN 0960-1481. doi: 10.1016/j.renene.2012.08.038.

[9] J.L. Acosta, K. Combe, S.Z. Djokić, and I. Hernando-Gil. Performance Assessment of Micro and Small-Scale Wind Turbines in Urban Areas. *Systems Journal, IEEE*, 6 (1):152–163, March 2012. ISSN 1932-8184. doi: 10.1109/JSYST.2011.2163025.

[10] Benno Grieser, Yasin Sunak, and Reinhard Madlener. Economics of small wind turbines in urban settings: An empirical investigation for Germany. *Renewable Energy*, 78:334–350, 2015. ISSN 0960-1481. doi: 10.1016/j.renene.2015.01.008. URL https://www.sciencedirect.com/science/article/pii/S0960148115000154.

[11] Sandra Eriksson, Hans Bernhoff, and Mats Leijon. Evaluation of different turbine concepts for wind power. *Renewable and Sustainable Energy Reviews*, 12(5):1419–1434, 2008. ISSN 1364-0321. doi: 10.1016/j.rser.2006.05.017.

[12] R. Dominy, P. Lunt, A. Bickerdyke, and J. Dominy. Self-starting capability of a Darrieus turbine. *Proceedings of the Institution of Mechanical Engineers, Part A: Journal of Power and Energy*, 221(1):111–120, 2007. doi: 10.1243/09576509JPE340. URL http://pia.sagepub.com/content/221/1/111.abstract.

[13] Supakit Worasinchai, Grant L. Ingram, and Robert G. Dominy. The Effects of Improved Starting Capability on Energy Yield for Small HAWTs. In *Proceedings of the ASME Turbo Expo 2011, June 6-10, Vancouver, British Columbia, Canada*, 2011. doi: 1115/GT2011-45674.

[14] Supakit Worasinchai. *Small Wind Turbine Starting Behaviour*. PhD thesis, School of Engineering and Computing Sciences, University of Durham, 2012.

[15] Supakit Worasinchai, Grant L. Ingram, and Robert G. Dominy. Effects of Wind Turbine Starting Capability on Energy Yield. *J Eng Gas Turb Power*, 134(4):042603–1 – 042603–9, February 2012. doi: 10.1115/1.4004741.

[16] Alessandro Bianchini, Giovanni Ferrara, and Lorenzo Ferrari. Design guidelines for H-Darrieus wind turbines: Optimization of the annual energy yield. *Energy Conversion and Management*, 89:690–707, 2015. ISSN 0196-8904. doi: 10.1016/j.enconman.2014.10.038. URL `https://www.sciencedirect.com/science/article/pii/S0196890414009194`.

[17] Zhenzhou Zhao, Dingding Wang, Tongguang Wang, Wenzhong Shen, Huiwen Liu, and Ming Chen. A review: Approaches for aerodynamic performance improvement of lift-type vertical axis wind turbine. *Sustainable Energy Technologies and Assessments*, 49:101789, 2022. ISSN 2213-1388. doi: 10.1016/j.seta.2021.101789. URL `https://www.sciencedirect.com/science/article/pii/S2213138821008031`.

[18] Alessandro Bianchini, Francesco Balduzzi, John M. Rainbird, Joaquim Peiro, J. Michael R. Graham, Giovanni Ferrara, and Lorenzo Ferrari. An Experimental and Numerical Assessment of Airfoil Polars for Use in Darrieus Wind Turbines - Part I: Flow Curvature Effects. *J Eng Gas Turb Power*, 138(3):032602–1–032602–10, September 2015. ISSN 0742-4795. doi: 10.1115/1.4031269. URL `http://dx.doi.org/10.1115/1.4031269`.

[19] Alessandro Bianchini, Francesco Balduzzi, John M. Rainbird, Joaquim Peiro, J. Michael R. Graham, Giovanni Ferrara, and Lorenzo Ferrari. An Experimental and Numerical Assessment of Airfoil Polars for Use in Darrieus Wind Turbines - Part II: Post-stall Data Extrapolation Methods. *J Eng Gas Turb Power*, 138(3):032603–1–032603–10, September 2015. ISSN 0742-4795. doi: 10.1115/1.4031270. URL `http://dx.doi.org/10.1115/1.4031270`.

[20] Hermann Schlichting and Klaus Gersten. *Grenzschicht-Theorie*. Springer-Verlag Berlin Heidelberg, 10. auflage edition, 2006.

[21] Herbert Sigloch. *Technische Fluidmechanik*. Springer-Verlag Berlin Heidelberg, 10. Auflage edition, 2017.

[22] Hermann Schlichting and Erich Trunkenbrodt. *Aerodynamik des Flugzeugs Erster Band: Grundlagen aus der Strömungstechnik Aerodynamik des Tragflügels (Teil I)*. Springer-Verlag Berlin Heidelberg, 3. auflage edition, 2001.

[23] H. H. Fernholz and D. Warnack. The effects of a favourable pressure gradient and of the Reynolds number on an incompressible axisymmetric turbulent boundary layer. Part 1. the turbulent boundary layer. *Journal of Fluid Mechanics*, 359:329–356, 1998. doi: 10.1017/S0022112097008513.

[24] D. Warnack and H. H. Fernholz. The effects of a favourable pressure gradient and of the Reynolds number on an incompressible axisymmetric turbulent boundary layer. part 2. the boundary layer with relaminarization. *Journal of Fluid Mechanics*, 359:357–381, 1998. doi: 10.1017/S0022112097008501.

[25] Bruno Stefes. *Turbulente Wandgrenzschichten mit und ohne negativen Druckgradienten unter dem Einfluss hoher Turbulenzintensität der Außenströmung*. Doctoral thesis, Technische Universität Berlin, Fakultät V - Verkehrs- und Maschinensysteme, Berlin, 2003. URL `http://dx.doi.org/10.14279/depositonce-805`.

[26] Karsten Knobloch. *Skalierungen und Zweipunkt-Geschwindigkeitskorrelationen in turbulenten Grenzschichten bei großen Reynoldszahlen.* Doctoral thesis, Technische Universität Berlin, Fakultät V - Verkehrs- und Maschinensysteme, Berlin, 2008. URL `http://dx.doi.org/10.14279/depositonce-2044`.

[27] H. Bergh and H. Tijdeman. Theoretical and Experimental Results for the Dynamic Response of Pressure Measuring Systems. Technical Report NLR-TR F.238, National Aero- and Astronautical Research Institute, 1965.

[28] National Instruments. cRIO-9045. `https://www.ni.com/docs/en-US/bundle/crio-9045-specs/page/specs.html`, 2022. (Last visited 07.06.2022).

[29] National Instruments. cDAQ-9188. `https://www.ni.com/docs/en-US/bundle/cdaq-9188-specs/page/specs.html`, 2022. (Last visited 07.06.2022).

[30] National Instruments. NI-9215. `https://www.ni.com/docs/en-US/bundle/ni-9215-specs/page/specs.html`, 2022. (Last visited 07.06.2022).

[31] National Instruments. NI-9220. `https://www.ni.com/docs/en-US/bundle/ni-9220-specs/page/specifications.html`, 2022. (Last visited 07.06.2022).

[32] CAN in Automation. Classical Controller Area Network (CAN). `https://www.can-cia.org/can-knowledge/can/classical-can/`, 2022. (Last visited 13.06.2022).

[33] International Organization for Standardization. ISO 11898-1:2015 Road vehicles – Controller area network – Part 1: Data link layer and physical signalling. `https://www.iso.org/standard/63648.html`, 2022. (Last visited 13.06.2022).

[34] International Organization for Standardization. ISO 11898-2:2016 Road vehicles – Controller area network – Part 2: High-speed medium access unit. `https://www.iso.org/standard/67244.html`, 2022. (Last visited 13.06.2022).

[35] International Organization for Standardization. ISO 11898-3:2006 Road vehicles – Controller area network – Part 3: Low-speed, fault-tolerant, medium-dependent interface. `https://www.iso.org/standard/36055.html`, 2022. (Last visited 13.06.2022).

[36] International Organization for Standardization. ISO 11898-4:2004 Road vehicles – Controller area network – Part 4: Time-triggered communication. `https://www.iso.org/standard/36306.html`, 2022. (Last visited 13.06.2022).

[37] International Organization for Standardization. ISO 11898-5:2007 Road vehicles – Controller area network – Part 5: High-speed medium access unit with low-power mode. `https://www.iso.org/standard/41284.html`, 2022. (Last visited 13.06.2022).

[38] International Organization for Standardization. ISO 11898-6:2013 Road vehicles – Controller area network – Part 6: High-speed medium access unit with selective wake-up functionality. `https://www.iso.org/standard/59165.html`, 2022. (Last visited 13.06.2022).

[39] Mattke AG Servotechnik. CANopen - Handbuch Servopositionierregler MDR 2000, V 1.5, 2006.

[40] Eurika Kaiser, Bernd R. Noack, Laurent Cordier, Andreas Spohn, Marc Segond, Markus Abel, Guillaume Daviller, Marek Morzyński, Jan Östh, Siniă Krajnović, and Robert K. Niven. Cluster-based reduced-order modelling of shear flows. *AIP Conference Proceedings*, 1636(1):151–158, 2014. doi: 10.1063/1.4903725.

[41] Eurika Kaiser, Bernd R. Noack, Laurent Cordier, Andreas Spohn, Marc Segond, Markus Abel, Guillaume Daviller, Jan Östh, Siniša Krajnović, and Robert K. Niven. Cluster-based reduced-order modelling of a mixing layer. *Journal of Fluid Mechanics*, 754:365–414, 2014. doi: 10.1017/jfm.2014.355.

[42] Aditya G. Nair, Chi-An Yeh, Eurika Kaiser, Bernd R. Noack, Steven L. Brunton, and Kunihiko Taira. Cluster-based feedback control of turbulent post-stall separated flows. *Journal of Fluid Mechanics*, 875:345–375, 2019. doi: 10.1017/jfm.2019.469.

[43] Stuart P. Lloyd. Least squares quantization in PCM. *IEEE Transactions on Information Theory*, 28(2):129 – 137, 1982. doi: 10.1109/TIT.1982.1056489.

[44] David Arthur and Sergei Vassilvitskii. K-Means++: The Advantages of Careful Seeding. In *SODA '07: Proceedings of the eighteenth annual ACM-SIAM symposium on Discrete algorithms*, pages 1027 – 1035, USA, 2007. Society for Industrial and Applied Mathematics. ISBN 9780898716245. URL `https://dl.acm.org/doi/10.5555/1283383.1283494`.

[45] Cameron Tropea, Alexander Yarin, and John Foss, editors. *Springer Handbook of Experimental Fluid Mechanics*. Springer-Verlag Berlin Heidelberg, 01 2007. ISBN 9783540251415. doi: 10.1007/978-3-540-30299-5.

[46] Mathworks. hilbert – Discrete-time analytic signal using Hilbert transform. `https://www.mathworks.com/help/signal/ref/hilbert.html`, 2022. (Last visited 21.06.2022).

[47] Richard Zahoransky, editor. *Energietechnik: Systeme zur Energieumwandlung. Kompaktwissen für Studium und Beruf*. Springer Fachmedien Wiesbaden, Wiesbaden, 2015. ISBN 978-3-658-07454-8. doi: 10.1007/978-3-658-07454-8_13.

[48] A. Sagharichi, M. J. Maghrebi, and A. ArabGolarcheh. Variable pitch blades: An approach for improving performance of Darrieus wind turbine. *Journal of Renewable and Sustainable Energy*, 8(5):053305, 2016. doi: 10.1063/1.4964310.

[49] Longhuan Du, Arganthaël Berson, and Robert G Dominy. Aerofoil behaviour at high angles of attack and at Reynolds numbers appropriate for small wind turbines. *Proceedings of the Institution of Mechanical Engineers, Part C: Journal of Mechanical Engineering Science*, 229(11):2007–2022, 2014. doi: 10.1177/0954406214550016. URL `http://pic.sagepub.com/content/229/11/2007`.

[50] Longhuan Du, Arganthaël Berson, and Robert G Dominy. NACA0018 behaviour at high angles of attack and at Reynolds numbers appropriate for small wind turbines. Technical Report ECS-TR 2014/08, School of Engineering and Computing Sciences, Durham University, Durham, UK, 2014. URL `https://www.dur.ac.uk/resources/ecs/research/technical_reports/2014_08.pdf`.

[51] Supakit Worasinchai, Grant L. Ingram, and Robert G. Dominy. A low-Reynolds-number, high-angle-of-attack investigation of wind turbine aerofoils. *Proceedings of the Institution of Mechanical Engineers, Part A: Journal of Power and Energy*, 225 (6):748–763, 2011. doi: 10.1177/0957650911405411.

[52] H. C. Garner, editor. *AGARDograph 109 - Subsonic Wind Tunnel Wall Corrections*. NATO - AGARD, Paris, France, 1966. URL `http://www.dtic.mil/dtic/tr/fulltext/u2/657092.pdf`.

[53] Jewel B. Barlow, William H. Rae Jr., and Alan Pope. *Low-Speed Wind Tunnel Testing*. John Wiley & Sons, Ltd - New York, 1999.

[54] D. Althaus. Tunnel-wall corrections at the laminar wind tunnel. `https://www.iag.uni-stuttgart.de/dateien/pdf/laminarwindkanal_messtechniken/althaus_1.pdf`, 2004. (Last visited 22.06.2022).

[55] B. F. R. Ewald, editor. *AGARDograph 336 - Wind Tunnel Wall Corrections*. NATO - AGARD, Neuilly-sur-Seine Cedex, France, 1998. URL `http://www.dtic.mil/dtic/tr/fulltext/u2/a356695.pdf`.

[56] Michael S. Selig, Robert W. Deters, and Gregory A. Wiliamson. Wind Tunnel Testing Airfoils at Low Reynolds Numbers. In *Aerospace Sciences Meetings*. American Institute of Aeronautics and Astronautics, January 2011. doi: 10.2514/6.2011-875.

[57] Wolf-Heinrich Hucho. *Aerodynamik der stumpfen Körper*, volume 2. Vieweg+Teubner Verlag Wiesbaden, 2012. ISBN 978-3-8348-8243-1. doi: 10.1007/978-3-8348-8243-1.

[58] S. Raghunathan, J. R. Harrison, and B. D. Hawkins. Thick airfoil at low reynolds number and high incidence. *Journal of Aircraft*, 25(7):669–671, July 1988. doi: 10.2514/3.45641.

[59] J. Gordon Leishman. *Principles of Helicopter Aerodynamics*. Cambridge university press, 2006.

Associated publications

D. Holst, A. B. Bach, C. N. Nayeri, and C. O. Paschereit. Influence of a Finite Width Micro-Tab on the Spanwise Lift Distribution. In *Proceedings of the ASME Turbo Expo 2013, June 3-7, San Antonio, Texas, USA*, page V008T44A011, June 2013. ISBN 978-0-7918-5529-4. doi: 10.1115/GT2013-94381. ASME Paper GT2013-94381.

D. Holst, A. B. Bach, C. N. Nayeri, C. O. Paschereit, and G. Pechlivanoglou. Wake Analysis of a Finite Width Gurney Flap. *J Eng Gas Turb Power*, 138(6):062602–1 – 062602–10, Nov. 2015. ISSN 0742-4795. doi: 10.1115/1.4031709.

D. Holst, G. Pechlivanoglou, C. T. Kohlrausch, C. N. Nayeri, and C. O. Paschereit. sHAWT Design: Airfoil Aerodynamics Under the Influence of Roughness. In *Proceedings of the ASME Turbo Expo 2016, June 13-17, Seoul, South Korea*, June 2016a. ISBN 978-0-7918-5529-4. doi: 10.1115/GT2016-56377. ASME Paper GT2016-56377.

D. Holst, G. Pechlivanoglou, F. Wegner, C. N. Nayeri, and C. O. Paschereit. Potential of Retrofit Passive Flow Control for Small Horizontal Axis Wind Turbines. *J Eng Gas Turb Power*, 139(6):032604–1 – 032604–8, Mar. 2016b. ISSN 0742-4795. doi: 10.1115/1.4034543.

D. Holst, K. Thommes, M. Schönlau, C. N. Nayeri, and C. O. Paschereit. *Entwicklung eines aerodynamischen Prüfstands zur Flügelprofiluntersuchung von Kleinwindkraftanlagen unter dynamischen Winkeländerungen auf Basis eines cRIO-9068*, chapter Mess-, Prüf- und Regelungstechnik in Virtuelle Instrumente in der Praxis 2016, pages 54–57. VDE VERLAG, Berlin, 2016c. ISBN 978-3-8007-4208-0.

M. Lennie, A. Selahi-Moghaddam, D. Holst, G. Pechlivanoglou, C. N. Nayeri, and C. O. Paschereit. Vortex shedding and frequency lock in on stand still wind turbines, a baseline experiment. *J Eng Gas Turb Power*, 140:112603–1–13, July 2018. doi: 10.1115/1.4039818. GTP-17-1616.

J. Saverin, D. Marten, D. Holst, G. Pechlivanoglou, C. N. Nayeri, C. O. Paschereit, and G. Persico. Comparison of experimental and numerically predicted three-dimensional wake behaviour of a vertical axis wind turbine. *J Eng Gas Turb Power*, 140:122601–1–9, Aug. 2018. doi: 10.1115/1.4039935. GTP-17-1608.